# High emissivity coating containing ceria on basic refractory brick for cement rotary kiln

Jindaporn Juthapakdeeprasert

This dissertation is submitted for the fulfilment of the degree of Doctor of Philosophy (PhD)

Supervisor: Prof. William Edward Lee

Department of Materials
Imperial College London
August 2020

# Declaration of Originality

I declare that this thesis has not been previously accepted in substance for any degree and is not being concurrently submitted in candidature for any degree. I state that this thesis is the result of my own independent work/investigation, except where otherwise stated.

Jindaporn Juthapakdeeprasert

Date: August 2020

# Abstract

For many decades, the world has been facing a major problem involving the significant increase in energy consumption and $CO_2$ gas emissions. The cement industry is one of the top five contributors to this crisis. In the production of cement, the raw material must be heated to temperatures as high as 1450°C. Unfortunately, 40% of this energy is lost from heat energy, and approximately 20% of this lost energy is through heat transfer from the refractory lining and kiln shell. This thesis addresses this problem by developing a high emissivity coating to be applied to the refractory lining in the upper transition zone of the cement rotary kiln. The function of this coating is to absorb and re-emit the heat back inside the rotary kiln, which will lead to energy savings. In other words, the same amount of cement will be able to be produced using less energy. As a result, mixing $CeO_2$ with $AlH_6O_{12}P_3$ and sintering at 1300°C produces a coating having an emissivity of 0.8 in the infrared range, which is double the emissivity of uncoated refractory bricks. The reason that this coating provides high emissivity in the infrared range is that the infrared represents heat energy and the presence of $CeO_2$ in the coating has a high thermal activation, which leads to high lattice vibration and polaron absorption. Although this coating has been proven to possess a high level of emissivity and has the potential to provide energy savings when used at high temperatures, it has shown a poor behaviour when it is in an alkaline environment. Therefore, further improvement of its alkaline corrosion resistance is needed. Moreover, experiments on abrasion resistance and thermal shock resistance are also required to confirm if this coating will survive the harsh environment of a cement rotary kiln.

# Acknowledgments

Firstly, I would like to express my sincere gratitude to my advisor Prof. Bill Lee for the continuous support of my Ph.D. study and related research, for his patience, motivation, and immense knowledge. His guidance helped me in all the time of research and writing of this thesis. I could not have imagined having a better advisor and mentor for my Ph.D. study.

Besides my advisor, I would like to thank the rest of my thesis committee: Prof. Luc J M Vandeperre, and Dr. Doni D Jayaseelan, for their insightful comments and encouragement, and also for the hard question which incentivised me to widen my research from various perspectives.

My sincere thanks also go to Prof. Jacques Poirier, Dr. Emmanuel Debilbao, Dr. Domingos De Sousa Meneses, Prof. S.K. Sundaram and Dr. Paul P Woskov, who provided me an opportunity to join their team, and who gave access to the laboratory and research facilities. Without their precious support it would not be possible to conduct this research.

I would like to pay my special regards to SCG cement -building materials for sponsoring me for my education, living and travelling expense. They have given me the opportunity to study abroad in one of the top institutes like Imperial College London.

I wish to thank all my fellows in CASC for supporting me and keeping me company in the laboratory and the office. CASC is filled with some of the most brilliant people I have known, and they have built such an academic and collaborative environment. I feel so fortunate to be part of the CASC. Special thanks go to Dr. Gwilliherm Kerherve for your effort in helping me with XPS and Dr. Oriol Gavalda Diaz for spending so much time helping me with TEM and for being one of my best friends. I also like to thank Dr. Alba M. Matas Adams for helping me with all the administration work and keeping my Ph.D. on track, and Dr. Annalisa Neri for being such a sweet friend and introducing me to Zumba since first year which really helped me stay sane throughout my Ph.D. My heartfelt thanks go to all my Thai friends in the UK for sharing all the fun and happiness moment with me, without them my day-to-day life in London would not be complete.

Last but not the least, I would like to thank my family: my parents, my brother, sister in law and my niece and nephew for their endless love, encouragement which supported me spiritually throughout writing this thesis and my life in general.

# Publications and presentations

- J. Juthapakdeeprasert, W. Lerdprom, D.D. Jayaseelan and W.E. Lee, Cerium-added alumina and cerium-added zircon as high emissivity coatings for cement rotary kilns, Materials Science and Technology 2017 (MS&T 2017), PA, USA, **October 2017** (manuscript and presentation)
- J. Juthapakdeeprasert, D.D. Jayaseelan and W.E. Lee, The study on reactions between $CeO_2$ and $AlH_6O_{12}P_3$ for high temperature coating, Department of Materials Post Graduate Day, Imperial College London, UK, **March 2018** (poster)
- J. Juthapakdeeprasert, W. Lerdprom, D. De Sousa Meneses, D.D. Jayaseelan and W.E. Lee, $CeO_2$ and $CePO_4$ – containing high emissivity coating for basic refractory bricks, Proceedings International Colloquium on Refractories, Aachen, Germany, **September 2018**, (manuscript and presentation)
- J. Juthapakdeeprasert, D. De Sousa Meneses, D.D. Jayaseelan and W.E. Lee, Development of multi-functional refractory coating for cement kiln, Department of Materials Post Graduate Day, Imperial College London, UK, **March 2019** (presentation)
- J. Juthapakdeeprasert, W. Lerdprom, D. De Sousa Meneses, D.D. Jayaseelan and W.E. Lee, High Emissivity Coatings for Basic Refractory Bricks, Proceedings United International Technical Conference on Refractories 2019 (UNITECR 2019), Yokohama, Japan, **October 2019** (manuscript and presentation)
- J. Juthapakdeeprasert, O.G. Diaz, W. Lerdprom, D. De Sousa Meneses, D.D. Jayaseelan and W.E. Lee, Reactions and emissivity of cerium oxide with phosphate binder coating on basic refractory brick, International Journal of Applied Ceramic Technology, **February 2020**, 17(2): 668-676.
- Awarded popular vote in a 1-minute pitch poster presentation on the topic of “High emissivity coating for cement rotary kiln”, Sammaggi Samagom (Thai students association in the UK), London, UK, **February 2020**

# Contents

# List of figures

# List of tables

# List of abbreviations and symbols

| | |
|---|---|
| APS | Air plasma spray |
| ASTM | American society for testing and materials |
| BFS | Blast furnace slag |
| BR | Basic refractory |
| BRCe | Basic refractory 70 vol% mixed with $CeO_2$ 30 vol% |
| BRCeK | Basic refractory 48 vol% mixed with $CeO_2$ 10 vol% and $K_2CO_3$ 42 vol% |
| BSAS | Barium strontium aluminosilicate |
| $C_3A$ | Tricalcium aluminate |
| $C_4AF$ | Tetracalcium aluminoferrite |
| $C_4A_3\overline{S}$ | Ye'elimite |
| CBR 1-3 | Coated basic refractory- 1 $CeO_2$: 3$AlH_6O_{12}P_3$ vol. ratio |
| CBR 1-5 | Coated basic refractory- 1 $CeO_2$: 5$AlH_6O_{12}P_3$ vol. ratio |
| CBR 1-12 | Coated basic refractory- 1 $CeO_2$: 12$AlH_6O_{12}P_3$ vol. ratio |
| Ce | $CeO_2$ |
| CMC | Ceramic matrix composites |
| CMS | Monticellite |
| $C_3MS_2$ | Merwinite |
| CS 1-3 | Coating slurry: 1 $CeO_2$- 3$AlH_6O_{12}P_3$ vol. ratio |
| CS 1-5 | Coating slurry: 1 $CeO_2$- 5$AlH_6O_{12}P_3$ vol. ratio |
| CS 1-12 | Coating slurry: 1 $CeO_2$- 12$AlH_6O_{12}P_3$ vol. ratio |
| $C_2S$ | Dicalcium silicate |
| $C_3S$ | Tricalcium silicate |
| $C\overline{S}$ | Calcium sulfate |
| CSA | Calcium sulfoaluminate |
| CSH | Calcium silicate hydrate |
| DSC | Differential scanning calorimeter |
| EBCs | Environmental barrier coating |
| EB-PVD | Electron beam physical vapour deposition |
| EDX | Energy dispersive X-ray spectrometer |
| FIB | Focused ion beam |
| FTIR | Fourier transform infrared spectrometer |

| | |
|---|---|
| glass | M-P-O glass |
| HT-XRD | High temperature X-ray diffraction |
| IREM | Infrared emissivity measurement |
| $M_2S$ | Forsterite |
| MLS | Melt-like structure |
| NRP | Nelson-Riley parameter |
| OPC | Ordinary Portland cement |
| REM | Radiometer emissivity measurement |
| REO | Rare earth oxide |
| RSF | Relative sensitivity factor |
| SAD | Selected area diffraction |
| SCS 1-3 | Sintered coating slurries- 1 $CeO_2$: 3 $AlH_6O_{12}P_3$ vol. ratio |
| SCS 1-5 | Sintered coating slurries- 1 $CeO_2$: 5 $AlH_6O_{12}P_3$ vol. ratio |
| SCS 1-12 | Sintered coating slurries- 1 $CeO_2$: 12 $AlH_6O_{12}P_3$ vol. ratio |
| SCSP | Sintered coating slurry pellet |
| SCSP 1-3 | Sintered coating slurries pellet- 1 $CeO_2$: 3 $AlH_6O_{12}P_3$ vol. ratio |
| SCSP 1-5 | Sintered coating slurries pellet- 1 $CeO_2$: 5 $AlH_6O_{12}P_3$ vol. ratio |
| SCSP 1-12 | Sintered coating slurries pellet- 1 $CeO_2$: 12 $AlH_6O_{12}P_3$ vol. ratio |
| SEI | Secondary electron imaging |
| SEM | Scanning electron microscopy |
| STEM | Scanning transmission electron microscopy |
| TBCs | Thermal barrier coating |
| TEC | Thermal expansion coefficient |
| TEM | Transmission electron microscopy |
| TGA | Thermogravimetric analysis |
| TRR | Thermal return reflection |
| UHTC | Ultra-high temperature ceramic |
| WHRSG | Waste heat recovery steam generator |
| XPS | X-ray photoelectron spectroscopy |
| XRD | X-ray diffraction |
| YSZ | Yttria stabilized zirconia |

# Chapter 1: Introduction

The cement industry is one of the major contributors to the emissions of $CO_2$ and accounts for 5-8% of the global anthropogenic $CO_2$ emissions [1, 2]. The industry emits approximately 700 kg $CO_2$/tonne cement in western Europe and 900 - 935 kg $CO_2$/tonne cement in the US, China and India [2, 3]. The $CO_2$ emissions come from three segments: 50% from the calcination of limestone ($CaCO_3$ -> $CaO + CO_2$), 40% from fuel combustion energy (heating large volumes of raw materials to temperatures as high as 1450$^o$C) and 10% from the use of electrical energy [3]. Although much of the $CO_2$ emissions come from calcining of limestone, emissions from the energy consumption are equivalent. The energy consumption to produce 1 tonne of clinker is about 3 - 5 GJ, and over 2.5 billion metric tonnes of clinker are produced around the globe annually [4-7]. Studies have shown that throughout the processing of cement, 86% of the energy is spent on fuels for the burner [4, 8]. Unfortunately, 40% of the input energy is lost as heat [4], with nearly half of that lost through the shell of the kiln [9]. To make the production more efficient, cement rotary kilns are continually heated to avoid kiln heat up-shut down cycles where the heat energy is most consumed. However, maintaining the kiln at 1450$^o$C also requires a large amount of energy. This is due to the temperature difference between the inside and the outside environments of the kiln causing heat loss. To resolve this problem, heat transfer must be taken into consideration. Many studies have aimed to reduce cement production energy consumption and $CO_2$ emissions, as will be further discussed in the literature review section (section 2.1). This research aims to reduce energy loss from the kiln shell because this will facilitate both lower energy consumption and the reduction of $CO_2$ emissions.

The focus of this research is on the reduction of the heat transfer in the cement rotary kiln by developing a high emissivity coating. To achieve this, background knowledge of cement production, the refractory lining, heat transfer and emissivity must be considered. The background of these subjects is presented in sections 1.1-1.4. The concept is to apply a coating with high emissivity properties onto the hot face surface of the refractory bricks. Therefore, when the rotary kiln is in operation at a high temperature, the coating will absorb and re-emit the heat back inside the kiln, as shown in Figure 1, which compares two cross-section images of the cement rotary kiln lining. Figure 1a shows a conventional (without coating) cross-section of a cement kiln. As heat energy reaches the refractory brick surface, the heat transfers through the refractory bricks and kiln shell to the atmosphere due to the temperature difference. Figure 1b shows a cross-section of the cement kiln with high emissivity coating applied on the refractory brick surface. As shown in Figure 1b, less heat

will be transferred towards the environment due to some of the heat being absorbed and re-emitted back inside the rotary kiln. This concept can consequently reduce heat loss and increase kiln efficiency.

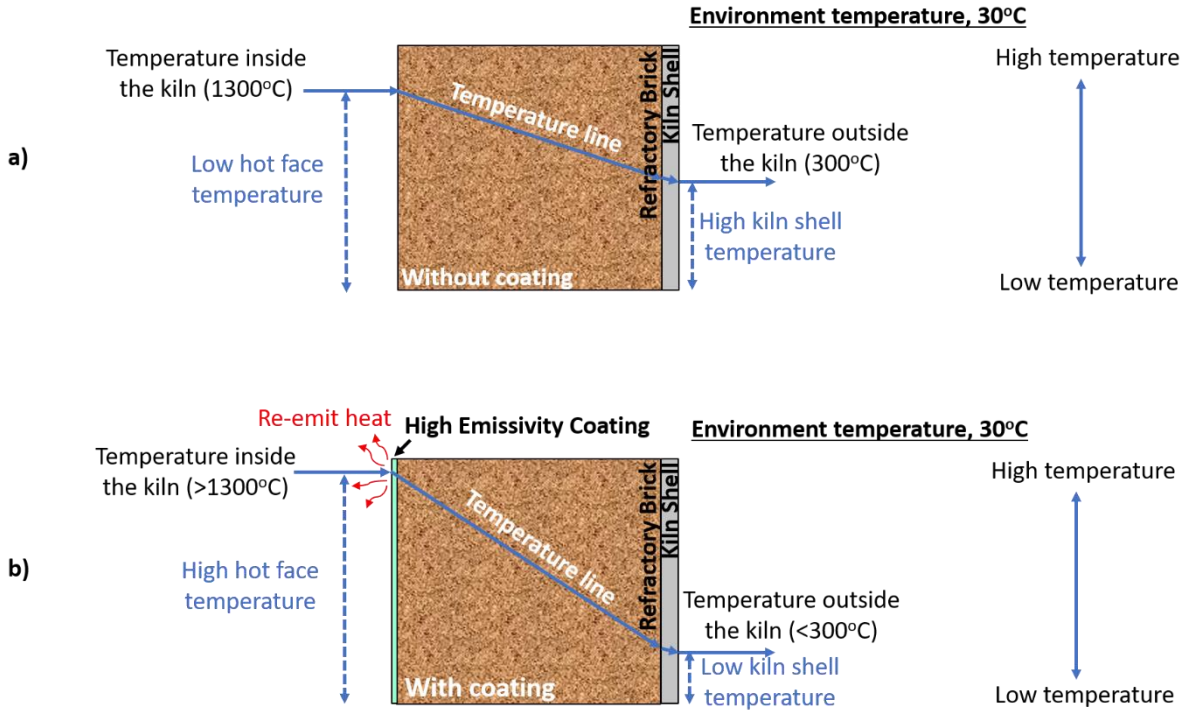


Figure 1. A schematic image of a cement rotary kiln cross-section. The blue solid line represents the temperature line and the blue dashed line represents the temperature difference between the temperature inside and outside the kiln in images a) and b). Image a) shows a normal cross-section without the high emissivity coating. The temperature inside the kiln is 1300°C and the temperature decreases, flowing along the temperature line, as heat passes through the refractory brick and kiln shell. The temperature reaching the kiln shell outer surface is 300°C. Image b) shows a cross-section with a high emissivity coating on the refractory brick inside the cement rotary kiln. The coating absorbs and re-emits heat back inside the kiln, increasing the inside temperature and decreasing the temperature of the kiln shell (author's figure).

The high emissivity coating will give its best efficiency when it is applied in a rotary kiln zone that has the highest temperature because the emissivity coating will work best in a zone that has the highest temperature difference between the inside and the outside of the kiln. The coating zone has the highest temperature (1450°C), making it appear to be the most suitable zone in the kiln on which to apply the high emissive coating. Unfortunately, this is not the case. The coating zone temperature causes the clinker raw materials to partially melt and change their phase. The partially melted clinker adheres to the refractory bricks and forms the clinker coating, which is the reason that this zone is referred to as the coating zone. In general, the clinker coating is approximately 450 mm thick and is desirable for the cement producers because it protects the refractory bricks and acts as an insulating

layer that reduces the amount of energy loss to the environment [4, 5]. However, the clinker coating limits the high emissivity coating efficiency by covering over the coating, thereby making its use to re-emit heat back into the kiln impossible. Therefore, applying a high emissivity coating to this zone is not practical.

The next highest temperature zone is the upper transition zone, where the inside temperature is approximately 1300°C. In this zone, the temperature is not high enough to partially melt the clinker, thus little if any of the clinker layer forms. The refractory bricks are directly exposed to the high temperatures and consequently, this zone is ideal for the application of the high emissivity coating. Therefore, the scope of this research is to develop a high emissivity coating that can be applied onto the refractory bricks in the upper transition zone of a cement rotary kiln for the purpose of heat loss reduction, which will also lower the $CO_2$ emissions.

## 1.1 Cement production

Concrete is the most common material used in building construction. When cement is mixed with water and aggregates; stone and sand, it hardens and becomes strong and durable and is then termed concrete. In cement production, the raw materials such as limestone and clay are preheated in a pre-heater cyclone to about 850°C. The raw materials flow from the top to the bottom of the cyclone then into the rotary kiln. Rotary kilns have various sizes with a diameter that can go up to 6 m and 60-200 m long. The kilns are 1-4° tilted and rotate 1-2 round per hour [9, 10]. This is designed for the raw materials to be able to flow from the high end of the kiln (inlet) down to the lower end (outlet). At the outlet, a burner provides heat. Therefore, as the raw materials flow down the kiln, towards the outlet, they get heated. The temperature at the outlet is about 1450°C. This is a temperature where raw material phases transform to clinker, the 4 main phases of which are 50-70% tricalcium silicate ($C_3S$), 15-30% dicalcium silicate ($C_2S$), 5-10% tricalcium aluminate ($C_3A$) and 5-15% tetracalcium aluminoferrite ($Ca_4AF$) [11, 12]. To stabilize these 4 phases, the clinker is quenched by flowing into a cooler. Later the clinker from the cooler is milled and mixed with additives such as gypsum and this mixture is called cement [12]. The clinker production process is shown in Figure 2.

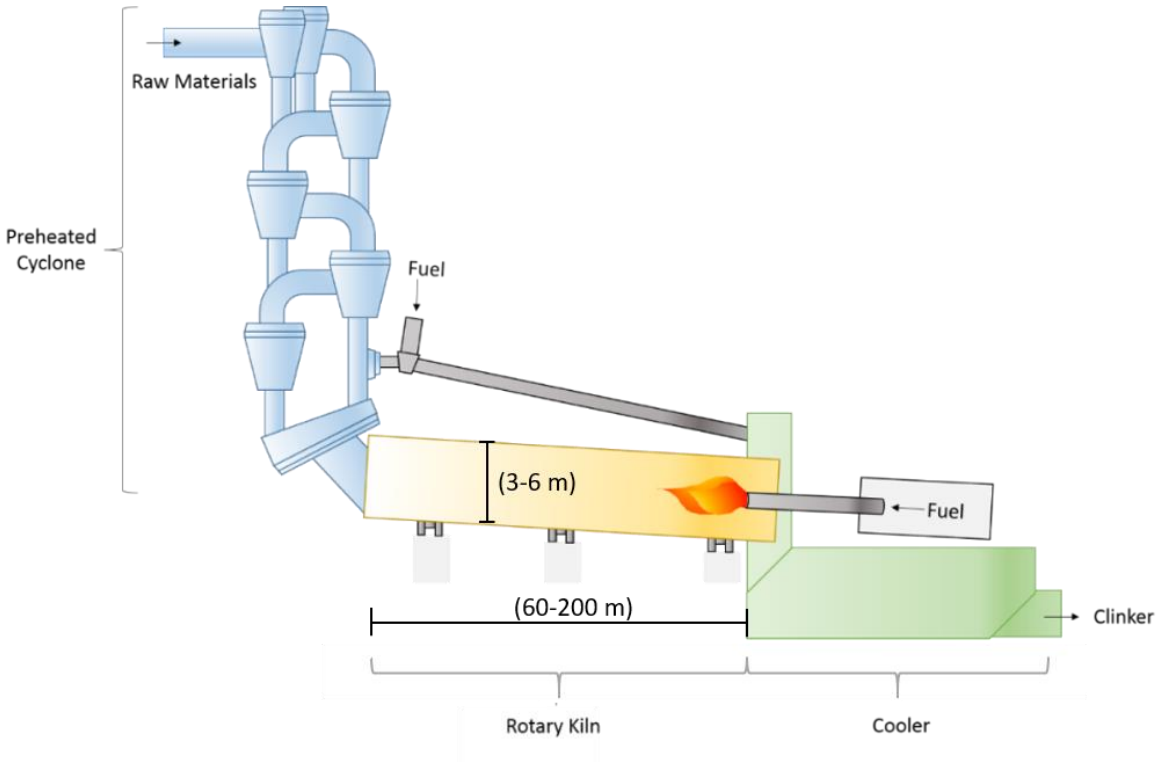


Figure 2. Cement kiln process. Raw materials first enter the preheated cyclone then to the rotary kiln and finally are quenched in the cooler. (author's figure)

## 1.2 Refractories in cement rotary kilns

Ceramics used for high temperature application are in 3 categories: refractories, ultra-high temperature ceramics (UHTC) and ceramic matrix composites (CMC). UHTCs are mostly used in aerospace applications [13, 14], CMCs are used in applications such as advanced engines, gas turbines for power/steam co-generation, heat exchangers, heat treatment and materials growth furnaces, as well as in nuclear reactors [15] while refractories are used in every other field that requires high temperature material, for example, steel, cement, glass and petrochemical industries [16].

ASTM C71 defines refractories as non-metallic materials having those chemical and physical properties that make them applicable for structures, or as components of systems, that are exposed to environments above 1,000 °F (~811 K or 538 °C) [17]. Refractories can be categorized in many ways including by chemical nature; acidic, basic, and neutral [18]. Categorizing refractories in this way helps pyro-processing manufacturers' select the refractory to match their application environment. Examples of refractory materials and their application of each chemical nature are presented in Table 1.

Table 1. Example of materials and applications of refractories categorized by chemical nature.

| Chemical Nature | Material | Application |
|---|---|---|
| Acidic | • Silica<br>• Fireclay | • Glass Melting Tank |
| Neutral | • Carbon, Graphite<br>• Alumina<br>• Chromia | • Metallurgical Furnace |
| Basic | • Magnesia<br>• Doloma | • Steel Making Process<br>• Non-ferrous Metallurgical Operations<br>• Cement Industries |

Refractory selection depends on the application temperature and environment. Different refractories are used in the different regions of the cement kiln. The preheater cyclone mainly uses fireclay and alumina because they have high refractoriness, strength and chemical resistance. The rotary kiln uses various refractory materials as further discussed in the next paragraph. The cooling zone uses both alumina and magnesia because of their good abrasion resistance.

Cement rotary kilns are divided into seven zones as shown in Figure 3. The most severe zones are the upper transition, coating and lower transition zones because it is where the highest temperature occurs, and the refractory bricks are in contact with the clinker. Clinker is a base material having a pH of about 12-13. These days fossil fuels used for burners are being replaced with alternative fuels, which generate alkaline vapour making the kiln environment become more basic. Therefore, basic refractories are used. Previously, magnesia chrome brick was used in the upper transition, coating and lower transition zones due to its high spalling resistance, high corrosion resistance and stable coating adhesion. However, the $Cr^{6+}$ in the refractory is carcinogenic and hence is now prohibited [9, 10, 19, 20]. Currently, magnesia chrome brick is being replaced with magnesia (MgO) combined with magnesia spinel ($MgAl_2O_4$) bricks due to their good physical, thermal and chemical properties and good compatibility with the basic clinker [21, 22].

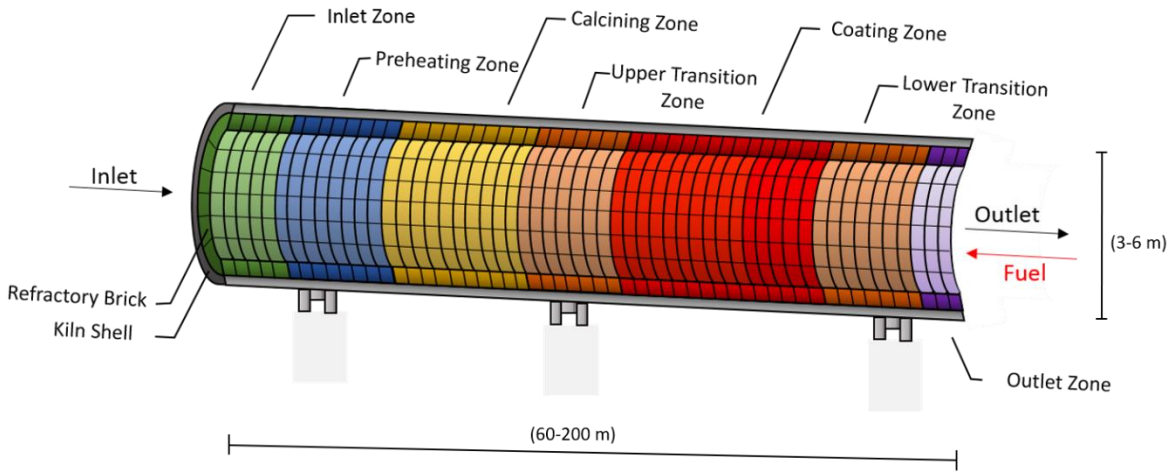


Figure 3. Seven zones of cement rotary kiln; inlet zone, preheating zone, calcining zone, upper transition zone, coating zone, lower transition zone and outlet zone (author's figure).

## 1.3 Heat transfer mechanisms in cement kilns

Heat transfer is a natural phenomenon that occurs when two or more objects that are at different temperatures come into contact. In this phenomenon, heat energy travels from the object with a higher temperature to the object with the lower temperature. The transfer stops when an equilibrium is reached (all objects are at the same temperature). There are three types of heat transfer: thermal conduction, thermal convection and thermal radiation. Thermal conduction takes place in all forms of matter, namely solid, liquid and gas. The transfer of heat from high to low temperature is dependent upon two mechanisms: atomic vibration and the motion of free electrons. These two mechanisms play various roles in different materials. In metals, thermal conductivity is dependent on the motion of free electrons. As the temperature increases, the atomic vibration also increases and obstructs the free electron paths, which leads to a decrease of thermal conductivity. For non-free electron materials such as ceramics, the thermal conduction is dependent upon atomic vibration. Thermal energy makes the atoms in the ceramic materials vibrate and creates a wavelike phonon. As the temperature increases, the atomic vibration also increases and creates the phonon conduction. With the increasing temperature, the vibration impedes phonon transport, which leads to reduced conductivity. For porous materials, the pores are filled with a low thermal conductivity gas, typically air; therefore, porous materials have lower conductivity than dense materials. In addition, the thermal transport across pores is mostly in the form of radiation, which is normally low but does increase slightly with temperature. Thermal convection is when heat travels from one location to

another by a fluid (liquid or gas). Thermal radiation is the electromagnetic spectra emitted from the thermal vibration of charged particles in the matter. For thermal conduction and convection to occur, media are required. In contrast, a medium is not required for thermal radiation, which makes it possible for it to occur anywhere, even in a vacuum. The amount of heat from each type of heat transfer phenomenon is given by Equation 1-Equation 3.

Equation 1. $$Q_{cond} = -kA\frac{dT}{dx}$$

where $Q_{cond}$ is heat conduction (W), k is thermal conductivity ($W\cdot(m\cdot K)^{-1}$), A is area of heat transfer surface ($m^2$), T is temperature (K) and x the distance that the heat travels (m).

Equation 2. $$Q_{conv} = Ah\Delta T$$

where $Q_{conv}$ is heat convection (W), A is area of heat transfer surface ($m^2$), h is heat transfer coefficient ($W\cdot(m^2\cdot K)^{-1}$), and ΔT temperature difference (K).

Equation 3. $$Q_{rad} = A\varepsilon\sigma(T_1^4 - T_0^4)$$

where $Q_{rad}$ is heat radiation (W), A is area of heat transfer surface ($m^2$), ε is surface emissivity, σ is the Stefan-Boltzmann constant ($5.67 \times 10^{-8}$ $W\cdot(m^2\cdot K^4)^{-1}$, $T_1$ is surface temperature (K), $T_0$ is ambient temperature (K)

Heat loss from cement rotary kilns occurs via all three types. First, the heat energy is conducted through the refractory brick (largely by phonon conduction but with some radiation through pores) and steel kiln shell (largely by free electrons moving through the structure in the metal). The heat then passes on to the environment via thermal convection and radiation as shown in Figure 4.

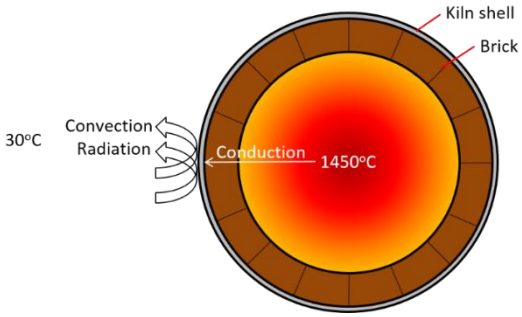


Figure 4. Heat transfer in a cement rotary kiln via thermal conduction, convection and radiation (author's figure).

To calculate for thermal conduction heat transfer in a cylinder shape of radius r, as in a cement rotary kiln, Equation 1 must be modified as below with r replacing x.

$$Q_{cond} = -kA\frac{dT}{dr} \qquad ; \mathrm{A} = 2\pi\mathrm{rL}$$

$$Q_{cond} = -k(2\pi\mathrm{rL})\frac{dT}{dr} \qquad ; \mathrm{T} = T_1 \text{ at } r = r_1, \mathrm{T} = T_o \text{ at } r = r_o$$

$$\frac{Q_{cond}}{2\pi\mathrm{L}}\int_{r_1}^{r_o}\frac{1}{r}dr = -k\int_{T_o}^{T_1}dT$$

$$\frac{Q_{cond}}{2\pi\mathrm{L}}\ln\frac{r_o}{r_1} = k(T_1 - T_o)$$

$$Q_{cond} = \frac{k2\pi\mathrm{L}(T_1 - T_o)}{\ln\frac{r_o}{r_1}}$$

$$Q_{cond} = \frac{k2\pi\mathrm{L}(T_1 - T_o)}{\ln\frac{r_o}{r_1}} \cdot \frac{(r_o - r_1)}{(r_o - r_1)} \qquad ; (r_o - r_1) \text{ is the thickness of the layer which is } x$$

$$Q_{cond} = \frac{(T_1 - T_0)}{\frac{r_o - r_1}{kA_{lm1}}} \qquad ; A_{lm} = \frac{2\pi\mathrm{L}(r_o - r_1)}{\ln\frac{r_o}{r_1}}$$

where $Q_{cond}$ is heat transfer via conduction (W), A is area ($m^2$), L is the length of the cylinder (m), $r_1$ is the outer radius of the cylinder and $r_o$ is the inner radius of the cylinder (m). $T_1$ is temperature inside

the cylinder (K), $T_o$ is temperature outside the cylinder (K), x is the thickness of each layer (m), k is thermal conductivity of each layer ($W \cdot m^{-1} \cdot K^{-1}$), $A_{lm}$ is log mean area of the heat transferring medium ($m^2$)

Cement rotary kilns transfer heat through two layers of material, refractory brick and kiln shell (metal), therefore, heat transfer is calculated from Equation 4.

Equation 4. $$Q_{cond} = \frac{(T_1 - T_0)}{\frac{x_1}{kA_{lm1}} + \frac{x_2}{kA_{lm2}}}$$

where $A_{lm1} = \frac{2\pi L(r_o - r_1)}{\ln\frac{r_o}{r_1}}$, $A_{lm2} = \frac{2\pi L(r_1 - r_2)}{\ln\frac{r_1}{r_2}}$, $r_o$ is outer radius of the kiln, $r_1$ is the inner radius of the kiln shell and $r_2$ is the inner layer of the refractory lining.

The thermal convection and thermal radiation of a cylinder can be calculated from Equation 2 and Equation 3, respectively. One direct way to reduce heat lost is by reducing one of these heat transfer mechanisms, for example, reducing the refractory bricks thermal conductivity to reduce thermal conduction loss, or creating a secondary kiln shell to reduce thermal convection loss or to reduce the temperature difference between the kiln shell and the kiln's surrounding in order to reduce thermal radiation. The most interesting type is thermal radiation because the radiation in Equation 3 includes the fourth power of the temperature difference, which means that reducing the temperature difference by a small amount can lead to high energy savings. To increase the efficiency, an indirect approach is implemented. Instead of reducing the thermal radiation in the low temperature difference zone (kiln shell and the surroundings), the thermal radiation is increased the high temperature difference zone (inside the kiln and on the hot-face refractory bricks). This approach can be employ by applying a high radiative coating on the hot face of the refractory bricks inside the kiln, which does not reduce any of the heat transfer directly but uses the thermal radiation mechanism to reduce the heat entering the refractory bricks by absorbing and re-emitting the heat back into the kiln.. Since radiation is dependent upon emissivity, the basic principle of emissivity is introduced in the next section.

## 1.4 Emissivity

Emissivity (ε) is the effectiveness of a material surface in emitting energy (emissive power, $W \cdot (m^2)^{-1}$) in electromagnetic waves. Electromagnetic waves are separated into radio, infrared (IR),

visible light, ultra-violet (UV) and gamma-rays distinguished by their wavelengths (Figure 5) [23]. The wavelength that represents thermal radiation is IR (700nm – 1mm). IR is emitted from every material that has a temperature above absolute zero (-273°C, 0 Kelvin). IR emission is a characteristic feature, meaning that each material does not emit the same amount of IR at the same temperature. A material that has the highest emittance at every wavelength and temperature is termed a blackbody material. The emissive power of a blackbody is expressed in Equation 5 (the Stefan- Boltzmann law) showing that the emission energy is dependent on the fourth power of the absolute temperature and area of emission [8, 24-27]. The blackbody emissive power is shown in Figure 6 which shows that its intensity increases with temperature and the maximum emissive power (the peak) shifts towards shorter wavelength (higher energy) with increasing temperature. The peak positions follows Wien's displacement law present in Equation 6 [8, 28].

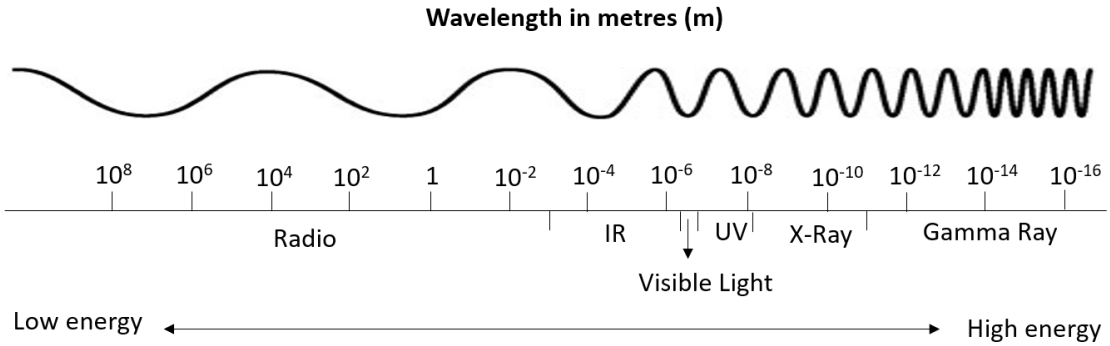


Figure 5. Electromagnetic spectrum, which is consists of radio, infrared (IR), visible light, ultraviolet (UV), X-ray and gamma-rays. (author's figure)

Equation 5. $$Q_{BB} = \sigma A T^4$$

where $Q_{BB}$ is radiative energy of a blackbody (W), $\sigma$ is the Stefan-Boltzmann constant; 5.6703 X $10^{-8}$ ($W/m^2K^4$), $T$ is absolute temperature (K) and $A$ is area of the emitting body ($m^2$).

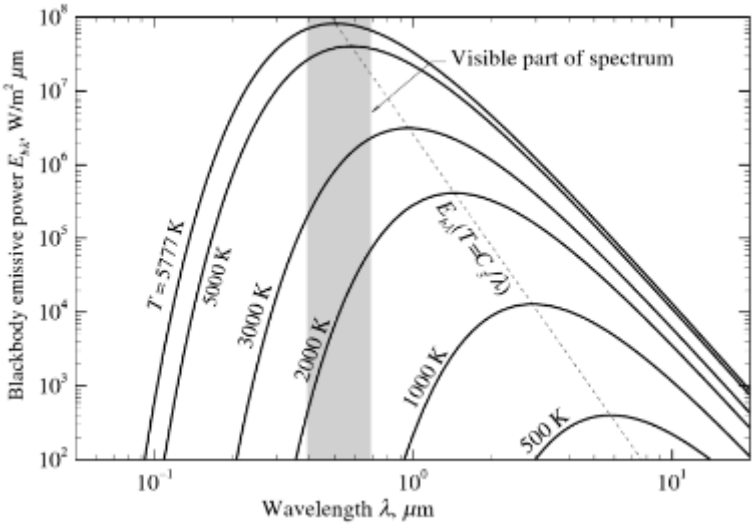


Figure 6. Blackbody emissive power spectrum [8]

Equation 6. $$\lambda_{max} = \frac{2.9 \times 10^{-3}}{T}$$

where $\lambda_{max}$ is the emissive power peak position (μm) and T is temperature (K).

A blackbody is an ideal material; real materials are termed greybodies. A greybody's emissive power is always lower than that of a blackbody. The ratio of the emissive power of a greybody to a blackbody at the same temperature is the definition of "emissivity". As already mentioned, emissivity is the effectiveness of how a greybody emits energy. Because emissivity is a ratio of the same variable (emissive power) it does not have a unit and its value is always between 0 and 1. Emissivity value close to 0 means that the material has low emission and a value close to 1 means that the material has a high emission. Therefore, to calculate the radiation energy of a greybody, a term for the emissivity (ε) is inserted into Equation 5 as shown in Equation 7.

Equation 7 $$Q_{BB} = \varepsilon \sigma A T^4$$

.

# Chapter 2: Literature Review

## 2.1 Cement production energy saving

Many studies have attempted to reduce or prevent heat loss during cement production. The three main ways examined are: using alternative binders to replace cement, recovering the heat waste for other use, and reducing the thermal conductivity of the refractory lining.

### 2.1.1 Alternative binders

Ordinary Portland cement (OPC) clinker, the most used material worldwide, is generally composed of 4 main phases; $3CaO{\cdot}SiO_2$, $2CaO{\cdot}SiO_2$, $3CaO{\cdot}Al_2O_3$ and $4CaO{\cdot}Al_2O_3{\cdot}Fe_2O_3$, which are formed from raw materials such as calcite, quartz, clay minerals and iron oxide, at high temperature (~1450°C) [11, 12]. Research is exploring new cement phases that form at a lower temperature or a new system, a process that can reduce production energy. Three major system being examined are; calcium sulfoaluminate (CSA) cements, geopolymers and celitement (calcium silicate hydrate, CSH).

CSA cements are of interest because they form at temperature 200°C lower than the OPC clinker showing a significant economic and environmental benefit [29-32]. CSA cements are mainly composed of ye'elimite ($C_4A_3\overline{S}$), belite ($C_2S$) and calcium sulfate ($C\overline{S}$)[1]. The minor components vary depending on the raw materials [33-35]. Other benefits of CSA clinker are, it is easier to grind and produces 30-60% $CO_2$ lesser than OPC cement [36, 37]. However, further studies on CSA cement still needed because introducing new clinker phases like CSA affects many aspects, for example, cement hydration, production and water to cement ratio [38, 39].

Geopolymers are a different category of material that might substitute for OPC. Geopolymer raw material is an aluminosilicate base that can be found in a natural source e.g. kaolin or waste of fly ash. Unlike OPC and CSA cements that hardens by hydration mechanisms (hardened when mixed with water), geopolymers harden by reacting with an alkali solution. Alkaline solution activates the aluminosilicate to form three-dimensional networks of amorphous inorganic material (geopolymerization) generating strength [37]. An advantage of geopolymers is that they do not go

[1] In cement field, chemical compounds are written as present in the parenthesis, where C is calcium oxide, A is aluminum oxide, $\overline{S}$ is sulfate and S is silicon dioxide.

through clinkerization process at high temperature, therefore requiring only low energy consumption, as well as low $CO_2$ emission. Geopolymers also have a higher resistance to acids and heat compared to OPC. Although geopolymers have many advantages they also have many disadvantages such as: the alkaline solution, used to activate the aluminosilicate causes an increased safety risk to the user; the geopolymerization reaction is sensitive to temperature making it a challenge in terms of quality control; high drying shrinkage and high cost [40-42].

Celitement (CSH based) is another material that has similar features to OPC but can be produced at a much lower temperature. Celitement raw materials are based on lime (CaO) and silicate source ($SiO_2$) such as sand, glass and blast-furnace slag (BFS). Celitement is produced following 2 main steps; first is hydrothermal preparation step where the raw materials (lime and silica) react in an autoclave at a temperature below 300°C. Second, the product from the hydrothermal preparation step is ground with silicate (mechanochemical) and celitement is created. Celitement composition is presented in Figure 7. The advantages of celitement are similar to those of geopolymers: low temperature processing so low energy consumption and lower $CO_2$ emission. Celitement is also activated with water just like OPC and CSA cement, therefore, it is more user-friendly than geopolymer. The disadvantage of celitement is in the complex mechanochemical process that is not yet suitable for mass production. The early strength of celitement is also lower compared to OPC but the late strength (after 7 days) is comparable [43-46].

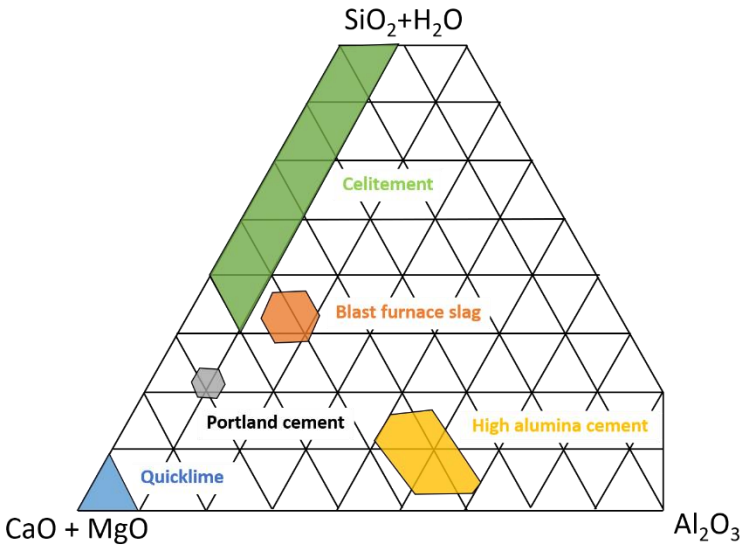


Figure 7. Phase diagram projection of the system (CaO+MgO)-$Al_2O_3$-($SiO_2$+$H_2O$) presenting celitement composition in the market. The distance between grid lines amounts to 10wt% (modify from [47]).

### 2.1.2 Waste heat recovery

Cement production energy consumption is divided into 5 main sectors as shown in Figure 8. The majority of the energy is used as thermal energy in the rotary kiln (86% kiln fuel) [5]. The cement rotary kiln heat efficiency is about 60%, meaning that 40% of the heat is lost during the production [4]. Engine and Ari [9] reported that out of the 40% heat loss, ~19% is from hot flue gas, ~6% from the cooler and ~15% from convection and radiation from the kiln shell surface. They also reported using a "waste heat recovery steam generator" (WHRSG) the cement plant can recover up to 1MW of energy. This works by the heat from the kiln exhaust gas and the hot air from the cooler being used to 1) power a steam turbine that drives the electrical generator for use in the cement plant and nearby community and 2) bring back heat into the system to pre-heat the clinker raw materials before they enter the rotary kiln [5, 9, 43]. These two uses of waste heat are well known and widely applied. As for heat loss from convection and radiation from the kiln shell surface, Engine and Ari [9] introduce a secondary shell system as shown in Figure 9. A secondary shell covers the primary rotary kiln shell with a 40 cm air gap and distance apart can reduce heat radiation lost from the kiln surface. With the secondary shell, there is hardly any heat loss from convection and therefore, convection can be neglected from the heat loss system. It should be noted that the secondary kiln shell must have windows for the engineer operators to be able to observe any local primary kiln shell burning which occurs when there is a loss refractory inside the kiln. An estimated 3MW can be saved by using a secondary shell when the temperature, emissivity and radius of the rotary kiln assumption are as in Figure 9.

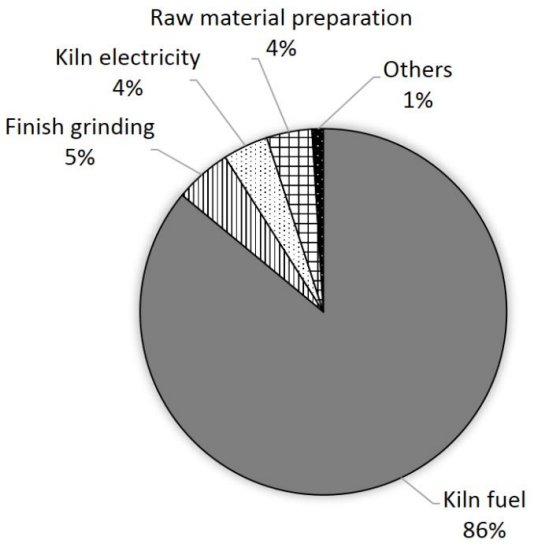


Figure 8. Total energy for cement manufacturing sector by process step (modify from [5]).

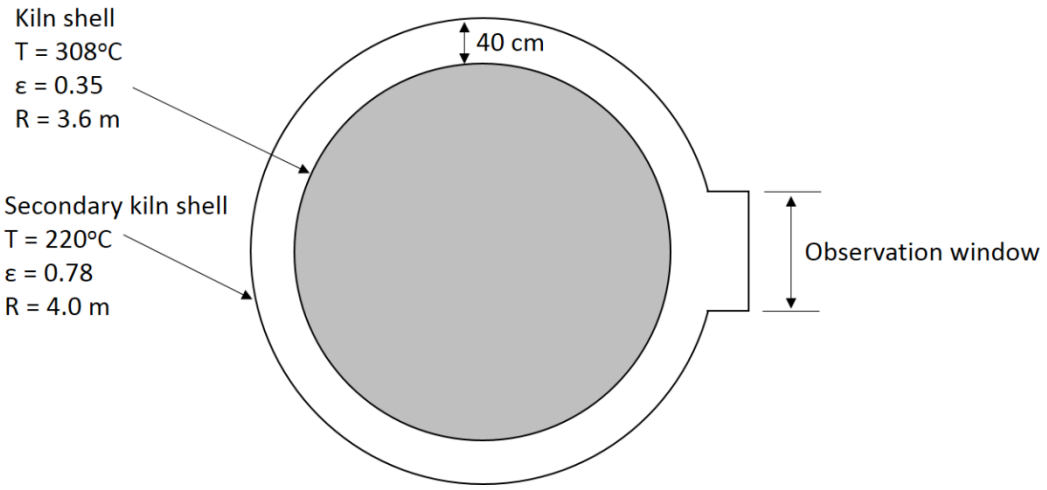


Figure 9. Secondary shell for cement rotary kiln energy saving (modify from [9]).

### 2.1.3 Reducing thermal conductivity

Much research has focused on reducing the thermal conduction of the refractory bricks by adding lightweight and/or combustible materials to generate porosity [48-51]. However, adding these materials reduces the refractory bricks strength, potentially leading to operation failure. Moreover, changing the refractory lining in the cement kiln is not ideal because trying new refractory linings may significantly impact the cement kilns economic viability. Using familiar refractory linings ensures the cement industry that at least the cement plant operating time is more or less the same as the last time making it convenient to manage to order new refractory bricks (no need to store refractory bricks in the cement plant).

Reducing heat loss via convection is a challenge because thermal convection depends on the velocity of the fluid, in this case, the environment around the furnace that carries the heat away which is unreliable and dependent on the season; rain and wind. Thermal radiation is the most interesting out of the 3 heat transfer phenomena because it is highly dependent on temperature difference by 4 orders of magnitude as shown in Equation 3 making it more dominant than thermal conduction and convection at high temperature [8]. Thermal radiation is also dependent on the area of the heat transfer surface, not the whole volume, therefore, only the surface of the refractory bricks needs to be treated. Developing a high radiative coating can enable the cement industry to save energy and still use its original refractory bricks.

## 2.2 High emissivity coating

### 2.2.1 Coating types

Before high emissivity coating was developed, high emissivity materials were first introduced. In 1971 Guazzoni [52] described high emissivity rare earth oxides with emissivity measured in the wavelength range of 0.5-5 μm at a maximum temperature of 1600°C. Guazzoni reported that these oxides emissivity varies with wavelength and temperature. Some give high emissivity at a wavelength while others give high emissivity at another wavelength. $Sm_2O_3$ and $Nd_2O_3$ had high emissivity almost throughout the measured spectral range. All material's emissivity increased with temperature at a wavelength of 0.6 μm (~16,667 $cm^{-1}$).

In 1991, Hellander [53, 54] reported energy saving from using high emissivity coatings in two electric furnaces. Furnace 1 had a coating applied to ceramic fibre-based modules and board which found that the coating can save energy cost about 17%. Furnace 2 used a coating on dense refractory and found that the coating saved 22.4 BTU of energy. This work indicated that the high emissivity coating concept is feasible in electric furnaces although it lacks materials understanding, the coating used in the report are defined by code names, and no emissivity measurements are reported. Hellander discussed why a highly emissive coating is more efficient than a highly reflective one, it being due to gas combustion (energy source) transferring heat by radiation and convection. The radiation is dominant. Radiated heat comes out at many frequencies, with some containing more energy than others. When the heat strikes the refractory surface some reflects, and some absorbs and re-radiates (re-emits). The heat reflected off the refractory surface has the same frequency as the heat striking it. The heat reflected (whose frequency is not changed on interaction with the solid) is absorbed by the combustion gas and does not go to the workload whereas the heat that was absorbed, is re-emitted at different frequencies and these the re-emitting frequency can pass through the combustion gas and go to the workload. Hollander also explained that increasing the emissivity value by a little, can significantly increase the percent heat re-emitted. The example used was if the emissivity value is 0.3, this means that 70% of energy is reflected and 30% is absorbed by the refractory. From this 30%, 5% is assumed to be a constant loss by conduction through the refractory brick, the remaining 25% is re-emitted back into the furnace. If the emissivity value is 0.7, the emissivity value increases by 133.33%, energy reflected is 30% and energy absorbed is 70%. Taking away the 5% from the constant loss by conduction leaves the energy re-emitting back at 65%, which

is an increase of 160% emittance. This example has shown that by increasing emissivity value by 133.33%, increases energy re-emittance by 160%.

Neuer [55] added SiC to silica which is the main material used for brick walls in the coke oven processing and glass tank furnace. The purpose of adding SiC was to increase the emissivity of the oven by suppressing the transparency of the silica leading to an increase of emissivity. Emissivity was measured using an in-house-built instrument in which the sample is placed inside a vacuum chamber, the sample is then heated by an electron beam and the emission of the sample is measured with a thermal radiation detector through a $CaF_2$ window. The sample temperature is measured with a pyrometer. Adding 12% SiC gave higher emissivity of about 0.8±0.12 in the temperature range of 400-1200°C at all wavelengths (0.5-8 μm) compared to pure silica.

Holcombe Jr *et al.* [56] filed a patent on "High emissivity coating" claiming that their coating consists of refractory pigment, high emissivity agent, which is a rare earth oxide especially $CeO_2$, and binder. They also claimed that after applying their coating by painting it on the furnace refractory, the exterior temperature of the furnace decreases by 3-6% when the furnace operated at 1400-1500°C. This patent while interesting lacks detail on the furnace interior (refractory substrate) and emissivity measurements.

Li *et al.* [57] used a different concept, that of low emissivity paint on the outer surface of the cement rotary kiln. Their coating was applied on a 3.23 m diameter 61m long kiln. The refractory brick and the kiln shell were 275mm and 22mm thick respectively. The temperature of the kiln surface and the ambient were assumed to be 300°C and 15°C respectively. Thermal convection and radiation of the kiln surface with and without low emissivity coating were calculated using Equation 2 and Equation 3 from section 1.3 revealing that the low emissivity paint increases the convection heat lost but decreases the radiation heat lost. However, the decrease of radiation heat loss is greater than the increase of the convection which leads to an overall energy saving. The low emissivity paint also increases the kiln shell temperature. Every 25°C that the kiln shell temperature increase, an increase of heat loss will also occur by 17%. The limits of the low emissivity coating are if the emissivity is too low (<0.5), energy would no longer be saved, and the kiln shell temperature would be too high. When the kiln shell temperature is too high, mismatch in thermal expansion of the kiln shell and the refractory lining inside the kiln leads to lining failure.

Brandt *et al.* [58], reported two different emissivity paints; HE6 and HE23, developed by Rolls-Royce but did not give the paint compositions. The paints were air sprayed on to nickel-based alloy

samples 15 mm in diameter and 3-6 mm thick. The samples were heated with induction heating and a linear pyrometer was used for emissivity measurement. They measured emissivity at wavelengths between 1.3-8.3 μm up to 1300°C and revealed that both coating's emissivities were above 0.85 and slightly lower as the temperature increased.

Staggs and Phylekton [59] examined the effect of high and low emissivity coatings on steel fire resistance in an attempt to improve steel properties at high temperature. The high emissivity coating was composed of carbon black pigment in a siloxane binder and the low emissivity coating was alumina flakes with the same binder. They used a cone calorimeter to determine coated volumetric heat capacity ($W\cdot(Km^3)^{-1}$) by letting the samples exposed to different heat flux ($kW\cdot m^{-2}$). Emissivity was then calculated by $\varepsilon = (\delta\rho c_p / q)dT/dt|_{t=0}$ where ε is emissivity, δ is thickness (m), $\rho c_p$ is volumetric heat capacity ($W\cdot(K\cdot m^3)^{-1}$), q is external heat flux from the cone heater ($W\cdot(m^2)^{-1}$), T is temperature at exposed surface (K) and t is time (s). The emissivity of the high and low emissivity coatings was 0.81 and 0.49 respectively. The coatings were then used to measure fire resistance in a furnace using BS476 standard, for fire testing of building materials and structures, parts 20 and 21 [60, 61], in which the maximum temperature was lower than 1000K (<727°C). Results indicated that convection is dominant at low temperature when the sample is first exposed to temperature. As the sample temperature increases, approaching the furnace temperature, convection becomes dramatically less significant and radiation becomes relatively more important. However, overall emissivity had a low-order effect of steel fire resistance in the furnace test. This research showed that emissivity coating is more likely to be efficient at high temperatures, possibly higher than 1000°C.

While these past reports suggest that high emissivity coating can increase the furnace efficiency, there was no solid explanation of how the coating functions. Even without the coating functionality understanding and emissivity measurements, high emissivity coatings have been introduced in the commercial market. In the 21st century, the high temperature coating focus has shifted to new applications such as coatings for space shuttle, thermal protection system tiles and turbine applications. In these applications, they are known as thermal barrier coatings (TBCs) and environmental barrier coating (EBCs). The differences between the two are TBCs are coated on metal alloy such as Ni alloy, with the purpose to protect the substrate from deforming at high temperature while EBCs are coated on ceramics (e.g SiC/SiC, ceramic matrix composition (CMC)) with the purpose to protect the substrate not just from high temperature but also from the environmental assault such as water vapour [39, 62-67].

Rare earth materials are used in TBCs/EBCs. Cao *et al.* [68] reviewed the properties required in TBCs applications and material advantages and limitations in this field. Among these materials, rare earth oxides were mentioned as dopant materials to improve the coating properties, for example, cerium oxide is used as an additive to yttria stabilize zirconia (YSZ) to increase thermal shock resistance [69, 70]. Rare earth oxides are also used to improve emissivity [71]. Rare earth oxides ($CeO_2$, $Pr_6O_{11}$, and $Tb_4O_7$) and $MnO_2$ were used as dopants in a NiCr spinel coating applied on to stainless-steel via air plasma spray (APS)[2] and improved the emissivity to 0.971 in the wavelength range 2.5-25 μm at 1000°C. The doping results in higher charge transition and lower symmetry of lattice vibration which both lead to higher IR emissivity [72]. Other studies reported that $Sm_2O_3$, $Er_2O_3$, $Tm_2O_3$ and $Nd_2O_3$ used with $ZrB_2$/SiC coatings improved emissivity when applied to a tungsten substrate for hypersonic applications [73, 74] as did $Tb_4O_7$, $Gd_2O_3$, $Sm_2O_3$ with a $HfO_2$ coating on a nickel-based alloy [75].

Huang *et al.* [76, 77] used rare earth oxide as the main material in a coating. Their first report compares two $CeO_2$ coatings which were porous and dense. The coatings were applied to a Ni-based alloy using an electron beam physical vapour deposition (EB-PVD)[3] technique. Emissivity was measured using a Fourier transform infrared spectrometer (FTIR) over the wavelength range 2.5-25 μm. Porous samples had a higher emissivity value of 0.64 at 1000°C compared to dense samples which have an emissivity value of 0.47 at the same temperature as the pores acts similarly to a blackbody where the electromagnetic wave (infrared) is multiply reflected in the pores and increases the absorption/re-emission. The focus of their second paper is on doping $CeO_2$ with lanthanum (La). The substrate details, applying process and emissivity measurement were done in the same fashion as in the first report. The La-doped $CeO_2$ increases the emissivity into the range of 0.7-0.9 at 1000°C, which is higher than the pure $CeO_2$ which emissivity falls in the range of 0.4-0.6 at the same temperature. The reason is that doping La into the $CeO_2$ structure means that $La^{3+}$ substitutes $Ce^{4+}$ creating lattice distortion leading to a new absorption model which improves lattice absorption and emissivity.

EBCs can resist higher temperature than TBCs and are applied to ceramic materials. They also provide environmental resistance, unlike TCBs which mainly focus on withstanding high temperatures.

[2] A technique where a plasma flame is generated between an anode and cathode at the tip of a spray gun. Coating materials (powder) are fed in front of the plasma flame which melts them, and they flow along the flame direction hitting on to a substrate and becoming a coating.

[3] A technique where electrons generated from tungsten filament under high vacuum strikes the solid coating material which becomes gaseous. The gaseous coating materials are then condensed back into a solid on a substrate creating a thin layer coating.

EBCs can be applied using the same techniques as TBCs (ASA, EB-PVD) or by sputtering and slurry deposition such as slurry dipping [65]. EBCs features are close to those of the high emissivity coatings to be studied in this thesis. However, there have been few studies of emissivity of EBCs. There have been studies using rare earth in the EBCs material but for improving water vapour resistance [64, 65]. This thesis will contribute emissivity knowledge for EBCs application.

These studies of high emissivity coatings developed as TBC, improved our understanding of coating function and how emissivity can be measured. *Sako et al.* [78] presented at the UNITECR 2019 congress, Yokohama, Japan that some of the commercial coatings in the market were actually low emissivity. The reason that these coatings increased the furnace efficiency was from reflectivity. They proved it by measuring some of the commercial coatings with an in-house-built emissivity apparatus, developed by Domingos De Sousa Meneses at Conditions Extrêmes et Matériaux : Haute Température et Irradiation (CEMHTI) UPR3079, Univ. Orléans, F-45071, Orléans, France [79] and described further in section 2.2.2 and 3.3.2 of this thesis. Sako *et al.'s* work aimed to achieve high emissivity coating for the purpose of furnace energy saving. They engineered magnesium aluminate spinel ($MgAl_2O_4$) by doping with different metallic ions leading to disruption of harmonic vibration and therefore increased emissivity. The modified structure $MgAl_2O_4$ emissivity increased to 0.4 whereas undoped normal $MgAl_2O_4$ emissivity was 0.2.

At the same UNITECR 2019 congress the approach of using low emissivity coating was also presented. Simmat *et al.* [80, 81], reported that a low emissivity (highly reflective) coating containing high alumina on an insulating refractory substrate could reduce heat transfer in a roller kiln, a tunnel kiln with a roller belt that transport ceramics product from one side of the kiln to another, at a temperature lower than 1300$^{o}$C. They determined the heat transfer from measuring the exterior temperature of the furnace wall and found that the temperature was 22$^{o}$C with the coating and was 33$^{o}$C without the coating. After running the furnace for almost two years, one year without the coating and one year with the coating, they found that the specific gas consumption has reduced when the low emissivity coating was applied. In the roller kiln zones with higher temperatures (>1300$^{o}$C), the coating still reduces heat transfer but less efficiently. Emissivity is expected to be more effective than reflectivity with respect to energy saving at high temperature because the effect of the 4 orders of magnitude of temperature difference is great at high temperature (Equation 3). For example, if the area (A) and emissivity ($\varepsilon$) are kept constant and temperature different is 50K, the heat re-emitting at 1300K ($q = A\varepsilon\sigma\ (1300^4\text{-}1250^4)$) is much higher than that re-emitting at 1100K ($q = A\varepsilon\sigma\ (1100^4\text{-}1050^4)$).

### 2.2.2 Emissivity measurement

Emissivity can be determined by two methods. First, from the second law of Kirchhoff [8]. When an incident electromagnetic wave strikes onto a material it reflects ($\rho$), absorbs ($\alpha$) and transmits ($\tau$). The sum of these three actions is equal to 1 (Equation 8). What is absorbed must be emitted back, therefore, absorption is equal to emission. For material with a sufficient thickness, transmission ($\tau$) is equal to 0. Therefore, knowing the reflection ($\rho$), absorption ($\alpha$) can be calculated and absorption is equal to emission (ε). This is considered as an indirect method [82, 83]. Second, from the emissivity definition where emissivity is the ratio of emissive power emitted by the sample and the blackbody (Equation 9). This method is based on measuring the normal spectral emittance of a sample and a blackbody. This is considered as a direct method.

Equation 8. $$1 = \rho(\sigma, T) + \alpha(\sigma, T) + \tau(\sigma, T)$$

Equation 9. $$\varepsilon(\sigma, T) = \frac{\Phi_{sample}(\sigma,T)}{\Phi_{blackbody}(\sigma,T)}$$

Infrared emission spectroscopy was fist introduce in 1908 by Coblentz [84], but it was in the 1950s where McMahon [83] reported a calculation of infrared emission on transparent materials. The emission of transparent materials such as glass is important because it relates to the glass temperature and the cooling rate of the glassware [85, 86]. Measuring emission of transparent materials is complicated because emission leaving the material surface not only comes from the absorption/re-emission but also from the emission that has travelled through the material and reflected back into the material once it meets another interface. If the reflection reaches the material's original surface and emits out, it must be taken into consideration as well. A schematic diagram of the emission path of a transparent material is shown in Figure 10. The first emission occurs at the interface of the environment and a material ($\varepsilon_1$ , Equation 10). The initial spectrum strikes on to the material, some of the energy is absorbed and re-emitted and some penetrates further into the material. The second emissions occur when the energy that penetrates into the materials meets a gap ($\varepsilon_2$ , Equation 11). If the energy of that second emission, makes it to the surface of the material, the third emission occurs ($\varepsilon_3$ , Equation 12). Much research has been done in this area to improve the calculation and measurement methods for the emissivity of transparent materials, for example, adjusting from unidirectional radiation to three-dimensional radiation or adding refractive index into the account of the rate of radiant emission [83, 85-89].

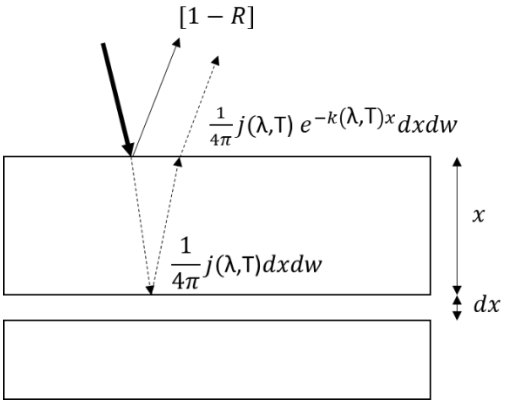


Figure 10. Emissivity of transparent materials (modify from [83]).

Equation 10. $$\varepsilon_1 = [1-R]$$

Equation 11. $$\varepsilon_2 = \frac{1}{4\pi} j(\lambda,T) dxdw$$

Equation 12. $$\varepsilon_3 = \frac{1}{4\pi} j(\lambda,T)\, e^{-k(\lambda,T)x} dxdw$$

where R is reflectivity, $j(\lambda,T)dx$ is emissive power of the material at wavelength $\lambda$ and temperature T and thickness $dx$, $dw$ represents a small solid angle, $k(\lambda,T)$ is the absorption coefficient characteristic at wavelength $\lambda$ and temperature T.

After commercial infrared emission spectroscopy was introduced to the market, in 1965, Low [90] used it to measure bulk opaque materials at a temperature close to room temperature over the wavenumber range of 500-3100 $cm^{-1}$. The materials were asbestos fibres, turquoise ($CuAl_6(PO_4)_4(OH)_8 \cdot 4H_2O$), jade ($NaAlSi_2O_6$), psilomane ($(Ba,H_2O)_2Mn_5O_{10}$), azurite ($Cu_3(CO_3)_2(OH)_2$), rhodocrocite ($MnCO_3$), muscovite ($(KF)_2(Al_2O_3)_3(SiO_2)_6(H_2O)$) and calcite ($CaCO_3$). Since then several experiments have been reported on infrared emission measurements [91-93].

Chase [94] used infrared emission spectroscopy to measure the emittance of polystyrene film and poly (methyl methacrylate) film at temperatures close to ambient (30°C) and lower. Samples were prepared by dissolving the materials in a suitable solvent, usually methylene chloride. Then they were deposited on a gold film and the solvent was left to evaporate. Four measurements were made, two on the samples at different temperatures and two on blackbody at different temperatures. Measurement on the sample at temperature $T_1$ can be written as Equation 13 and measurement sample at temperature $T_2$ can be written as Equation 14. For the blackbody measurement, emissivity

(ε) equal to 1 and reflectance ($\rho$) equal to 0. Therefore, the measurement of the blackbody at temperature $T_1$ and $T_2$ can be written as in Equation 15 and Equation 16 respectively. With these four equations, instrument background can be removed, and the emittance of the sample can be calculated by Equation 17.

Equation 13. $S_1(\nu,T_1) = R(\nu)\,[H(\nu,T_1)\varepsilon(\nu,T_1) + B(\nu) + I(\nu)\rho(\nu)]$

Equation 14. $S_2(\nu,T_2) = R(\nu)\,[H(\nu,T_2)\varepsilon(\nu,T_2) + B(\nu) + I(\nu)\rho(\nu)]$

Equation 15. $S_3(\nu,T_1) = R(\nu)\,[H(\nu,T_1) + B(\nu)]$

Equation 16. $S_4(\nu,T_2) = R(\nu)\,[H(\nu,T_2) + B(\nu)]$

Equation 17. $\varepsilon = \frac{S_2 - S_1}{S_4 - S_3}$

where $S_1$ is collected signal from the sample at temperature $T_1$, $S_2$ is collected signal from the sample at temperature $T_2$, $S_3$ is collected signal from the blackbody at temperature $T_1$, $S_4$ is collected blackbody from the sample at temperature $T_2$, $R(\nu)$ is instrument response function, $H(\nu,T)$ is Plank function, $\varepsilon(\nu,T)$ is emissivity, $B(\nu)$ is background radiation, $I(\nu)$ is background radiation reflected off the sample and $\rho(\nu)$ is reflectance of sample.

Limitations reported in this experiment were, the wavenumbers are only limited to lower than 2000 $cm^{-1}$ because the signals at higher wavenumber are low at a temperature close to ambient. Also, the emittance sensitivity increases at temperature lower than ambient ($<30^oC$). Therefore, for high signals, higher material amount, thicker film, is required.

DeBlase and Compton [95] reviewed theoretical and experimental studies of IR emission spectroscopy. Their review indicated that maximizing the sample and detector temperature difference also helps to improve the intensity of the signals.

During 1990-1994, Markham *et al.* measured emissivity using FT-IR from 100 to over $2000^oC$ [96-98]. The wavelength ranges used were in the mid-IR (0.8-1.6 μm) and near-IR (1.6-20 μm) using an indium-gallium-arsenide and liquid nitrogen cooled mercury-cadmium-telluride detectors respectively. The sample sizes were 25.4-38.1 mm square or diameter with a thickness of 6.35 mm. Samples were heated by various methods: gas torch flame, focused infrared radiation from high-

intensity lamps, and focused infrared radiation from a $CO_2$ laser (25W, continuous wave). Two references were used in the experiment: a blackbody and a perfect reflector. The near -blackbody was a cubic inch block of material which was grooved into pyramid shape as shown in Figure 11 to minimize the reflectivity and maximize the emissivity. Holes are drilled in the blackbody for inserting heating element and thermocouple. In the report, both silicon carbide and 316 stainless steel were demonstrated as a satisfactory near-blackbody material. The perfect reflector used in this experiment was a gold mirror (spectral directional-hemispherical reflectivity is 1). With these two references, the emissivity of a sample was determined from three main measurements; the sample radiance ($M1_v$, Equation 18), the sample radiance from the sample together with radiance of the blackbody from the spectrometer ($M2_v$, Equation 19) and the gold reference reflectance from the spectrometer ($M_v^{ref}$, Equation 20). The subscript $v$ relates to wavenumber ($cm^{-1}$). The emissivity is calculated from Equation 18-Equation 23.

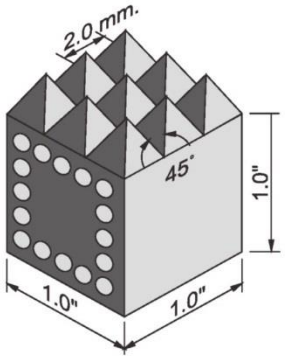


Figure 11. Schematic of blackbody used in Markham *et al.*'s experiment. The top surface is grooved into pyramid shape to minimize the reflectivity and maximize the emissivity. The circles on the side are holes for inserting heating element and thermocouple (modify from [96])

Equation 18. $$M1_v = \varepsilon_v(T_s)R_v^b(T_s)$$

Equation 19. $$M2_v = M1_v + \rho_v(T_s)R_v^b(T_{bb})$$

Equation 20. $$M2_v - M1_v = \rho_v(T_s)R_v^b(T_{bb})$$

Equation 21. $$M_v^{ref} = \rho_v^{gold}R_v^b(T_{bb}) = R_v^b(T_{bb})$$

Equation 22. $$\frac{M2_v - M1_v}{M_v^{ref}} = \frac{\rho_v(T_s)R_v^b(T_{bb})}{R_v^b(T_{bb})} = \rho_v(T_s)$$

Equation 23. $$\varepsilon_v(T_s) = 1 - \rho_v(T_s)$$

where $M1_v$ is sample radiance, $\varepsilon_v(T_s)$ is the emissivity of the sample at temperature $T_s$, $R_v^b(T_s)$ is the Planck function at temperature $T_s$, $M2_v$ is the sample radiance from the sample together with radiance of the blackbody from the spectrometer, $\rho_v(T_s)$ is the sample reflectivity at temperature $T_s$ and $R_v^b(T_{bb})$ is the Planck function at a temperature of $T_{bb}$, $M_v^{ref}$ is the gold reference reflectance the from the spectrometer, $\rho_v^{gold}$ is the gold reference reflectivity which is 1, $\rho_v(T_s)$ is the absorption of the sample at temperature $T_s$.

This instrument was originally developed for the U.S. Air Force. Markham *et al*. [96-98] have been providing measurements for the US government and commercial clients since 1995. Nowadays it is also available for outside research groups and they have limited the wavelength range to just near-IR (2-20 μm) and the maximum temperature to 1000°C. Unfortunately, this maximum temperature was not high enough for this research project.

In 2006 the emissivity measurement standard was published as ASTM C835-06 [99]: standard test method for total hemispherical emittance of surfaces up to 1400°C. A specimen is made into a strip ~13 mm wide and 250 mm long, the sample strip is then placed in a vacuum chamber and is heated with an electric current to the desired temperature. The power dissipated from the central area of the sample and the temperature of the area is measured. The two measurement values are used to calculate emissivity using the heat transfer radiation equation (Equation 3) or can be re-written as Equation 24.

Equation 24 $$\varepsilon = \frac{Q}{\sigma A(T_1^4 - T_2^4)}$$

where $\varepsilon$ is emissivity, $Q$ is hear generated in the sample over the test sample in the central area. $\sigma$ is the Stefan-Boltzmann constant ($5.669 \times 10^{-8}$ W·$(m^2K^4)^{-1}$), A is the surface area of the sample over which heat generation is measured ($m^2$), $T_1$ is the temperature of the heated sample (K) and $T_2$ is the temperature of the bell jar inner surface (K).

After the standard was released, much research used the standards to measure emissivity [100-104]. However, because the sample is heated via an electric current, it is suitable for samples that are electrically conductive such as Inconel alloys and stainless steel but is not suitable for materials that have low electrical conductivity such as many ceramics. Knowing the emissivity of materials is useful in developing nuclear reactors where removing heat from the ceramic fuels and metal cladding is crucial for their operation.

In 2005, just a year before the standard was released, Rousseau *et al.* [105] published a method to determine a sample surface temperature from Christiansen wavelength. It was indicated in this study that emissivity is dependent on temperature, wavelength, thickness, texture of the material, chemical composition and the presence of impurities. This makes it a challenge to determine emissivity. Christiansen wavelength is a wavelength at which a material, which is a heteropolar dielectric compound, behaves like a blackbody. Christiansen wavelength occurs when the refractive index (n) is 1 at the interface of air and the material. When the refractive index is 1, the reflectivity is 0. When the reflectivity is 0 and the material thickness is sufficient and the extinction coefficient is very low, the emissivity of the material becomes close to 1 like a blackbody as derived in Equation 25 ($e$ to the power of a larger minus value (large d value) gives a value close to 0) [28]. Therefore, once the Christiansen wavelength is determined, emissivity at that wavelength is known to exceed 0.999 making it possible to determine the surface temperature.

Equation 25. $$\varepsilon(\sigma,T) = \frac{\left(1-\rho\,(\sigma,T)\right)\cdot\left(1-e^{-4\pi k(\sigma,T)d}\right)}{1-\rho\,(\sigma,T)\cdot e^{-4\pi k(\sigma,T)d}}$$

where $\varepsilon$ is emissivity, $\sigma$ is wavenumber ($cm^{-1}$), $T$ is temperature (°C), $\rho$ is reflectivity, $k$ is extinction coefficient, and $d$ is thickness (m)

Sousa Menses *et al.* [79] used the Christiansen wavelength to determine materials temperature and determine emissivity using two spectroscopies. The two spectroscopies were used to measure two different ranges of wavelength: one in the far-mid IR range and another in the mid IR – visible range. Using a $CO_2$ laser heat source, they measured the blackbody reference temperature and emissivities for ruby ($Al_2O_3$: Cr crystal) and $NdGaO_3$ crystals. Emissivity was determined with a direct method, from the ratio between the emittance flux of a sample to an emittance flux of a blackbody at the same temperature. Blackbody used in the experiment was a PYROX PY8 furnace. The blackbody temperatures were determined by measuring the emittance flux of the furnace at 3 different temperatures: at a temperature of interest and at a higher and a lower temperature. The

fluxes were calculated into ratios. The ratios were computed and fitted into a model. Once the temperature of the blackbody is known the emitted flux of the blackbody furnace was measured via an indirect method (Equation 23). As a result, the PYROX PY8 furnace gave normal spectral emittance very close to 1 over wavenumbers 800-20000 $cm^{-1}$ at 1288 K (1015°C) confirming it is a good blackbody reference over this wavenumber range and temperature. The stability of the heating source is also important in measuring materials emissivity, especially when a $CO_2$ laser is used. The Sousa Menses *et al.* uses a coherent laser K500 (able to reach up to 2500 K) with a beam diameter of 1 mm ensure temperature homogeneity in the experiment. The stability of the laser was stabilised by monitoring a normal spectral emittance and temperature of an alumina crystal (ruby) for about half an hour at ~700 K, 1150 K and 1750 K. Temperature fluctuation was observed at different temperatures although it did not have a significant impact on the flux emitted by the sample. The fluctuation of the $CO_2$ laser heating source thus only gave a minor error and this heat source is suitable for emissivity measurement. After calibrating the emissivity apparatus, Sousa Menses *et al.* [79] measured the emissivities of ruby (800 μm thick) and $NdGaO_3$ (500 μm thick). Three measurements were measure at each temperature: background, blackbody, and sample. As a result, the ruby shows an imposed lattice vibration at 1000 $cm^{-1}$ and an emission band of electronic transitions between levels of $Cr^{3+}$ at >7500 $cm^{-1}$. $NdGaO_3$, which is a dielectric material, shows many electronic bands at wavenumber above 3000 $cm^{-1}$ due to the compound contains Nd which is a rare earth element.

Sundaram *et al.* [106-108] have proposed a different approach in measuring emissivity. They measured emissivity using a thermal return reflection method (TRR). The concept is to measure voltage across heated samples from a reflected and un-reflected mirror. The voltage signals were converted to temperature and the ratio of these temperatures can be used to calculate reflectivity as in Equation 26. The reflectivity is then used to calculate emissivity from the indirect method, where ε = 1-$\rho$ when the sample is opaque. They conducted the experiment at a radio frequency of 137 GHz, which falls into a gap where there is low absorption by the atmosphere. Measuring at this frequency allows the sample to be heated in a regular electric furnace which symbolizes the real application because radio waves do not penetrate through the furnace or the equipment waveguide.

Equation 26. $$r = \frac{1}{\tau_K \tau_{bs}^2 \tau_{wg}^2}\left(1 - \frac{T_{eff}}{T'_{eff}}\right)$$

where r is reflectivity, $\tau_K$ is return reflection coupling factor (constant), $\tau_{bs}$ is beam splitter transmission (constant), $\tau_{wg}$ waveguide transmission (constant), $T_{eff}$ is temperature converted from heated sample reflection signal and $T'_{eff}$ is temperature converted from heated sample un-reflection signal.

Materials Sundaram *et al.* measured include alumina brick, Inconel plate, and two grades of SiC heated to 1150°C [106]. The reflectivity and emissivity of these materials are presented in Table 2, which shows that this method can be applied to many different types of materials.

Table 2. Reflectivity (r) and emissivity (ε) of alumina brick, Inconel plate, high and low resistivity SiC measure with TRR method at 1150°C

| Material | r | ε |
|---|---|---|
| Alumina brick | 0.17±0.01 | 0.83±0.01 |
| Inconel | 0.95±0.03 | 0.05±0.03 |
| SiC grade 1 | 0.24±0.01 | 0.76±0.01 |
| SiC grade 2 | 0.38±0.01 | 0.62±0.01 |

Previous work [94, 96-98] shows that there is no standard emissivity measurement technique for ceramic materials but there is a pattern of how it is done. Several measurements are conducted such as measurement on a sample, on a blackbody or on a reflector depending on the experimental set up. These measurements are used to calculate together mostly by subtracting or dividing to one another to eliminate factors such as background to leave either emissivity or absorption, which is used to generate emissivity by subtracting it from 1.

Sundaram and Sousa Menses [79, 105-108] also used this pattern to calculate for emissivity. Their work stands out from the others because their experiment set up also fits all the criteria that are required for this research project: the ability to measure emissivity at high temperature, suitable for ceramic samples, reliable heating source and simple sample preparation. Therefore, Sundaram's TRR method was chosen for emissivity measurement in a radio frequency range and Sousa Menses's spectroscopy method was chosen for emissivity measurement in an infrared range. Sundaram's

method has the benefit of being able to measure the sample emissivity similar to the real application environment; sample heated in a general electric furnace, and Sousa Menses's method has the benefit of being able to measure the emissivity in the infrared range; a range representing heat energy.

## 2.3 Corrosion of refractories and coated refractories.

In the cement process, undesirable compounds are generated from the raw materials, coal and secondary fuels, that corrode the refractory lining. Commonly these are alkalis, chlorides and sulfates [109, 110] which are aggressive via their chemical nature and high temperature behaviour such as phases change, thermal expansion, density and volume change (Table 3). Schlegel *et al.* [111, 112] has categorized four causes of refractories corrosion. First, melt formation. Refractory materials selected for each application normally have a high heat resistance (high melting point), however, when they react with a corrosive compound, it may form a low melting phase which lowers the refractory strength. For example, MgO is a main refractory component used in the upper transition zone in cement rotary kiln and has a melting point of 2840$^{o}$C. When MgO reacts with $K_2CO_3$, the compounds melting point reduce to about 895$^{o}$C as shown in the phase diagram in Figure 12a. A similar reaction occurs with $K_2SO_4$, the melting point reduce to about 1067$^{o}$C, Figure 12b. Second, change of density and volume. When alkalis react with refractories at high temperature, they create a new compound with a lower density leading to volume expansion. Volume expansion may distort the refractory structure reducing strength leading to spalling. If the expansion is dramatic (> 50%) it can lead to bursting (alkali bursting). Third, expansion as a result of salt stored in pores. In some cases, the compound penetrates the brick and deposits in refractory pores. In the limited pore space volume expansion distorts the refractory structure. Finally, corrosion from water condensation. Water may condense inside the refractory and generate saturated water base salt solution leading to electrochemical corrosion. Another common effect that alkali has on refractory bricks is it penetrates through the brick pores and increases the brick's density so decreasing the brick's flexibility. As the alkali penetrates deeper into the bricks, the alkali densifies and does not penetrate further due to the temperature gradient. This creates a density difference in the refractory brick (high density in the hot face and lower density in the cold face). When external stress is applied to the brick, the hot face of the brick easily peeled off due to lack of flexibility leading to failure [113].

Table 3. Salt phases after heating at 1100°C [114].

| Corrosion compound | Phase at 1100°C | Thermal expansion ($x10^{-6}$ $K^{-1}$) at 600°C | Density ($g/cm^3$) | | Hygroscopic |
|---|---|---|---|---|---|
| | | | Density of solid | Density of melt | |
| $K_2CO_3$ | molten | 58 | 2.43 | 1.96 | No |
| $K_2SO_4$ | molten | 90 | 2.66 | 1.89 | No |
| KCl | Evaporated | 52 | 1.99 | 1.52 | Yes |
| $CaSO_4$ | sintered | 16 | 2.96 | N/A | no |

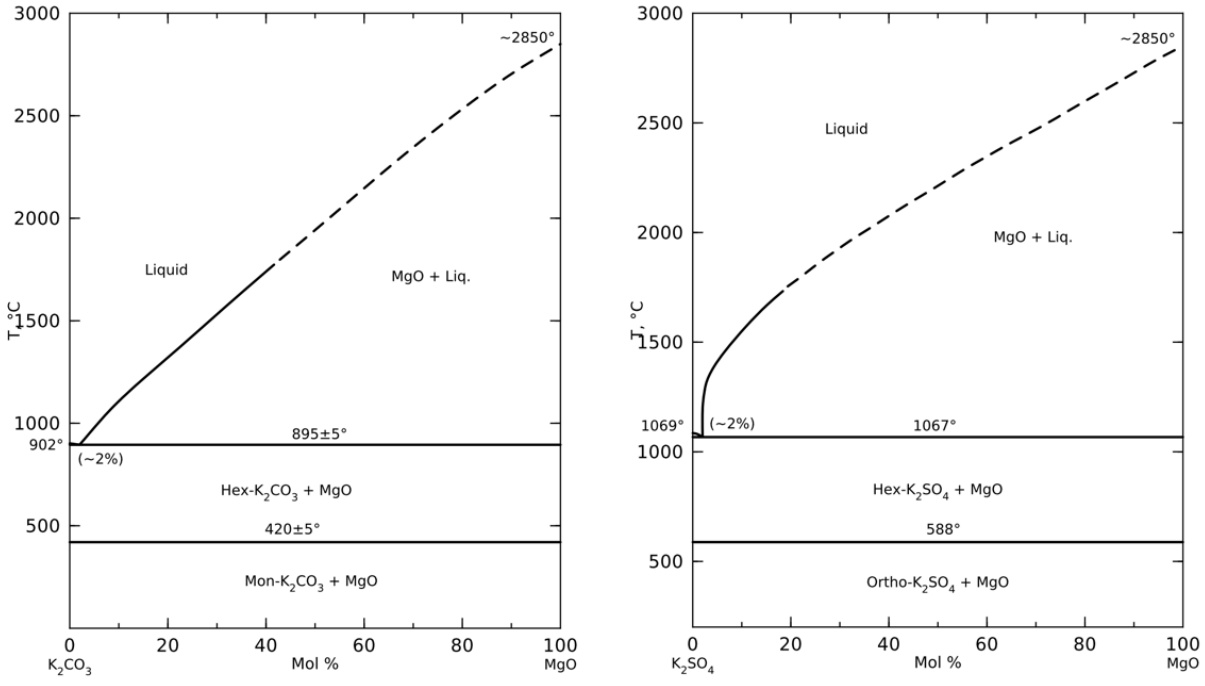


Figure 12. Phase diagrams of a) $K_2CO_3$ and MgO [115] and b) $K_2SO_4$ and MgO [116].

Other than alkali corrosion, the refractory bricks used to line the cement rotary kiln also have to face corrosion from the cement clinker raw materials [20, 117]. Excessive sulfates in the rotary kiln can react with calcium silicates and magnesia to form low melting phases such as merwinite ($Ca_3Mg(SiO_4)_2$, $C_3MS_2$), monticellite ($CaMgSiO_4$, CMS) and forsterite ($Mg_2SiO_4$, $M_2S$) as shown as an example in Equation 27, Equation 28 and Equation 29 [118, 119]. These equations reveal $CaSO_4$ is formed and penetrate through the bricks causing densification differences in the brick.

Equation 27. $2C_2S + MgO + SO_3 \rightarrow CaSO_4 + C_3MS_2$

Equation 28. $C_3MS_2 + MgO + SO_3 \rightarrow CaSO_4 + 2CMS$

Equation 29. $CMS + MgO + SO_3 \rightarrow CaSO_4 + M_2S$

Many testing methods are available for chemical corrosion tests in refractory industries. Each method has its advantages and disadvantages. To understand the reactions between the corrosion compound and the refractory raw materials, the most common test is a “disc-test” which is a straightforward test where the corrosion compound and the refractory raw material are mixed then pressed to discs (pellets). The discs are weighed, and dimension is measured before and after heat-treating at a certain temperature and time. Weight and volume changes are determined. Damage observation can sometimes be determined from the disc’s physical appearance. Brachhold and Aneziris [120] have used the disc test to synthesize $KAlSiO_2$. $KAlSiO_2$ was mixed from different potassium sources in the ratio of 30:70 by weight. The potassium sources were 1:1:1 ratio of $K_2SO_4$: $K_2CO_3$: KCl. The mixtures were uniaxially pressed to a pellet with a size of 50 mm diameter, 7 mm height with an approximate weight of 20 g. The pellets were sintered at 1100$^{o}$C for 5 h in an electric furnace. As a result, they were able to identify which synthesized $KAlSiO_2$ can be considered as an alkali corrosion resistance material from a benchmark that a diameter changes less than 2% is acceptable. Sassi *et al.* [121] also used the disc test in their work. Different raw materials (fireclay, andalusite, mullitized andalusite, mullite, fused zirconia mullite, bauxite, white corundum, β-alumina and calcium hexa-aluminate) were mixed with either $K_2CO_3$ or $Na_2CO_3$ in the ratio of 70:30 by weight. The mixtures were pressed to pellets in the size of 13 mm in diameter with a weight of 1.5 g and the pellets heated at 1200$^{o}$C for 5 h for the corrosion test. Volume change was used as an indicator of corrosion resistance. As a result, only β-alumina and calcium hexa-aluminate survived from both $K_2CO_3$ and $Na_2CO_3$ corrosion tests without destruction from volume expansion. This is because $(K,Na)Al_{11}O_{17}$ was

formed during the corrosion test and, as it is a non-expansive phase, its formation does not destroy the sample.

Naeshirozako *et al.* [122] used another approach to study alkali vapour attack. An alkali vapour environment was created by adding 0.2 g of $Na_2CO_3$ (alkali source) in an alumina crucible (40.5 mm diameter). The top of the crucible was closed with a sample which in the study was polycrystalline alumina and silica wool. Different sample density was used for the experiment. The sample sizes were 60 x 60 mm. Alumina tubes were used as spacers between the sample and the alumina crucible preventing adhesion. The sample and the crucible were then heated at 1350°C for 24 h in an electric furnace. Weight, thickness, phase and microstructure change, including $Na_2O$ concentration, was observed in the study. Samples with higher silica content had greater weight change and sample thickness decreased after they were exposed to alkali vapour. Alumina and silica in the alkali environment create several reactions, the final products were $NaAlO_2$ and glass.

Lee and Zhang [123] reviewed corrosion penetration and saturation in refractories. Most testing methods are designed for refractory use in the steel industries which have the largest market share of refractory use. Refractories in the steel industry face a different corrosion mechanism because the corroded source is mostly hot slag, not alkaline. However, the testing methods are applicable to cement kiln refractories. Corrosion rates depend on many factors such as temperature, refractoriness, environment, density, diffusivity and degree of agitation. Corrosion tests can be divided into two types; static corrosion test and dynamic corrosion test. The two tests are schematically shown in Figure 13. Figure 13a shows the static test in which a small amount of corroding agent is placed on the refractory specimen and then heated up to the testing temperature and held for some time allowing it to wet and react with the refractory. This method can be used to determine the interface and surface energies of the system; however, it does not represent the situation where the hot viscous fluid rapidly interacts with the refractory. Figure 13b shows a refractory specimen immersed inside molten fluid for some period. The advantage of this method is that it is easy to control the fluid composition. The disadvantage of this method is that it does not have a temperature gradient and therefore does not represent the manufacturing situation. Figure 13c illustrates one of the most popular methods because it is easy to prepare. The refractory is cored in the middle, filled with chemicals such as potassium carbonate and sodium carbonate, and heated to temperature. However, this method also lacks a temperature gradient, chemical flow and rapid interaction between the refractory and hot fluid. Figure 13d illustrates a static/dynamic test, in which the fluid is placed in a refractory crucible that is surrounded by another layer of refractory to create a temperature gradient. When the fluid is slag, molten steel is also added to generate a flow of the slag. However, the flow

control in this method could be challenging. Figure 13e shows a setting that represents a flow pattern of a glass tank. This method is almost like a combination of b) and d) with addition of rotating refractory specimens. Figure 13f shows another corrosion method, the rotary slag test. This method has many advantages; many samples can be tested in a single test, it provides temperature gradient and composition, and the fluidity of the chemical can also be partially controlled. The disadvantage of this method is the temperature is difficult to control, and it does not give a good reproducibility [123, 124].

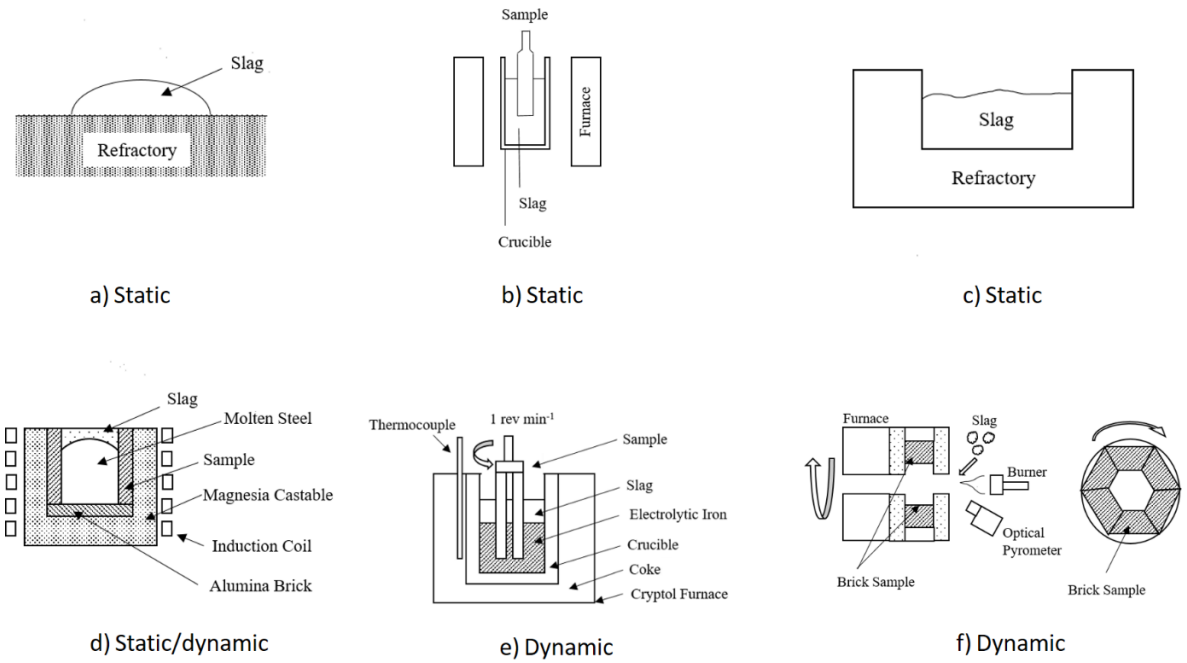


Figure 13. Corrosion Test Types. a)-c) is a static test, d) is a combination of static and dynamic test and e)-f) is a dynamic test (modify from [123]).

Lui *et al.* [20] conducted a *post-mortem* examination of a periclase-composite spinel brick which had been used in a cement burning zone for 10 months and reported that alkali salts were detected in pores, crack and grain boundaries. This observation indicates the alkali salts penetrated and reacted with the refractory which may be an advantage by improving sintering form a dense reaction layer. This layer prevents further alkali penetration through the refractories. However, this layer also generates stress between the dense layer and the rest of the refractories which causes the layer to spall off the refractory.

This thesis is mainly focused on understanding coating behaviour and emissivity properties. However, we also are interested in conducting initial corrosion testing to indicate how the coating

reacts with alkaline vapour. Two corrosion tests were performed; alumina crucible test and static cup test. These tests cannot be used to indicate corrosion resistance for real application because many variables are different, such as the amount of alkaline source, the time and temperature of the corrosion test, porosity, size of pores, local dissolution and interfacial reactions, and viscosity of liquids. However, this experiment tries to keep as many variables constant (the amount of alkaline source, the time and temperature of the corrosion test) and do several tests to reduce other uncontrollable variables (porosity, size of pores and local dissolution) so it can be used to rank the corrosion resistance among the samples. This rank would be expected to relate to the corrosion resistance in the real application.

## 2.4 Adhesion, abrasion and thermal shock resistance

To ensure the coating lifetime, measurements other than corrosion are needed such as adhesion, abrasion and thermal shock resistance. Adhesion determines the strength of attachment between the coating and the substrate. Abrasion determines the coating abrasive resistance. Thermal shock resistance determines how well the coating can resist the stresses that occur associated with sudden temperature change. These methods are described below.

### 2.4.1 Adhesion

There are three well known adhesion measurements; peel/pull-off, indentation and scratch methods. The peel-off methods are such as tape test: a tape is attached to the coating surface and was pulled-off to determine the coating detachment stress [125]. Another example of a pull-off method is a rods test, where two rods are attached to the sample surface, usually with an epoxy or resin. One rod on the coating and another at the back of the substrate. The two rods must be aligned with one another. The two rods are pulled in opposite directions to force the detachment of the coating from the substrate [126]. A limitation of the peel/pull-off methods is the force between the coating and substrate must be lower than the force of the type or the rods attach to the sample. The indentation methods involve applying mechanical force to the coating surface using indenters such as Brale or Vickers [127-129]. From these methods, fracture toughness of the coating is determined. Scratch methods are conducted by using a stylus to cross over the coating surface. The force of the stylus continues to increase until the coating is detached [130]. The damage that the stylus causes to the coating is identified by light microscopy, scanning electron microscopy or using acoustic emission to avoid unreliable visual judgment [131].

## 2.4.2 Abrasion

Abrasion in a cement rotary kiln is mostly from raw material/ cement clinker dust flowing in from the inlet through to the outlet (Figure 3). Therefore, the abrasion occurs parallel to the coating and refractory substrate surface, Figure 14, at temperature depending on the kiln zones.

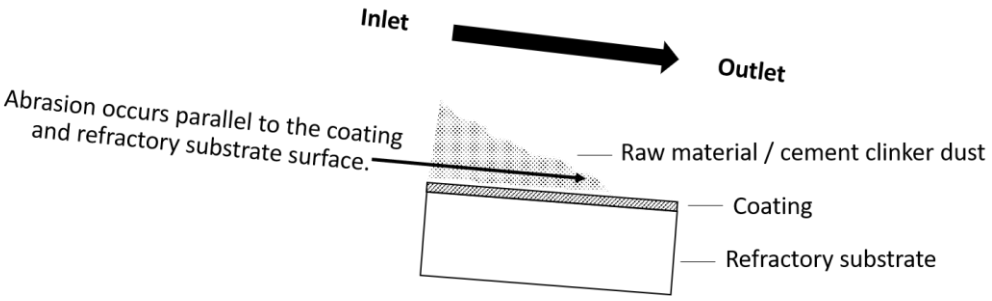


Figure 14. Schematic of raw material/ cement clinker dust flowing in from the inlet through to the outlet of the cement rotary kiln (author's figure).

Coating abrasion resistance can be tested with an ASTM D4060, "standard test method for abrasion resistance of organic coatings by the taber abraser" [132]. Figure 15 is a schematic of the abrasion test. This standard is suitable for organic coatings. The specimen is mounted on a turntable platform. Two vertical abrasive turning wheels with a load of 1000 g per wheel are pressed against the specimen. When the turntable turns, it creates an abrasion between the specimen and the abrasive wheels. This standard measured 1) wear index (average loss in weight (mg) per thousand cycles), 2) weight loss (loss in weight (mg) determined at a specific number of cycles) and 3) wear cycles per millimeter (number of cycles of abrasion required to wear a coating through to the substrate per millimeter of coating thickness). The limitations of this standard are the coating hardness must be less than the abrasion wheel or else the abrasion will occur on the wheel, not the specimen and this standard is only applied at room temperature.

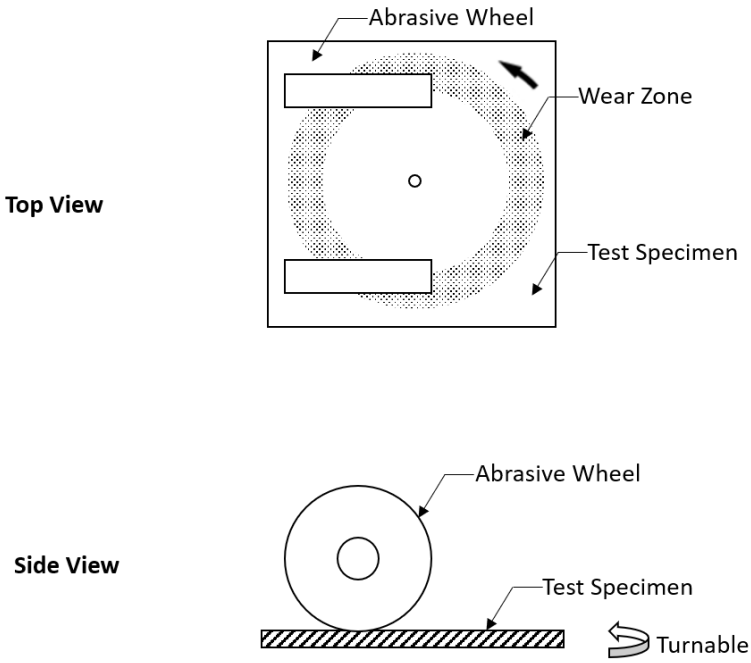


Figure 15. Schematic of wheel position in relation to the test specimen (modify from [132]).

The standard abrasion test for refractories is ASTM C704/C704M-15, "abrasion resistance of refractory materials at room temperature"[133], in which silicon carbide (SiC) is sprayed at right angles to the sample at a fixed velocity at room temperature. The abrasion resistance is determined by the weight loss of the sample. Such a method would not be suitable for testing coating abrasion resistance because it destroys not just the coating but also the refractory substrate. Wellmen *et at*. [134] have developed an abrasion testing instrument for TBCs. The schematic of the experimental device is shown in Figure 16. The compressor (C) and pressure vessel (P) are used to ensure that a constant of compressed air is supplied to the heating chamber (H). The heating chamber electrically heats the air and feeds the air into the acceleration tube (T). Abrasive material such as alumina grit is fed via screw feeder (F) into the acceleration tube and accelerates by the compressed air hitting the specimen in the sample chamber (S) at an angle to the specimen surfaced. The abrasion resistance will be determined by measuring the mass loss. This instrument is interesting due to many parts being adjustable to the user needs such as the abrasive material velocities (50-400 m/s), the abrasive material size rang (20-1000 µm), the impact angles (30, 45, 60, 77 and 90$^{o}$) and the abrasive material feed rate (0.1-10 g·min$^{-1}$). Even though this method uses abrasive material that flows along with the air that can be heated up to 900$^{o}$C, the specimen is measured at room temperature. There is research in progress for abrasion testing at high temperatures, but none is yet set up the abrasion in a largely parallel direction to the specimen.

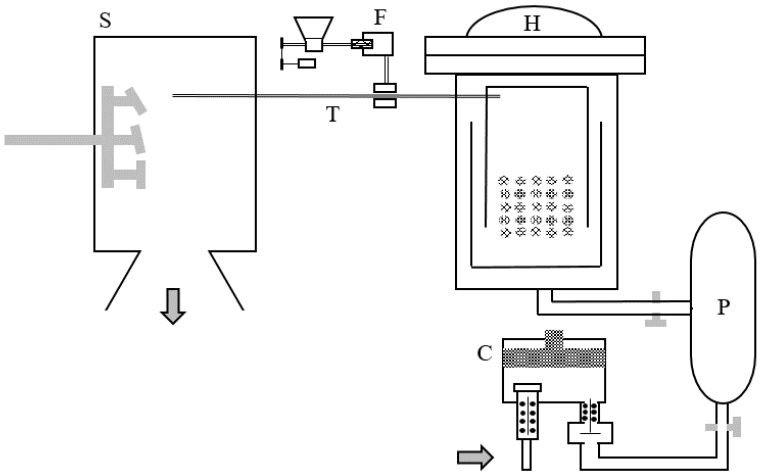


Figure 16. Schematic of the in-house abrasion testing instrument by Wellmen *et at*. C is a compressor. P is a pressure vessel. H is a heating chamber. F is a screw feeder. T is acceleration tube. S is sample chamber (modify from [134]).

### 2.4.3 Thermal shock

Thermal shock is when temperatures change dramatically in a short period. The thermal shock resistance on refractory can depend on many factors, for example, density, thermal conductivity, thermal expansion, poison's ratio, specific heat. For coating, the thermal expansion mismatch between the coating and substrate is the main factor that would cause the coating to peel off the substrate. Thermal shock resistance test is conducted by 1) heating the sample to a stable temperature, 2) quenching the sample to room temperature, the severity of the test can be increase by blowing air onto the sample or dropping it into water. To this point it is considered that the sample has been through 1 cycle of thermal shock test. Finally, 3) the sample is put back into the hot furnace and held until its temperature is stable with the furnace temperature then step 2 is repeated [135, 136]. These steps continue in cycles until the sample is physical damaged; cracks form or the coating peels off. The more cycles that can be repeated to failure the greater the samples resistance to thermal shock. Shinozaki *et al.*[135] reported that thicker coatings tend to spall off the substrate more quickly due to the greater stored elastic strain energy per unit area or the interface.

## 2.5 Literature gaps and thesis objectives

The research in this thesis aims to narrow the gap among current knowledge of emissivity commercial coatings, TBCs and EBCs coatings and the lack of knowledge of their potential application in cement kilns. Table 4 presents aspects of the emissivity of commercial coatings, TBCs and EBCs and the bold contents are the ones adopted for this thesis experiment.

Table 4. Comparing different coating fields on different aspects. Bold contents are the overlap aspects used in this thesis.

| | Thesis coating aim | Commercial emissivity coating | TBCs | EBCs |
|---|---|---|---|---|
| Substrate material | **Basic refractory brick (magnesia based)** | **Refractories brick most likely to be alumina** | Stainless steel and alloy | **Ceramics, CMCs most likely to be silica base** |
| Coating material | **Rare earth oxide** | **Rare earth oxide, carbon and unidentified materials** | **Mostly YSZ, rare earth oxides are used to improve emissivity** | Barium strontium aluminosilicate (BSAS), Rare earth mono- and di- silicates (REMS, REDS), $HfO_2$ and $ZrO_2$ based systems. |
| Apply technique | **Air spray** | **Air spray, paint** | APS, EB-PVD | APS, EB-PVD, sputtering, slurry deposition |
| Temperature range | **>1300°C** | **>1000°C** | <1200°C | **1200-1650°C** |
| Emissivity measurement | **Yes, TRR and using spectroscopy methods** | N/A | **Yes, there are many methods. Mostly involve FTIR** | N/A |
| Phases & Microstructure | **Yes, XRD, HT-XRD, SEM, EDX, TEM** | N/A | **Yes, XRD, SEM, EDX, TEM** | **Yes, XRD, SEM, EDX, TEM** |
| Corrosion testing | **Yes (alkaline vapour)** | N/A | N/A | **Yes (water vapour)** |

The challenging part for this adaptation is applying the coating via air spray instead of using APS or EB-PVD, which gives better adhesion between the coating and the substrate. APS and EB-PVD are not suitable for cement application because the coating has to be applied on-site and the substrate surface is lined in rings. The most effective, economic and practical way is to apply the coating by spraying or painting. To be able to do so, a binder has to be introduced into the coating system. The

binder purpose is giving simple fabrication, adhesion between the ceramic powder and the substrate and adhesion among the ceramic powders. Another important feature needed for the coating is heat resistance. Aluminium phosphate-based binders fit all these requirements, giving good strength, high temperature stability and abrasion resistance [137-139]. Aluminium phosphate-based binders are commonly used in ceramic systems. [138, 140].

Chen *et al.* [138] used aluminium phosphate binder with $Al_2O_3$-SiC as an abrasive resistant coating on steel for power plants. The binder was synthesized from mixing $Al(OH)_3$ and $H_3PO_4$ in different ratios. The mixtures were stirred until they become clear. X-ray diffraction (XRD) revealed the main coating phase is $AlH_3(PO_4)_2{\cdot}3H_2O$. Differential thermal analysis (DTA) indicated that on heating from 60-1000°C, two endothermic reactions occur. One at 101°C indicating dehydration of $AlH_3(PO_4)_2{\cdot}3H_2O$ to $AlH_3(PO_4)_2{\cdot}1H_2O$ and two at 218°C indicating dehydration of $Al(H_2PO_4)_3$ to $AlH_2P_3O_{10}$. The synthesized binders were also mixed with $Al_2O_3$-SiC (abrasive material) and MgO (curing additives) for abrasion testing. The coatings were deposited on the substrate via spaying to a thickness of 125-150 μm, then heated at 200°C for 2 h. Abrasion testing was conducted with a PMJ-1 wear machine which determined weight loss after using emery cloth (180#), under a load of 0.5 kg, sliding frequency of 60 Hz for 35 min. Coated samples lost half the weight of those that were uncoated. Chen *et al.* [138] concluded that abrasion depended on many factors, for example, the ratio of the $Al_2O_3$-SiC/binder, particle size distribution, the binder density and the Al/P ratio in the binder. Formanek *et al.* [140] used inorganic aluminium phosphate binder in a protective coating for Inconel walls in water boiler power plants. The coating was spayed using arc spraying or high-velocity oxygen fuel spraying onto an Inconel 625 substrate. As a result, their coating was usable in aggressive corrosion and abrasive atmospheres. They also report that the coating is resistant to thermal shock and has high emissivity at temperatures above 800°C. Abyzov [141] developed lightweight refractory concrete using aluminium-magnesium phosphate binder instead of foam or burn-out additives (filings, polymer spheres and other organic materials). Using aluminium-magnesium phosphate binder gave 3 main benefits. One, it consumed less energy because there are no materials to burn out. Two, it gave lower shrinkage, therefore, larger products can be produced. Three, it can increase the product working temperature.

It must be noted that phosphate-based binders must be used with caution. If they become glassy at elevated temperature, their thermal expansion coefficient (TEC) is relatively high (20-24 X $10^{-6}$ $K^{-1}$) [142, 143]. This is higher than the refractory substrate (12-16 X $10^{-6}$ $K^{-1}$) and $CeO_2$ TEC (~13 X $10^{-6}$ $K^{-1}$) [144]. The refractory substrate and $CeO_2$ have a similar TEC which if present in the coating means they would expand and shrink at the same rate but with phosphate glass that has a higher TEC, thermal

expansion mismatch between the substrate and the coating occurs. Thermal expansion mismatch occurs in two scenarios; the coating's TEC > the substrate's TEC and the coating's TEC < the substrate's TEC. If the coating's TEC is larger than the substrate's, during heating, the coating expand more than the substrate but it cannot expand freely because it is attach to the substrate and therefore creates a compression stress in the coating (Figure 17a). During cooling, the coating contracts more than the substrate creating tensile stress in the coating (Figure 17b). Vice versa, if the coating's TEC is less than the substrate's TEC, during heating, the coating expand less than the substrate creating tensile stress in the coating (Figure 17c). During cooling, the coating contracts less than the substrate creating compressive stress in the coating (Figure 17d). [145, 146]. Therefore, thermal expansion mismatch is undesirable because it generates stress in the coating which can lead to cracks.

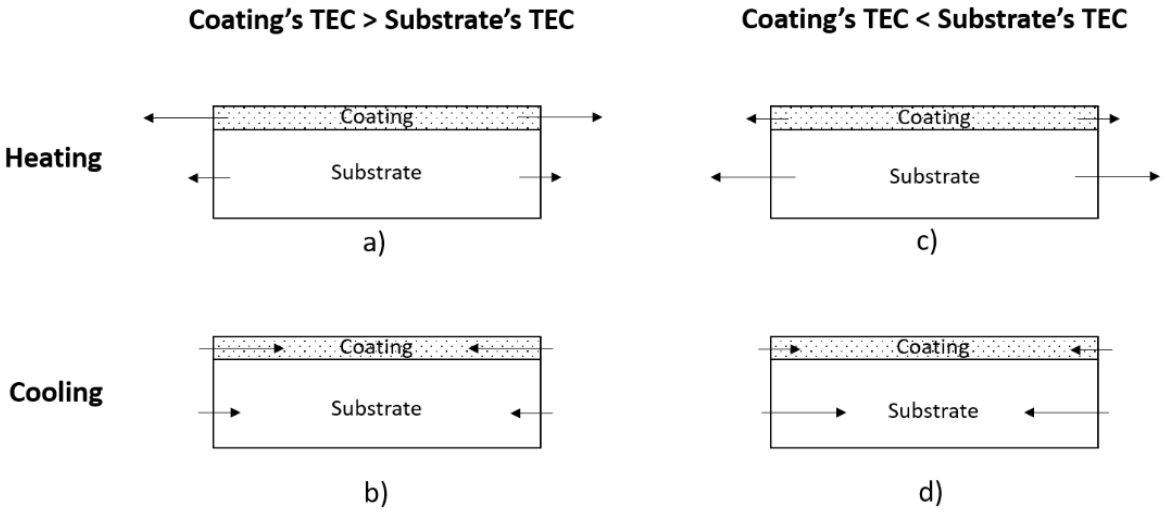


Figure 17. Schematic thermal expansion mismatch scenarios. a) coating in compression when TEC of the coating > substrate, during heating. b) coating in tensile when TEC of the coating > substrate, during cooling. c) coating in tensile when TEC of the coating < substrate, during heating. d) coating in compression when TEC of the coating < substrate, during cooling (author's figure).

In order to develop coatings to improve cement kiln efficiency gaps in our current knowledge need addressing include coating composition, method of application and emissivity measurements. Therefore, the research in this thesis will use the most abundant (and hence economical) rare earth oxide (cerium oxide, [147]) as a raw material with high temperature binder (aluminium phosphate-based binder) applied on a basic refractory brick via a simple gun spray. We aim to conduct emissivity measurements at 1300$^{o}$C and to examine the behaviour of the coatings in simulated cement kiln corrosion testing.

# Chapter 3: Experimental methodology

## 3.1 Refractory characterisation

In developing a high temperature coating, it is essential to understand the nature of the substrate on which it is to be deposited. The substrate used in this thesis is a basic refractory brick with a commercial name of MSN80 provided by The Siam Refractory Industry Co., Ltd, Saraburi, Thailand. The basic refractory brick was analyzed via phase and physical characterisation.

The phase content of the refractory bricks was determined via X-ray diffraction (XRD) which is a well-known technique for determining material phase composition and cell lattice parameters [148]. A schematic diagram of an XRD instrument is shown in Figure 18. A known X-ray wavelength is generated from an X-ray source, passing through a slit assembly hitting the sample and diffracting through another slit assembly and then into the detector. The slit assemblies act as a monochromator defining the wavelength of the X-ray incident beams. Crystal planes of different crystal structures diffract X-ray beams at a characteristic angle; therefore, an unknown phase can be determined by matching its diffraction pattern collected from the detector with a database pattern of known material. According to lattice parameters, knowing the wavelength of the X-ray and the scattering $\theta$ angle, the atom interspacing (d-spacing) can be calculated using the Bragg equation (Equation 30). The Bragg equation is derived from diffraction from atoms in crystal planes in materials (Figure 19).

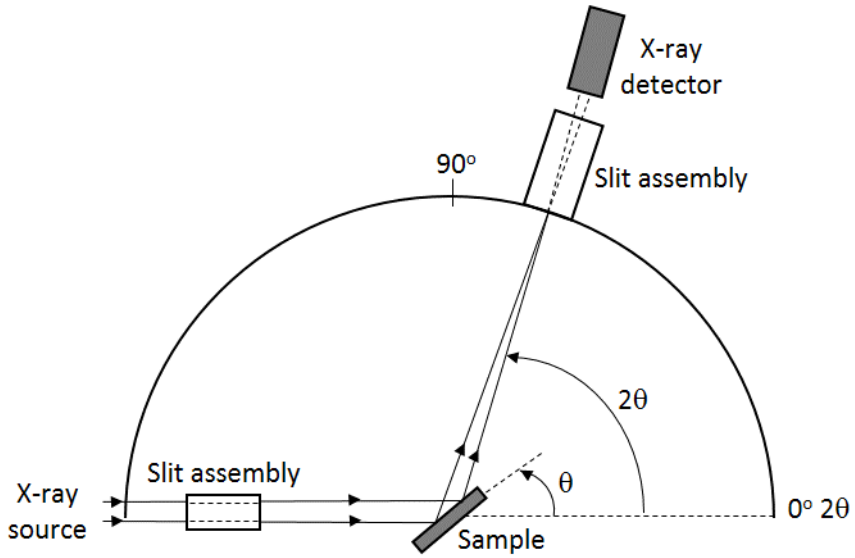


Figure 18. Schematic of X-ray path in an X-ray diffraction instrument (modified from [148]).

Equation 30. $$n\lambda = 2dsin\theta$$

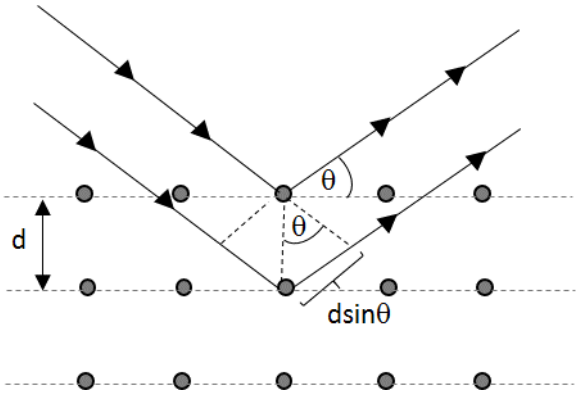


Figure 19. Schematic of X-ray path on diffraction from crystal planes (modified from [148]).

In this research, the refractory brick was ground with a pestle in a mortar to powder. The powder passing through a 325-mesh sieve (~44 µm) were used for XRD. XRD (D2 phaser, Bruker, Karlsruhe, Germany) was carried out with Cu-Kα radiation of wavelength 1.54 Å over 15-65° 2θ with count time of 1 second and step size of 0.034°. Intensity data versus 2θ angle was analysed via the X'Pert Highscore Plus program (Malvern Instruments Ltd, Malvern, UK) to determine the refractory phases present. It must be noted that XRD is unable to detect a phase in small amount (material dependent, commonly <3%) due to the peaks being embedded in the noise [149].

The microstructure of the refractory brick was analyzed to understand the overview of the substrate structure, topography and composition before the developed coating is applied on it. Microstructures were observed using an SEM. A schematic of an SEM is shown in Figure 20. Electrons generated from an electron gun pass through a set of electromagnetic lenses which narrow down and focus the electrons onto the sample. The whole system is under a vacuum of 1.1 x $10^{-5}$ torr. Once the electron beam hits the sample, several effects occur. The most common are; 1, the electrons knock out an electron from an atom present near the surface (to a depth of ~50 Å) of the sample generating secondary electrons, 2, the electrons are reflected off the sample surface (back-scattered electrons) and 3, an excited electron moves to a stable state and releases a characteristic X-ray (emission X-ray). These are called characteristic X-ray because they give a specific energy of a certain element which is excited. The energy levels of the shells are different for every element with a different atomic number. The energy levels are knowingly different even for the adjacent atomic numbers. This circumstance follows the Moseley's relation as expressed in Equation 31 [150]. A schematic of these 3 interactions is illustrated in Figure 21. The secondary electrons energy from the near surface of the sample to a depth of ~50 Å while back-scattered electron comes from deeper to ~500 Å and characteristic X-rays analyses even deeper to ~5 μm into the sample as shown in Figure 22. A common way to determine the maximum electron penetration range is from Kanayo-Okayama range (Equation 32) [150]. In general, the range is in-between 0.5-5 μm. Different detectors are used to detect these different electrons and X-rays. Secondary electrons, which are used for imaging in this thesis, were detected using an Everhart Thornley secondary electron detector (Zeiss Leo Gemini 1525, Oberkochen, Germany). The electron detectors transfer the signals collected from the sample (sample space) by modulating the brightness of a cathode ray tube (CRT, display space). Images are generated by scanning the electron beam on the sample in the X-Y direction and simultaneously the signals are transfer to the CRT which scans synchronously with the electron beam. In other words, an SEM image is a constructed map on the CRT [149, 150]. Regarding, X-ray spectrum, its detector passes the signal to another device: The Energy Dispersive X-ray Spectrometer (EDX). The detector used in this thesis was the lithium-drifted silicon Si(Li) (Oxford Instruments, Abingdon, UK). EDX is an additional device connected to the SEM and as mentioned earlier these X-ray spectra is characteristic, as a consequence it is used for element analysis [150]. Although EDX adds analytical capability to the SEM, it must be kept in mind that the X-rays collected are emitted from a greater depth (up to 5 μm from the surface) than the electrons collected for the SEM imaging (50-500 Å). Hence, the X-rays collected for the EDX gives information not for only what is seen in the SEM image but also what is underneath it.

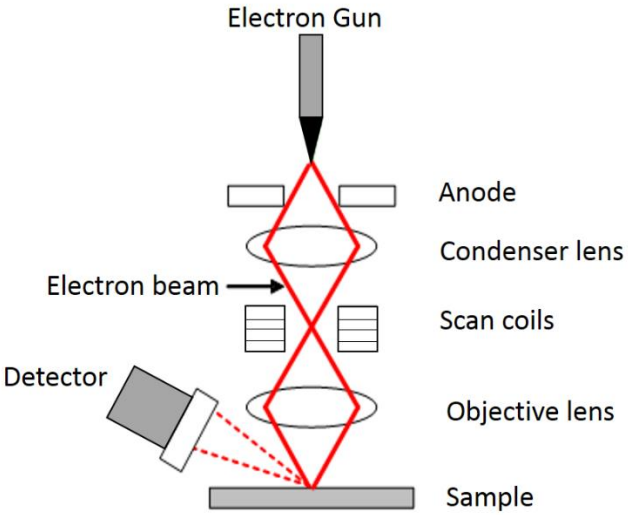


Figure 20. Schematic diagram of electron beam path for imaging and diffraction mode in SEM (author's figure).

Equation 31. $$\lambda = \frac{B}{(Z-C)^2}$$

were $\lambda$ is wavelength of the characteristic X-ray, Z is atomic number and B and C are constants which are different for each X-ray line family (e.g. K family consists of $K_\alpha$ and $K_\beta$).

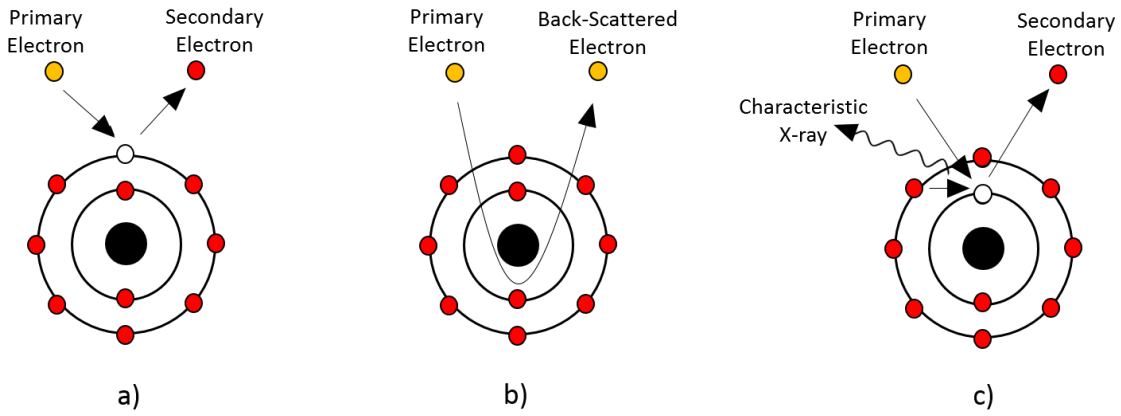


Figure 21. Schematic diagram of three interactions between a primary electron and an atom. a) primary electron knocks out an electron from an atom creating a secondary electron. b) primary electron reflected off an atom becoming a back-scattered electron and c) primary electrons excite an electron in an atom, and as the electrons from an outer shell comes to fill the empty space a characteristic X-ray is released (author's figure).

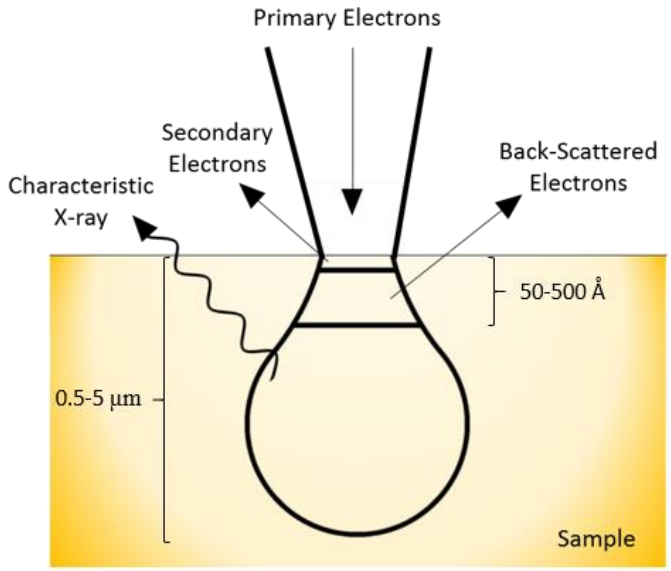


Figure 22. Schematic diagram of different electron signals generated via SEM and their region of origin (author's figure).

Equation 32. $$R_{KO} = \frac{0.0276AE_0^{1.67}}{Z^{0.889}\rho}$$

where $R_{KO}$ is Kanaya-Okayama range. $A$ is atomic mass, $E_0$ is primary electron beam energy (keV), $Z$ is sample atomic number and $\rho$ is sample density (g·cm$^{-1}$)

Dealing with an electron beam, it is essential for SEM and EDX samples to have a path for the electrons to travel along the sample. Electrons can pass through the sample if the sample is electrically conductive. If the sample is not conductive, there are several options to create an electron path. For example, coat the sample with a conductive material such as gold or chromium. Conductive tape or paint such as carbon tape or silver paint can also be used to create an electron path.

The refractory brick microstructure was observed with an SEM (Zeiss Leo Gemini 1525, Oberkochen, Germany) at an accelerating voltage of 5 keV for imaging and 20 keV for EDX analysis. The system was of a vacuum of $1.1 \times 10^{-5}$ torr. A semi-quantitative chemical analysis was performed by analyzing areas using EDX (X-MaX20, Oxford Instruments, Abingdon, UK). A conducting path for the samples was created by attaching the sample onto a carbon tape on the sample holder. The sample was then coated with 10 nm chromium on its top surface. The top chromium coating and the carbon tape underneath the sample was linked with silver paint.

## 3.2 Coating characterisation

### 3.2.1 Raw materials and mixing procedure

To develop a high emissivity coating for high temperature applications, the coating must contain highly emissive material that also has high heat resistance and a binder to improve the coating flowability and adhesion. For an application temperature higher than 1000°C, a ceramic material is a suitable choice. Cerium oxide ($CeO_2$) is a rare earth ceramic that has a high melting point of 2477°C and has a high emissivity of 0.9 in the range of 1000-2000°C. It also has a good base and acid chemical resistance properties and has a relatively low cost among the rare earth oxides [56, 63, 76, 77]. Therefore, $CeO_2$ was selected as the emissive ceramic for this research. $CeO_2$ was used as received as cerium (IV) oxide, 99.5% (REO)[4] lot number A10Z032 supplied by Alfa Aesar, Heysham, Lancashire, England. $CeO_2$ compositions are presented in Table 5 which is from the supplier certificate of analysis for this lot number. The $CeO_2$ particles size was measured with Mastersizer 2000 particle size analyzer with Hydro 2000SM dispersion unit, Malvern panalytical, Malvern, UK. Results show of d(0.5) = 9.688 μm and particle distribution curve are presented in Figure 23. As mentioned earlier, the ceramic material must be mixed with a binder to create flowability and adhesion to the substrate. Phosphate binders are commonly used for high temperature coatings [137, 140, 141]. Alumina dihydrogen phosphate ($AlH_6O_{12}P_3$) was selected as a binder in this thesis. It was also used as received as a 50 wt% aqueous solution supplied from Alfa Aesar, Heysham, Lancashire, UK. For future reference, the samples that are used throughout this research are coded and prepared as shown in Table 6.

[4] REO (Rare Earth Oxide) is used in rare earth industry in presenting the rare earth compound purities. It represents the specific rare earth oxide compared to the total rare earth oxides (TREO) i.e. cerium (IV) oxide, 99.5% (REO) means that $CeO_2$/TREO is 99.5 wt%.

Table 5. Cerium (IV) oxide, 99.5% (REO) lot number A10Z032 compositions. Standard deviation was not supplied.

| Compound | Amount |
|---|---|
| $CeO_2$/REO | ≥99.5% |
| $La_2O_3$/REO | 0.024% |
| $Pr_6O_{11}$/REO | ≤0.003% |
| $Nd_2O_3$/REO | ≤0.0015 |
| $Sm_2O_3$/REO | 0.0005% |
| $Y_2O_3$/REO | ≤0.0005% |
| $Fe_2O_3$ | 0.0003% |
| $SiO_2$ | 0.0022% |
| CaO | 0.0024% |
| CuO | <0.0005% |
| PbO | <0.0005% |
| $MnO_2$ | <0.0005% |
| $P_2O_5$ | <0.06% |
| $SO_4$ | <0.01% |

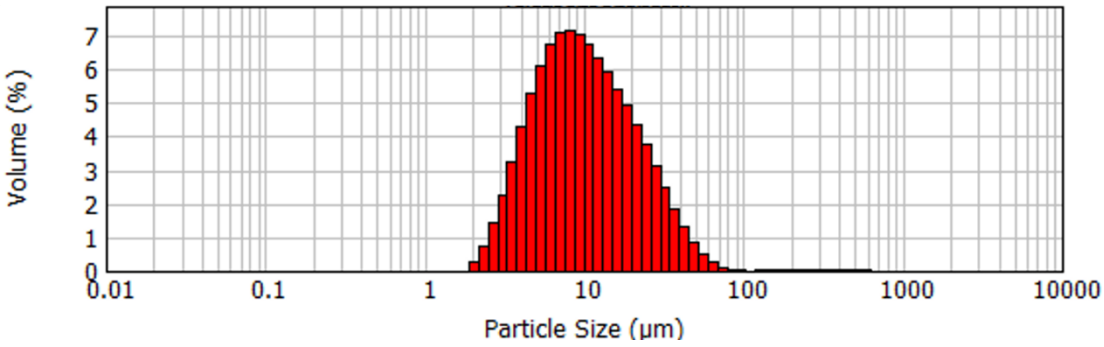


Figure 23. $CeO_2$ powder (cerium (IV) oxide, 99.5% (REO) lot number A10Z032 supplied by Alfa Aesar, Heysham, Lancashire, England) particle distribution measured via Mastersizer 2000 particle size analyser with Hydro 2000SM dispersion unit.

Table 6. Sample names are linked to their appearance; coating slurry is a mixture of $CeO_2$ (solid) and $AlH_6O_{12}P_3$ (solution) in a slurry form, basic refractory is refractory in a brick form and coated basic refractory is the basic refractory coated with the coating slurry. The sample names are shortened to code names and are used as a reference throughout this thesis. The sample names and code names are also related to the different composition of $CeO_2$:$AlH_6O_{12}P_3$ volume ratio. The volume ratios are given for a better understanding of the volume amount of $CeO_2$ and $AlH_6O_{12}P_3$ present in each coating. The weight ratios are converted from volume ratio and given for convenience in preparing the coatings. In this thesis, $CeO_2$ in each coating is set to be constant at 10g. Preparation and procedure represent how the coatings are mixed and applied.

| Sample names | Code name | $CeO_2$:$AlH_6O_{12}P_3$ volume ratio | $CeO_2$:$AlH_6O_{12}P_3$ weight ratio | Preparation procedure |
|---|---|---|---|---|
| Coating slurry 1-3 | CS 1-3 | 1:3 | 10:6.7 | $CeO_2$ was mixed with $AlH_6O_{12}P_3$ in a beaker with a magnetic stirrer for 2 hours |
| Coating slurry 1-5 | CS 1-5 | 1:5 | 10:10 | |
| Coating slurry 1-12 | CS 1-12 | 1:12 | 10:25 | |
| Basic refractory | BR | - | - | Receive from a supplier and is cut with to the size of 10x10x3 $mm^3$ |
| Coated basic refractory 1-3 | CBR 1-3 | 1:3 | 10:6.7 | The coating slurry (CS 1-3, 1-5 and 1-12) gun sprayed onto a basic refractory brick and was left to try overnight. |
| Coated basic refractory 1-5 | CBR 1-5 | 1:5 | 10:10 | |
| Coated basic refractory 1-12 | CBR 1-12 | 1:12 | 10:2.5 | |

### 3.2.2 Rheology

Rheology is the study of fluid flow; in this case liquid fluid. Liquid rheology is categorised as Newtonian or non-Newtonian. The viscosity of a liquid is defined from a scenario where there are two surfaces with a gap of fluid (h). One surface is fixed and another is free to move along the x-direction with a velocity (v). When the movable surface moves, it creates a velocity gradient in the fluid. A simplified image of the scenario is shown in Figure 24. From this scenario and Newton's law of

viscosity, shear stress ($\tau$) is equal to the product of viscosity (η) and velocity gradient ($\frac{dv_x}{dy}$). In this scenario, velocity gradient is the velocity of the movable surface ($v$) divided by the distance between the two surfaces (h) which is also known as the shear rate (ϒ). Newton's law of viscosity for this scenario is presented in Equation 33.

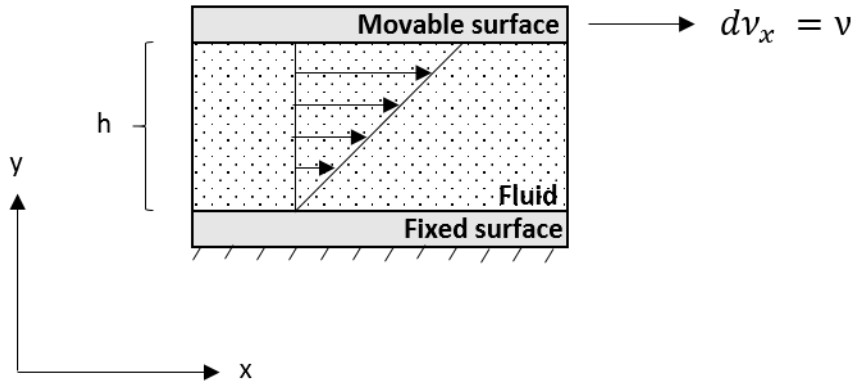


Figure 24. A simplified image of a scenario that describes the Newton's law of viscosity. The fluid is placed between and fixed surface and a movable surface with a gap "h". When the movable surface movies with a velocity of "v", the shear rate is calculated by dividing h with v. Viscosity can then be calculated from dividing shear stress (measured from a rheometer) with shear rate (h/v) (author's figure).

Equation 33. $$\tau = \eta \cdot \frac{dv_x}{dy} = \eta \cdot \frac{v}{h}$$

Viscosity (η) is defined as the resistance of flow. If the viscosity is constant, the fluid is considered a Newtonian fluid. If the viscosity is not constant and is a function of shear rate ($\eta(\Upsilon)$), it is considered a non-Newtonian fluid. Various non-Newtonian fluids are known. In one, the viscosity increases with shear rate. This is known as a shear thickening effect. In another, the viscosity decreases as the shear rate increases. This is known as a shear thinning effect. Plotting viscosity versus shear rate, the Newtonian fluid and the non-Newtonian fluid of both shear thickening and shear thinning can be seen as in Figure 25.

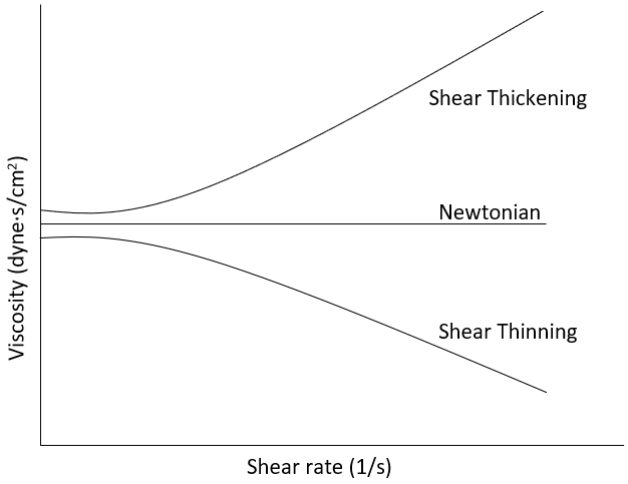


Figure 25. Example graphs of Newtonian and non-Newtonian flows (shear thickening and thinning) (author's figure).

In this research, the viscosity of the coating is important because it helps understand the flowability of the coating when used in the application, in which the coatings are applied onto the substrates via gun spay. Low viscosity (high flowability) is required when pressure (high shear rate) is applied to push the coating through the nozzle. However, when the coating hits the substrate (low shear rate) it is required to have a high viscosity (low flowability) so it does not slip off the substrate. This is shown schematically in Figure 26. Therefore, a shear thinning fluid is preferable for the coating in this research.

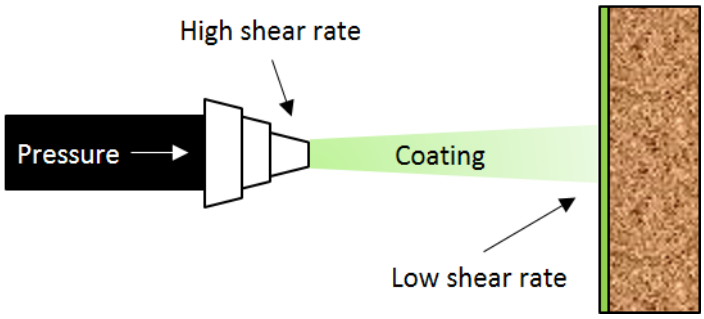


Figure 26. Schematic of spraying process (author's figure).

A hybrid rheometer, (Discovery HR-1, TA Instruments, New Castle, Delaware, USA) was used for measuring the viscosity of the coatings. The hybrid rheometer mimics the scenario mentioned earlier in Figure 24. A spindle plate is connected to an electric motor and a tensiometer. The spindle plate is placed parallel with a fixed stage. The coating sample is applied in between the spindle plate and the fixed stage. As the motor turns to create a shear rate, the tensiometer reads the sample flow

resistance. The hybrid rheometer calculates viscosity from the force applied by the tensiometer with the spindle size, shear rate, the gap between the spindle plate and the fixed stage and temperature. The conditions used in this experiment were shear rates ranging from 1-100 $s^{-1}$ within 60 seconds, 8 mm plate gap and 25°C respectively. A plot of viscosity versus shear rate indicates whether the coating is a Newtonian or a non-Newtonian fluid. Four samples were used for rheology measurement, CS 1-3, CS 1-5, CS 1-12 and $AlH_6O_{12}P_3$ on its own. Three measurements were made for each sample for average values and standard deviation.

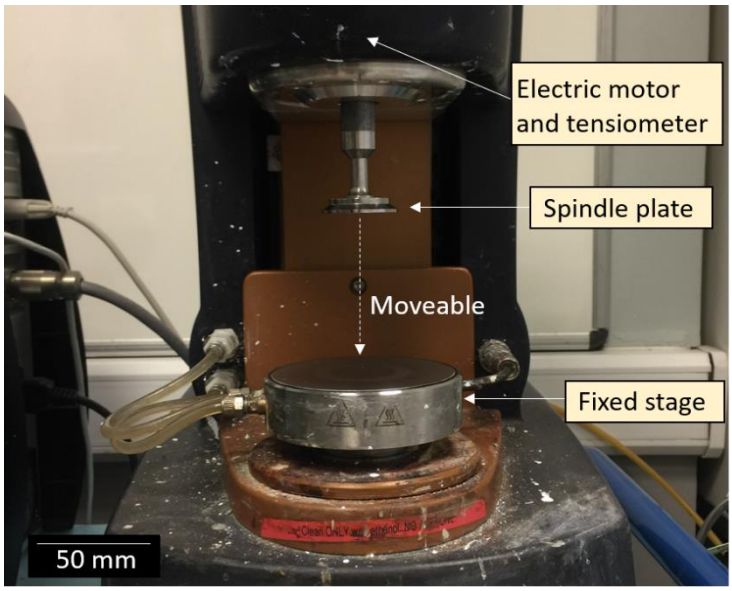


Figure 27. Hybrid rheometer showing the position of the electric motor and tensiometer, spindle plate and fixed stage (author's figure).

## 3.2.3 Coating phase evolution with temperature.

### 3.2.3.1 Differential scanning calorimetry (DSC) and Thermogravimetric analysis (TGA)

A differential scanning calorimeter (DSC) is a device that measures heat flow going in and coming out of a material. A schematic overview of the DSC set up is shown in Figure 28. A sample and a reference are connected to a temperature sensor (thermocouple) inside a furnace. The temperature sensor tracks the temperature difference between the sample and the reference. When the temperature of the two is different, the power of the furnace is adjusted to keep the sample temperature equivalent to the reference. Consequently, heat fluxes going in and coming out of the sample are measured. When the sample temperature is lower than the reference, it indicates that the sample is absorbing heat more than the reference and therefore, more heat must be put into the

sample to achieve an equivalent temperature. The troughs on the graphs are known as endotherms. Vice versa, if the sample temperature is higher than the reference, it indicates that the sample is releasing more heat than the reference and less heat needs to be input into the sample. The peaks on the graphs are known as exotherms. DSC is normally used simultaneously with thermogravimetric analysis (TGA). TGA is a technique that measures weight change as a function of temperature and time. Knowing the weight loss and gain helps to understand whether the sample is releasing gas/vapour or reacting with the gas in the furnace and producing a new compound [151]. For accuracy, several factors must be taken to consideration. Some factors are considering to be a "built-in" factor which is different for every instrument and is difficult to change e.g. sample container, thermocouple characteristic. In this thesis, the same DCS and TGA is used throughout the experiment to avoid these factors. Other factors are controllable. The significant ones in this thesis are the sample weight, the heating rate and the sample surrounding. Sample weight is proportional to peak area and is shown in Equation 34. Therefore, enough sample must be used for the measurement. In this thesis, 0.5 ±0.015 g of sample was used. According to the heating rate, increasing the heating rate increases the procedural peak temperature (peaks shift to higher temperature) and the area of the peaks. However, it decreases the resolution of the peaks so we might not be able to distinguish adjacent peaks. Generally, 5 or 10°C/min is recommended. The heating rate for this thesis was kept content at 5°C/min. As for the sample surrounding, flowing gas atmosphere is preferable over static atmosphere because as degradation or decomposition from the sample occurs, the sample surrounding changes. Therefore, a flowing gas atmosphere helps to blow away those volatiles, keeping the atmosphere around the sample constant [151]. In this thesis, an ambient gas flow of 20 ml/min was used.

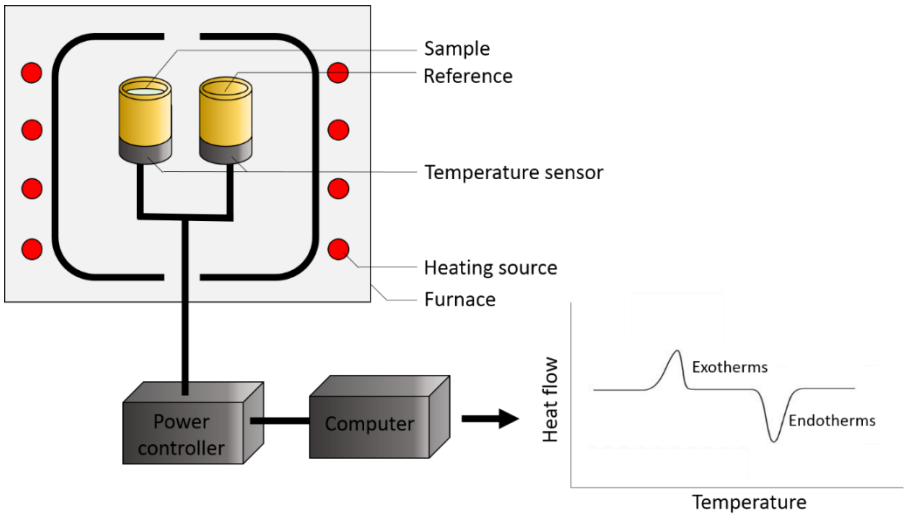


Figure 28. Schematic diagram of a Differential Scanning Calorimeter (DSC) (author's figure).

Equation 34. $$A = \pm m \cdot \Delta H \cdot K$$

where $A$ is peak area, m is sample mass, $\Delta H$ is enthalpy change and K is calibration constant

Differential scanning calorimetry (DSC) and thermogravimetric analysis (TGA); NETZSCH STA 449F1, Selb, Germany, were used to measure the heat flow, weight change and temperature in this experiment. The instrument was first calibrated with empty alumina crucibles (one for adding sample and another was used as reference). Second, 3 coating slurries, CS 1-3, CS 1-5 and CS 1-12, were prepared in the way mentioned in section 3.2.1. Coating slurries were weighed and one coating at a time was added to the sample alumina crucible. The sample and reference crucible are then heated in air to 1500°C.

3.2.3.2 High temperature X-ray diffraction (HT-XRD), X-ray diffraction (XRD)

Phase analysis was carried out using high temperature X-ray diffraction (HT-XRD) unit D8 Advance, Bruker, Karlsruhe, Germany, to study the interaction between cerium oxide ($CeO_2$) and aluminium dihydrogen phosphate ($AlH_6O_{12}P_3$) at different temperatures. A sample was prepared by using a magnetic stirrer to mix $CeO_2$ powder (cerium (IV) oxide, 99.5% (REO), Alfa Aesar, Heysham, Lancashire, UK) with $AlH_6O_{12}P_3$ (50% w/w aq. soln., Heysham, Lancashire, England) at a ratio of 1:6 by volume for 2 h. The mixture was dried overnight at 110°C in an oven (MOV -112, Sanyo Moriguchi City, Osaka, Japan). After, it was calcined at 600°C, 3°C/min in an electric furnace (EHF 1800, Lenton, Hope, Hope Valley, UK) for 1 h to get rid of excessive water. The calcined sample was crushed then mixed with alcohol so it could be dispersed evenly on a platinum heating strip of the HT-XRD as shown in Figure 29. The HT-XRD measurement conditions were Cu-K, radiation with wavelength 1.54 Å, 15-60° of $2\theta$ with count time of 0.4 seconds and step size of 0.04°. The measurement started at 30°C then temperature was increased to 500°C at a rate of 50°C/min. From 500°C, the temperature continued to rise to 1500°C at a heating rate of 10°C/min. XRD measurements were made at every 50°C interval. After the temperature reached 1500°C, the temperature was held constant for 10 minutes before another measurement was done and then the unit cooled down. The heating steps are shown in Figure 30.

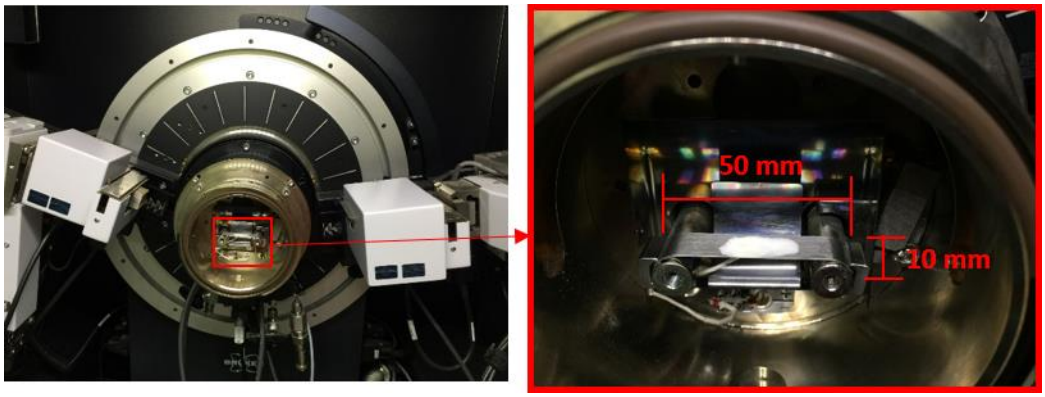


Figure 29. The left figure presents an overview of an HT-XRD chamber. The right figure is a magnified image of the left figure presenting crushed calcined coating on the platinum heating strip for HT-XRD (author's figures).

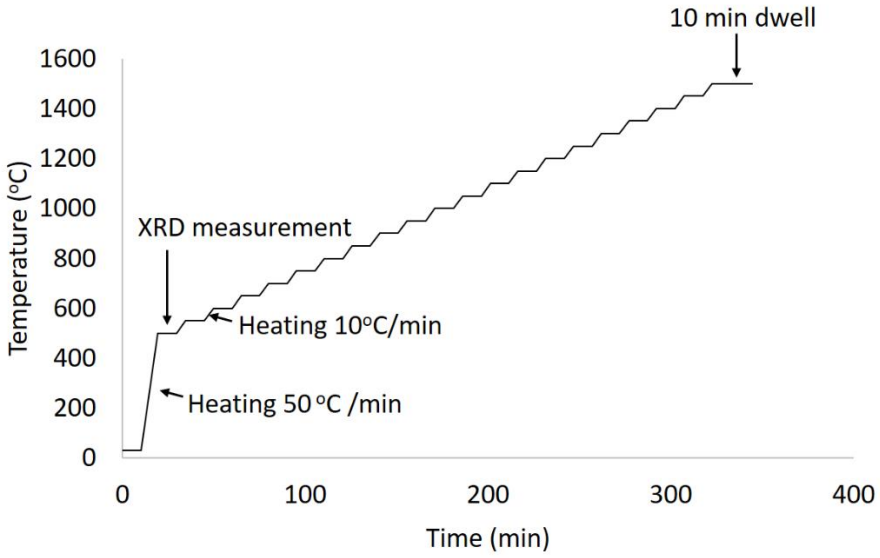


Figure 30. Heating profile of high temperature XRD measurement where the heating rate from 30°C to 500°C was 50°C/min and then was dropped to 10°C/min from 500°C to 1500°C. The temperature was held at every 50°C interval for XRD measurement (author's figure).

HT-XRD is designed to give an understanding of the phase changes of materials at different temperatures, however, it is noted that there is a drawback of this technique. The downside of HT-XRD is that the peak intensities are lower than those given from a room temperature powder XRD. This makes it a challenge to collect low-intensity peaks due to the small sample quantity. In this case, only 0.25 $cm^3$ of crushed calcined coating mixed with alcohol was used for HT-XRD measurements which is more than 10 times smaller those used in a room temperature powder XRD. Increasing the intensity of the peaks may be done by increasing the count time of the measurement. However, this increases

the overall measurement time and is not always suitable. A room temperature powder XRD was conducted to observed reactions between $CeO_2$ and $AlH_6O_{12}P_3$ with a ratio of 1-5 by volume in un-sintered samples heat treated to 800°C and 1550°C for 3 h. The room temperature powder XRD conditions were Cu-K, 1.54 Å, 15-60° of 2θ with count time of 1 second and step size of 0.034°.

HT-XRD measurement used lower sample quantity than a normal room temperature XRD and the X-ray scanning at each temperature is fast (1 second), Nelson-Riley parameters (NRP) were used to determine whether there is a systematic error. NRP (1/2[(cos2θ/sinθ) + (cos2θ/θ)]) is a function that can indicate the degree of systematic error in peak position due to sample displacement or misalignment [152]. Plotting the NRP on the x-axis with lattice parameter (a) on the y-axis shows whether there is a lattice parameter change or there is a systematic error. Lattice parameter (a) for a cubic structure can be calculated from the Miller indices (h,k,l) and d-spacing (d) as presented in Equation 35. Two features were taken into consideration: the slope and the interception. The slope represents the degree of systematic inaccuracy due to sample displacement. The closer the slope is to zero the less the systematic error. The second feature is the intercept of the line which represents the true lattice parameter – the higher the intercept the more the lattice parameter has changed. Figure 31 presents two scenarios that are possible. The first is shown in Figure 31a, where the temperature increases the slope changes, but the intercept does not, meaning that there is a change in specimen displacement as the temperature increases. Figure 31b, shows that as the temperature increases, the intercept changes, while the slope does not, indicating that the shift in peak positions is due to a lattice parameter increase.

Equation 35. $$a = \sqrt{h^2 + k^2 + l^2} \cdot d$$

where $a$ is lattice parameter, h, k, l are Miller indices, and d is d-spacing.

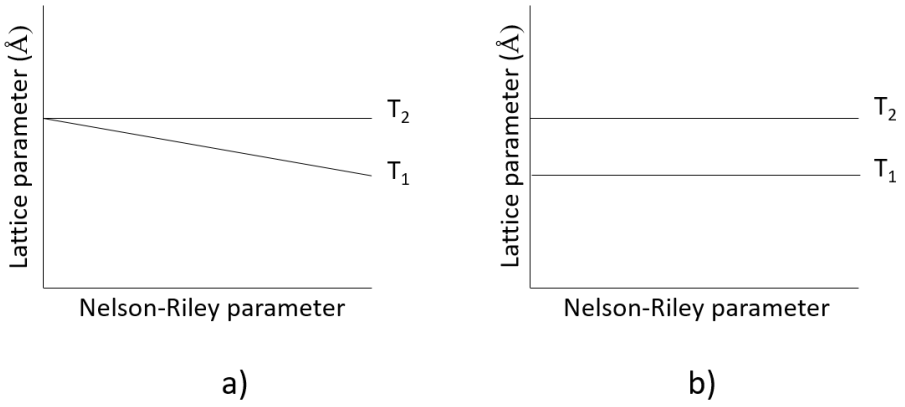


Figure 31. Schematic images of Nelson Riley parameter versus lattice parameter where temperature 1 ($T_1$) is lower than temperature 2 ($T_2$). a) Represents scenario 1 where the slope changes with temperature and b) Represents scenario 2 where lattice parameter change with temperature (author's figure).

XRD experiments were also done with samples containing different compositions. This helps us to understand how the coating composition affects the coating phase composition at high temperatures. Sintered coating slurries of different ratios of $CeO_2$: $AlH_6O_{12}P_3$ 1:3, 1:5 and 1:12 (SCS 1-3, SCS 1-5 and SCS 1-12) were used for this experiment. The coating slurry was sintered at 1300°C for 3 h. and XRD conditions were Cu-K, 1.54 Å, 15-60° of 2θ with count time of 1 second and step size of 0.034°.

3.2.3.3 X-ray photoelectron spectroscopy (XPS)

X-ray photoelectron spectroscopy (XPS) was first developed by Siegahn and his research group in the mid 1960s [153]. The technique is based on the concept of a photon used to describe the ejection of electrons from a surface when photons impinge upon it. Here Al or Mg Kα X-ray photons of respective energies of 1486.6 eV or 1253.6 eV illuminate a sample in a vacuum leading to the ejection of electrons. The kinetic energy of the ejected electrons ($E_{Kinetic}$) is in direct relation with their binding energy ($E_{binding}$) in the atom. The relation is given by Equation 36.

Equation 36. $$E_{Kinetic} = E_{photon} - E_{binding} - \Phi$$

where $\Phi$ is the work function of the solid.

The energy of the photoelectrons leaving the sample is determined using an energy analyzer which, after scans of a certain range of energies, gives a spectrum where the electron current is plotted

against the energy. In this spectrum (Figure 32), peaks can be observed which are characteristic of the elements of the sample. Analyzing the spectrum peaks, surface elements to the depth of 10-15 nm can be identified by matching the unique binding that each element has to a known element catalogue. The peak area can be used to determine the relative concentration of those elements. The shape and the position of the peaks can be slightly altered by the chemical and oxidation state of the emitting atom. Hence XPS can provide chemical bonding information.

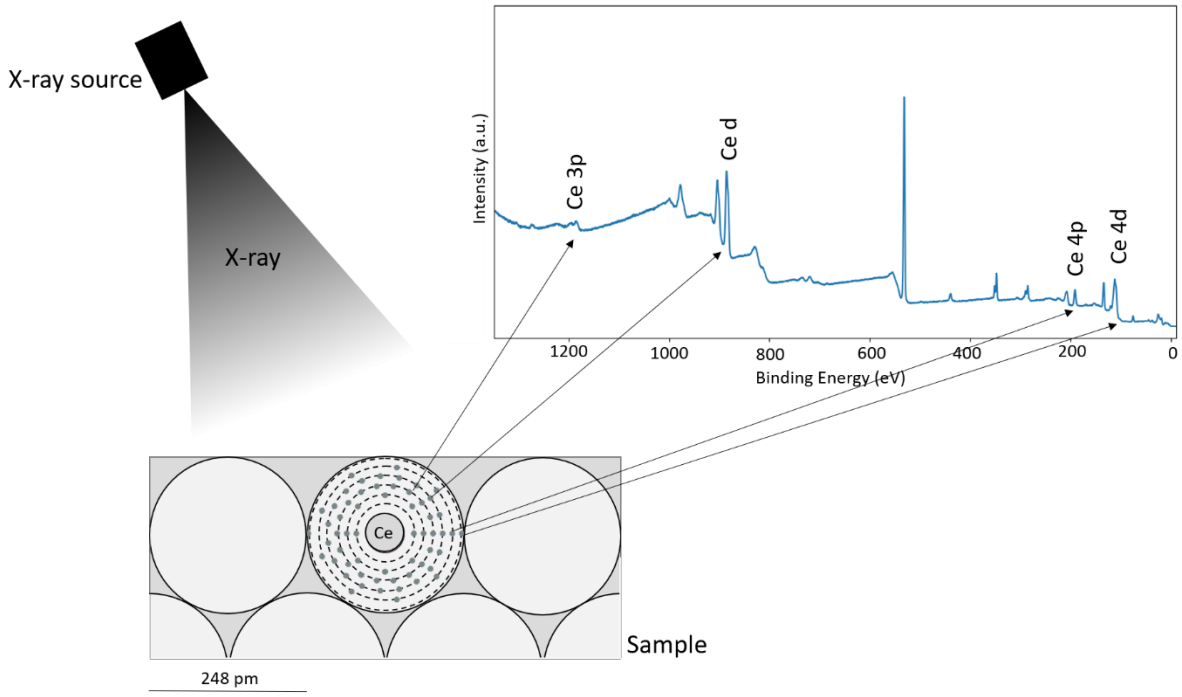


Figure 32. Schematic of XPS where an X-ray is shone on a sample leading to ejection of electrons. Kinetic energy of the ejected electron is measured and used to determine sample atom binding energy (author's figure).

Cerium XPS data was analysed as follows. Cerium has an atomic number of 58 and its electron configuration can be written as $1s^2\ 2s^2\ 2p^6\ 3s^2\ 3p^6\ 3d^{10}\ 4s^2\ 4p^6\ 4d^{10}\ 4f^1\ 5s^2\ 5p^6\ 5d^1\ 6s^2$ ([Xe] $4f^1\ 5d^1\ 6s^2$). It can also be written in sub-levels and orbitals as shown in Figure 33. n is the main energy level (1, 2, 3, 4, 5 ,6). s, p, d and f are sub-levels (l). They are also known as numbers where s=0, p=1, d=2 and f=3. Squares in Figure 33 are orbitals. s sub-level has 1 orbital, p has 3, d has 5 and f has 7. In each orbital, only a maximum of two electrons can be contained. Therefore, s sub-level can contain 2 electrons, p can contain 6, d can contain 10 and f can contain 14 electrons. The electron in each orbital can either spin up or down which are represented as ½ and -½. The sub-levels present in the simplified schematic, Figure 34, are split into sub-orbitals (j). Sub-orbitals only occur in the p, d and f sub-levels and the

name of the sub-orbitals are defined as l + 1/2 and l – 1/2. Therefore, p sub-level contains 1/2 and 3/2 sub-orbitals, d sub-level contains 3/2 and 5/2 sub-orbitals, f sub-level contains 5/2 and 7/2 sub-orbitals. Figure 35 is a schematic of electrons that emerge from different sub-orbitals leading to doublet peaks. The number of elections of each sub-orbital is in ratios and is summarized in Table 7. Therefore, the areas of the doublet peaks are also in the same ratios as electron ratios.

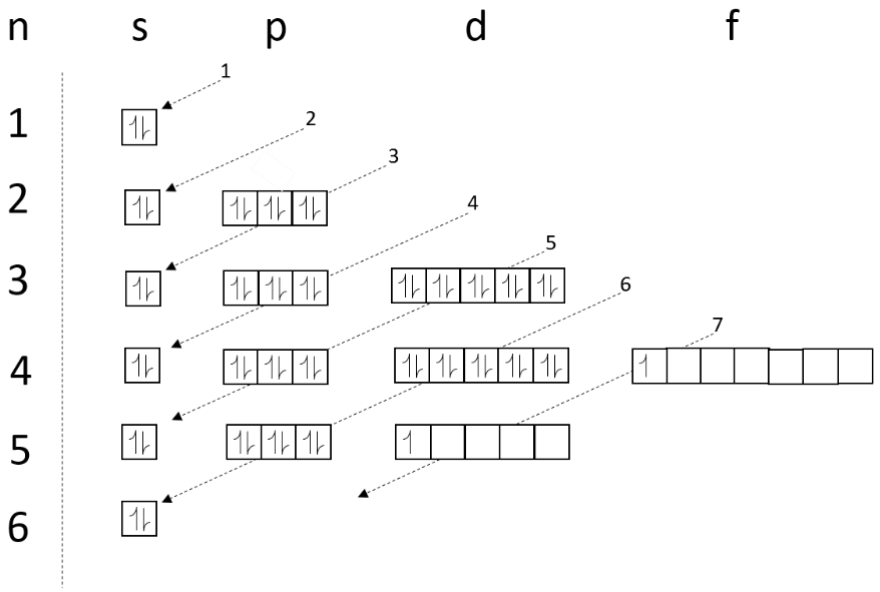


Figure 33. Schematic image of cerium electrons arrangement in atom orbitals. n is level number. s, p, d, and f are sub-levels. Squares are orbitals. ↑ is electron spin up (1/2) and ↓ is electron spin down (-1/2). The electron arrangement follows the numbered dashed line (author's figure).

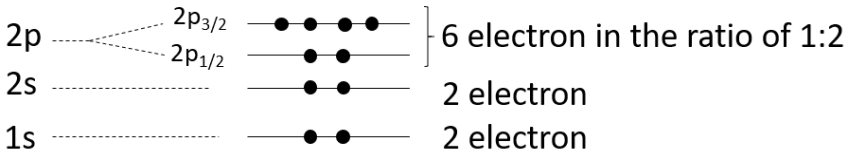


Figure 34. Schematic image of sub-orbitals of $2p_{1/2}$ and $2p_{3/2}$ and the number of electrons arranged in them (author's figure).

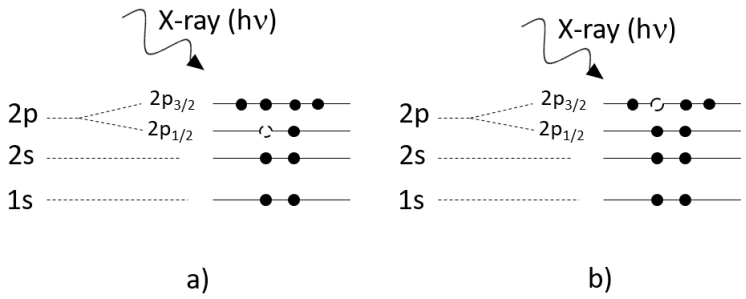


Figure 35. Schematic image of sub-orbitals being hit by X-ray beam. a) An electron from $2p_{1/2}$ suborbital is ejected which creates $2p_{1/2}$ peaks. b) An electron from $2p_{3/2}$ sub-orbitals are ejected which creates $2p_{3/2}$ peak. $2p_{1/2}$ and $2p_{3/2}$ appear close together and are called the doublet peak (author's figure).

Table 7. Ratios between the number of electrons in each sub-orbital

| Sub-shell | j values | Ratio |
|---|---|---|
| S | 1/2 | N/A |
| P | 1/2, 3/2 | 1:2 |
| D | 3/2, 5/2 | 2:3 |
| f | 5/2, 7/2 | 3:4 |

In this thesis, sinter CS 1-5 (SCS 1-5) was used for XPS observation. The CS 1-5 sample were prepared as described in section 3.2.1 (magnetically stirred in a beaker for 2 h). The coating slurries were cast on an alumina block as shown in Figure 36. The coatings were then heat treated at 1550°C for 3 h. The samples were removed from the alumina block carefully, ensuring only the coating was taken without any alumina block contamination. The removed coatings were ground and used for X-ray photoelectron spectroscopy (XPS) and true density measurement. The XPS spectra were recorded on a K-Alpha$^{+}$ X-ray photoelectron spectrometer (UK Thermo Fisher Scientific, East Grinstead, UK) operating at $2\times10^{-9}$ mbar base pressure. This system incorporates a monochromated, microfocused Al *Kα* X-ray source (*hv* = 1486.6 eV) and a 180° double focusing hemispherical analyser with a 2D detector. The X-ray source was operated at 6 mA emission current and 12 kV anode bias providing an X-ray spot size of 400 µm$^2$. Survey spectra were recorded at 200 eV pass energy and 20 eV pass energy

for core level. A flood gun was used to minimize the sample charging that occurs when exposing an insulated sample to an X-ray beam. XPS analyses the sample surface over an area of 400 × 400 μm, 10-15 nm deep. XPS spectra were recorded and analysed using the Advantage Data System software (UK Thermo Fisher Scientific, East Grinstead, UK) which generates the binding energy (eV, x-axis) versus intensity (a.u., y-axis) graph showing peaks positions and graph fitting for peak areas to determined element concentrations.

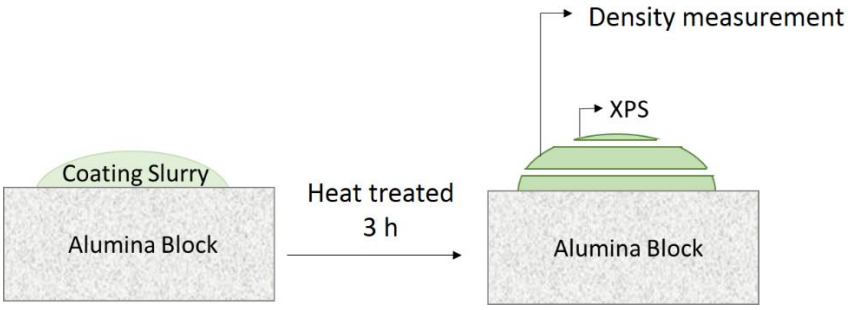


Figure 36. Schematic image of how XPS and true density samples were prepared. The coating slurries were cast on an alumina block, then the casted alumina block was heated at 1550°C for 3 h. Sintered coatings were removed from the alumina block for XPS and density measurements (author's figure).

3.2.3.4 Scanning electron microscopy (SEM)

In this thesis scanning electron microscopy (SEM, Zeiss Leo Gemini 1525, Oberkochen, Germany) was used to study the microstructure and measure the thickness of the coating on the substrate. CBR 1-5 was chosen as a representative composition for this study. SEM and EDX set up are the same described in section 3.1.

3.2.3.5 Transmission electron microscopy (TEM)

Transmission electron microscopy (TEM) was chosen to study the melted morphology phases (matrix) structure and composition which was identified from the SEM. The sample chosen for this experiment was a cross-section of the CRB 1-5 heat treated at 1300°C, 3 h. Electron transparent samples were prepared following a standard FIB (Focussed Ion Beam) lift-out technique with a DualBeam Helios NanoLab SEM (FEI, Field Electron and Ion Company, Hillsboro, Oregon, USA). Figure 37 shows the sample area selected for the experiment containing particles and the matrix area.

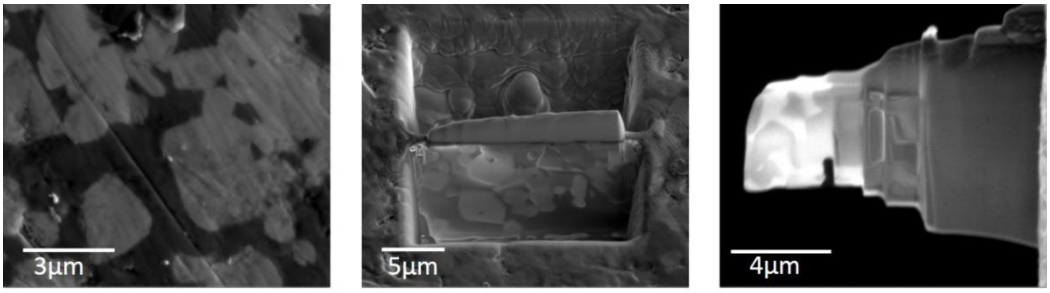


Figure 37. Sample area chosen for FIB a) SEM image (Secondary Electron imaging mode, SEI)) of area containing matrix and particles. b) SEM image (SEI) showing platinum covering part of sample surface for protection when ion beam was used to carve out sides. c) Sample was cut then attached to TEM sample holder and thinned to electron transparency (author's figures).

The electron transparent sample was placed in the TEM/STEM JEM-2100F (JEOL, Japanese Electron Optics Limited, Tokyo, Japan) equipped with an EDX X-Max detector (Oxford Instruments, Abingdon, UK). A simple overview of a TEM is presented in Figure 38. The electron gun generates electrons that travel through an electro-magnetic lens that act as an anode to accelerate the electrons through an ultra-high vacuum chamber (~$10^{-11}$ Torr) and pass through the ultra-thin sample. In this case, the sample was imaged at an accelerating voltage of 200 kV. The condenser lens helps to converge and focus the electron beam onto the sample. The aperture controls the size and intensity of the beam onto the sample. Electrons transmitted through the sample, then go through the objective lens which magnifies and controls the focus of the image. After, they go through an objective aperture, which permits specific diffracted rays to be projected, controlling the image contrast. Last, the diffracted electron rays go through the projector lens. The projector lens magnifies the image and focuses the rays into an image on the detector screen. TEM diffraction patterns can be obtained in a similar way as imaging, but, instead of using an objective aperture, a selected area diffraction (SAD) aperture was used, and information in the back focal plane of the objective lens acquired [154].

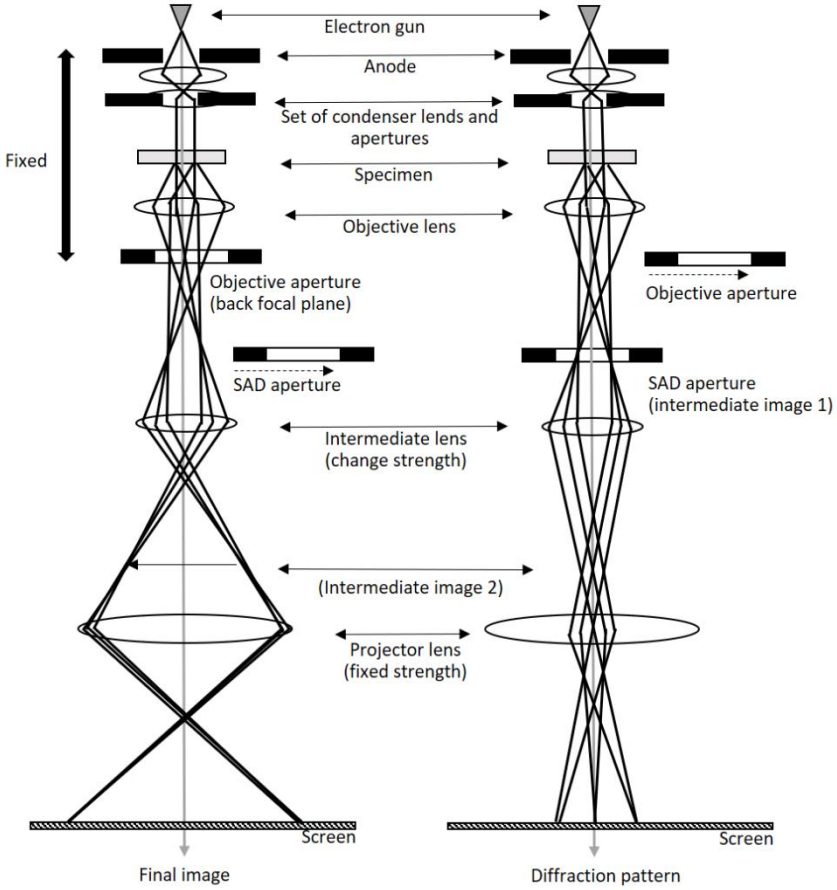


Figure 38. Schematic of electron beam path for imaging and diffraction mode in TEM (modify from [155]).

### 3.2.4 Coating density

Two experiments were conducted for density measurement. The first investigated temperature effects on coating density and the second composition effects on coating density. Temperature effects on density were determine by bulk density and apparent porosity using the ASTM C20 [156]. Measuring bulk density via this method simultaneously gives apparent porosity data as well. Bulk density samples; CS 1-5, prepared as described previously in section 3.2.1., were heated at 300°C for 30 min to remove excessive liquid phases leaving flakes behind as shown in Figure 39. After drying, the flakes were ground then pressed into pellets. The pellet's average size was measured with callipers, 3 times for each side for average values and standard deviation. The size is 13.50 ±0.04 mm diameter and 3.25 ±0.03 mm thick. The pellets were heat treated at 800, 1000, 1200 and 1500°C for 3 h.

The impact of composition on coating density was determined for bulk density apparent porosity and true density. Samples used in the experiment were CS 1-3, 1-5 and 1-12. For bulk density and apparent porosity measurements pellets were prepared in the same fashion as for the temperature effect. The pellets were heat treated at 1300°C, 3 h. As for true density, the measurement was done using a pycnometer (Ultrapycnometer-1000, Quantachrome Ltd, Florida, USA). 20 measurements were done for each sample. CS 1-3, 1-5 and 1-12 were mixed as explained in section 3.2.1 and cast as described in section 3.2.3.3. The samples were sintered at 1300°C, 3h. Henceforth, the sintered coating slurry pellet of CS 1-3, 1-5 and 1-12 will be referred to SCS 1-3, 1-5 and 1-12 respectively.

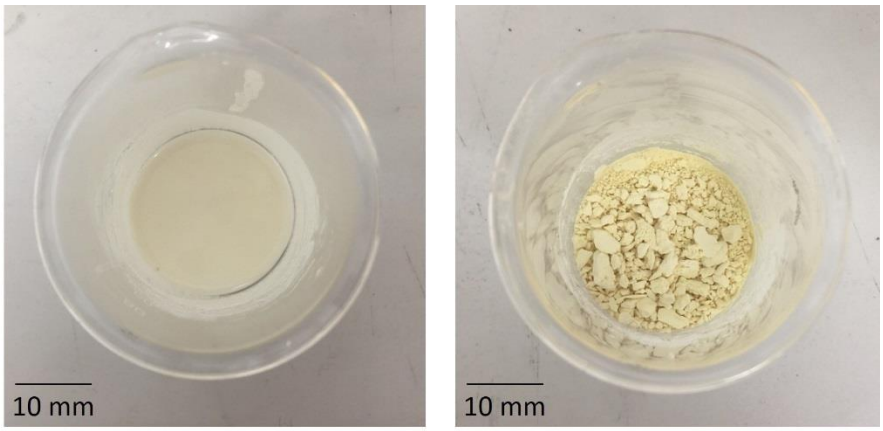


Figure 39. Top view of a coating in a beaker a) coating slurry after stirring, b) coating flakes after heating at 300°C (author's figures).

Bulk density and apparent porosity were measured using ASTM C20 (standard test methods for apparent porosity, water absorption, apparent specific gravity, and bulk density of burned refractory brick and shapes by boiling water method) [18, 156, 157]. ASTM C20 bulk density and apparent porosity are calculated based on Equation 37 and Equation 38. $W_{Dry}$ (g) is the dry weight of the sample in air. $W_{Sat}$ is the weight of the sample when its open pores are filled with a media (in this case water was used as a media). $W_{Sat}$ can be achieved by saturating the samples in boiling water for at least 2 hours to ensure the open pores are filled with water then removing excess water by dabbing the samples gently on a moistened cloth before weighing on a balance in the air. $W_{sus}$ is the weight of the sample suspended in the media (water). $\rho_m$ is the media density which is 0.9982 g/cm$^3$ for water. The ASTM C20 mentions standard deviation values which are determined by sending samples to be measured at different laboratories by different operators. They have reported the standard deviation values to be 0.14 g/cm$^3$ and 1.15 % for the bulk density and apparent porosity respectively. It should

be mentioned that the refractory brick used in this thesis is a heterogeneous brick, therefore, results values within each brick will vary. Considering these errors, three samples of refractory brick were measured and an average and a single standard deviation among them was reported.

Equation 37. $$Bulk\ Density = \left(\frac{W_{Dry}}{W_{Sat}-W_{Sus}}\right) \cdot \rho_m$$

Equation 38. $$Apparent\ porosity = \left(\frac{W_{Sat}-W_{Dry}}{W_{Sat}-W_{sus}}\right) \cdot 100$$

## 3.3 Emissivity measurement

There is no international standard for conducting emissivity measurements. In this research, two methods were chosen: a radiometer emissivity measurement method (REM) and an infrared emissivity measurement method (IREM). Both methods have their advantages and disadvantages. REM's advantage is in allowing the sample to heat in a general electric furnace in air, similar to the real application. However, the wavelength chosen for this method must be chosen carefully. The wavelength must be in the range that does not interfere with air in the environment and would not penetrate through the furnace and equipment. According to a known transmission window in the air with low humidity at approximately 2.07-2.31 mm, therefore, 2.19 mm (137GHz) was chosen as the wavelength measured from the REM. This is a disadvantage because 2.19 mm is in the radio wave range and not infrared which is considered "a heatwave". One the other hand, IREM allowed the sample to be measured in the infrared range, but because infrared can penetrate through the furnaces and the equipment, therefore the sample must be heated in a vacuum with a $CO_2$ laser instead of a normal furnace. The sample heating is different from how the coating is used in the real application, but emissivity can be measured in an infrared range.

### 3.3.1 Radiometer emissivity measurement method (REM)

The REM was measured by a thermal return reflection (TRR) technique. The experiment was conducted with help and guidance from Professor S. K. Sundaram, Dr Paul P Woskov and Mr. David Dobesh at Alfred University, NY, USA. The REM device was designed and built in-house by Professor S. K. Sundaram and Dr Paul P Woskov at Alfred University, NY, USA. The layout of the REM device is shown in Figure 40 and for better understanding a schematic of the instrument is shown in Figure 41. The sample is placed in an insulating firebrick crucible, which is then placed in a bottom-loaded

furnace and the furnace is closed. The crucible must be aligned with the mullite waveguide, which is inserted at the top of the furnace. Insulating firebrick is chosen as a material for the crucible and waveguide because it has recorded low thermal loss in previous studies [158, 159]. Once the furnace is heated; the sample emits electromagnetic waves at all wavelengths of different intensities. Those with short wavelengths penetrate through the waveguide and furnace walls and those with longer wavelengths, specifically of 137 GHz frequency, travel along the waveguide path. The long-wavelength waves travel through the mullite waveguide hitting a mitre mirror which reflects them, so they change from a vertical to horizontal direction. The waves then pass through a Teflon plate which acts as a barrier window preventing heat from the furnace damaging the rest of the instrument. After the waves have passed through the Teflon plate, they continue to travel along in a circular corrugated aluminum waveguide. The waves are then split with a chopper and/or beam splitter into receiver 1 or 2. According to emissivity measurement, four different wave paths are produced. The first path is a voltage signal of a blackbody at room temperature ($V_r$) used in the calculations. The second path is a voltage signal of the blackbody at liquid nitrogen temperature ($V_C$) used as calibration signal. The third path is a voltage signal of the sample ($V_s$). The fourth path is voltage signal from the sample combined with its series of reflections ($V_s'$).

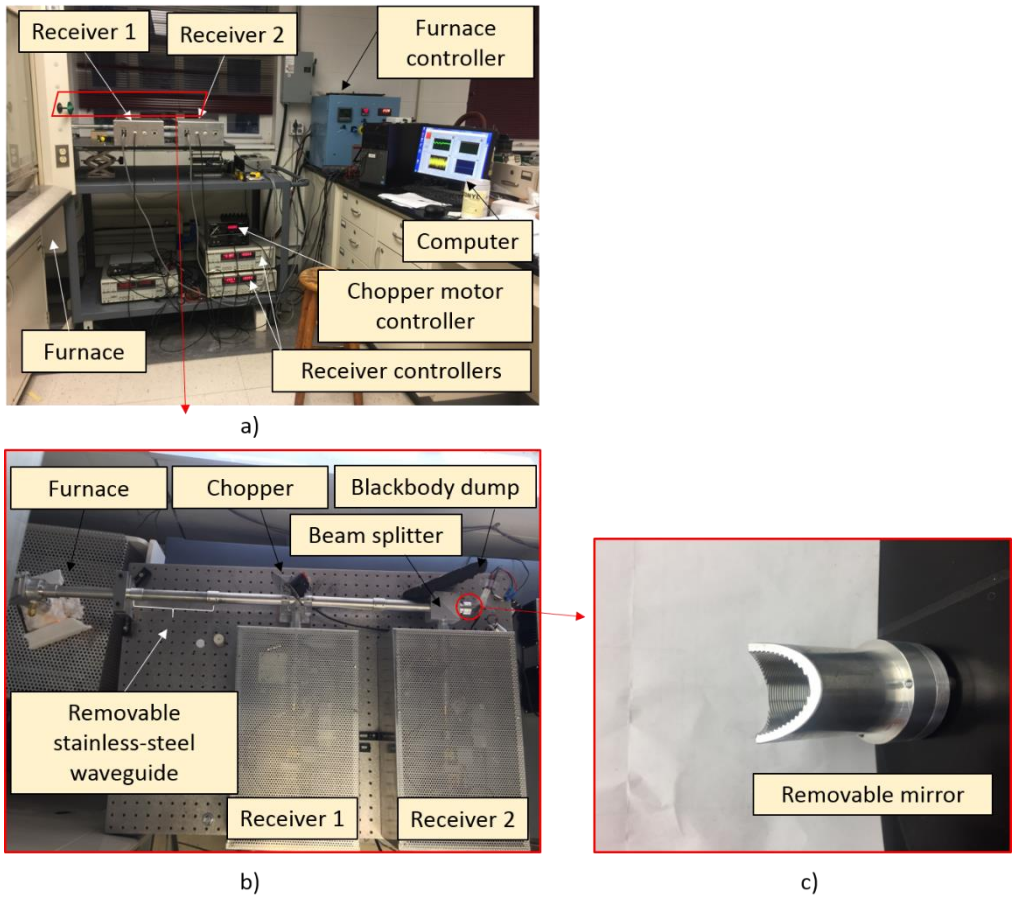


Figure 40. Layout of REM device. a) Front view of instrument showing position of furnace, receivers, furnace controller, computer, chopper motor controller and receiver controllers. b) Top view of instrument showing position of receivers, removable aluminium waveguide, furnace, chopper, beam splitter and blackbody dump. c) Image of removable mirror, which terminates this short guide (author's figure).

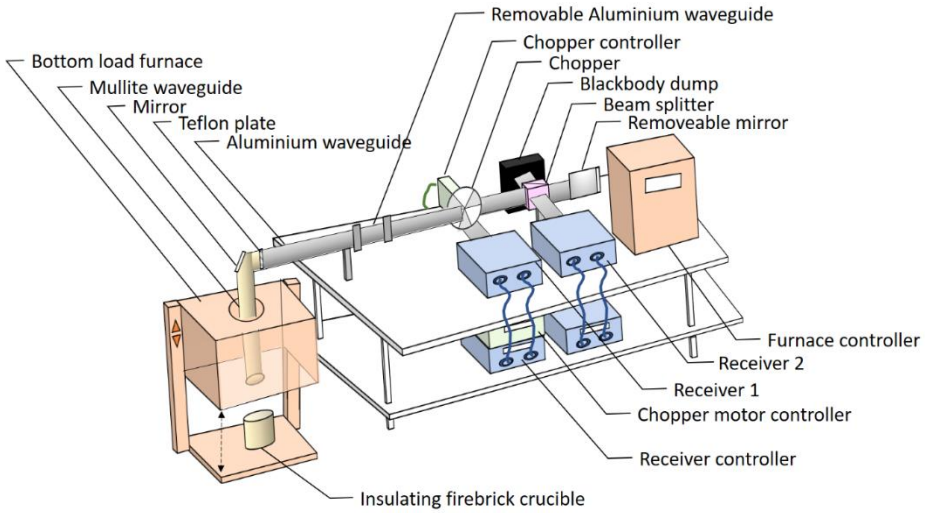


Figure 41. Schematic of thermal return refection (TRR) equipment (author's figure).

The 4 different paths depend on 1) the source of the signal (blackbody or sample), 2) chopper position, which is a micro-polished flat stainless steel two blade disk rotating continuously blocking or unblocking the waveguide at 100 Hz, and 3) removable mirror position (without a mirror, with a mirror). Path 1, a blackbody is used as a signal source at the removable waveguide section. The chopper alternately blocks and passes the blackbody emission signal to receivers 1 and 2, respectively. There is no difference whether the removable mirror is present or not because the blackbody has no reflectivity. When the blackbody is at room temperature the detected signal establishes the room temperature instrumentation offset. When the blackbody is cooled to liquid nitrogen temperature it establishes the receivers signal for a temperature difference between room temperature and liquid nitrogen. The receivers measure temperature relative to room temperature irrespective of being hotter or colder. The temperature difference ($\Delta$T) is the actual variable measured and tracked through the experiment.

The blackbody used in this experiment is carbon impregnated foam plastic (Eccosorb™) (Figure 42). The blackbody is designed to have a pyramid-like pattern to help in creating a continued reflection path deeper towards the pyramid base and helps to avoid reflection back to the system (Figure 43). For this path, the signal from the blackbody reflects on the chopper into receiver 1 or passes to receiver 2 when the chopper blade rotates out of the view (Figure 44). The signal voltage from path 1 ($V_r$) can be expressed as Equation 39. Further in the experiment, C refers to $\mathrm{KG}k_B dv(1+\alpha\mathrm{V})^{-1}$, therefore, Equation 39 can be simplified to Equation 40.

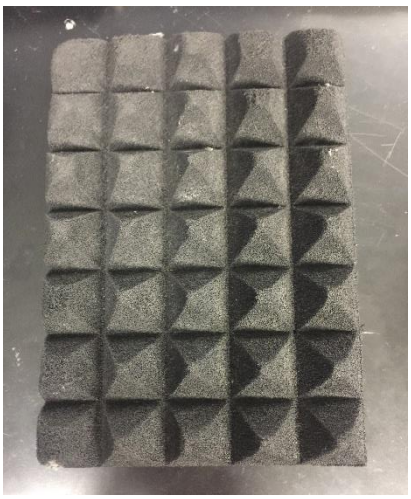

Figure 42. Carbon impregnated foam plastic (Eccosorb™), used as blackbody (author's figure).

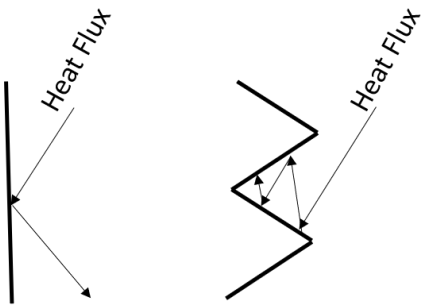


Figure 43. Heat flux reflection path on a) flat and b) pyramid-like surfaces. The heat flux reflected from a flat surface returns into the system whereas heat flux reflected from a pyramid-like surface continues to travel deeper towards the pyramid base so reducing reflection back into the system making the object behave like a blackbody (author's figures).

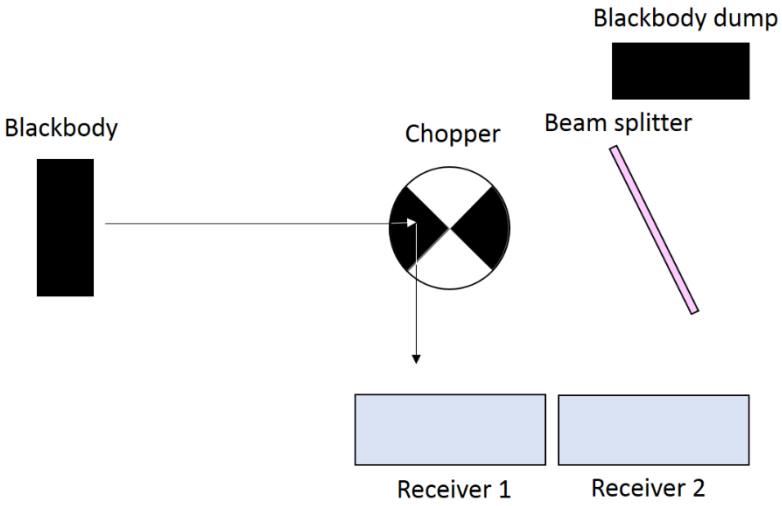


Figure 44. Schematic of path1; signal from the room temperature blackbody to chopper to receiver 1 (author's figure).

Equation 39. $$V_r = \mathrm{KG}k_B dv(1+\alpha\mathrm{V})^{-1}(T_i + T_r)$$

where $V_r$ is signal at room temperature (Volts), K is the diode response (Volts), G is all the signal gain[5] of the receiver circuit , $k_B$ is Boltzmann's constant ($1.38065 \times 10^{-23}$ J·K$^{-1}$), $dv$ is the frequency

[5] Gain is a factor that an amplifier in a receiver uses to increase the input signal. For example, if the input signal is 1 volt and the amplifier increase this signal making the output signal to be 60 volts. Then the signal gain is 60. In other words, gain of an amplifier is output signal divided by input signal.

interval of observation, $\alpha$ is the detector nonlinearity, V is radiometer signal (Volts), $T_i$ is receiver noise temperature (Kelvin) and $T_r$ is room temperature of chopper (Kelvin).

Equation 40. $$V_r = C(T_i + T_r)$$

In path 2, a liquid nitrogen calibration blackbody is used as a signal source placed inside the furnace when it is at room temperature at the end of the mullite waveguide where the sample is to be located. With chopper unblocked, the signal from the blackbody passes through the mullite waveguide, aluminium waveguide and the chopper before hitting the beam splitter for receiver 2. The signal is split into 2 beams; one goes through the beam splitter and the other is reflected into receiver 2 (Figure 45). The signal from the blackbody passing through the waveguide is $\tau_{wg}T_{LN}$. The mullite waveguide also emits a signal which is $\varepsilon_{wg}T_{wg}$. The corrugated aluminium waveguide has not been taken into consideration like the mullite waveguide because it has no detectable losses in the dimensions used here for the fundamental $HE_{11}$ propagation mode of the receivers' field of view. These $\tau_{wg}T_{LN}$ and $\varepsilon_{wg}T_{wg}$ signals can be written together as $T_c$, which is the temperature of liquid nitrogen, $LN_2$ (-196°C, 77K) in this experiment. As these two signals reflect on the beam splitter into receiver 2, a beam splitter reflectiveness ($r_{bs}$) term is added. Furthermore, another signal from the blackbody dump also transmits through the beam splitter into receiver 2 and is expressed as $\tau_{bs}T_r$. The signals of path 2 ($V_C$) are shown in Equation 41 and with a simplified version in Equation 42.

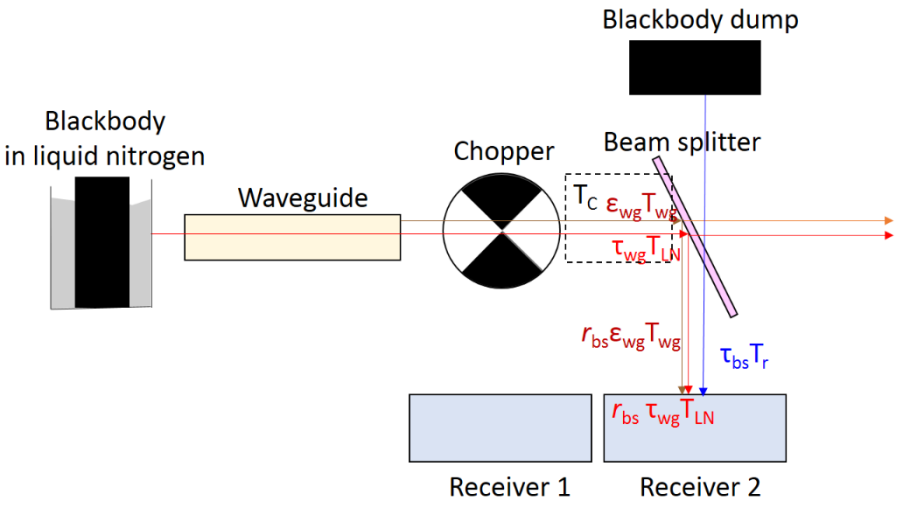


Figure 45. Schematic of path2; the red signal is from a liquid $N_2$ cooled blackbody through the waveguide to chopper to beamsplitter to receiver 2, brown signal is from the waveguide to chopper to beamsplitter and blue signal is from a blackbody dump through the beamsplitter (author's figure).

Equation 41. $$V_C = C(T_i + \tau_{bs}T_r + r_{bs}\varepsilon_{wg}T_{wg} + r_{bs}\tau_{wg}T_{LN})$$

Equation 42. $$V_C = C(T_i + \tau_{bs}T_r + r_{bs}T_C)$$

where $V_C$ is voltage signal of the blackbody at $LN_2$ temperature; -196°C or 77K (Volt), $\tau_{bs}$ is transmission factor of beam splitter, $T_r$ is room temperature (Kelvin), $r_{bs}$ is beam splitter reflectiveness, $\varepsilon_{wg}$ is emissivity of the waveguide, $T_{wg}$ is temperature of the waveguide (Kelvin), $\tau_{wg}$ is transmission through waveguide and $T_{LN}$ is temperature of the liquid nitrogen (Kelvin).

To achieve accurate $V_C$ value, it is necessary to correct for high temperature operation when the mullite waveguide acts as both a source and loss of thermal signal. It is not possible to put a calibration blackbody inside the furnace when it is hot. Therefore, $V_C$ is determined by a calculation shown in Equation 43 in this experiment. The calibration at the removable aluminium waveguide section ($V_C'$), which can be made the furnace is hot, is corrected for the reduced sample signal losses at high temperature. In this experiment, the mullite waveguide transmission efficiency at room temperature was found to be 0.75, in other words, there is a 0.25 lost through the waveguide. Considering that approximately half the mullite waveguide is heated to the furnace temperature, the hot waveguide thermal emission makes up the half the sample transmission signal transmission losses measured at room temperature. The emission loss at high temperatures is 0.125 (0.25 multiplied with 0.5). Consequently, the mullite waveguide efficiency at high temperatures is 0.875 (1 minus 0.125). Therefore $V_C$ can be calculated by using the signal from the blackbody cooled to $LN_2$ temperature placed in front of the waveguide (outside the furnace at room temperature, $V_C'$) multiplied by 0.875. $V_C'$ signal path is shown in Figure 46 and can be calculated with Equation 44.

Equation 43. $$V_C = V_C' * Wg_{eff}$$

where $V_C'$ is voltage signal of the blackbody at $LN_2$ temperature with no waveguide, and $Wg_{eff}$ is mullite waveguide efficiency.

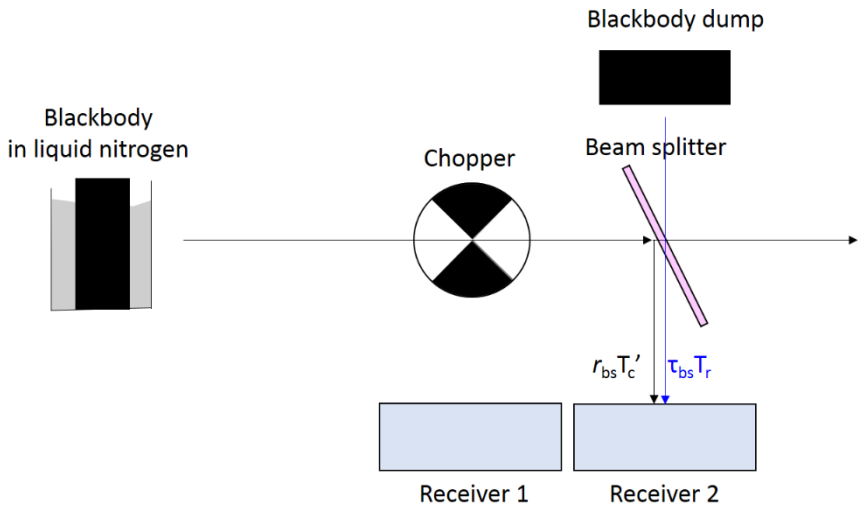


Figure 46. Schematic of path 2; the black signal is from blackbody to chopper to beamsplitter to receiver 2 and blue signal is from a blackbody dump through the beamsplitter (author's figure).

Equation 44. $$V_C' = C(T_i + \tau_{bs}T_r + r_{bs}T_C')$$

where $T_C'$ is calibrated temperature, which is the temperature of $LN_2$ (77 Kelvin) in this experiment.

In path 3, the sample is used as a signal source (the blackbody is removed, and the removable aluminium waveguide put in place), the chopper is unblocked, without a mirror (the removable mirror is removed from the instrument). Three signals are generated shown in Figure 47. First signal is from the sample ($\tau_{wg}\varepsilon_s T_s$ , a red path). Second signal is from the mullite waveguide ($\varepsilon_{wg}T_{wg}$, a brown path). Third signal is waveguide thermal signal from the reflection of the view sample ($r_s\tau_K\varepsilon_{wg}T_{wg}$, green path) as sample is now the signal source not the blackbody in this path.

In path 3, the signal from the sample passes through the mullite waveguide and then through the chopper before hitting the beam splitter behind. The signal is then again split into 2 beams; one passes through the beam splitter and the other is reflected into receiver 2 similar to path 2. Therefore, the signal from path 3 entering receiver 2 is the three signals multiply with $r_{bs}$ and can be expressed as Equation 45. The first three terms are the same as in path 2 and the last two term as mentioned above. Equation 45 can be simplified to Equation 46, where $T_{eff}$ is $\varepsilon_{wg}T_{wg} + \tau_{wg}\varepsilon_s T_s + \tau_s\tau_K\varepsilon_{wg}T_{wg}$.

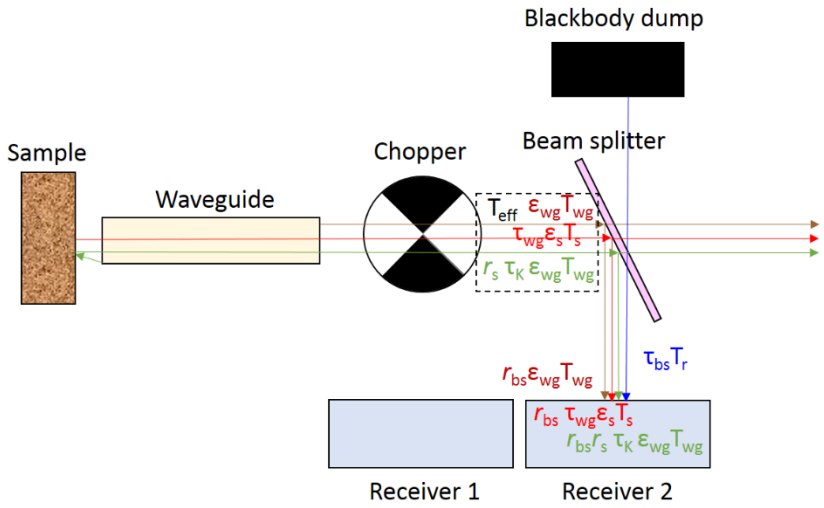


Figure 47. Schematic of path 3; the red signal is from a liquid $N_2$ cooled blackbody through the waveguide to chopper to beamsplitter to receiver 2, brown signal is from the waveguide to chopper to beamsplitter, green signal is from the waveguide and reflection of the view sample to chopper to beamsplitter and blue signal is from a blackbody dump through the beamsplitter (author's figure).

Equation 45. $$V_s = C(T_i + \tau_{bs}T_r + r_{bs}\varepsilon_{wg}T_{wg} + r_{bs}\tau_{wg}\varepsilon_s T_s + r_{bs}\tau_s\tau_K\varepsilon_{wg}T_{wg})$$

where $V_s$ is voltage signal of sample (Volt), $\varepsilon_{wg}$ is emissivity of the waveguide, $T_{wg}$ is temperature of the waveguide (Kelvin), $\tau_{wg}$ is transmission of waveguide, $\varepsilon_s$ is emissivity of the sample, $T_s$ is temperature of the sample (Kelvin), $\tau_s$ is transmission of the sample, and $\tau_K$ is the transmission from return reflection coupling.

Equation 46. $$V_s = C(T_i + \tau_{bs}T_r + r_{bs}T_{eff})$$

In path 4, the sample is used as a signal source, the chopper is unblocked, with mirror (a mirror is put in place behind the beam splitter as shown in Figure 41). The signal paths are similar to path 3 but with additional signals from the mirror reflection as shown in Figure 48. These are: 1) a thermal signal that passes through the beam splitter and reflects from the mirror back to the beam splitter ($\tau_{bs}T_{eff}$). This signal is the starting signal of the additional signals; 2) the signal reflected from the mirror passed through the beam splitter and chopper entering the waveguide ($\tau_{bs}^2T_{eff}$); 3) the signal then passes through the waveguide hitting the sample ($\tau_{wg}\tau_{bs}^2T_{eff}$); and 4) the signal reflects from the sample back through the waveguide ($r_s\tau_K\tau_{wg}^2\tau_{bs}^2T_{eff}$) before hitting the beam splitter and is split into two paths which reflect into receiver 2 ($r_{bs}r_s\tau_K\tau_{wg}^2\tau_{bs}^2T_{eff}$) and transmit through the beam

splitter ($r_s\tau_K\tau_{wg}^2\tau_{bs}^3T_{eff}$) and continues to repeat from 1) again. Therefore, the addition of signals is a continuous series of signals of $T_{eff} + r_s\tau_K\tau_{wg}^2\tau_{bs}^2T_{eff} + (r_s\tau_K\tau_{wg}^2\tau_{bs}^2)^2T_{eff} + (r_s\tau_K\tau_{wg}^2\tau_{bs}^2)^3T_{eff}$ +…+ $(r_s\tau_K\tau_{wg}^2\tau_{bs}^2)^nT_{eff}$, which is simplified to $T'_{eff}$. From a Taylor series expansion (Equation 47), the additional $T'_{eff}$ can be simplified as Equation 48 and the signals for path 4 can then be expressed as Equation 49.

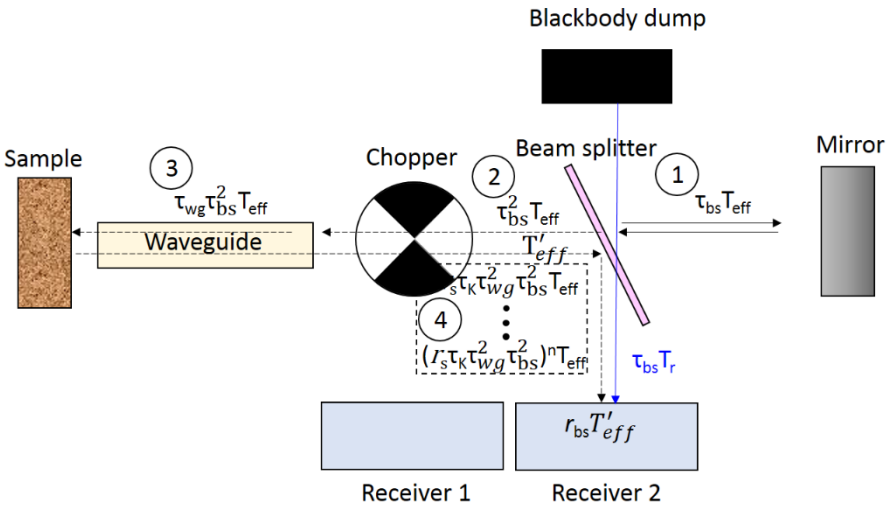


Figure 48. Schematic of path 4; the additional signal from 1) the signal that passes through the beam splitter and is reflected from a mirror. 2) Reflected signal passing through the beam splitter entering the waveguide. 3) Signal coming out of the waveguide hitting sample. 4) Signal reflected from the sample entering back into the waveguide and splitting into two signals with the beam splitter (author's figure).

Equation 47. $$\frac{1}{1-x} = 1 + x + x^2 + x^3 + \cdots + x^n$$

Equation 48. $$T'_{eff} = \frac{T_{eff}}{1-r_s\tau_K\tau_{wg}^2\tau_{bs}^2}$$

Equation 49. $$V'_s = C(T_i + \tau_{bs}T_r + r_{bs}T'_{eff})$$

where $V'_s$ is voltage signal from the sample (Volt) combined with its series of reflection.

The 4 signal paths demonstrated above can be used to calculate temperatures $T_{eff}$ and $T'_{eff}$ and will be demonstrated further. Once $T_{eff}$ and $T'_{eff}$ are known, they can be used to calculate with the $\tau_K$ , $\tau_{wg}$ and $\tau_{bs}$ , which are constant values, for $r_s$ from Equation 48. Knowing $r_s$, the emissivity

of the sample can be calculated from Equation 50. It must be noted that Equation 50 is only accurate when the sample is thick enough and there is no transmission through the sample.

Equation 50. $$\varepsilon_s = (1 - r_s)$$

To achieve $T_{eff}$, two voltage signals must first be calculated which are $V_{cal}$ and $V_{sig}$. $V_{cal}$ is the difference between $V_c$ (from path 2) and $V_r$ (from path 1). $V_{cal}$ can be expressed as Equation 51 and can be simplified to Equation 52. $V_{sig}$ is the difference between $V_s$ (from path 3) and $V_r$ (from path 1). $V_{sig}$ can be expressed as Equation 53 and can be simplified to Equation 54. $T_{eff}$ can be calculated by dividing $V_{cal}$ with $V_{sig}$ as present in Equation 55, and $T_{eff}$ is defined as Equation 56. $T'_{eff}$ can be calculated similarly to $T_{eff}$ by replacing $V_{sig}$ with $V'_{sig}$. $V'_{sig}$ calculated from the difference of $V'_s$ (path4) and $V_r$ (path1) as shown in Equation 57 and can be simplified to Equation 58. $T'_{eff}$ can be calculated by dividing $V_{cal}$ with $V'_{sig}$ as shown in Equation 59 and therefore, $T'_{eff}$ can be defined as Equation 60.

Equation 51. $$V_{cal} = (V_c - V_r)$$

$$V_{cal} = C(T_i + \tau_{bs}T_r + r_{bs}T_c) - C(T_i + T_r)$$

$$V_{cal} = C\tau_{bs}T_r + Cr_{bs}T_c - CT_r$$

$$V_{cal} = Cr_{bs}T_c - Cr_{bs}T_r$$

Equation 52. $$V_{cal} = Cr_{bs}(T_c - T_r)$$

Equation 53. $$V_{sig} = (V_s - V_r)$$

$$V_{sig} = C(T_i + \tau_{bs}T_r + r_{bs}T_{eff}) - C(T_i + T_r)$$

$$V_{sig} = C\tau_{bs}T_r + Cr_{bs}T_{eff} - CT_r$$

$$V_{sig} = Cr_{bs}T_{eff} - Cr_{bs}T_r$$

Equation 54. $$V_{sig} = Cr_{bs}(T_{eff} - T_r)$$

Equation 55. $$\frac{V_{cal}}{V_{sig}} = \frac{Cr_{bs}(T_c - T_r)}{Cr_{bs}(T_{eff} - T_r)}$$

Equation 56. $$T_{eff} = \frac{V_{sig}}{V_{cal}}(T_c - T_r) + T_r$$

Equation 57. $$V'_{sig} = (V'_s - V_r)$$

$$V'_{sig} = C(T_i + \tau_{bs}T_r + r_{bs}T'_{eff}) - C(T_i + T_r)$$

$$V'_{sig} = C\tau_{bs}T_r + Cr_{bs}T'_{eff} - CT_r$$

$$V'_{sig} = Cr_{bs}T'_{eff} - Cr_{bs}T_r$$

Equation 58. $$V'_{sig} = Cr_{bs}(T'_{eff} - T_r)$$

Equation 59. $$\frac{V_{cal}}{V'_{sig}} = \frac{Cr_{bs}(T_c - T_r)}{Cr_{bs}(T'_{eff} - T_r)}$$

Equation 60. $$T'_{eff} = \frac{V'_{sig}}{V_{cal}}(T_c - T_r) + T_r$$

Rearranging Equation 48 to Equation 61 , $r_s$, can be calculated. In this experiment $T_r$ is the blackbody dump temperature measured with an infrared thermometer, $\tau_K$ and $\tau_{wg}$ are determined from the furnace and calibration measurement here as 0.67 and 0.75 respectively, and $\tau_{bs}$ is measured separately by Dr. Paul P. Wokov at MIT as 0.62. In conclusion, the steps for calculating for emissivity with the thermal return reflection (TRR) method are shown in Figure 49. For accuracy it must be kept in mind that $V'_C * Wg_{eff}$ is used to calculate $V_c$ (Equation 43).

Equation 61. $$r_s = \frac{1}{\tau_K \tau_{wg}^2 \tau_{bs}^2}\left(1 - \frac{T_{eff}}{T'_{eff}}\right)$$

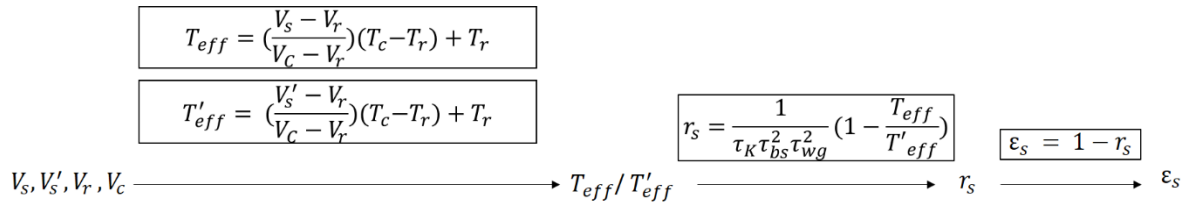


Figure 49. Emissivity calculation steps via TRR method. The $V_s$, $V_s'$, $V_r$, $V_C$ are collected. These values are used to calculate for $T_{eff}$ and $T'_{eff}$. The $T_{eff}$ and $T'_{eff}$ are used to calculate for $r_s$ which is used to calculate for emissivity.

Three sample conditions; CBR 1-3, 1-5 and 1-12, prepared as mentioned in section 3.2.1. are heat treated at 1300°C, 3 h. Three temperatures were chosen for REM; 1000, 1300 and 1500°C. Two measurement were made for each sample condition. The sample sizes were 20 × 20 × 3 mm. The furnace heating profiles are shown in Figure 50. The bottom load furnace was heated from room temperature at a rate of 10°C/min to 1000°C. The temperature was held at temperature for 1 h for TRR measurements. The TRR measurements were done by removing the reflective mirror and placing it back at least 5 times. Calibration was done by measuring $V_c$ after measuring the TRR. After, the furnace continued to heat up to 1300°C with the same rate and held at temperature for the same amount of time. The same heating profile was repeated in the same condition to 1500°C. The furnace cooled naturally and was held at 1300°C and 1000°C for 1 h for the cooling measurements.

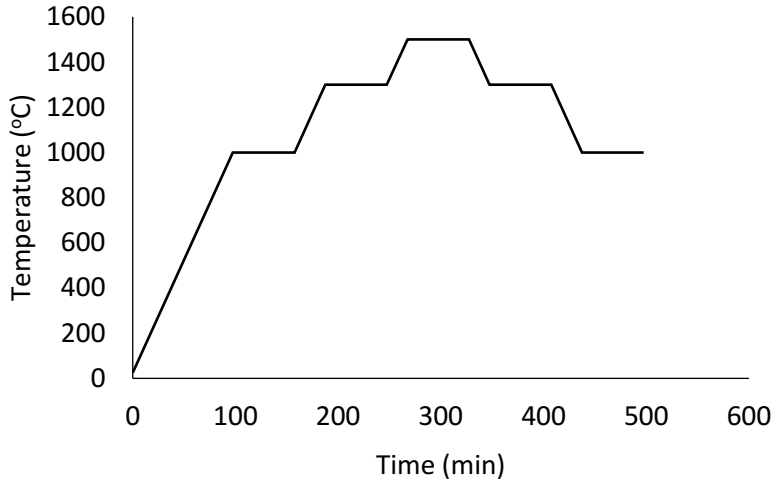


Figure 50. Heating and cooling profile of the REM. The furnace was heated from room temperature at a rate of 10°C/min to 1000°C, 1300°C and 1500°C. The temperature was held at each temperature for 1 h for TRR measurement. The furnace cooled naturally and was held at 1300°C and 1000°C for 1 h for the cooling measurements (author's figure).

The measurement procedure is summarized below.

1. **Turning on:** Turn on the instrument starting from the power supply, the chopper, then receivers. Once everything was turned on, the receivers start to collect the voltage information continuously.
2. **Calibration:** Room temperature and $LN_2$-cooled blackbodies were placed at the removable aluminium waveguide section. The room temperature offset voltage signals ($V_r$) and the $LN_2$ calibration signals ($V_c$) were recorded for both receivers.
3. **Sample loading:** The sample was placed in an insulating fireclay crucible. The crucible was placed directly under the mullite waveguide in the bottom load furnace. The bottom load furnace was then closed.
4. **Heating:** The furnace was turned on and was heated from room temperature to 1000°C with a rate of 10°C/min. Once the temperature reached the set values, it was held for 1 h.
5. **Measurement:** During the 1 h that the temperature was held, the removable mirror was removed for about 15-20 s and was placed back in place for another 15-20 s. The removable mirror was removed and put back into place for at least 5 times generating $V_s$ and $V_s'$ respectively from receiver 2 to get a good signal averaging.
6. **High temperature calibration:** After the five measurements, calibration was repeated (step 2) to determine thermal drift of the calibration during the course of the sample measurement campaign. The room and $LN_2$ temperature blackbodies were placed at the removable waveguide section for 15-20 s, generating $V_c'$. Room temperature ($T_r$) was also collected at this stage with an infrared thermometer on the blackbody dump, the furnace continues to heat up to 1300°C and 1500°C repeating from step 4.

### 3.3.2 Infrared emissivity measurement method (IREM)

IREM was carried out at CNRS, CEMHTI UPR3079, Univ. Orléans, F-45071, Orléans, France using the emissivity apparatus internal designed and built by Dr. Domingos De Sousa Meneses at CEMHTI UPR3079, Univ. Orléans, F-45071, Orléans, France [79]. Support and training for the experiment were also provided by Dr. Domingos De Sousa Meneses. The emissivity apparatus consisted of two Bruker spectrometers; Vertex 80V and Vertex 70 (Germany). Vertex 80V was used

for measuring emissivity in the 700-4000 $cm^{-1}$ range (mid-IR) with a DLaTGS[6]/KBr detector. Vertex 70 was used to measure two ranges; 4000-9000 $cm^{-1}$ (near-IR) with InGaAs detector and 9000-12000 $cm^{-1}$ (near-IR) with a Si-diode detector. After measuring the emissivity for the three wavenumber ranges, data were merged creating emissivity data ranging from 700-12000 $cm^{-1}$ (mid-IR to near-IR). For each measurement over each wavenumber range, three sub-measurements were carried out; flux measurement of the blackbody furnace (PYROX PY8), sample and ambient contribution. Flux of the blackbody furnace and sample were needed to calculate the emissivity referring to the definition which is flux emitted from the sample surface over flux emitted by a blackbody at the same temperature. Ambient (background) contribution was determined so the effect of the instrument surroundings could be removed giving greater accuracy. Measuring three sub-measurements (blackbody, sample and ambient) for three different wavenumber ranges (700-4000 $cm^{-1}$, 4000-9000 $cm^{-1}$ and 9000-12000 $cm^{-1}$) can be time consuming if the setup is not well designed. To maximise the time efficiency, the blackbody and the sample are placed in a focus point when the optical system is collecting the fluxes on a rotatable stage. Therefore, when the emittance of the blackbody reference is collected with one spectrometer, the emittance of the sample is collected with another. Then the stage rotates, switching the blackbody furnace and the sample position to a different spectrometer enabling the next measurement to be done in a vice versa manner. A $CO_2$ laser is used as a heating source for the sample and can reach a temperature up to 2500 K. To avoid damage to the spectrometer, the laser was not aimed at the sample directly but at an angle. The $CO_2$ laser is also placed on a rotary stage keeping the heat constant even during rotation. The layout of the IREM device is shown in Figure 51 and for a better understanding, a schematic of the experimental device is given in Figure 52.

Data collected from the IREM were organized and analysed in 3 steps shown as a diagram in Figure 53. Step 1, sets of data containing three-measurement; ambient, blackbody and sample heat flux were calculated for an emissivity value ($\varepsilon_o$) with a program called Emittance. This program was written specifically for the IREM method by Dr. Domingos De Sousa Meneses. Step 2, power (Watts) is converted to temperatures using a program call Emittance as well. The program converts power to temperature using Christiansen point which is a point where the materials has a refractive index close to 1 leading to reflectivity close to 0 and therefore, emissivity close to one. In other words, the materials at Christiansen point behave like a blackbody. Christiansen point is a function of wavenumber and temperature, therefore, knowing the Christiansen point and wavenumber,

[6] Deuterated, L-alanine doped triglycine sulphate (DLaTGS)

temperature can be determined [105]. Step 3, the emissivity values for the different infrared ranges were merged.

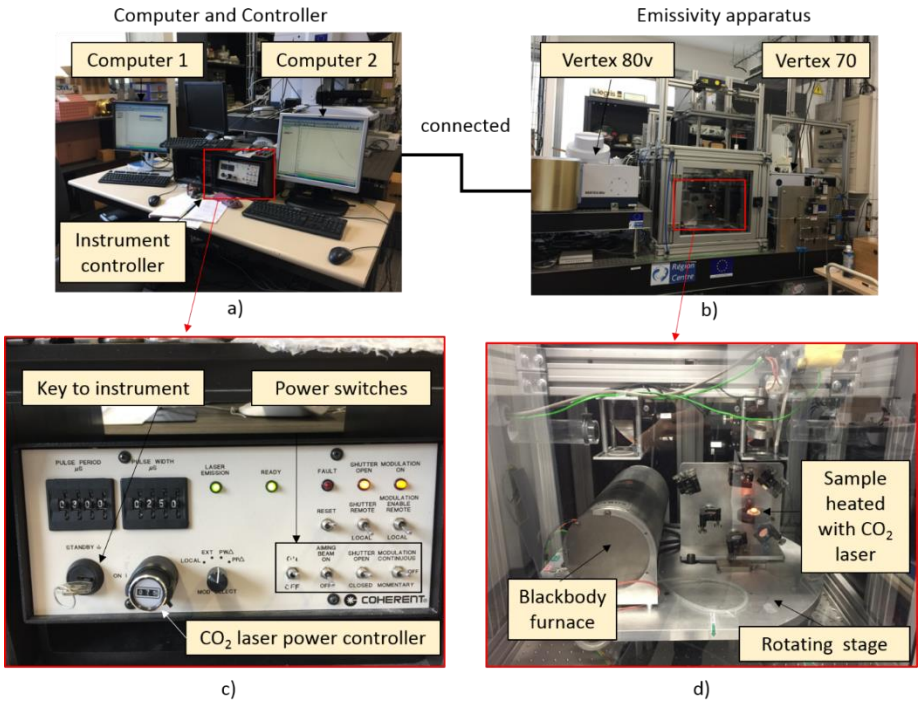


Figure 51. Layout of the IREM device. a) Computers and instrument controller. Computer 1 analysed data received from spectroscopy Vertex 70 (wavenumber 4000-12000 $cm^{-1}$) and computer 2 analysed data received from spectroscopy Vertex 80v (wavenumber 700-4000 $cm^{-1}$). A controller is also present in this image. b) The spectroscopes; Vertex 80v and Vertex 70, are used to measure the electromagnetic spectrum from blackbody furnace and the sample located inside a vacuum chamber. c) Magnified image of the controller. It presents the key to turn on-off the instrument, power switches and the $CO_2$ laser power controller. d) Magnified image of inside the vacuum chamber where the blackbody furnace, sample are placed on a rotating stage (author's figure).

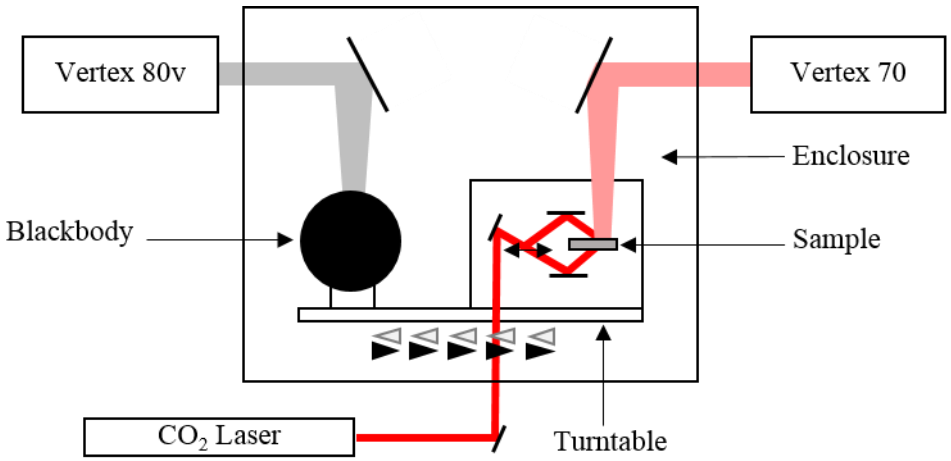


Figure 52. Schematic diagram of the IREM device (modify from [79]).

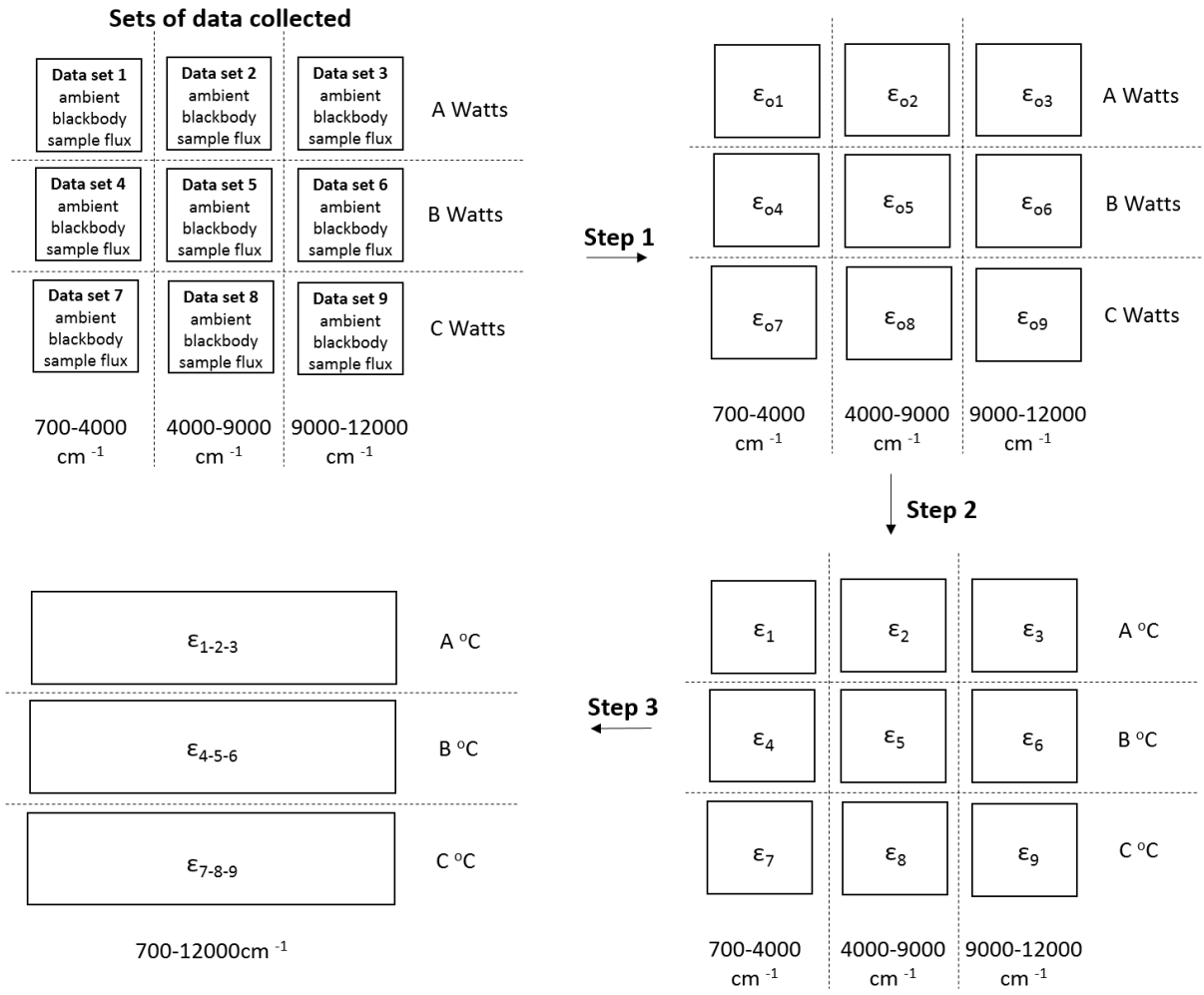


Figure 53. Diagram of sets of data collected from IREM measurements which is analysed in three steps. Step 1 used ambient, blackbody and sample heat flux to calculate emissivity ($\varepsilon_o$). Step 2 converts power (watts) to temperature (°C) through Christiansen point giving an accurate emissivity value (ε). Step 3 merges emissivity values at different wavenumbers (author's figure).

The $CO_2$ laser power determines the sample temperature. Three power levels; 54, 71 and 100 Watts were chosen to try to accomplish three temperatures which are 1000, 1300 and 1500°C. Different power is needed for different material to reach the same temperature because material with higher heat absorption required higher power to reach the desired temperature. Six samples are used to in this experiment: 1) BR, 2) CBR 1-3, 3) CBR1-5, 4) CBR 1-12 and 5) thicker coating of CRB 1-5 (TRB 1-5) and 6) sintered $CeO_2$ pellet. Sample 2-4 thickness was in the 100 ± 50 μm range. Sample 5 thickness was 280±15 μm.

## 3.4 Corrosion testing

Corrosion testing was conducted to understand how the coating is affected in an alkaline environment. This is important because the alkaline vapour is present in the cement kilns coming from the raw materials and alternative fuels. In this research, two corrosion tests were conducted which are vapour test and cup test.

The vapour test was conducted to better understand how the alkaline vapour reacts with the coating. The experiment is set up by filling an alumina crucible with 0.5 g of $K_2CO_3$ then used a coated sample as a lid. The coated sample is placed with the coating side faced down towards the alkaline $K_2CO_3$. The alumina crucible and coated sample are then placed in an electric furnace and heated at 1300°C for 30 min, 6°C/min in air. A schematic of the vapour test set up is shown in Figure 54. Samples chosen for this experiment are BR, CBR 1-3, CBR 1-5 and CBR 1-12 heat treated at 1300°C, 3 h. SEM was used to study the microstructure of the tested samples.

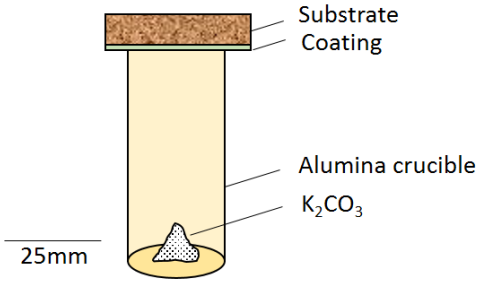


Figure 54. Schematic diagram of the vapour test set up (author's figure).

The cup test was conducted to understand an alkaline corrosion and penetration through the basic refractory brick on its own and with coating. The basic refractory bricks are cut and drilled into a cup shape with a dimension as shown in Figure 55. Inside of the cups were coated with CS 1-3, 1-5 and 1-12, 3 cups of each. Two cups are left un-coated. All cups are filled with 15 g of $K_2CO_3$. The top of the cups was closed with a lid made from the same material as the cup. To ensure the cups were sealed properly, an adhesive paste was applied to the joint between the cup and the lid. The adhesive paste was made from mixing 15 g of magnesium oxide with 7.5 g of sodium silicate. The closed cups are heated in an electric furnace at 1300°C for 30 min, 6°C/min. After the furnace is cooled down naturally, the cup lids are cracked open and the cups are then cut into half vertically and used to study the corrosion and the penetration volume. Corrosion measures the volume of the refractory material that was corroded by the alkaline leading to material loss causing the refractory brick to become

thinner. Corrosion is mostly dependent on material composition. Penetration measures the volume of the refractory material that was penetrated by the alkaline. Penetration is mostly dependent on the number of pores and cracks. When the alkaline penetrates through and densify the refractory matrix it causes a density gradient between the penetrated region and unpenetrated region leading to spalling as mentioned in section 2.3. A schematic diagram of corrosion and penetration are presented in Figure 56., The red and blue regions represent alkaline corrosion and penetration regions respectively. The corrosion and the penetration can be measured as present in Figure 57 and calculated from Equation 62 and Equation 63 [123, 160].

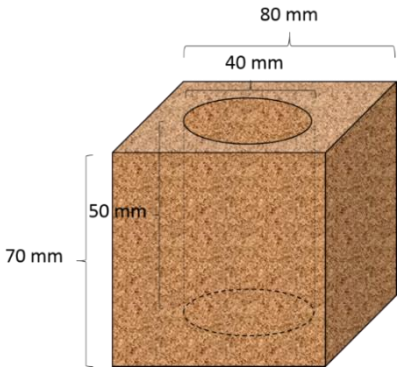


Figure 55. Schematic diagram showing dimensions on the sample cut and drilled into a cup shape (author's figure).

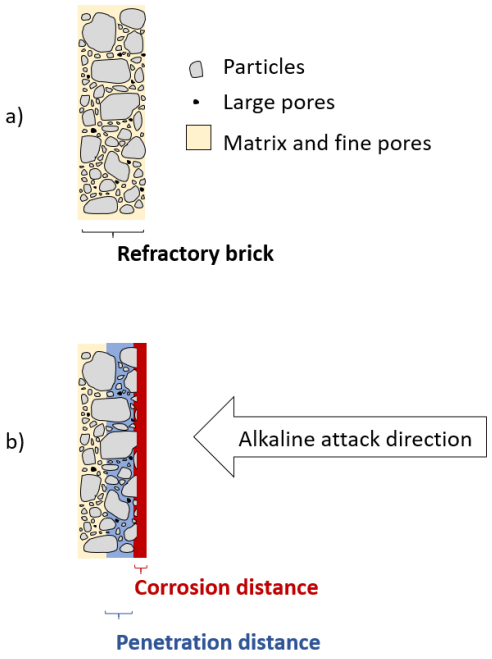


Figure 56. Schematic image of a) refractory brick. b) refractory that is being attacked by alkaline. The red and blue regions represent alkaline corrosion and penetration effects on the refractory brick respectively (author's figure).

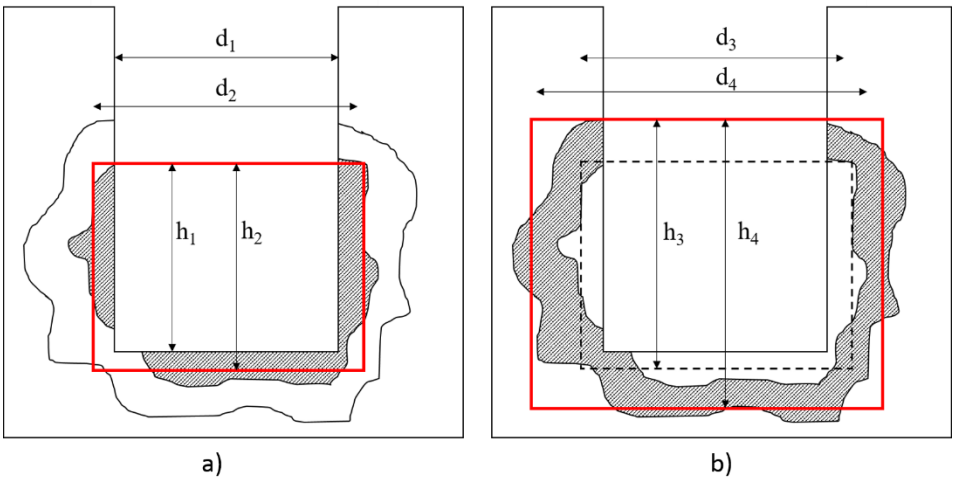


Figure 57. Schematic diagram showing dimensions for a) solubility and b) saturation volume measurement (modified from [161]).

Equation 62. $$\text{Corrosion Volume} = \left\{\pi \cdot \left(\frac{d_2}{2}\right)^2 \cdot h_2\right\} - \left\{\pi \cdot \left(\frac{d_1}{2}\right)^2 \cdot h_1\right\}$$

Equation 63. $$\text{Penetration Volume} = \left\{\pi \cdot \left(\frac{d_4}{2}\right)^2 \cdot h_4\right\} - \left\{\pi \cdot \left(\frac{d_3}{2}\right)^2 \cdot h_3\right\}$$

The alkaline corrosion and penetration on refractory bricks or coating may or may not be related to one another depending on the scenarios (Figure 58). Four possible scenarios are presented as below:

**Scenario 1:** Low penetration and low corrosion: this is an ideal goal for corrosion resistance because there are hardly any changes on the refractory brick or coating leading to a long-life usage (the brick and coating thickness hardly change).

**Scenario 2:** Low corrosion and high penetration: transport is dominant. No reactions between the corrosive material and the sample materials, which is good. Corrosive materials penetrating the sample materials can cause problems, for example, from different levels of densification (high density in the hot face and lower density in the cold face) leading to spalling/peeling as explained in section 2.3 [113].

**Scenario 3:** High corrosion and low penetration: chemistry is dominant, and alkaline penetration into the refractory brick is low because

a) The refractory brick or coating is dense, contains low porosity and capillarity.

b) The corrosive material (alkaline source) is viscous.

c) The corrosion consumed the sample materials leaving less material to infiltrate.

**Scenario 4:** High corrosion and high penetration of alkaline on the refractory bricks or coating: this is the scenario that should be avoided because it led to refractory or coating thickness reduction and decreases the refractory lifetime.

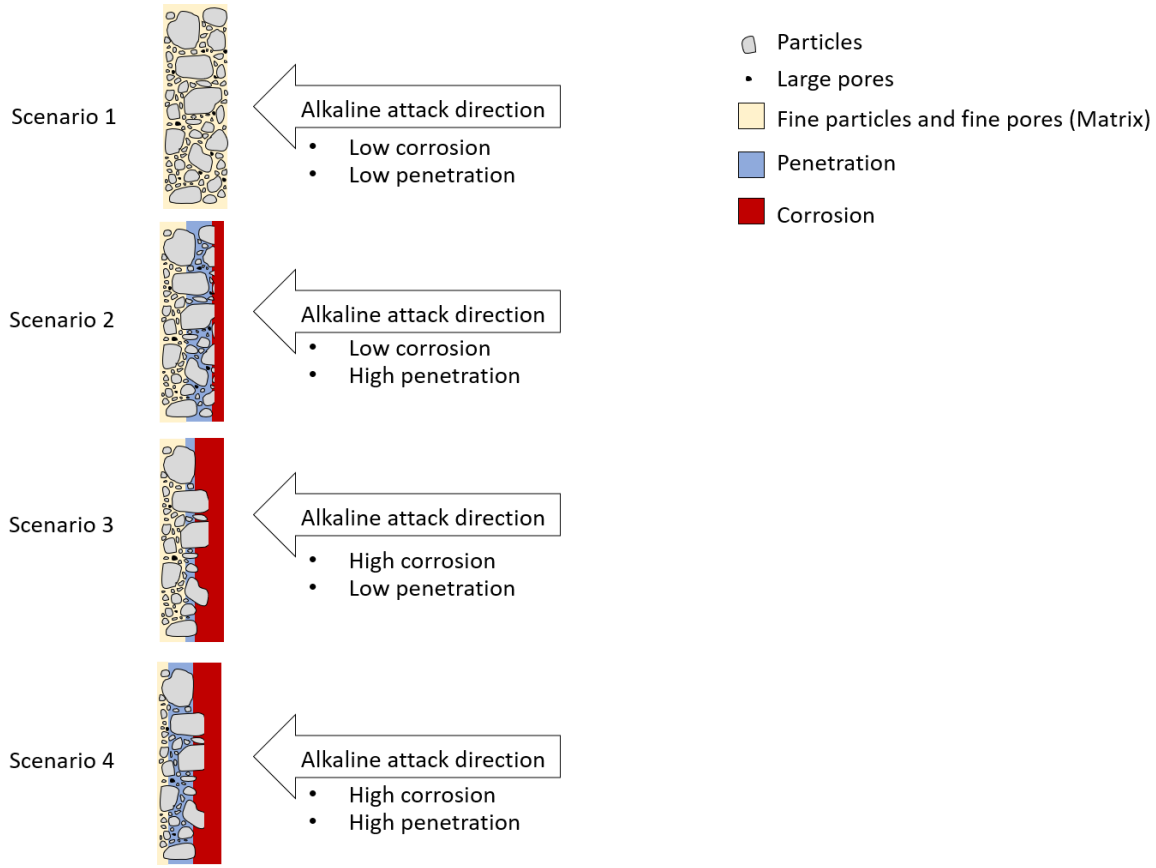


Figure 58. Schematic of 4 scenarios that alkaline corrosion and penetration effects the refractory bricks (author's figure).

# Chapter 4: Refractory brick and coating characterisation results

## 4.1 Refractory characterisation results

Phase analysis XRD of refractory brick (MSN80) received from the Siam Refractory Industry Co., Ltd, Saraburi, Thailand (SRIC) is presented in Figure 59. The phases were identified using X'Pert Highscore Plus software (Malvern Panalytical, Malvern, UK) as described in section 3.1. Reference and ICSD collection codes are shown in Table 8 revealing that the refractory brick is composed of magnesia (MgO) and magnesium aluminate spinel ($MgO{\cdot}Al_2O_3$, $MgAl_2O_4$).

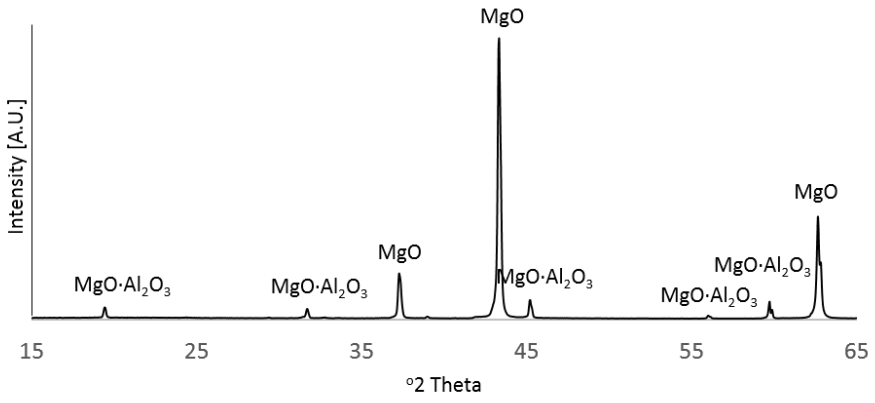


Figure 59. XRD of refractory brick.

Table 8. XRD information database of MgO and $MgO{\cdot}Al_2O_3$ used for identifying phases in this thesis.

| Compound name | Chemical formula | Reference code | ICSD collection code | Lattice parameters | | | | | | Crystal system |
|---|---|---|---|---|---|---|---|---|---|---|
| | | | | a (Å) | b (Å) | c (Å) | α (°) | β (°) | γ (°) | |
| Periclase | MgO | 01-087-0651 | 064928 | 4.2160 | 4.2160 | 4.2160 | 90.00 | 90.00 | 90.00 | Cubic |
| Magnesium alumina spinel | $MgAl_2O_4$ | 01-074-1132 | 026845 | 8.0832 | 8.0832 | 8.0832 | 90.00 | 90.00 | 90.00 | Cubic |

Microstructure was observed with SEM as shown in Figure 60. The refractory brick has a heterogeneous microstructure comprising of MgO, $MgO{\cdot}Al_2O_3$ and pores. Various size of MgO, ranging from 45μm- 4mm, and $MgO{\cdot}Al_2O_3$ particles, ranging 0.6-3 mm, were seen to create high packing density. The bulk density and apparent porosity of the refractory brick were 2.9 ±0.05 g/cm$^3$ and 16 ±2% respectively.

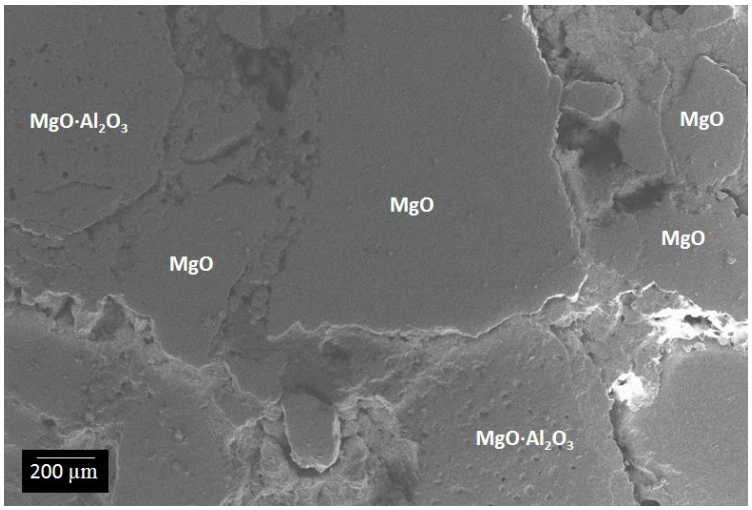


Figure 60. SEM image of refractory brick.

# 4.2 Coating characterisation

## 4.2.1 Rheology

Viscosities of four coating compositions were measured; coatings with the ratio of $CeO_2$: $AlH_6O_{12}P_3$ of 1:3, 1:5 1:12 (CS 1-3, CS 1-5 and CS 1-12) and $AlH_6O_{12}P_3$ itself. Coating viscosities (Pa.s) at different shear rates (1/s) on a log scale are shown in Figure 61. The coating slurry of CS 1-3 has the highest viscosity followed by CS 1-5, CS 1-12 and $AlH_6O_{12}P_3$. This is attributed to the solid ($CeO_2$ powder) content. $AlH_6O_{12}P_3$ is a Newtonian fluid where the viscosity is independent of the shear rate, unlike the other three coatings that contain $CeO_2$. The coatings containing $CeO_2$ are shear thinning; viscosity decreases as the shear rate increases. Shear thinning is beneficial because it is suitable for coatings to be applied with the gun spraying technique as discribed in section 3.2.2.

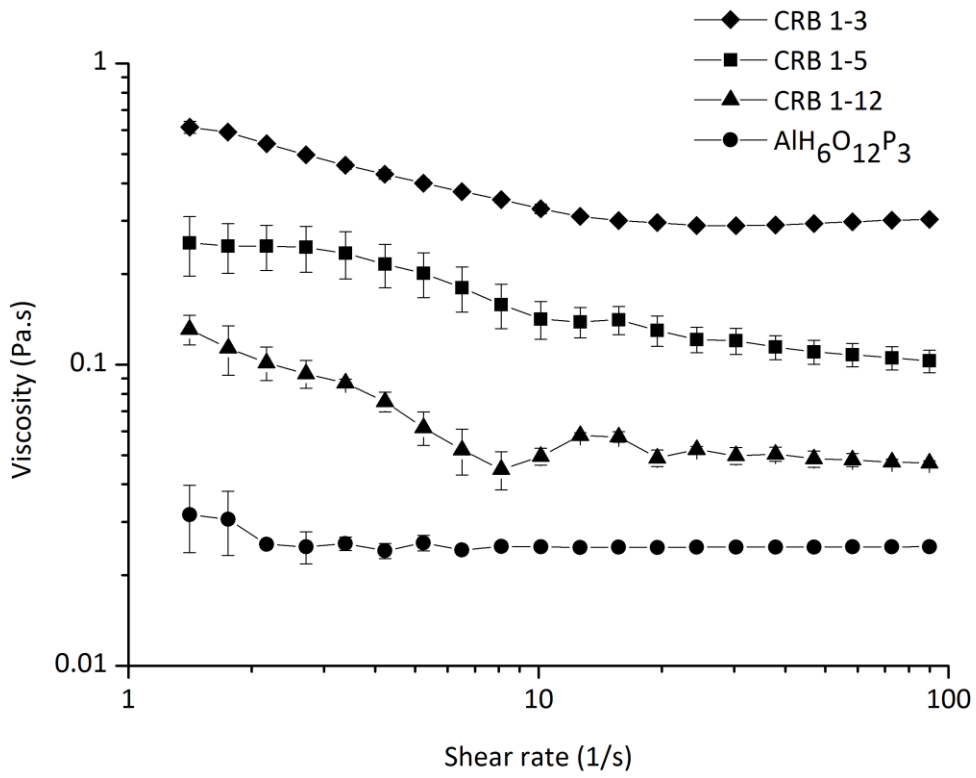


Figure 61. Viscosity of $CeO_2$ mixed with $AlH_6O_{12}P_3$ at different volume ratios.

## 4.2.2 Coating phase evolution with temperature

### 4.2.2.1 Differential scanning calorimetry (DSC) and Thermogravimetric analysis (TGA)

Three samples; CS 1-3, CS 1-5 and CS1-12, were studied by DSC/TGA at 1500°C with a heating rate of 5°C/min. Results are presented using two x-axes, in two colours, blue for TGA results and red for DSC results. TGA results revealed a straightforward sample weight loss whereas the DSC reveals indirect information of a change in enthalpy ($\Delta H$) which has a direct variation with the peak area as present in Equation 34 [151]. The peak area was divided into 2 regions as shown in Figure 62. Area 1 is endothermic, meaning heat is being absorbed to break chemical bonds in the sample. Area 2 is exothermic, meaning heat is being released from chemical bonds forming together in the sample.

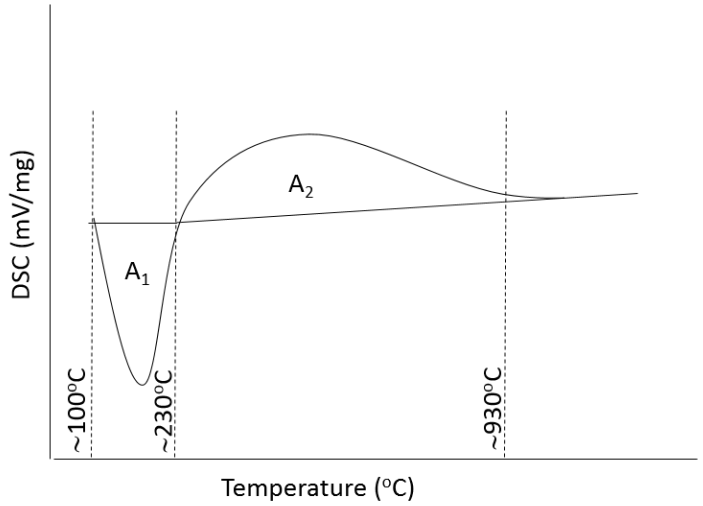


Figure 62. Schematic image of DSC result. $A_1$ represents area 1 (endothermic) and $A_2$ represents area 2 (exothermic) (author's figure).

Results of the coating slurry are presented in order of CS 1-3, CS 1-5 and CS 1-12. CS 1-3 as shown in Figure 63. TG results show a mass loss of about -1 ±0.04 wt% (negative sign indicating mass loss) which initially occurred due to the vaporization of water at ~100°C.

$$AlH_6P_3O_{12} \rightarrow AlH_2P_3O_{10} + 2H_2O$$

At 500°C the weight loss continues to -15±0.03 wt% from dehydrogenation from $AlH_6O_{12}P_3$ reported by Chiou and Chung [162].

$$AlH_2P_3O_{10} \rightarrow Al(PO_3)_3 + 2H_2O$$

However, at 500°C there was no significant weight loss and therefore, further investigation is needed i.e. HT-XRD and XRD. The weight loss (blue line) from water vaporization and dehydration explains the endothermic reaction (red line) of area 1. CS 1-3 peaks of area 1 were measured from a starting temperature of 101°C ±0.58 to 226°C ±0.29 and the area value was 6 ±0.13 unit$^2$. Area 2 is exothermic and was measured from temperature 226°C ±2.65 to 920°C ±6.08 and the area was 37 ±1.3 unit$^2$. The cause of the exotherm in area 2 is discussed further with the high temperature XRD and XRD results in section 4.3.1.

CS 1-5 results are shown in Figure 64. The weight loss of this sample is -3 ±0.06 wt% and -24 ±0.02 wt% due to water vaporization and dehydrogenation from $AlH_6O_{12}P_3$ respectively. There is more weight loss in this CS 1-5 sample than in the CS 1-3 because it contains more $AlH_6O_{12}P_3$ and therefore, more water to vaporize. Area 1 is endothermic and was measured at a starting temperature of 104°C ±5.20 to 239°C ± 4.58 and the area value was 10 ± 0.57 unit$^2$. Area 1 value is also higher compared to the CS 1-3 due to the same reason as the weight loss. Area 2 is exothermic and was measured from 239°C ± 4.58 to 926°C ±7.07 and the area value was 25 ±1.57 unit$^2$. Area 2 of CS 1-5 sample is smaller than area 2 of the CS 1-3 sample. The cause of the exothermic in area 2 is discussed further with the high temperature XRD and XRD results in section 4.3.1.

CS 1-12 results are shown in Figure 65. The weight loss of this sample is -4 ±0.10 wt% and -41 ±2.45 wt% due to water vaporization and dehydrogenation from $AlH_6O_{12}P_3$ respectively. CS 1-12 has the highest weight loss because it has the highest $AlH_6O_{12}P_3$ binder content. However, the measurement for sample CS 1-12 was not successful because the dehydrogenation was strong leading to a sample spilling out of the alumina crucible and so the measurement was stopped. Summarization of the CS 1-3, CS 1-5 and CS1-12 data are presented in Table 9.

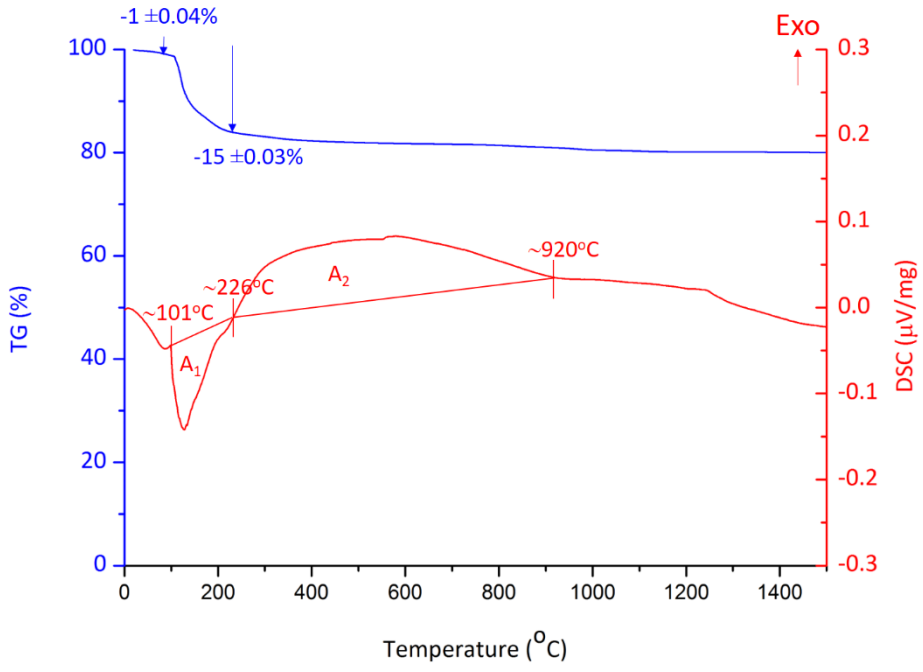


Figure 63. DSC/TG profiles for CS 1-3 slurry in air. Blue graph is TG and red is DSC. $A_1$ and $A_2$ represent Area 1 and 2 respectively.

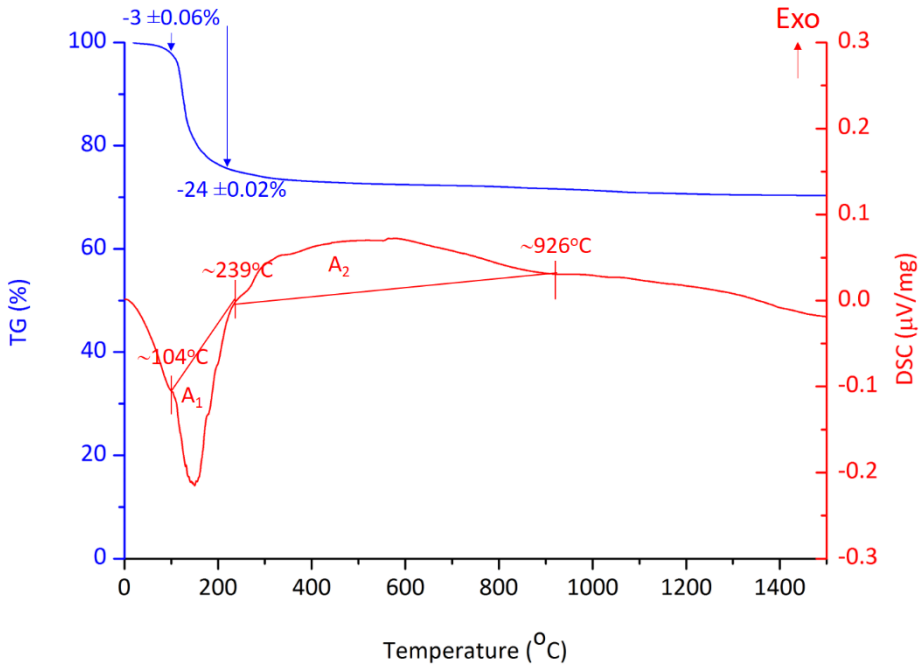


Figure 64. DSC/TG profiles for CS 1-5 slurry in air. Blue graph is the TG and red is the DSC. $A_1$ and $A_2$ represent Area 1 and 2 respectively.

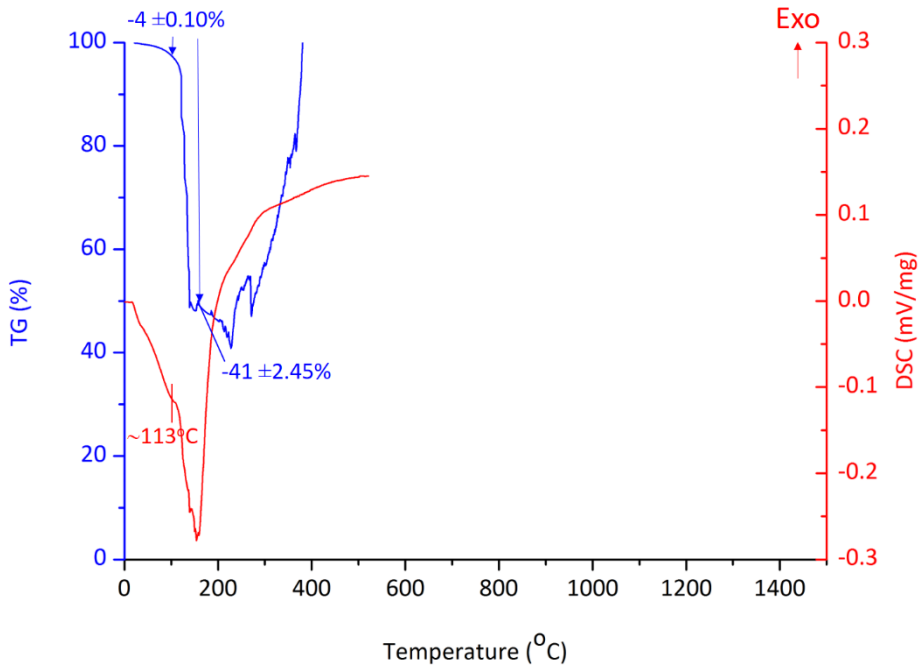


Figure 65. DSC/TG profiles for CS 1-12 slurry in air. Blue graph is TG and red graph is DSC.

Table 9. Summary of CS 1-3, CS 1-5 and CS 1-12 DSC data.

| Sample | Area 1 temperature range (°C) | Area 1 (unit$^2$) | Area 2 temperature range(°C) | Area 2 (unit$^2$) |
|---|---|---|---|---|
| CS 1-3 | 101±0.58 to 226±0.29 | 6 ±0.13 | 226 ±2.65 to 920 ±6.08 | 37±1.30 |
| CS 1-5 | 104 ±5.20 to 239 ± 4.58 | 10 ±0.57 | 239 ± 4.58 to 926 ±7.07 | 25 ±1.57 |
| CS 1-12 | N/A | N/A | N/A | N/A |

4.2.2.2 High temperature X-ray diffraction (HT-XRD), X-ray diffraction (XRD)

The *in-situ* XRD patterns from the heating HT-XRD for 1 $CeO_2$: 6 $AlH_6O_{12}P_3$ volume ratio sample are shown in Figure 66. They were analysed as described in section 3.1.1 (see Table 10). Figure 66 reveals that $CeO_2$ is the dominant phase from room temperature to 800°C indicating that there was no interaction between $CeO_2$ and $AlH_6P_3O_{12}$ or reactions are small, so any new peaks formed were too small to be detected by the HT-XRD. The DSC results of exothermic area 2 suggest that there is a reaction occurring in the temperature range of about 300-900, therefore, it is likely there are reactions, but they were not detectable by the HT-XRD. At 800°C the $CeO_2$ peaks shift to a lower angle as discussed in the next paragraph. From 850°C to 1500°C, $CeO_2$ peak intensities gradually decrease as temperature increases while cerium phosphate (monazite, $CePO_4$) peak intensities increase indicating that $CeO_2$ transforms to $CePO_4$ above 850°C. Hydrogen- and aluminium-containing phases from $AlH_6O_{12}P_3$ were not detected indicating hydrogen transfer to gas phase and aluminium dissolved in the glassy phase (discussed in the EDS analysis later). Platinum peaks in XRD are from the sample heating stage.

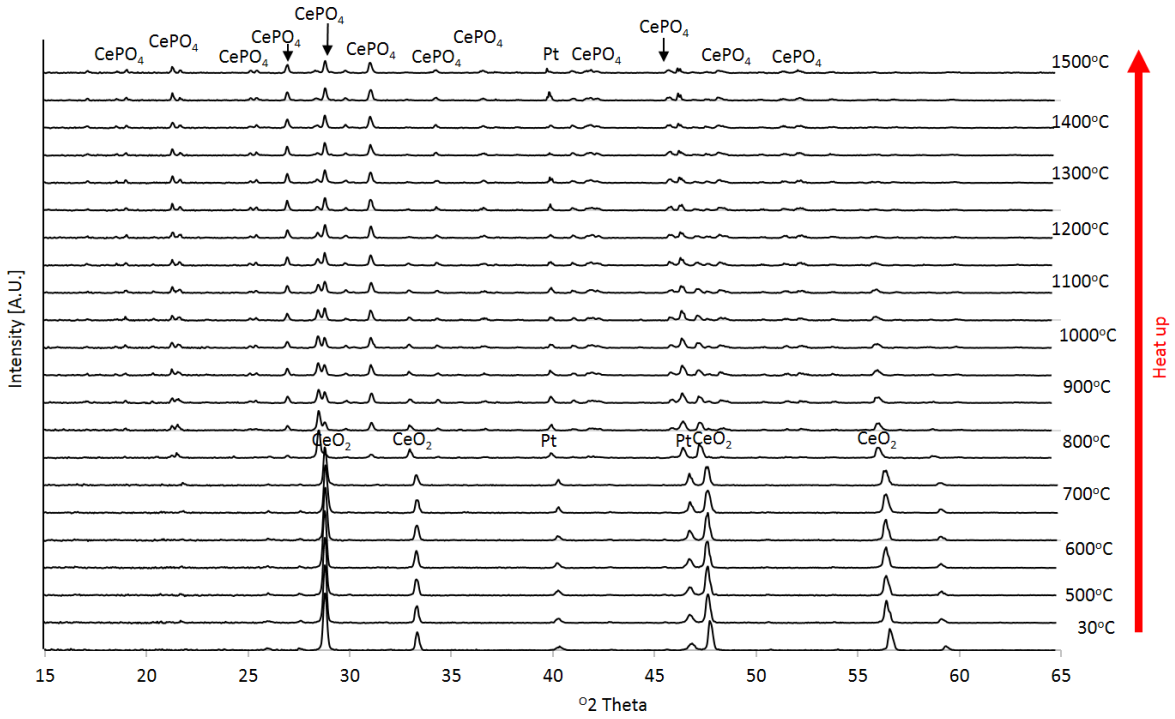


Figure 66. HT-XRD patterns on heating of 1 $CeO_2$: 6 $AlH_6O_{12}P_3$ volume ratio sample.

$CeO_2$ peak shift to a lower angle when temperature increases from 750°C to 800°C is now addressed. The shift can be from two causes, the lattice parameters of the $CeO_2$ changes due to thermal expansion or there was a displacement in the sample surface due to a shift in sample or platinum heating stage. NRP (mentioned in section 3.2.3.2) was used to resolve this problem. 4 peaks of the $CeO_2$ lattice (111, 200, 220, 311) have been analysed for systematic error in peak position due to sample displacement or misalignment as described in section 3.2.3.2 and plane information is presented in Table 11. Graphs of Nelson-Riley parameter versus lattice parameter, plotted for temperatures between 650-900°C, are presented in Figure 67. The plot shows that as temperature increases in the range of 650-750°C the slope is relatively constant at about -0.02 while the intercept increases slowly due to thermal expansion. When the temperature increased from 750°C to 800°C, the slope changed significantly from about -0.021 to -0.009 and became closer to zero indicating that there is a change in sample displacement. As the temperature increases from 750°C to 800°C, there is a continual intercept change indicating a continual increase in $CeO_2$ lattice parameter. On average, the rate of intercept increase was 8.8 X $10^{-4}$ Å·$K^{-1}$ which is higher than $CeO_2$ thermal expansion (12-16 X $10^{-6}$ $K^{-1}$). This indicates that while heating, before $CeO_2$ reacts with $AlH_6O_{12}P_3$ generating $CePO_4$, $CeO_2$ lattice parameters grew larger. This information confirms the $CeO_2$ peaks shift is a combination of systematic error from specimen displacement and lattice parameter expansion.

Table 10. XRD information database of $CeO_2$ and $CePO_4$ used for identifying phases in this thesis.

| Compound name | Chemical formula | Reference code | ICSD collection code | Lattice parameters | | | | | | Crystal system |
|---|---|---|---|---|---|---|---|---|---|---|
| | | | | a | b | c | $\alpha$ | $\beta$ | $\gamma$ | |
| Cerium oxide | $CeO_2$ | 01-078-0694 | 061595 | 5.4109 | 5.4109 | 5.4109 | 90.00 | 90.00 | 90.00 | Cubic |
| Monazite-(Ce) | $CePO_4$ | 01-083-0650 | 079746 | 6.7902 | 7.0203 | 6.4674 | 90.00 | 103.38 | 90.00 | Monoclinic |

As mentioned in section 3.2.3.2 XRD peak intensities collected from high temperature XRD are much lower than those collected from standard powder XRD. Therefore, another experiment was conducted using coating slurry 1-5 (CS 1-5) that was heat treated at 800°C (where the phases start to change in the HT-XRD) and 1550°C (over the maximum temperature of the HT-XRD). The results are shown in Figure 68. Un-sintered sample (green) mainly contained $CeO_2$. Sample sintered at 800°C shows 3 phases which were $CeO_2$, $CePO_4$ and $Ce(PO_3)_3$. The $CeO_2$ and $CePO_4$ were identified using the same database as for the HT-XRD data in Table 10. $Ce(PO_3)_3$ databased in presented in Table 12. Observing $CeO_2$, $CePO_4$ phase is consistent with the HT-XRD data. However, $Ce(PO_3)_3$ phase was not previously observed. The $Ce(PO_3)_3$ peak intensities are considered low even in the normal room temperature XRD and it is possible that it is embedded in the noise in the HT-XRD. As for the sample heat treated to 1550°C, only $CePO_4$ phase was present. From this information, it can be understood that at about 800°C, $CeO_2$ reacts with $AlH_6O_{12}P_3$ and forms $Ce(PO_3)_3$ and $CePO_4$. As the temperature increases, the reaction continues and $Ce(PO_3)_3$ phase changes to $CePO_4$ at about 930°C [163]. Consequently, when the temperature reaches 1550°C only $CePO_4$ phase was present.

Table 11. $CeO_2$ lattice and planes information. $2\theta$ collected from the HT-XRD were divide by 2 for $\theta$ which was used for Nelson Riley Parameter (NRP, $1/2[(\cos^2\theta/\sin\theta) + (\cos^2\theta/\theta)]$). d-spacing was also collected from the HT-XRD and was used together with the Miller indices (from the data presented in Table 10) for the lattice parameter (LP) using Equation 35.

| Temperature | Peak | $2\theta$ | $\theta$ | NRP | d-spacing | Miller indices | | | LP |
|---|---|---|---|---|---|---|---|---|---|
| | | | | | | h | k | l | |
| 650°C | 1 | 28.7865 | 14.39325 | 3.841 | 3.10142 | 1 | 1 | 1 | 5.37 |
| | 2 | 33.2984 | 16.6492 | 3.259 | 2.69078 | 2 | 0 | 0 | 5.38 |
| | 3 | 47.5839 | 23.79195 | 2.111 | 1.91102 | 2 | 2 | 0 | 5.41 |
| | 4 | 56.3481 | 28.17405 | 1.674 | 0.2824 | 3 | 1 | 1 | 5.42 |
| 700°C | 1 | 28.7992 | 14.3996 | 3.838 | 3.10008 | 1 | 1 | 1 | 5.37 |
| | 2 | 33.3117 | 16.65585 | 3.256 | 2.68973 | 2 | 0 | 0 | 5.38 |
| | 3 | 47.5683 | 23.78415 | 2.112 | 1.91161 | 2 | 2 | 0 | 5.41 |
| | 4 | 56.3420 | 28.171 | 1.674 | 1.63298 | 3 | 1 | 1 | 5.42 |
| 750°C | 1 | 28.7837 | 14.39185 | 3.841 | 3.10171 | 1 | 1 | 1 | 5.37 |
| | 2 | 33.2649 | 16.63245 | 3.264 | 2.69341 | 2 | 0 | 0 | 5.39 |
| | 3 | 47.5469 | 23.77345 | 2.113 | 1.91242 | 2 | 2 | 0 | 5.41 |
| | 4 | 56.2876 | 28.1438 | 1.676 | 1.63443 | 3 | 1 | 1 | 5.42 |
| 800°C | 1 | 28.4764 | 14.2382 | 3.885 | 3.13448 | 1 | 1 | 1 | 5.43 |
| | 2 | 32.9639 | 16.48195 | 3.297 | 2.71731 | 2 | 0 | 0 | 5.43 |
| | 3 | 47.1984 | 23.5992 | 2.133 | 1.92572 | 2 | 2 | 0 | 5.45 |
| | 4 | 55.9591 | 27.97955 | 1.690 | 1.64324 | 3 | 1 | 1 | 5.45 |
| 850°C | 1 | 28.4779 | 14.23895 | 3.885 | 3.13432 | 1 | 1 | 1 | 5.43 |
| | 2 | 32.9632 | 16.4816 | 3.297 | 2.71737 | 2 | 0 | 0 | 5.43 |
| | 3 | 47.2027 | 23.60135 | 2.133 | 1.92556 | 2 | 2 | 0 | 5.45 |
| | 4 | 55.9419 | 27.97095 | 1.691 | 1.6437 | 3 | 1 | 1 | 5.45 |
| 900°C | 1 | 28.4667 | 14.23335 | 3.889 | 3.13553 | 1 | 1 | 1 | 5.43 |
| | 2 | 32.9696 | 16.4848 | 3.297 | 2.71686 | 2 | 0 | 0 | 5.43 |
| | 3 | 47.1552 | 23.5776 | 2.136 | 1.92739 | 2 | 2 | 0 | 5.45 |
| | 4 | 55.9818 | 27.9909 | 1.689 | 1.64263 | 3 | 1 | 1 | 5.45 |

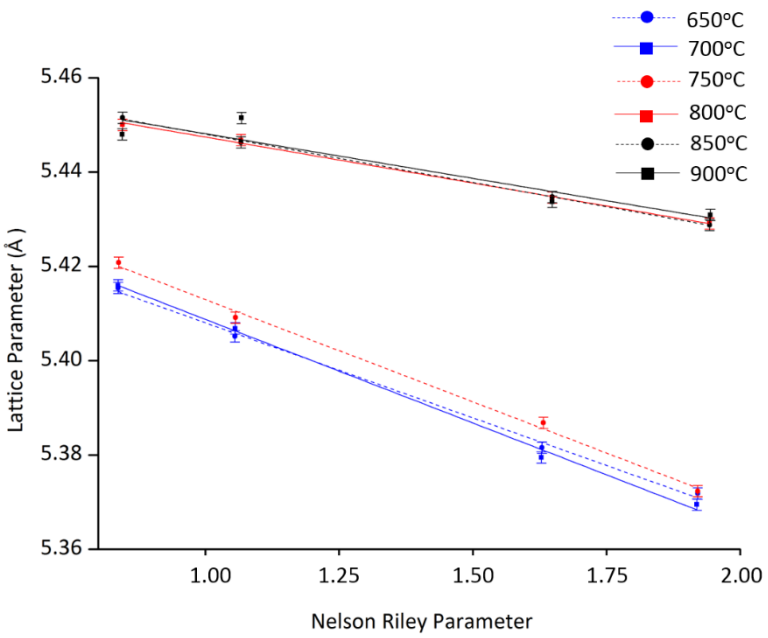


Figure 67. Nelson-Riley parameter versus lattice parameter at different temperatures.

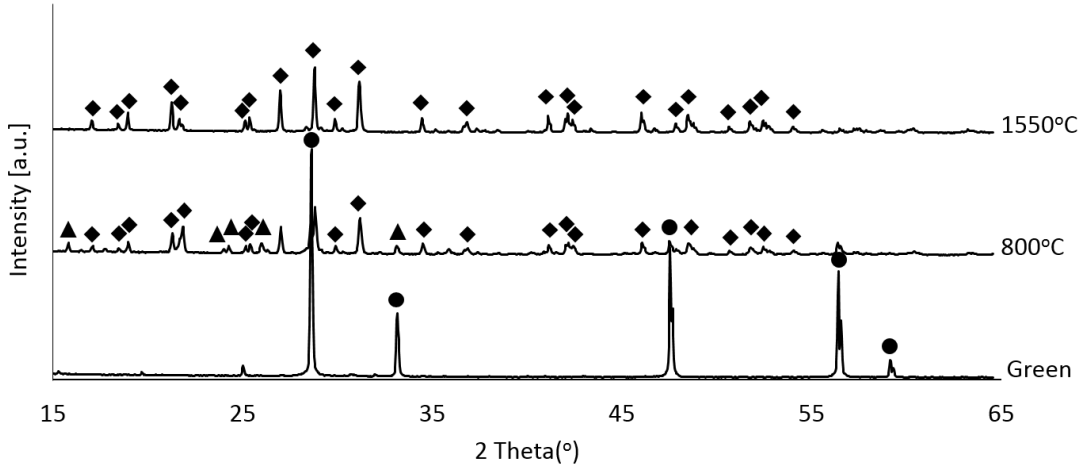


Figure 68. XRD of green coating and coatings heat treated at 800°C and 1550°C, 3h. Circles (●) are $CeO_2$, diamonds (◆) are $CePO_4$, triangles (▲) are $Ce(PO_3)_3$. Information of $CeO_2$ and $CePO_4$ databased in presented in Table 10 and $Ce(PO_3)_3$ in Table 12.

Table 12. XRD information database of $Ce(PO_3)_3$ used for identifying phases in this thesis.

| Compound name | Chemical formula | Reference code | ICSD collection code | Lattice parameters | | | | | | Crystal system |
|---|---|---|---|---|---|---|---|---|---|---|
| | | | | a | b | c | α | β | γ | |
| Cerium Phosphate | $Ce(PO_3)_3$ | 00-033-0336 | N/A | 11.33 | 8.61 | 7.33 | 90.00 | 90.00 | 90.00 | Orthorhombic |

XRD was also used to investigate coating phases with different compositions (sintered CS 1-3, 1-5 and 1-12) heat treated at 1300°C, 3h. Figure 69 reveals that all three coatings contain $CeO_2$ and $CePO_4$. $CeO_2$ is from the raw material and $CePO_4$ is from the reaction between $CeO_2$ and $AlH_6O_{12}P_3$. Mixing different $CeO_2$: $AlH_6O_{12}P_3$ ratios consequently gives rise to different amounts of $CePO_4$ and unreacted $CeO_2$ as indicated by the different peak intensities/areas. Sintered CS 1-3, which has the highest $CeO_2$ content, presents the highest $CeO_2$ and the lowest $CePO_4$ peak intensities. $CeO_2$ peak intensity decreases and $CePO_4$ peak intensity increases as the $CeO_2$: $AlH_6O_{12}P_3$ ratio decreases. This can be seen clearly in Figure 69b which is a magnified image of Figure 69a (2theta ranging from 25-35° where the highest peaks of both $CeO_2$ and $CePO_4$ are presented).

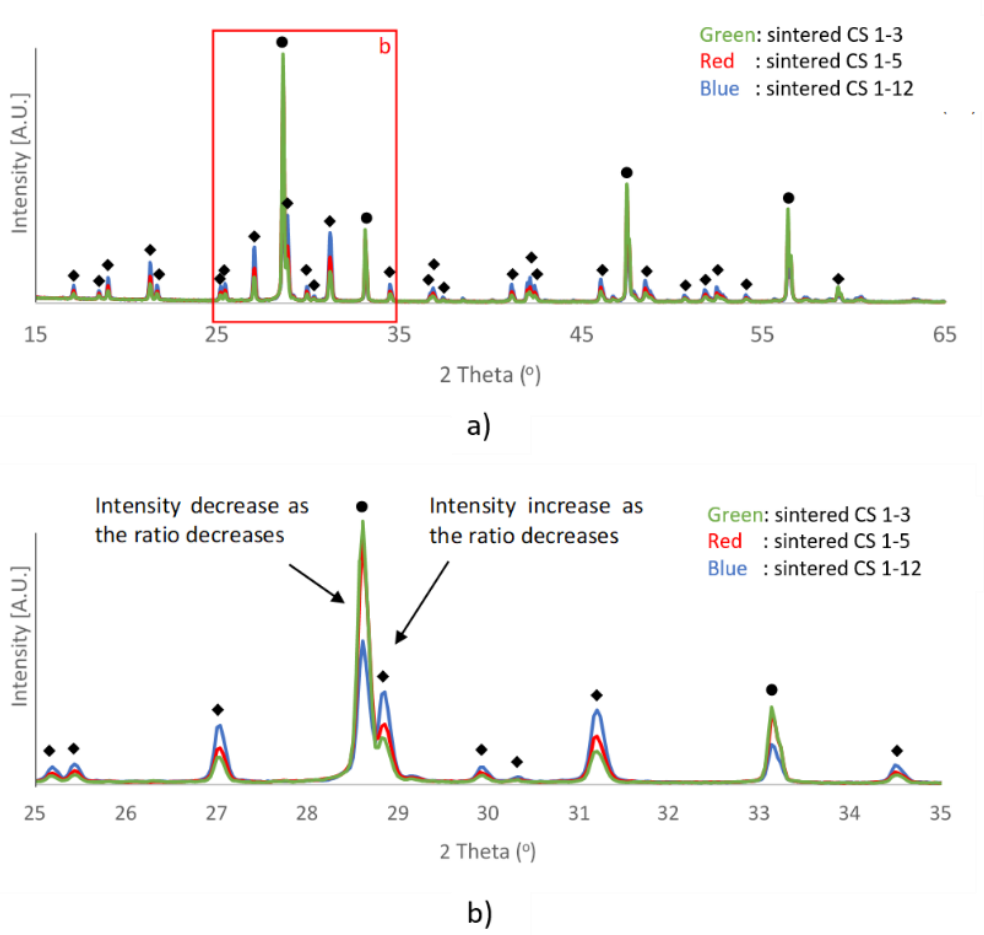


Figure 69. XRD of coatings heat treated at 1300°C, 3h. a) is of all three coatings for 15-65° 2theta, b) is a magnified image of a) for15-25°2theta. The coating contained different ratios of composition of $CeO_2$: $AlH_6O_{12}P_3$ of 1:3, 1:5 and 1:12 presented in green, red and blue, respectively. Circles (●) are $CeO_2$ and diamonds (◆) are $CePO_4$.

4.2.2.3 X-ray photoelectron spectroscopy (XPS)

XPS measurements start by running a survey scan to give an overview of the elemental composition of the sample. After, peaks of interest were selected for a higher energy scan with a lower count rate for quantitative analysis. An XPS survey scanned of the CS 1-5 heat treated at 1550°C, 3 h is shown in Figure 70. Peaks at each binding energy were identified by matching them with an open source NIST XPS database [164, 165]. The element peaks are also shown in Figure 70, and some of these have more than one peak (doublet peaks), i.e. Ce 3d and Ce 4p because electrons emerge from a different sub-orbital. Background on orbitals and sub-orbitals of cerium is given in section 3.2.3.3.

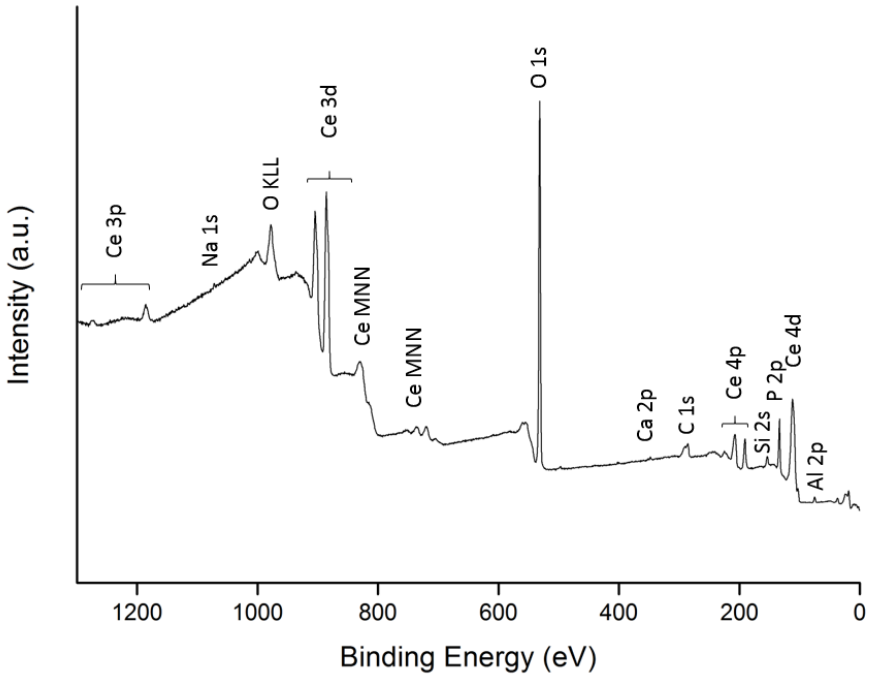


Figure 70. XPS survey scan of CS 1-5 heat treated to 1500°C, 3 h.

Narrow scans of each element peaks are examined for area fitting. It must be noted that only the sensitive peaks of each element are chosen. Sensitive peaks are peaks that have high intensity and if possible, do not overlap with other peaks e.g. cerium sensitive peaks are Ce 3d peaks [166-171]. Once the area of the sensitive peaks is measured, the relative sensitivity factor (RSF) is used to scale the measured peaks so variations in the peak areas are representative of the amount of material in the sample surface [170, 172]. Variations in peak areas occur because the electrons in an element can emerge from various energy levels, therefore, the peak areas measured must be scaled to ensure the same quantity.

A narrowed scan of CS 1-5 heat treated to 1550°C, 3 h is shown in Figure 71. Elements chosen for the narrowed scan were Ce, O and P. The peak fitting for area measurement is used for percentage atomic ratio calculation. As a result, the percent atomic ratio of Ce:P:O was 15.2:18.3:66.5 with a standard deviation of 2 atomic %. The ratio is close to 1:1:4 confirming that it is $CePO_4$. Satellite peaks are labelled "Sat." and arise from hybridization between O 2p and Ce 4f sub-level. The XPS result is useful for further work, where emissivity is enhanced by doping other rare earth elements, for instance lanthanum (La), so XPS is one of the easiest ways to identify the success of doping [77].

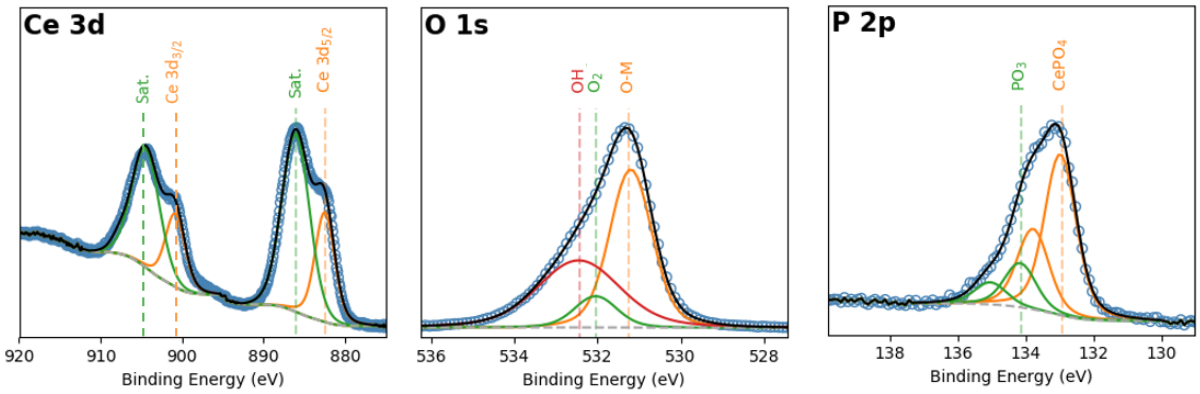


Figure 71. XPS narrow scans and peaks identified to be Ce, O, C and P and peak fitting for areas used for atom percentage calculation.

4.2.2.4 Scanning electron microscopy (SEM)

The microstructure of the 1:5-$CeO_2$: $AlH_6O_{12}P_3$ cross-section was analysed using SEM. Figure 72a clearly distinguished the coating and the substrate. Coating thickness was 280 ±15 µm measured from Figure 72a. The coating contained four features: pores, large grains (~10µm), small grains (~2µm) and a phase with a smoothed morphology indicative of melting (matrix). The four features are shown in Figure 72b. Pores are generated from dehydrogenation of $AlH_6O_{12}P_3$ at 500°C [173]. The large and small grains were identified by EDX analysis as $CeO_2$ and $CePO_4$ respectively (Figure 72c). Figure 73, shows a magnified image of the interface between the coating and the substrate. Figure 73a is in the same area as Figure 72b. Figure 73b is a magnified image from the red square in Figure 73a showing particles and matrix in the coating and part of the substrate. Figure 73c is a result of the EDX mapping of Figure 73b. The mapping revealed that the substrate in this area consists of Mg, Al and O which is $MgO{\cdot}Al_2O_3$ spinel. It also revealed that the particles consist of Ce and O and so are $CeO_2$. The matrix consists of Mg, Al, P and O. Al and P are from the binder. It must be noted that there was only a small trace of Al explaining why it was not detected by the XRD. O comes from both the binder and the

substrate. The presence of Mg and P is interesting. Mg is originally from the substrate, however, EDX mapping has shown that Mg can also be found in the matrix of the coating which leads to an assumption that Mg from the substrate diffuses into the coating. P behaves oppositely, where it is originally from the coating and diffused into the substrate.

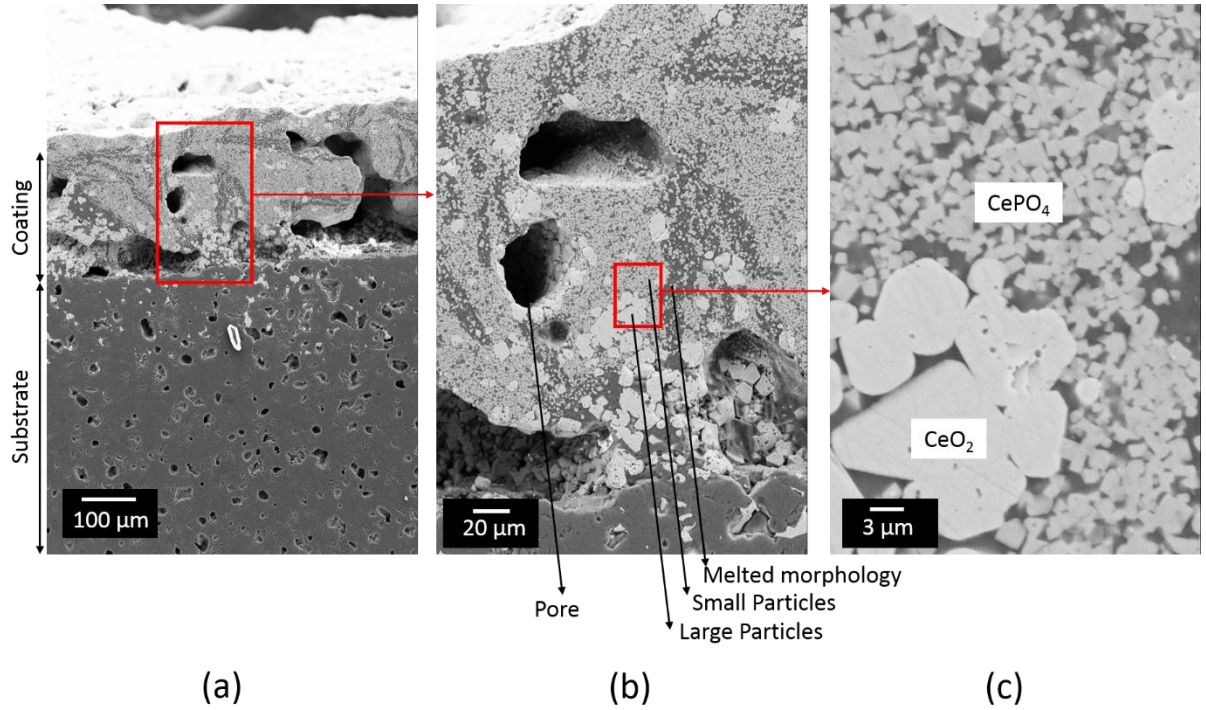


Figure 72. SEM images of CBR 1:5 vol. $CeO_2$: $AlH_6O_{12}P_3$ cross-section heat treated for 3h at 1300°C. a) Overview image of substrate and coating. b) Magnified image from boxed section shown in a) revealing pores, large grains (~10µm), small grains (~2µm) and a likely melt-formed phase. c) Magnified image from the boxed section shown in b) revealing large ($CeO_2$) and small grains ($CePO_4$) [174].

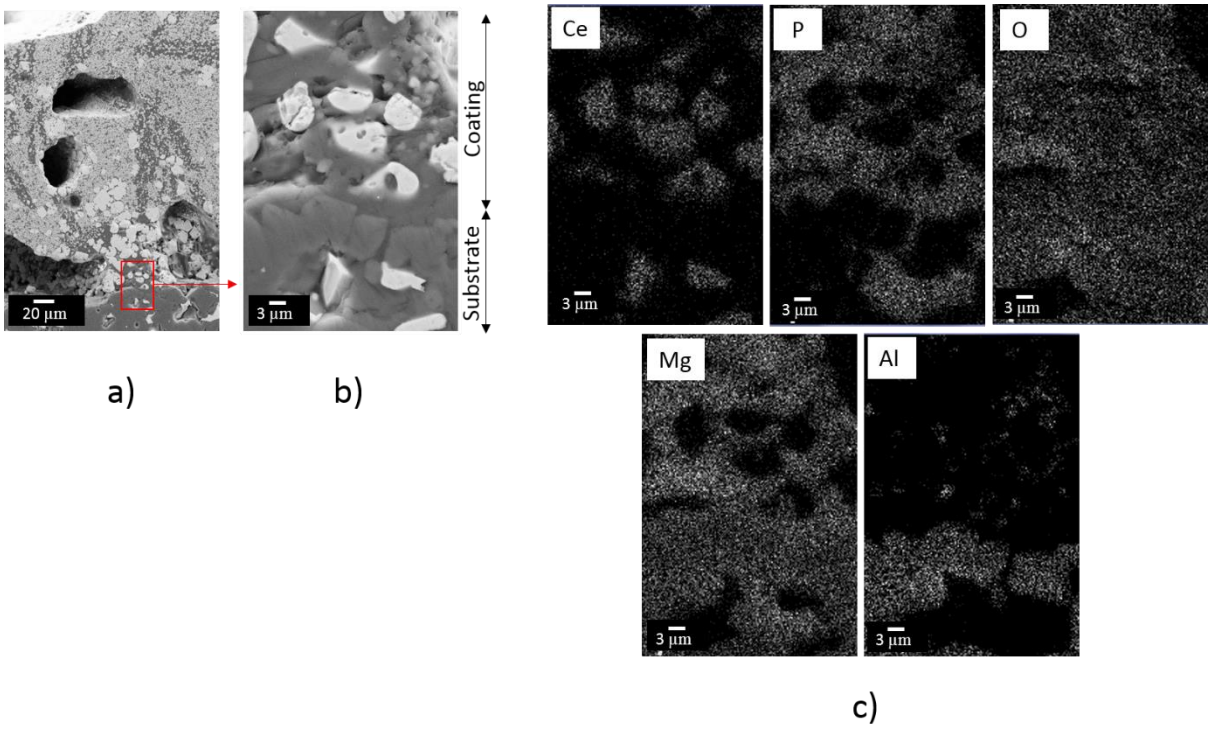


Figure 73. SEM image of CBR 1:5 vol. $CeO_2$: $AlH_6O_{12}P_3$ cross-section heat treated for 3h at 1300°C. a) Same area as Figure 72b. b) Magnified image from the boxed section shown in a), an area of the interface between substrate and coating. c) EDX mapping of b) revealing the substrate in this area is $MgO{\cdot}Al_2O_3$ and the coating consists of Ce-P-O and Al.

#### 4.2.2.5 Transmission electron microscopy (TEM)

The phase evolution of the coating was revealed by high temperature XRD and SEM (section 4.2.2.2 and 4.2.2.4) which showed that $CeO_2$ and $AlH_6O_{12}P_3$ react and form $CePO_4$ and a phase whose morphology is indicative of melting (matrix). However, it is still uncertain whether the matrix is single crystal, polycrystalline or amorphous. TEM (as described in section 3.2.3.5) is an instrument that can reveal this ambiguity. In the first scenario where the matrix has a single crystal structure, the TEM diffraction pattern would be a spot pattern. In the second scenario, if the matrix has a polycrystalline structure, TEM diffraction would give concentric rings. Lastly, if the matrix is amorphous, scattering in the TEM would give diffuse rings.

Microstructural characterisation was done using (S)TEM and EDX. The area selected contained small particles and matrix as shown in Figure 74a. In the figure, small particles are present as “P” and the matrix is present as “M”. EDX was used to conduct element mapping to determine chemical composition, Figure 74b, revealing that the particles contained Ce-P-O. Matching the EDX mapping with the XRD analysis revealed that the particles are $CePO_4$. As confirmed by electron diffraction

(Figure 74c). The d-spacings were 4.678Å and 4.118Å giving an axis close to $[01\bar{1}]$ and $[11\bar{1}]$ respectively for $CePO_4$. The plane angles were measured via image j program (open source image processing program [175]) giving the angle between these two planes to be in the range of 38-40°. When the data is compared with the $CePO_4$ reference pattern it reveals a match with $CePO_4$ monoclinic single crystal structure down the [001] zone axis. As for the matrix, EDX revealed that it contained Mg-P-O. While it is slightly surprising that Al was not detected, local variation in the matrix glass composition would be expected as the system is not at equilibrium. Figure 74d, the likely melted phase did not show any diffraction spots only diffuse rings confirming it has a glassy structure. Therefore, the melted phase is likely magnesium phosphate glass. It must be noted that while conducting this experiment, analysing the diffraction pattern must be done carefully and quickly because the electron beam energy leads to crystallisation of the amorphous structure with time (a few tens of seconds) as shown in Figure 75.

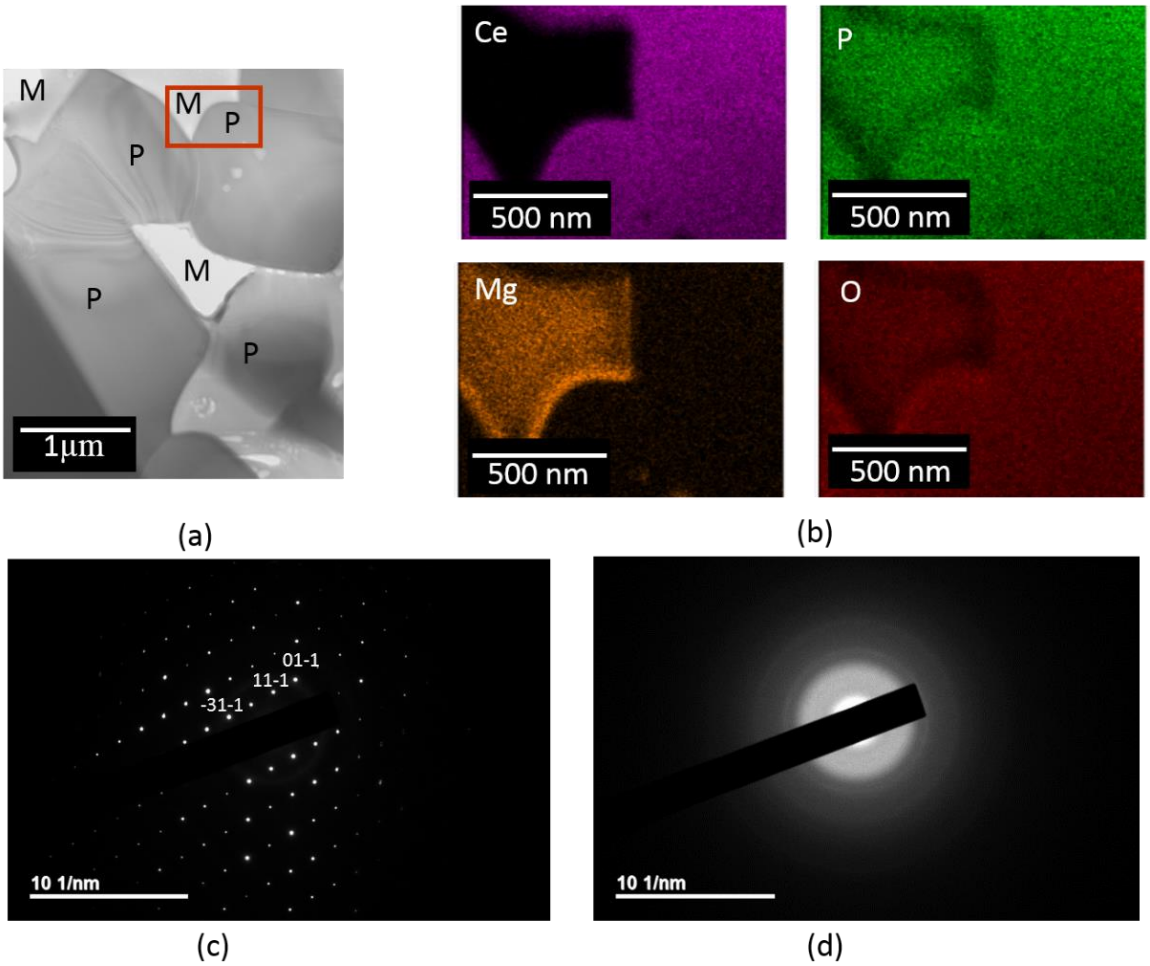


Figure 74. STEM-EDX microstructure of the coating 1-5 (a) STEM bright-field image of particles (P) and matrix (M) area. (b) EDX map of magnified (box) section shown in (a). (c) TEM diffraction pattern of $CePO_4$ particles (P). (d) Electron diffraction pattern of matrix indicating its glassy nature (M).

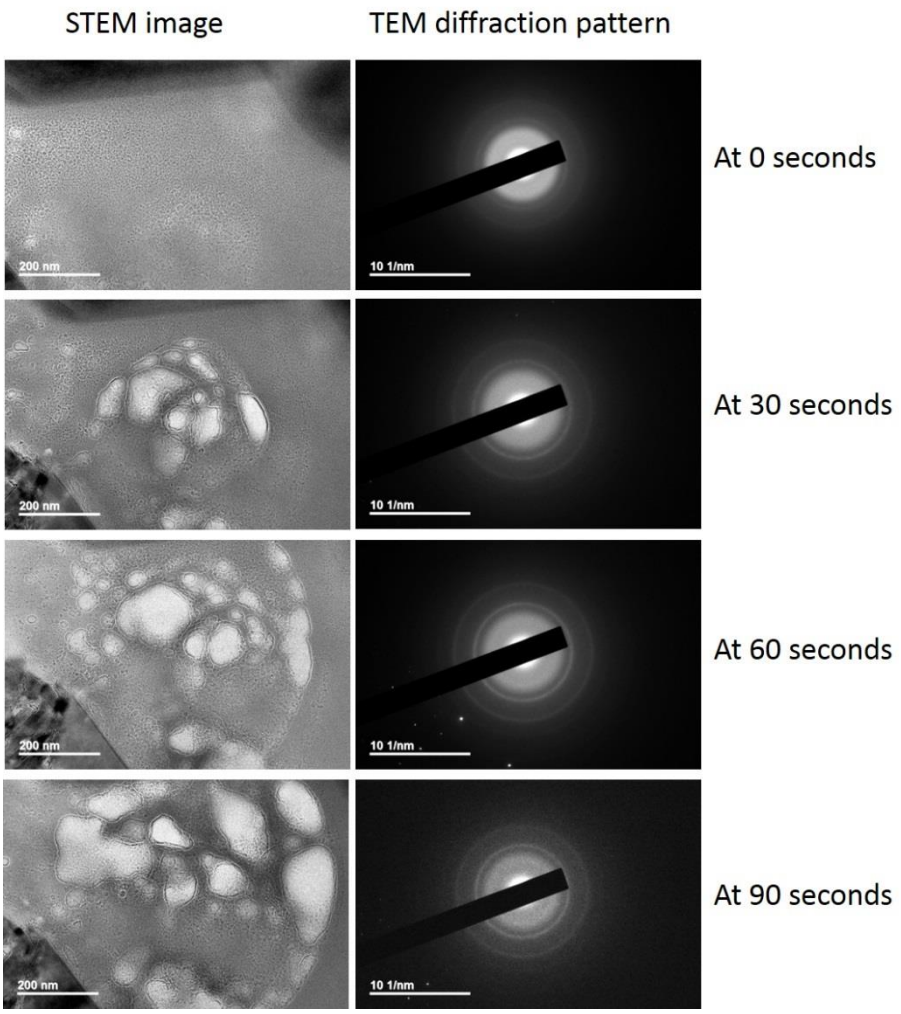


Figure 75. STEM and TEM diffraction pattern images of matrix crystallized as a function of time.

### 4.2.3 Coating density

The effect of two variables on density was examined: temperature and coating composition. Firstly, the effect on bulk density and apparent porosity of a sintered coating slurry pellet (SCSP) with a coating containing $CeO_2$: $AlH_6O_{12}P_3$ of 1:5 sintered at 800, 1000, 1200 and 1500°C for 3h was examined. Three samples of each pellet were measured for bulk density and apparent porosity following ASTM C20. Secondly, the effect on bulk density, apparent porosity and true density on the coating with different composition was examined which were $CeO_2$: $AlH_6O_{12}P_3$ of 1:3, 1:5 and 1:12. Samples were sintered to 1300°C, 3h, twenty measurements were made for true density and 3 measurements for bulk density and apparent porosity.

Images of samples after treatment at various temperatures are shown in Figure 76 which shows that bloating occurred when the coating pellets are sintered to 1000°C and more so at 1200°C. There were fewer signs of bloating for samples sintered at 1500°C. This correlates with the bulk density and apparent porosity results shown in Figure 77 and Figure 78. Bulk density decreases from 2.55 ±0.01 g/cm$^3$ to 2.39 ±0.05 g/cm$^3$ for sample sinters at 800°C and 1000°C. The bulk density continues to decrease to 2.23±0.08 g/cm$^3$ for sample sintered at 1200°C and becomes statistically stable for samples sintered at 1500°C. Apparent porosity gives an inverse result of bulk density. It increases from 47±0.24% to 53±0.75% for samples sintered at 800°C and 1000°C. It also continues to increase to 58±1.99 g/cm$^3$ for sample sintered at 1200°C and becomes statistically stable for samples sintered at 1500°C.

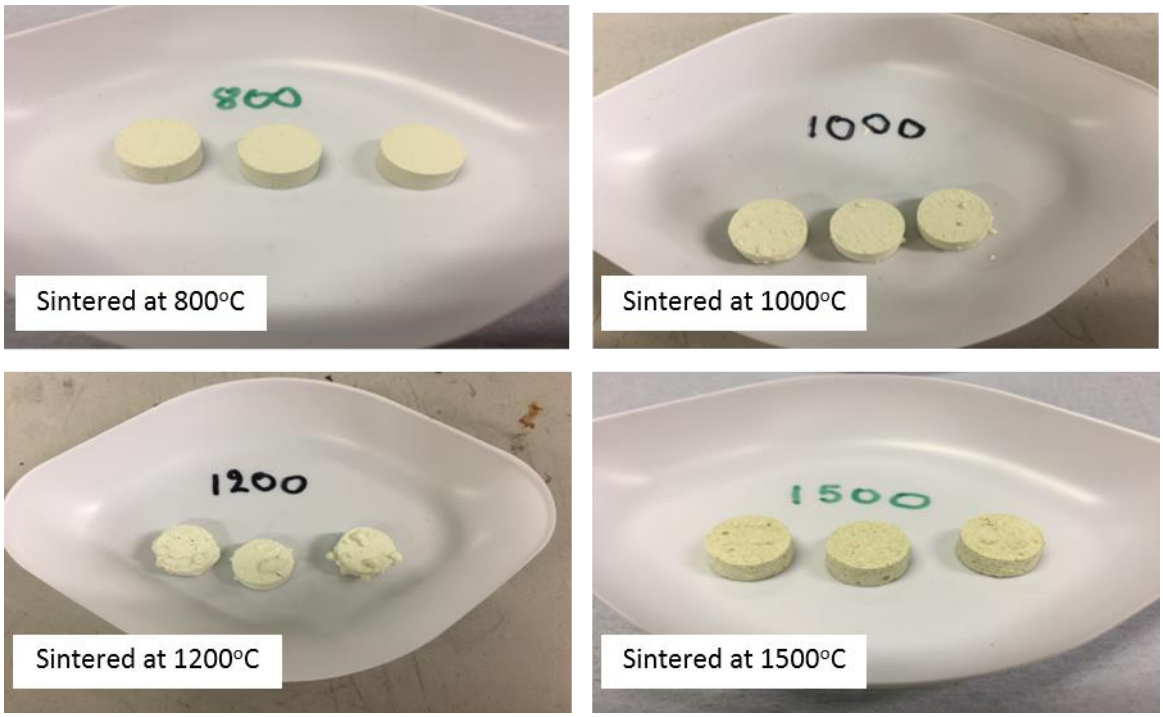


Figure 76. Sintered coating slurry pellet (SCSP) of coating containing $CeO_2$:$AlH_6O_{12}P_3$ of 1:5 (SCSP 1-5) images after sintering at different temperatures (author's figure).

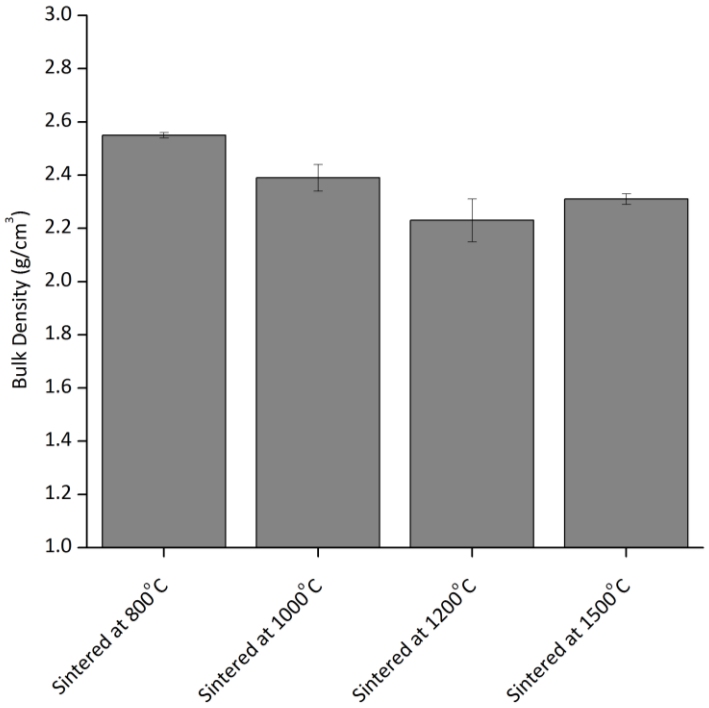


Figure 77. Sintered coating slurry pellet (SCSP) of coating containing $CeO_2$:$AlH_6O_{12}P_3$ of 1:5 (SCSP 1-5) bulk density (g/cm$^3$) sintered at different temperatures.

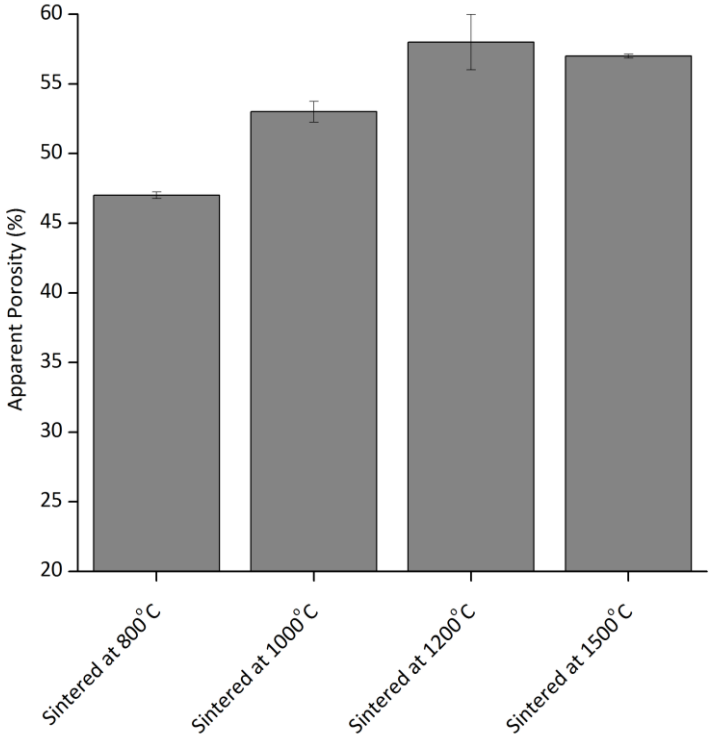


Figure 78. Sintered coating slurry pellet (SCSP) of coating containing $CeO_2$:$AlH_6O_{12}P_3$ of 1:5 (SCSP 1-5) apparent porosity (%) sintered at different temperatures.

Varying coating composition results for bulk density, apparent porosity and true density of sintered coating slurry pellets of a coating containing $CeO_2$: $AlH_6O_{12}P_3$ of 1:3, 1:5 and 1:12 (SCSP 1-3, 1-5 and 1-12) sintered at 1300°C, 3h are presented in Figure 79, Figure 80 and Figure 81 respectively. bulk density, apparent porosity results revealed that both SCSP 1-3 and SCSP 1-5 gave bulk density about 2.37 ± 0.05 g/cm$^3$ but SCSP 1-12 gave a much lower density of 1.09 ±0.05 g/cm$^3$. All samples had about the same apparent porosity of 54 vol%. This makes sample SCSP 1-12 interesting because it has the lowest density but the same apparent porosity as the other compositions. This indicates that pores in the SCSP 1-12 sample are closed. The true density of coating slurry 1-3, 1-5 and 1-12 sintered at 1300°C, 3h (Figure 81) show that the true density of all samples was 5.94 ± 0.04 g/cm$^3$. This indicates that coating composition has little to no effect on true density.

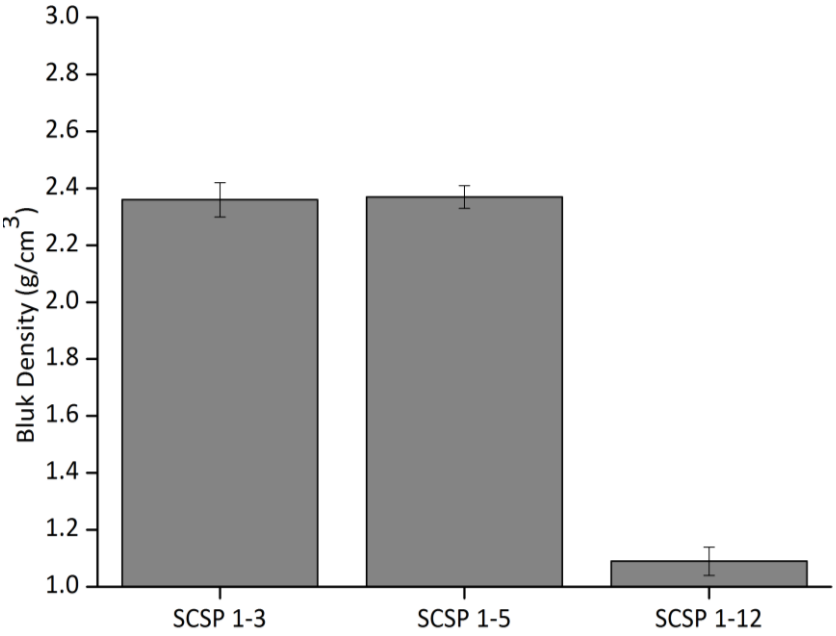


Figure 79. Sintered coating slurry pellet (SCSP) with $CeO_2$:$AlH_6O_{12}P_3$ ratio of 1:3, 1:5 and 1:12 (SCSP 1-3, 1-5 and 1-12) sintered at 1300°C, 3 h, bulk density.

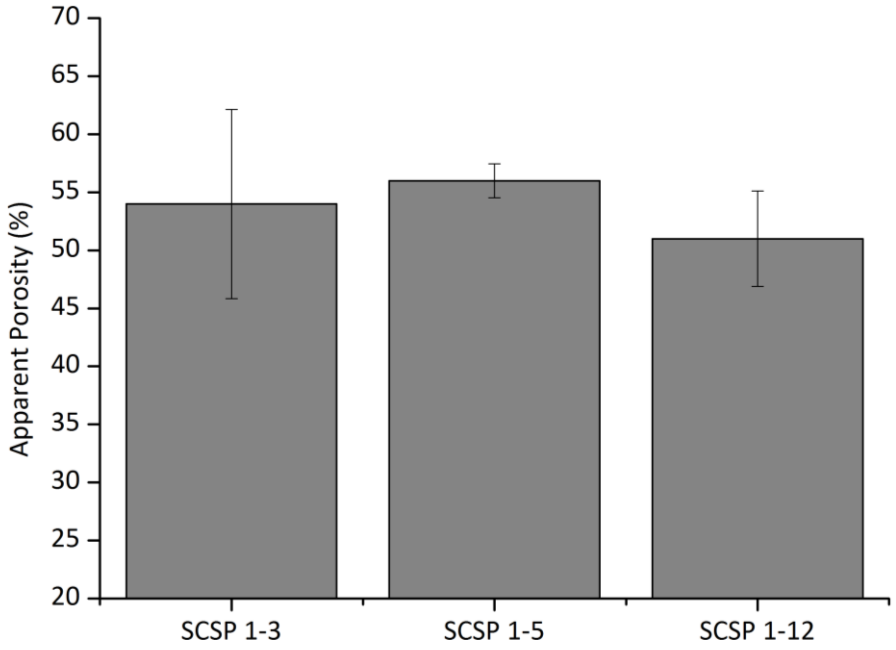


Figure 80. Sintered coating slurry pellet (SCSP) with $CeO_2$:$AlH_6O_{12}P_3$ ratio of 1:3, 1:5 and 1:12 (SCSP 1-3, 1-5 and 1-12) sintered at 1300°C, 3h, apparent porosity.

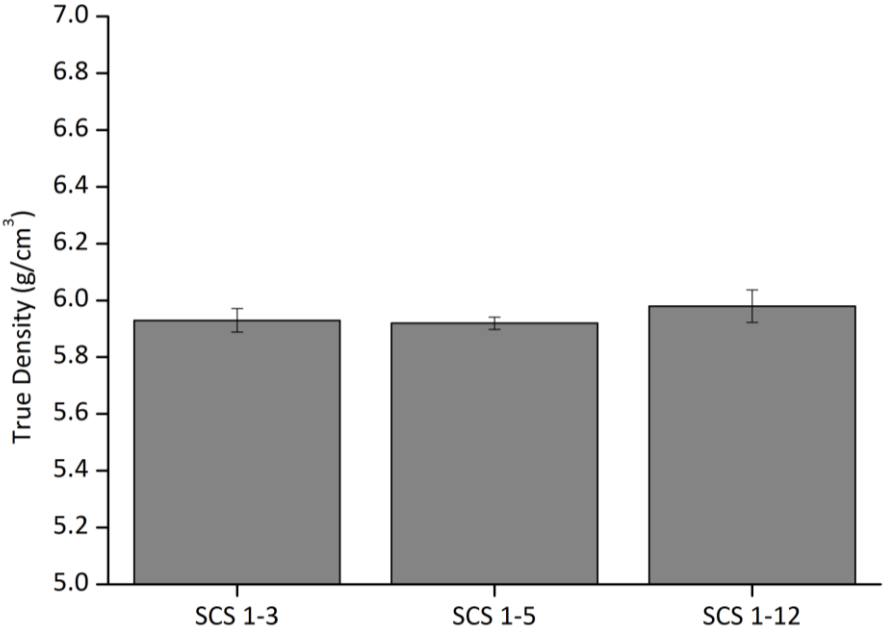


Figure 81. Sintered coating slurry pellet (SCSP) with $CeO_2$:$AlH_6O_{12}P_3$ ratio of 1:3, 1:5 and 1:12 (SCSP 1-3, 1-5 and 1-12) sintered at 1300°C, 3h, true density.

## 4.3 Discussion

This section discusses the coatings evolution with temperature, their microstructures and composition dependence.

### 4.3.1 Coating evolution with temperature

Coating phases present at different temperatures revealed by HT-XRD, XRD combined with DSC results are summarized in Figure 82. According to the DSC results (section 4.2.2.1), the endotherms of area 1 from Figure 63 and Figure 64 are from water vaporizing and dehydrogenation of $AlH_6P_3O_{12}$ which becomes $AlH_2P_3O_{10}$ [162]. $AlH_2P_3O_{10}$ dehydrogenation occurs at 500°C and it becomes $Al(PO_3)_3$ [162] This reaction is also an endothermic reaction, however, it falls in area 2 in Figure 63 and Figure 64 which is exothermic. This arises because there is a simultaneous exothermic reaction between $CeO_2$ and $Al(PO_3)_3$ (product of $AlH_6O_{12}P_3$ dehydrogenation) forming $Ce(PO_3)_3$ and $CePO_4$ which has a higher influence on the overall heat flux in the system. At about 930°C, $Ce(PO_3)_3$ transforms to $CePO_4$ and released $P_2O_5$ (gas) [163, 176]. Even though these are endothermic reactions, their influence is not as strong as the reaction forming $CePO_4$ which is exothermic. However, they are strong enough to reduce the overall peak of 2 areas. DSC indicates that $CePO_4$ starts forming around 500°C, however, it was observable at about 800°C from the HT-XRD. The reason is that the two measurements were conducted at a different heating rate, DCS at 5°C/min and HT-XRD at 10°C/min, and slower rates lead to a lower reaction temperature. $CePO_4$ formation continues and becomes almost complete at about 1500°C from the HT-XRD where $CeO_2$ can hardly be observed at 1500°C (section 4.2.2.2). XPS reveals only $Ce^{3+}$ peaks and not the $Ce^{4+}$ peaks in samples sintered to 1550°C (section 4.2.2.3). Density decreased in samples sintered to 1200°C due to the water vaporization and all the dehydrogenation mentioned earlier. The density stops decreasing at a temperature higher than 1200°C indicating that gases (pores) are no longer generated. Apparent porosity results show the opposite trend to bulk density. The reactions that generate an exotherm in the temperature range of 230-500°C are still ambiguous due to overlapping reactions.

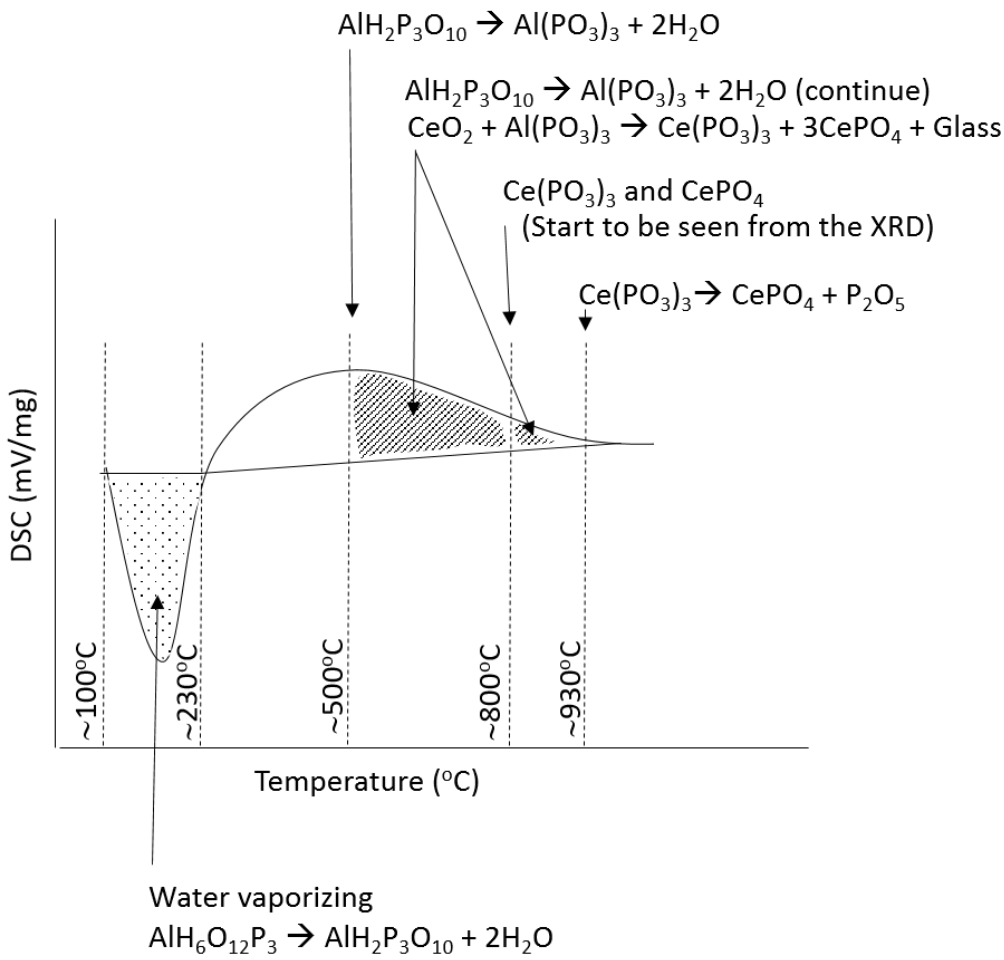


Figure 82. Summary schematic of DSC results explained using previous work [162, 163], HT-XRD and XRD results. Dotted area represents area 1. Striped area represents area 2 whose reactions can be explained. White area represents area 2 in which reactions are ambiguous due to overlapping reactions (author's figure).

### 4.3.2 Coating microstructural evolution

At room temperature, the coating applied to the substrate contained only two phases: $CeO_2$ and $AlH_6P_3O_{12}$. After the coating is heat treated at 1300°C, 3h several reactions occurred as discussed in section 4.3.1 affecting the microstructure of the coating. SEM revealed, four phases after heat treatment; large particles of $CeO_2$ (~10µm), small particles (~2µm) of $CePO_4$, pores generated from the releasing gases ($H_2O$ and $P_2O_5$) and glassy phase. XRD revealed that $CeO_2$ has a cubic structure while $CePO_4$ is monoclinic (Table 10) and a schematic image of these structures is presented in Figure 83. The glassy phase is known to mainly contain Mg-P-O from the TEM and EDS analysis (Figure 74). P-O is normally present in a phosphate form which is a tetrahedral as shown in Figure 84a. $Mg^{2+}$ is a

divalent cation and when it is present in the phosphate structure, it serves as an ionic cross-link between the two phosphates as present in Figure 84b, and a schematic overview of the structure is shown in Figure 85 [177].

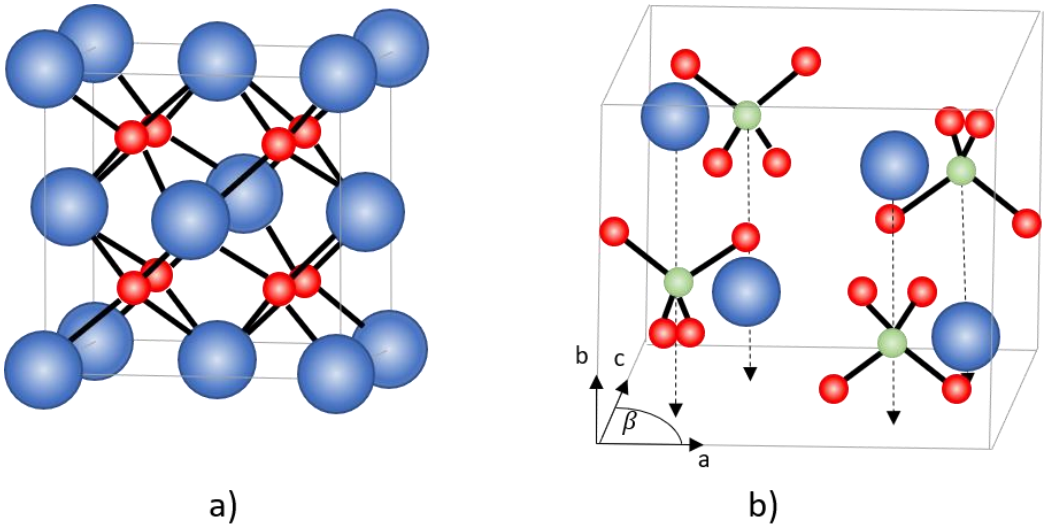


Figure 83. Structure of a) Cubic $CeO_2$: blue spheres are cerium and red spheres are oxygen (modify from [178]). b) monoclinic $CePO_4$: blue spheres are cerium, green spheres are phosphorus and red spheres are oxygen (modify from [179]).

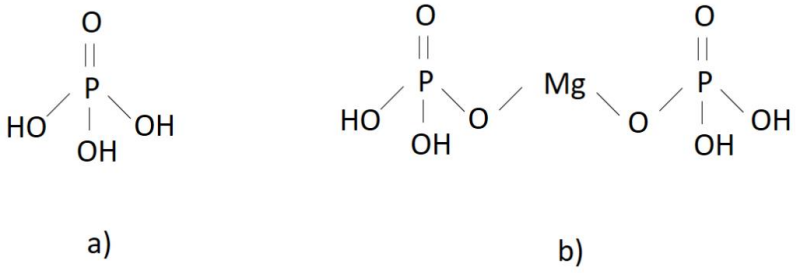


Figure 84. Schematic image of phosphate structure a) is an orthophosphate structure and b) is a phosphate structure linked with Mg cation (author's figure).

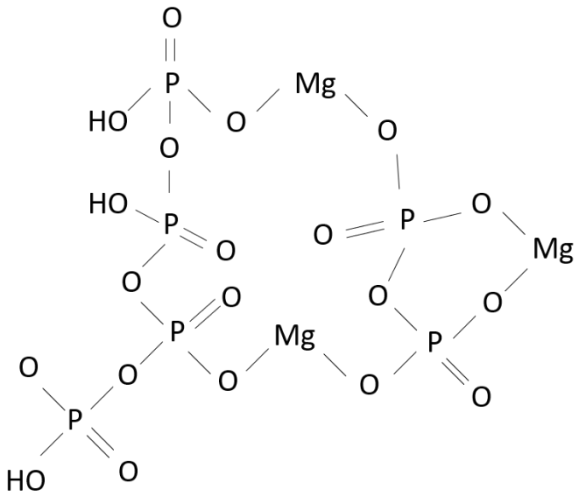


Figure 85. Schematic of M-P-O glass structure where the phosphate is from an orthophosphate structure and some of these are randomly linked with Mg cations (author's figure).

### 4.3.3 Coating composition dependence

Coating with different ratios of $CeO_2$ and $AlH_6O_{12}P_3$ affected rheology, $CePO_4$ formation, density and cost. High solid ($CeO_2$ particles) content gives a high viscosity slurry. All coatings (CBR 1-3, 1-5 and 1-12) could be applied via the air spraying technique assisted by their shear thinning behaviour as explained in section 3.2.2. Solid content also influences $CePO_4$ formation. XRD results (Figure 69) revealing that the higher the ratio between $CeO_2$ to $AlH_6O_{12}P_3$, the lower the amount of $CePO_4$ is formed and the more un-reacted $CeO_2$ remains. The true density of the coatings was about 16.5% higher than $CePO_4$ density (5.15 g/cm$^3$) indicating that excluding pores, the coating density is mostly from $CePO_4$. The reason that it's higher than the average $CePO_4$ density is that the coating also contains some $CeO_2$ which has a higher density of 7.22 g/cm$^3$ and has a greater influence than the Mg-P-O glass which has a density of about 2.5 g/cm$^3$ [180]. To calculate exact densities further experiments are needed as discussed in chapter 9. The bulk density is much lower than the true density because the samples contain pores generated from water vapour and $P_2O_5$ gas as discussed in section 4.3.1.

The amount of solid loading also affects the cost of the coating. In 2020, the laboratory grade cerium (IV) oxide, 99.5% (REO) supplied by Alfa Aesar, Heysham, Lancashire, England cost about 1 £/g and $AlH_6O_{12}P_3$ 50 wt% aqueous solution supplied from Alfa Aesar, Heysham, Lancashire, UK about 0.05 £/g. The density of $CeO_2$ (7.22 g/cm$^3$) and $AlH_6O_{12}P_3$ (1.50 g/cm$^3$) were used to convert the prices to pound per cubic centimetres (£/cm$^3$) which $CeO_2$ is 7.22 £/cm$^3$ and $AlH_6O_{12}P_3$ is 0.08 £/cm$^3$. To

calculate the coating price, the volume of the coating needed to cover the cement kiln upper transition zone is required. The upper transition zone area is calculated by $2\pi rh$, where r is the kiln radius and h is the length of the upper transition zone. An average kiln size is about 4 metres diameter [4, 9, 181]. Rotary kiln shell thickness can vary from 0.015-0.050 m, this calculation used an approximate average of 0.03 m thick and refractory bricks is generally 0.22 m thick. The inner diameter, where the coating is aimed to be applied, is therefore 3.50 metres (1.75 metres radius). The length of the upper transition zone is approximated about 3 times longer than the outer diameter, which in this case is 12 metres. Dimensions of the rotary kiln are shown in Figure 86. Assuming the coating thickness to be 120 μm, therefore, the volume of the coating needed in this assumption is 0.015840 $m^3$ (15,840 $cm^3$), the upper transition refractory inner-surface area multiplies with the coating thickness. The prices of coatings containing $CeO_2$: $AlH_6O_{12}P_3$ 1:3, 1:5 and 1:12 are calculated from Equation 64 and are presented in Table 13. The coating price decrease with the decrease of $CeO_2$: $AlH_6O_{12}P_3$ ratio. Even though $CeO_2$ is the most abundant rare earth, its price is still high. The amount of $CeO_2$ used must be considered cautiously. If the cost of the coating is too expensive, it might not be worth using for energy saving. This topic will be discussed further in section 5.3.3.

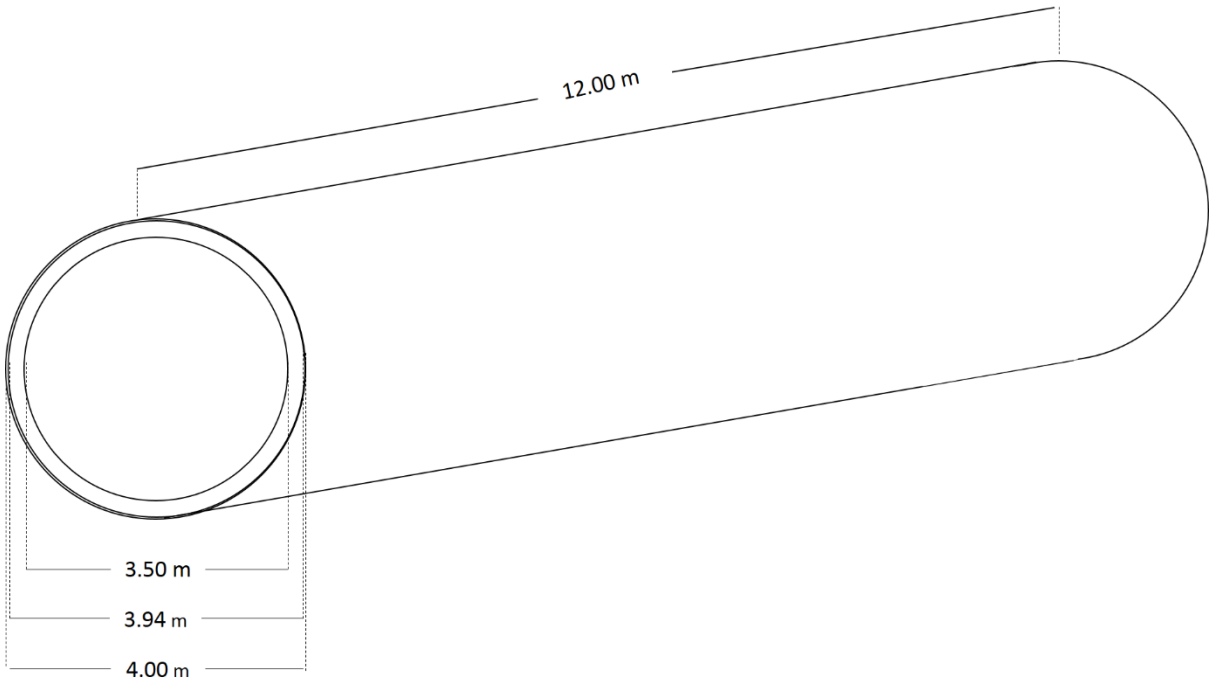


Figure 86. Kiln size used for coating cost calculation (author's figure).

Equation 64. $$(\frac{Fraction\ \ coating\ volume}{Total\ coating\ volume})\cdot(Volume\ in\ cm^3)\cdot(Price\ in\ £/cm^3)$$

Table 13. Calculations of coating costs at different $CeO_2$: $AlH_6O_{12}P_3$ ratios.

| Coating code | $CeO_2$ fraction coating volume | $AlH_6O_{12}P_3$ fraction coating volume | Total Coating volume | $CeO_2$ price (£) | $AlH_6O_{12}P_3$ price (£) | Total price (£) |
|---|---|---|---|---|---|---|
| CS 1-3 | 1 | 3 | 4 | $(\frac{1}{4})\cdot(15840)\cdot$ (7.22) = 28,591 | $(\frac{3}{4})\cdot(15840)\cdot$ (0.08) = 891 | 29,482 |
| CS 1-5 | 1 | 5 | 6 | $(\frac{1}{6})\cdot(15840)\cdot$ (7.22) = 19,061 | $(\frac{5}{6})\cdot(15840)\cdot$ (0.08) = 990 | 20,051 |
| CS 1-12 | 1 | 12 | 13 | $(\frac{1}{12})\cdot(15840)\cdot$ (7.22) = 8,797 | $(\frac{12}{13})\cdot(15840)\cdot$ (0.08) = 1,097 | 9,894 |

# Chapter 5: Emissivity results from coatings on refractory brick.

As described in chapter 3, emissivity was measured using two methods: REM and IREM. The REM measurements were done on four samples (two for each) which were basic refractory (BR) and three coated basic refractories where the coatings contain different volume ratio of $CeO_2$: $AlH_6O_{12}P_3$; 1:3, 1:5 and 1:12 (CBR 1-3, CBR 1-5 and CBR 1-12). Sample preparation was explained in section 3.2.1. The emissivity was measured using the thermal return reflection (TRR) technique at 137Hz, the significance of this frequency was explained in the first paragraph in section 3.3. IREM measurements were done on six samples (one of each) which were BR, CBR 1-3, CBR 1-5, CBR 1-12, thick CBR 1-5 (TCBR 1-5) and a sintered $CeO_2$ pellet. Emissivity was measured using IREM with two spectrometers over wavenumbers ranging 700-12000 $cm^{-1}$.

## 5.1 Radiometer emissivity measurement method (REM)

Following the REM measurement procedure (summarized at the end of section 3.3.1), two voltage signals are collected, one from receiver 1 and the other from receiver 2. Plotting the two voltage signals against time gives a graph where $V_r$, $V_c$, $V_s$ values can be collected. CBR 1-3 is chosen as an example of how the values are collected. CBR 1-3 voltage signals plotted against time are present in Figure 87. The blue signal represents the signal from receiver 1 and the red signal represents the signal from receiver 2. The raw signal from receiver 1 is higher than 2 because receiver 2 reads only a part of the signal that was reflected by the beam splitter in front of receiver 2. A magnified image of the red square in Figure 87 is shown in Figure 88 to demonstrate where $V_r$, $V_c$ and $V_s$ values are determined. Knowing these values and room temperature ($T_r$) and calibrated temperature ($T_c$, liquid nitrogen temperature (77K, -196°C)) the signal voltage can be converted to temperature from Equation 56 and Equation 60 from section 3.3.1. $V_r$, $V_c$ and $T_r$ measured values are shown in Table 14.

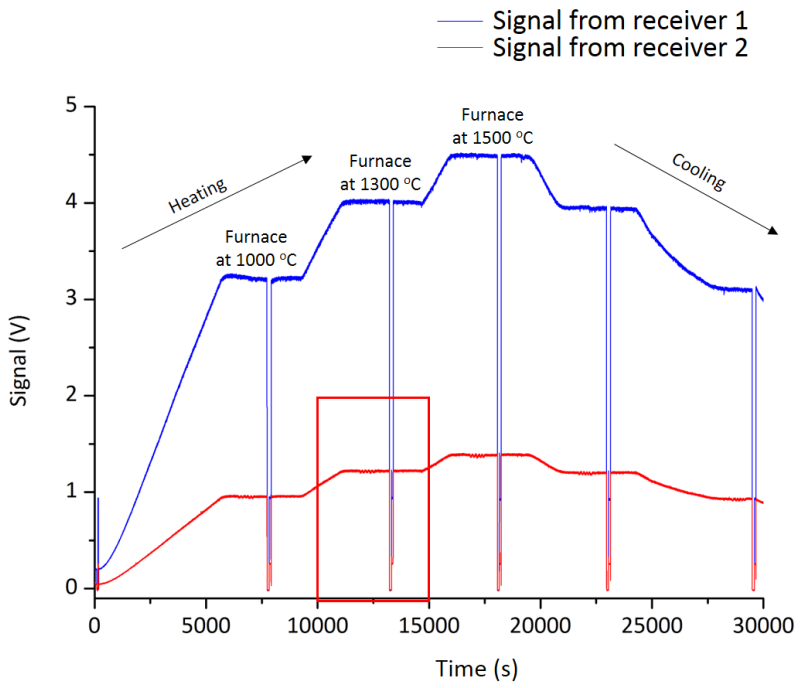


Figure 87. CBR 1-3 signal (y-axis) for heating and cooling cycle with time (x-axis). Blue signal is a signal received from receiver 1 and the red signal is signal received from receiver 2.

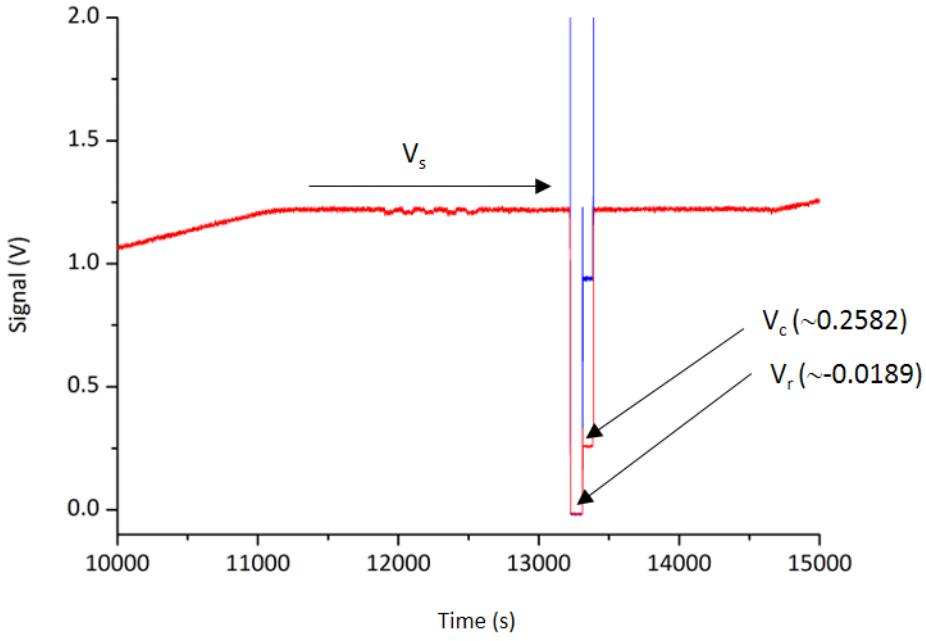


Figure 88. Magnified image of the red square of Figure 87 showing where $V_r$, $V_c$ and $V_s$ values are collected.

Table 14. $T_r$, $V_r$ and $V_c$ values of BR, CBR1-3, CBR 1-5 and CBR 1-12, at 1000, 1300 and 1500°C during heating (H) and cooling (C) are presented. Two of each sample were measured and represented as sample number 1 and 2.

| Sample Name | Sample Number | Furnace temperature, °C | $T_r$ ±1°C | $V_r$ ±0.0012V | $V_c$ ±0.0025V |
|---|---|---|---|---|---|
| BR | 1 | 1000 (H) | 23.0 | -0.0181 | 0.2502 |
| | | 1300 (H) | 23.6 | -0.0176 | 0.2518 |
| | | 1500 | 23.9 | -0.0171 | 0.2534 |
| | | 1300 (C) | 23.7 | -0.0170 | 0.2538 |
| | | 1000 (C) | 23.3 | -0.0184 | 0.2596 |
| CBR 1-3 | 1 | 1000 (H) | 24.3 | -0.0187 | 0.2580 |
| | | 1300 (H) | 24.9 | -0.0189 | 0.2582 |
| | | 1500 | 25.5 | -0.0187 | 0.2571 |
| | | 1300 (C) | 25.3 | -0.0170 | 0.2559 |
| | | 1000 (C) | 25.0 | -0.0168 | 0.2545 |
| CBR 1-5 | 1 | 1000 (H) | 23.0 | -0.0140 | 0.2534 |
| | | 1300 (H) | 23.0 | -0.0140 | 0.2534 |
| | | 1500 | 23.0 | -0.0140 | 0.2534 |
| | | 1300 (C) | 23.0 | -0.0140 | 0.2534 |
| | | 1000 (C) | 23.0 | -0.0140 | 0.2534 |
| CBR 1-12 | 1 | 1000 (H) | 25.0 | -0.0166 | 0.2548 |
| | | 1300 (H) | 25.6 | -0.0189 | 0.2552 |
| | | 1500 | 26.8 | -0.0182 | 0.2517 |
| | | 1300 (C) | 24.5 | -0.0120 | 0.2555 |
| | | 1000 (C) | 24.3 | -0.0120 | 0.2582 |
| BR | 2 | 1000 (H) | 25.0 | -0.0191 | 0.2572 |
| | | 1300 (H) | 26.3 | -0.0185 | 0.2572 |
| | | 1500 | 26.9 | -0.0186 | 0.2556 |
| | | 1300 (C) | 26.5 | -0.0190 | 0.2546 |
| | | 1000 (C) | 25.4 | -0.0189 | 0.2554 |
| CBR 1-3 | 2 | 1000 (H) | 25.1 | -0.0185 | 0.2620 |
| | | 1300 (H) | 25.8 | -0.0131 | 0.2620 |
| | | 1500 | 27.7 | -0.0179 | 0.2613 |
| | | 1300 (C) | 26.5 | -0.0184 | 0.2586 |
| | | 1000 (C) | 24.8 | -0.0190 | 2.604 |
| CBR 1-5 | 2 | 1000 (H) | 24.6 | -0.0184 | 0.2650 |
| | | 1300 (H) | 26.3 | -0.0187 | 0.2656 |
| | | 1500 | 27.5 | -0.0182 | 0.2640 |
| | | 1300 (C) | 27.6 | -0.0179 | 0.2662 |
| | | 1000 (C) | 26.8 | -0.0183 | 0.2691 |
| CBR 1-12 | 2 | 1000 (H) | 24.8 | -0.0190 | 0.2600 |
| | | 1300 (H) | 25.8 | -0.0185 | 0.2580 |
| | | 1500 | 27.2 | -0.0177 | 0.2567 |
| | | 1300 (C) | 27.8 | -0.0178 | 0.2563 |
| | | 1000 (C) | 27.8 | -0.0175 | 0.2578 |

The $V_s, V_r$, $V_c$, $T_c$ and $T_r$ values are used to calculate temperature ($T_{eff}, T'_{eff}$). The same sample of CBR1-3 is used as an example of a temperature and time profile Figure 89. Figure 90 is the red square area in Figure 89 magnified when the furnace is heated to 1300°C . The graph presents the time (x-axis) from 11700-12800 s and the calculated temperature (y-axis) from 1000-1250°C. Over these ranges 5 $T_{eff}$ and 5 $T'_{eff}$ values are presented, acquired by pulling the removable reflective mirror in and out 5 times. The $T_{eff}$ 1-5 and $T'_{eff}$ 1-5 were paired up as $T_{eff}$ 1 with $T'_{eff}$ 1 , $T_{eff}$ 2 with $T'_{eff}$ 2, and so on to calculate the reflectivity of the sample ($r_s$) using Equation 61. $r_s$ was used to calculate emissivity (ε) with Equation 50. $T_{eff}$ , $T'_{eff}$, $r_s$ and ε values of all the samples are shown in Table 15 and Table 16.

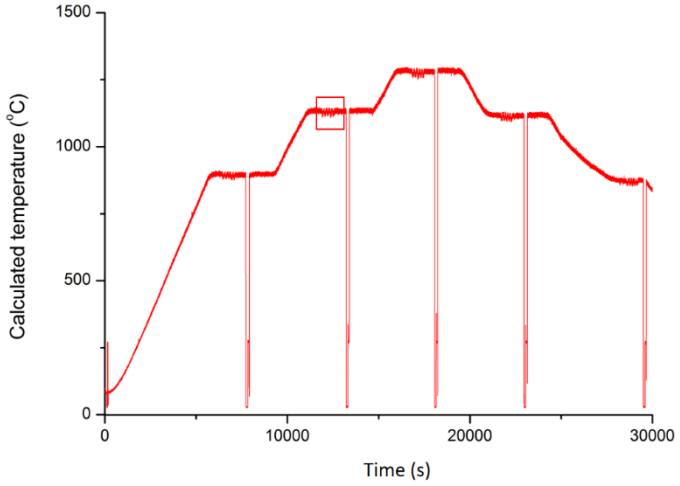


Figure 89. CBR 1-3 calibrated temperature versus time when furnace temperature is at 1300°C.

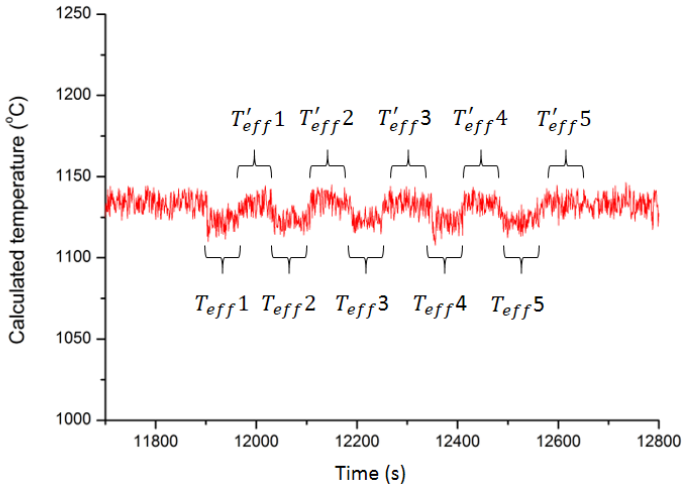


Figure 90. Magnified image in the red square of Figure 89 showing where the removable mirror was pulled out and in 5 times giving $T_{eff}$ and $T'_{eff}$.

Table 15. $T_{eff}$ , $T'_{eff}$, $r_s$ and ε values of BR, CBR1-3, CBR 1-5 and CBR 1-12, sample 1 and 2 , at 1000, 1300 and 1500°C during heating (H) and cooling (C) are presented. S/S No. 1 /T represents sample name/ sample number / temperature. M No. represents measurement number. The standard deviation of $T_{eff}$ and $T'_{eff}$ is ±6.

| S/ S No. /T | M No. | $T_{eff}$ | $T'_{eff}$ | $r_s$ | ε |
|---|---|---|---|---|---|
| BR / 1 / 1000°C (H) | 1 | 887 | 907 | 0.15 | 0.85 |
| | 2 | 886 | 897 | 0.09 | 0.91 |
| | 3 | 878 | 899 | 0.17 | 0.83 |
| | 4 | 875 | 889 | 0.11 | 0.89 |
| | 5 | 870 | 895 | 0.20 | 0.80 |
| BR / 1 / 1300°C (H) | 1 | 1135 | 1160 | 0.15 | 0.85 |
| | 2 | 1139 | 1163 | 0.15 | 0.86 |
| | 3 | 1141 | 1164 | 0.14 | 0.86 |
| | 4 | 1137 | 1163 | 0.15 | 0.85 |
| | 5 | 1141 | 1165 | 0.14 | 0.86 |
| BR / 1 / 1500°C | 1 | 1286 | 1304 | 0.10 | 0.90 |
| | 2 | 1284 | 1312 | 0.14 | 0.86 |
| | 3 | 1286 | 1311 | 0.13 | 0.87 |
| | 4 | 1288 | 1313 | 0.13 | 0.87 |
| | 5 | 1288 | 1310 | 0.12 | 0.88 |
| BR / 1 / 1300°C (C) | 1 | 1146 | 1146 | 0.13 | 0.87 |
| | 2 | 1144 | 1144 | 0.14 | 0.86 |
| | 3 | 1150 | 1150 | 0.11 | 0.89 |
| | 4 | 1151 | 1151 | 0.09 | 0.91 |
| | 5 | 1151 | 1151 | 0.11 | 0.89 |
| BR / 1 / 1000°C (C) | 1 | 886 | 909 | 0.12 | 0.88 |
| | 2 | 886 | 901 | 0.11 | 0.89 |
| | 3 | 886 | 901 | 0.12 | 0.88 |
| | 4 | 886 | 901 | 0.11 | 0.89 |
| | 5 | 885 | 901 | 0.12 | 0.88 |
| CBR 1-3 / 1 / 1000°C (H) | 1 | 889 | 899 | 0.07 | 0.93 |
| | 2 | 889 | 897 | 0.07 | 0.93 |
| | 3 | 889 | 899 | 0.07 | 0.93 |
| | 4 | 887 | 897 | 0.08 | 0.92 |
| | 5 | 887 | 895 | 0.06 | 0.94 |
| CBR 1-3 / 1 / 1300°C (H) | 1 | 1123 | 1134 | 0.07 | 0.93 |
| | 2 | 1124 | 1136 | 0.08 | 0.92 |
| | 3 | 1124 | 1134 | 0.06 | 0.94 |
| | 4 | 1123 | 1135 | 0.07 | 0.93 |
| | 5 | 1123 | 1134 | 0.07 | 0.93 |
| CBR 1-3 / 1 / 1500°C | 1 | 1275 | 1289 | 0.08 | 0.92 |
| | 2 | 1275 | 1288 | 0.07 | 0.93 |
| | 3 | 1270 | 1287 | 0.09 | 0.91 |
| | 4 | 1272 | 1286 | 0.08 | 0.92 |
| | 5 | 1272 | 1287 | 0.08 | 0.92 |
| CBR 1-3 / 1 / 1300°C (C) | 1 | 1122 | 1135 | 0.08 | 0.92 |
| | 2 | 1123 | 1136 | 0.08 | 0.92 |
| | 3 | 1122 | 1134 | 0.08 | 0.92 |
| | 4 | 1122 | 1133 | 0.07 | 0.93 |
| | 5 | 1117 | 1133 | 0.10 | 0.90 |
| CBR 1-3 / 1 / 1000°C (C) | 1 | 879 | 889 | 0.08 | 0.92 |
| | 2 | 878 | 888 | 0.08 | 0.92 |
| | 3 | 879 | 887 | 0.06 | 0.94 |
| | 4 | 879 | 890 | 0.07 | 0.93 |
| | 5 | 880 | 891 | 0.08 | 0.92 |

| S/ S No. /T | M No. | $T_{eff}$ | $T'_{eff}$ | $r_s$ | ε |
|---|---|---|---|---|---|
| CBR 1-5 / 1 / 1000°C (H) | 1 | 893 | 904 | 0.09 | 0.91 |
| | 2 | 894 | 903 | 0.07 | 0.93 |
| | 3 | 897 | 907 | 0.08 | 0.92 |
| | 4 | 898 | 908 | 0.08 | 0.92 |
| | 5 | 897 | 911 | 0.11 | 0.89 |
| CBR 1-5 / 1 / 1300°C (H) | 1 | 1155 | 1173 | 0.11 | 0.89 |
| | 2 | 1160 | 1173 | 0.08 | 0.92 |
| | 3 | 1161 | 1176 | 0.09 | 0.91 |
| | 4 | 1161 | 1179 | 0.10 | 0.90 |
| | 5 | 1162 | 1176 | 0.08 | 0.92 |
| CBR 1-5 / 1 / 1500°C | 1 | 1320 | 1341 | 0.11 | 0.89 |
| | 2 | 1317 | 1341 | 0.13 | 0.87 |
| | 3 | 1322 | 1336 | 0.07 | 0.93 |
| | 4 | 1318 | 1341 | 0.12 | 0.88 |
| | 5 | 1320 | 1341 | 0.11 | 0.89 |
| CBR 1-5 / 1 / 1300°C (C) | 1 | 1180 | 1192 | 0.07 | 0.93 |
| | 2 | 1177 | 1195 | 0.10 | 0.90 |
| | 3 | 1178 | 1194 | 0.09 | 0.91 |
| | 4 | 1181 | 1197 | 0.09 | 0.91 |
| | 5 | 1183 | 1197 | 0.08 | 0.92 |
| CBR 1-5 / 1 / 1000°C (C) | 1 | N/A | N/A | N/A | N/A |
| | 2 | N/A | N/A | N/A | N/A |
| | 3 | N/A | N/A | N/A | N/A |
| | 4 | N/A | N/A | N/A | N/A |
| | 5 | N/A | N/A | N/A | N/A |
| CBR 1-12 / 1 / 1000°C (H) | 1 | 923 | 933 | 0.07 | 0.93 |
| | 2 | 923 | 931 | 0.06 | 0.94 |
| | 3 | 922 | 933 | 0.08 | 0.92 |
| | 4 | 924 | 931 | 0.05 | 0.95 |
| | 5 | 921 | 930 | 0.07 | 0.93 |
| CBR 1-12 / 1 / 1300°C (H) | 1 | 1145 | 1158 | 0.08 | 0.92 |
| | 2 | 1144 | 1154 | 0.06 | 0.94 |
| | 3 | 1144 | 1155 | 0.07 | 0.93 |
| | 4 | 1141 | 1154 | 0.08 | 0.92 |
| | 5 | 1141 | 1152 | 0.07 | 0.93 |
| CBR 1-12 / 1 / 1500°C | 1 | 1306 | 1324 | 0.10 | 0.90 |
| | 2 | 1311 | 1323 | 0.06 | 0.94 |
| | 3 | 1314 | 1333 | 0.10 | 0.90 |
| | 4 | 1321 | 1337 | 0.08 | 0.92 |
| | 5 | 1325 | 1339 | 0.07 | 0.93 |
| CBR 1-12 / 1 / 1300°C (C) | 1 | 1131 | 1145 | 0.09 | 0.91 |
| | 2 | 1137 | 1149 | 0.07 | 0.93 |
| | 3 | 1139 | 1152 | 0.08 | 0.92 |
| | 4 | 1143 | 1151 | 0.05 | 0.95 |
| | 5 | 1140 | 1148 | 0.04 | 0.96 |
| CBR 1-12 / 1 / 1000°C (C) | 1 | 910 | 918 | 0.06 | 0.94 |
| | 2 | 906 | 916 | 0.08 | 0.92 |
| | 3 | 909 | 917 | 0.06 | 0.94 |
| | 4 | 911 | 918 | 0.05 | 0.95 |
| | 5 | 911 | 918 | 0.05 | 0.95 |

Table 16. $T_{eff}$ , $T'_{eff}$, $r_s$ and ε values of BR, CBR1-3, CBR 1-5 and CBR 1-12, sample 1 and 2, at 1000, 1300 and 1500°C during heating (H) and cooling (C) are presented. S/S No. 2 /T represents sample name/ sample number / temperature. M No. represents measurement number. The standard deviation of $T_{eff}$ and $T'_{eff}$ is ±6.

| S/ S No. /T | M No. | $T_{eff}$ | $T'_{eff}$ | $r_s$ | ε |
|---|---|---|---|---|---|
| BR / 2 / 1000°C (H) | 1 | 878 | 888 | 0.08 | 0.92 |
| | 2 | 876 | 889 | 0.10 | 0.90 |
| | 3 | 876 | 889 | 0.10 | 0.90 |
| | 4 | 877 | 887 | 0.08 | 0.92 |
| | 5 | 876 | 886 | 0.07 | 0.93 |
| BR / 2 / 1300°C (H) | 1 | 1149 | 1162 | 0.07 | 0.93 |
| | 2 | 1151 | 1162 | 0.07 | 0.93 |
| | 3 | 1152 | 1162 | 0.06 | 0.94 |
| | 4 | 1152 | 1165 | 0.08 | 0.92 |
| | 5 | 1151 | 1165 | 0.08 | 0.92 |
| BR / 2 / 1500°C | 1 | 1311 | 1333 | 0.11 | 0.89 |
| | 2 | 1318 | 1331 | 0.07 | 0.93 |
| | 3 | 1315 | 1331 | 0.09 | 0.91 |
| | 4 | 1316 | 1329 | 0.07 | 0.93 |
| | 5 | 1317 | 1331 | 0.08 | 0.92 |
| BR / 2 / 1300°C (C) | 1 | 1147 | 1163 | 0.10 | 0.90 |
| | 2 | 1151 | 1166 | 0.09 | 0.91 |
| | 3 | 1148 | 1164 | 0.09 | 0.91 |
| | 4 | 1150 | 1164 | 0.08 | 0.92 |
| | 5 | 1151 | 1164 | 0.08 | 0.92 |
| BR / 2 / 1000°C (C) | 1 | 879 | 891 | 0.09 | 0.91 |
| | 2 | 880 | 892 | 0.09 | 0.91 |
| | 3 | 880 | 890 | 0.08 | 0.92 |
| | 4 | 878 | 889 | 0.09 | 0.91 |
| | 5 | 878 | 889 | 0.08 | 0.92 |
| CBR 1-3 / 2 / 1000°C (H) | 1 | 836 | 850 | 0.11 | 0.89 |
| | 2 | 831 | 844 | 0.10 | 0.90 |
| | 3 | 825 | 840 | 0.12 | 0.88 |
| | 4 | 824 | 842 | 0.15 | 0.85 |
| | 5 | 824 | 838 | 0.11 | 0.89 |
| CBR 1-3 / 2 / 1300°C (H) | 1 | 1067 | 1087 | 0.13 | 0.87 |
| | 2 | 1068 | 1088 | 0.13 | 0.87 |
| | 3 | 1069 | 1093 | 0.15 | 0.85 |
| | 4 | 1071 | 1088 | 0.11 | 0.89 |
| | 5 | 1067 | 1089 | 0.14 | 0.86 |
| CBR 1-3 / 2 / 1500°C | 1 | 1248 | 1264 | 0.09 | 0.91 |
| | 2 | 1246 | 1256 | 0.05 | 0.95 |
| | 3 | 1245 | 1265 | 0.11 | 0.89 |
| | 4 | 1247 | 1266 | 0.11 | 0.89 |
| | 5 | 1260 | 1285 | 0.13 | 0.87 |
| CBR 1-3 / 2 / 1300°C (C) | 1 | 1100 | 1116 | 0.10 | 0.90 |
| | 2 | 1100 | 1117 | 0.10 | 0.90 |
| | 3 | 1106 | 1117 | 0.07 | 0.93 |
| | 4 | 1100 | 1122 | 0.13 | 0.87 |
| | 5 | 1104 | 1117 | 0.08 | 0.92 |
| CBR 1-3 / 2 / 1000°C (C) | 1 | 845 | 857 | 0.09 | 0.91 |
| | 2 | 844 | 856 | 0.10 | 0.90 |
| | 3 | 842 | 855 | 0.10 | 0.90 |
| | 4 | 843 | 857 | 0.11 | 0.89 |
| | 5 | 845 | 858 | 0.10 | 0.90 |

| S/ S No. /T | M No. | $T_{eff}$ | $T'_{eff}$ | $r_s$ | ε |
|---|---|---|---|---|---|
| CBR 1-5 / 2 / 1000°C (H) | 1 | 794 | 815 | 0.18 | 0.82 |
| | 2 | 796 | 816 | 0.17 | 0.83 |
| | 3 | 799 | 817 | 0.14 | 0.86 |
| | 4 | 796 | 810 | 0.12 | 0.88 |
| | 5 | 798 | 818 | 0.16 | 0.84 |
| CBR 1-5 / 2 / 1300°C (H) | 1 | 1045 | 1069 | 0.16 | 0.84 |
| | 2 | 1041 | 1068 | 0.18 | 0.82 |
| | 3 | 1043 | 1065 | 0.15 | 0.85 |
| | 4 | 1045 | 1068 | 0.15 | 0.85 |
| | 5 | 1047 | 1065 | 0.12 | 0.88 |
| CBR 1-5 / 2 / 1500°C | 1 | 1244 | 1261 | 0.09 | 0.91 |
| | 2 | 1240 | 1252 | 0.07 | 0.93 |
| | 3 | 1234 | 1251 | 0.09 | 0.91 |
| | 4 | 1236 | 1256 | 0.11 | 0.89 |
| | 5 | 1239 | 1252 | 0.07 | 0.93 |
| CBR 1-5 / 2 / 1300°C (C) | 1 | 1110 | 1125 | 0.09 | 0.91 |
| | 2 | 1110 | 1119 | 0.06 | 0.94 |
| | 3 | 1104 | 1119 | 0.09 | 0.91 |
| | 4 | 1103 | 1116 | 0.08 | 0.92 |
| | 5 | 1098 | 1109 | 0.07 | 0.93 |
| CBR 1-5 / 2 / 1000°C (C) | 1 | 842 | 851 | 0.08 | 0.92 |
| | 2 | 839 | 851 | 0.09 | 0.91 |
| | 3 | 839 | 849 | 0.08 | 0.92 |
| | 4 | 839 | 853 | 0.11 | 0.89 |
| | 5 | 842 | 853 | 0.09 | 0.91 |
| CBR 1-12 / 2 / 1000°C (H) | 1 | 886 | 897 | 0.08 | 0.92 |
| | 2 | 889 | 900 | 0.08 | 0.92 |
| | 3 | 889 | 898 | 0.06 | 0.94 |
| | 4 | 889 | 901 | 0.09 | 0.91 |
| | 5 | 890 | 899 | 0.07 | 0.93 |
| CBR 1-12 / 2 / 1300°C (H) | 1 | 1123 | 1138 | 0.09 | 0.91 |
| | 2 | 1122 | 1137 | 0.09 | 0.91 |
| | 3 | 1121 | 1139 | 0.11 | 0.89 |
| | 4 | 1122 | 1138 | 0.10 | 0.90 |
| | 5 | 1124 | 1138 | 0.09 | 0.91 |
| CBR 1-12 / 2 / 1500°C | 1 | 1290 | 1310 | 0.11 | 0.89 |
| | 2 | 1290 | 1305 | 0.08 | 0.92 |
| | 3 | 1288 | 1308 | 0.11 | 0.89 |
| | 4 | 1293 | 1307 | 0.07 | 0.93 |
| | 5 | 1285 | 1300 | 0.08 | 0.92 |
| CBR 1-12 / 2 / 1300°C (C) | 1 | 1126 | 1140 | 0.09 | 0.91 |
| | 2 | 1123 | 1138 | 0.09 | 0.91 |
| | 3 | 1123 | 1139 | 0.10 | 0.90 |
| | 4 | 1123 | 1135 | 0.07 | 0.93 |
| | 5 | 1122 | 1137 | 0.09 | 0.91 |
| CBR 1-12 / 2 / 1000°C (C) | 1 | 890 | 905 | 0.12 | 0.88 |
| | 2 | 889 | 908 | 0.15 | 0.85 |
| | 3 | 891 | 901 | 0.08 | 0.92 |
| | 4 | 893 | 908 | 0.12 | 0.88 |
| | 5 | 891 | 910 | 0.14 | 0.86 |

Emissivity results from the REM of the BR, CBR 1-3, CBR 1-5 and CBR 1-12 at different temperatures are shown in Figure 91-Figure 94 respectively which reveal that emissivity falls in the range of 0.84-0.93. These data show that there is a statistically insignificant change in emissivity with temperature, indicating that the emissivity of the basic refractory and the coatings are temperature independent at 137GHz.

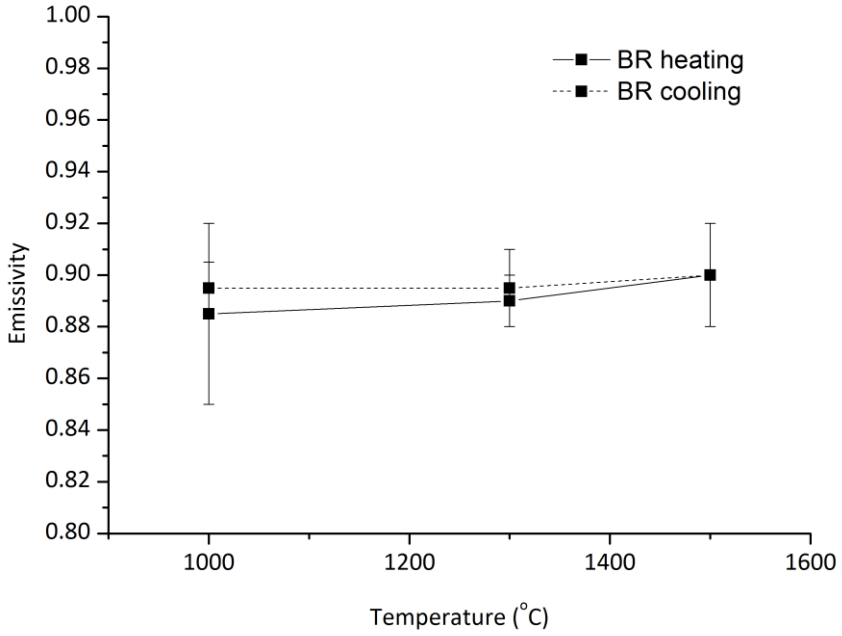


Figure 91. Emissivity of BR 1000, 1300 and 1500°C on heating (solid line) and cooling (dash line) at 137GHz (radio frequency).

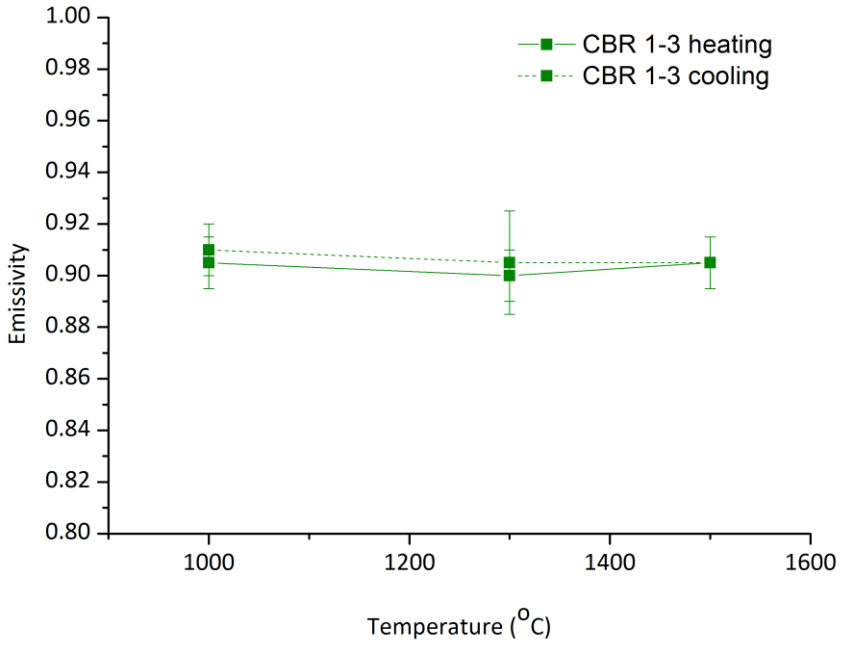


Figure 92. Emissivity of CBR 1-3 1000, 1300 and 1500°C on heating (solid line) and cooling (dash line) at 137GHz (radio frequency).

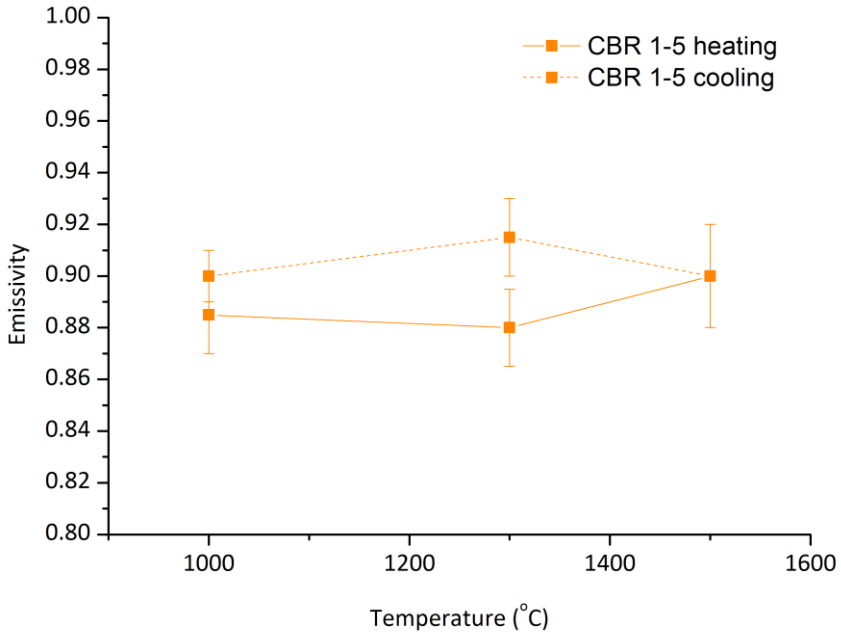


Figure 93. Emissivity of CBR 1-5 1000, 1300 and 1500°C on heating (solid line) and cooling (dash line) at 137GHz (radio frequency).

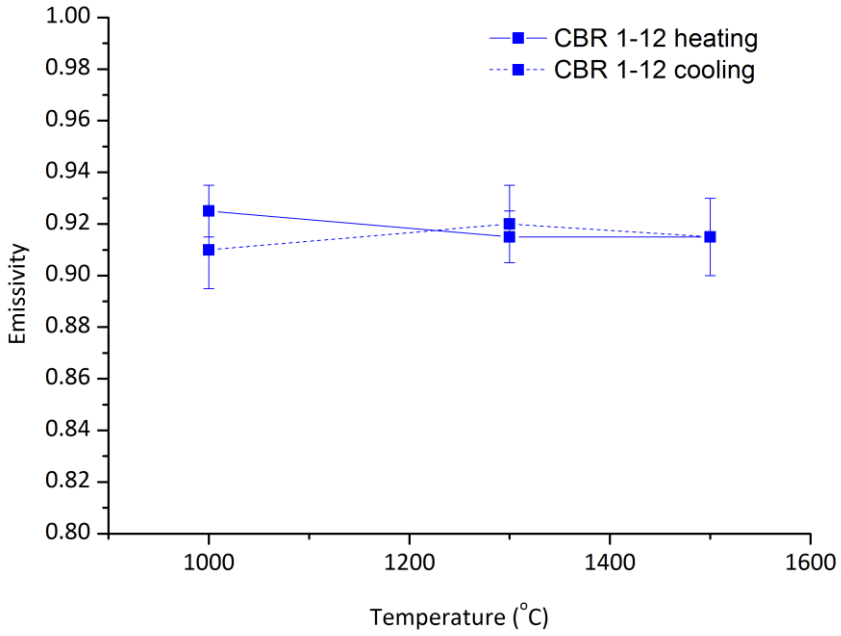


Figure 94. Emissivity of CBR1-12 at 1000, 1300 and 1500°C on heating (solid line) and cooling (dash line) at 137GHz (radio frequency).

## 5.2 Infrared emissivity measurement methods (IREM)

Sample, blackbody and ambient heat flux of six samples (BR, CBR 1-3, CBR 1-5, CBR 1-12, TCBR 1-5 and $CeO_2$ pellet) were collected and converted to emissivity using the emittance program as explained in section 3.3.2. Then, the power values (Watts) of each sample were converted to temperature (°C) also using the emittance program and results are presented in Table 17. Next, the emissivity values at different wavelength are merged. The emissivity result of BR, CBR1-3, CBR1-5, CBR-12, TCBR1-5 and $CeO_2$ pellet are shown in Figure 95, Figure 98- Figure 102 respectively. The x-axis presents wavenumber ($cm^{-1}$) ranging from 700-12000 $cm^{-1}$ and the y-axis presents emissivity ranging from 0-1.

Basic refractory (BR) emissivity is shown in Figure 95 revealing its Christiansen point at approximately 800 $cm^{-1}$. Although the Christiansen point might represent a high emissivity value of 1, it presents at a low wavenumber (low energy) which does not provide heat energy. The emissivity of BR decreases from 800-3000 $cm^{-1}$ with increasing wavenumber. This is a trend commonly observed for dielectric materials. It is due to the nearly exponential decrease of the absorption coefficient induced by multi-phonon processes [105]. However, as wavenumber continues to increase, emissivity

also starts to increase because the increased wavenumber (energy) activates an increase of charge carriers that are not completely free (electronic or hole defects) creating hopping motions in the structure. The hopping motion coupled with lattice vibrations (such as polaronic absorption) increases energy absorption which is later released as an emission [182]. A schematic diagram of an electronic defect is shown in Figure 96 revealing an electron defect attracting the positive and repulsing the negative ions causing hopping motions. The overall effect is shown in Figure 97. The emissivity becomes steady from 7000-11000 $cm^{-1}$. Considering temperature dependency, Figure 95 also reveals that emissivity in this wavenumber range is dependent on temperature. As temperature increases from 1125°C to 1319°C and 1550°C, present as blue, red and black lines respectively, the emissivity in the steady range of BR also increases from 0.36 to 0.37 and 0.42 ±0.002 respectively. These values are in the same range of those previously reported [183].

Table 17. Power and temperatures achieved for BR, CBRs samples and $CeO_2$ sintered pellet.

| ***Power*** | ***BR*** | ***CBR 1-3*** | ***CBR 1-5*** | ***CBR 1-12*** | ***TCBR 1-5*** | ***$CeO_2$ Pellet*** |
|---|---|---|---|---|---|---|
| ***Watts*** | **Temperature (°C) ±20** | | | | | |
| *54* | 1125 | 1034 | 1034 | 1032 | 1077 | 1157 |
| *71* | 1319 | 1161 | 1152 | 1159 | 1194 | 1278 |
| *100* | 1550 | 1314 | 1293 | 1302 | 1328 | 1420 |

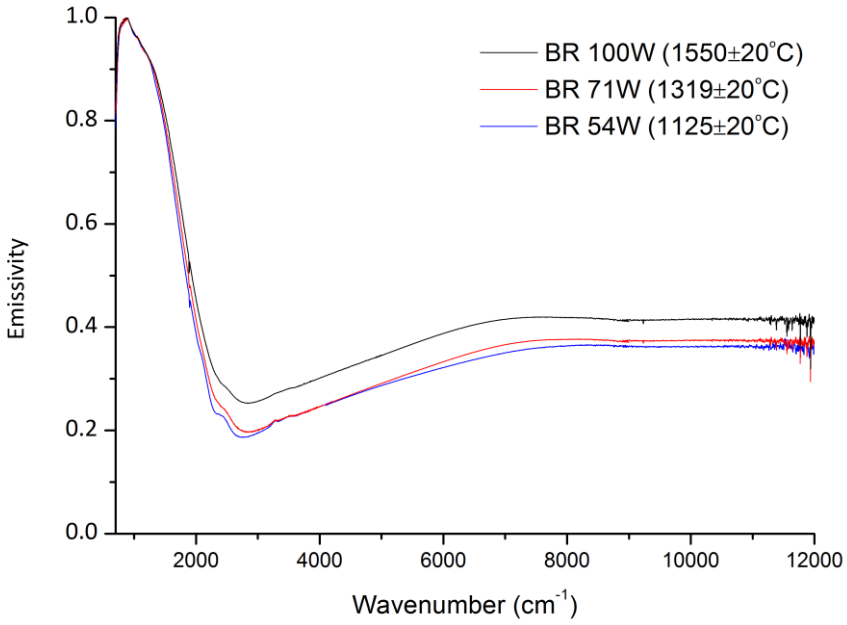


Figure 95. Emissivity of basic refractory (BR) in the 700-12000 $cm^{-1}$ (infrared range). Emissivity at 1125, 1319 and 1150°C given by blue, red and black lines respectively.

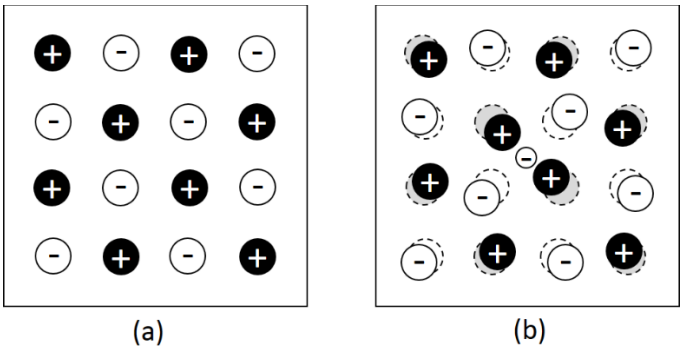


Figure 96. Schematic diagram of (a) a perfect ionic structure and (b) an ionic structure with an electron defect which attracts the positive and repulses the negative ions causing hopping motions (modified from [184]).

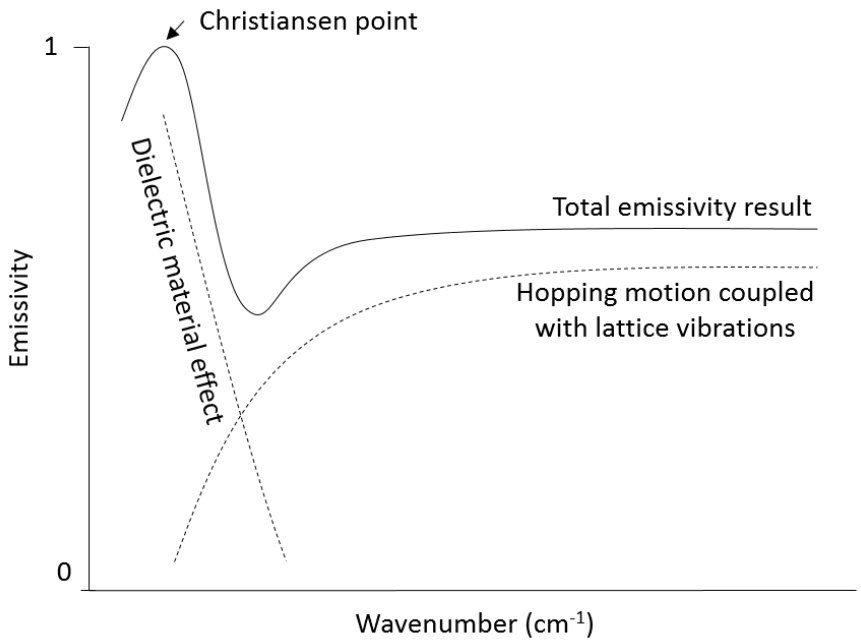


Figure 97. Schematic diagram of impact of various processes on emissivity (author's figure).

CBR 1-3 emissivity is shown in Figure 98. The Christiansen points at all three temperatures are at approximately 700 $cm^{-1}$. At 1034 and 1161°C, the emissivity decreases as wavenumber increases from 800-2700 $cm^{-1}$, and at 1314°C, the emissivity decreases as the wavenumber increases from 800-2500 $cm^{-1}$, for the same reason as occurred with BR; a common effect on dielectric material ($CeO_2$ in the coating is a dielectric material [185]). A dip in the signal at 1150 ±50$cm^{-1}$ is due to stretching motions of $PO_4$ tetrahedra [186]. Emissivity increases with increased wavenumber from 2700-9000 $cm^{-1}$ and became stable from 9000-12000 $cm^{-1}$ at 1034°C. For measurement temperature of 1161 and 1314°C, emissivity becomes steady after 2700 $cm^{-1}$ and 2500$cm^{-1}$ respectively. The steady emissivity values at 1034, 1161 and 1314°C were 0.49, 0.65 and 0.78 ±0.004 respectively. The decrease and increase in emissivity values were not as large as in the BR sample because the coating has a much higher polaron absorption. CBR 1-5 and CBR 1-12 emissivity are shown in Figure 99 and Figure 100 respectively. Both show a similar trend as CBR 1-3. The emissivity in the steady range of CBR 1-5 is 0.45, 0.66 and 0.81±0.004 at 1034, 1152 and 1293°C. The emissivity of CBR 1-12 are 0.46, 0.66 and 0.80 ±0.006 at 1032, 1159 and 1302°C. Thick coated basic brick 1-5 (TCBR 1-5) also have similar trends with the other coated samples presented in Figure 101. The emissivity in the steady range of TCBR 1-5 at 1077, 1194 and 1328°C is 0.42, 0.73 and 0.81 ±0.005. Sintered $CeO_2$ pellet emissivity was also measured as a material reference (Figure 102). There was an error while measuring emissivity in the 4000-9000 $cm^{-1}$. However, the results show that there is an obvious trend and therefore made it possible to estimate the missing emissivity shown by the dashed lines. The sintered $CeO_2$ pellet

emissivity shows a similar trend between 700-2900 $cm^{-1}$. The emissivity values at the stable range were 0.48, 0.60 and 0.71 at 1157, 1278 and 1420°C.

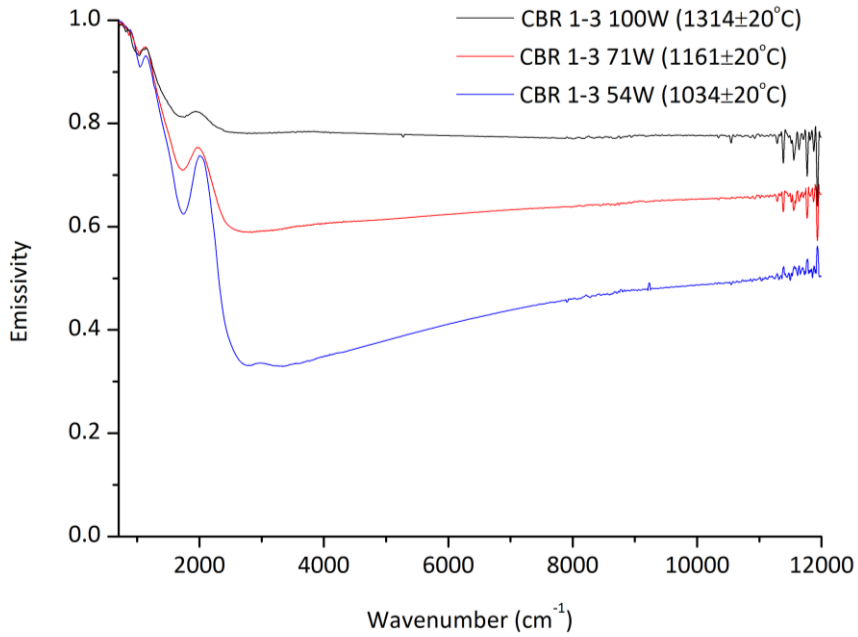


Figure 98. Emissivity of coated basic refractory 1-3 (CBR 1-3) in the 700-12000 $cm^{-1}$ (infrared range) at 1034, 1161 and 1314°C represented with blue, red and black lines respectively.

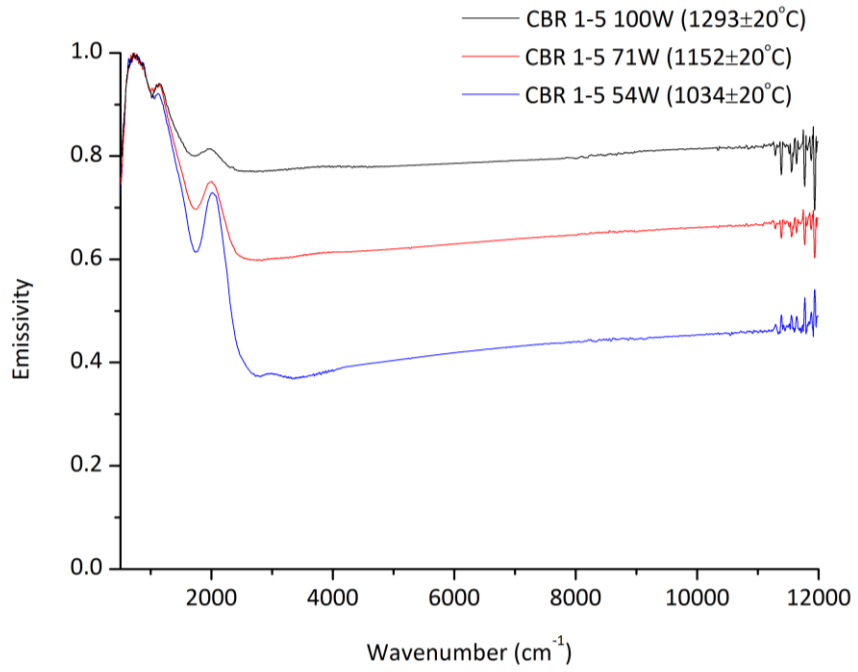


Figure 99. Emissivity of coated basic refractory 1-5 (CBR 1-5) in the 700-12000 $cm^{-1}$ (infrared range) at 1034, 1152 and 1293°C represented with blue, red and black lines respectively.

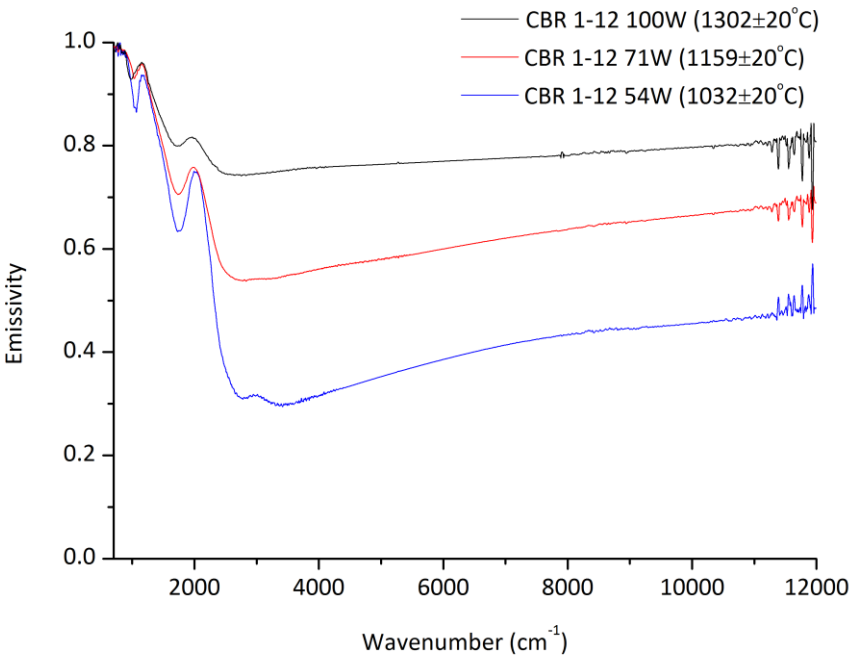


Figure 100. Emissivity of coated basic refractory 1-12 (CBR 1-12) in the 700-12000 $cm^{-1}$ (infrared range) at 1032, 1159 and 1302°C represented with blue, red and black lines respectively.

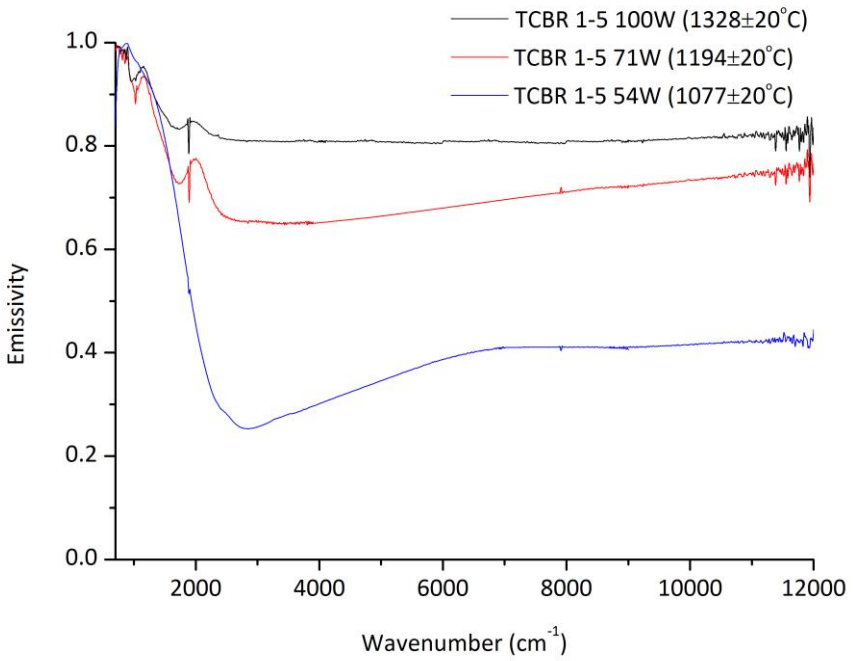


Figure 101. Emissivity of thick coated basic refractory 1-5 (TCBR 1-5) in the 700-12000 $cm^{-1}$ (infrared range) at 1077, 1194 and 1328°C represented with blue, red and black lines respectively.

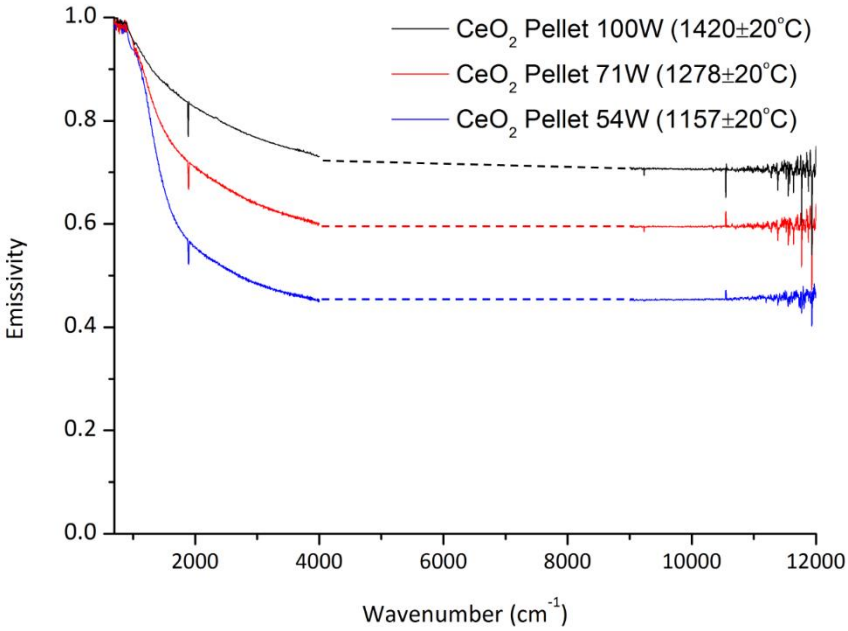


Figure 102. Emissivity of sintered $CeO_2$ pellet in the 700-12000 $cm^{-1}$ (infrared range). Emissivities at 1157, 1278 and 1420°C represented with blue, red and black lines respectively. Dash lines represent the emissivity trend where there was an error during the measurements.

## 5.3 Discussion of emissivity results

### 5.3.1 High emissivity coatings

#### 5.3.1.1 REM

Emissivity results from all coatings are compared in Figure 103. Our data reveal no significant trend, showing that the coating does not improve the emissivity of the basic refractory brick at 137GHz. Therefore, it can be concluded that the emissivity of a basic refractory (BR) with and without the coating is independent of temperature on both heating and cooling at 137GHz. This might be because the differences in emissivity occurred at higher frequency (shorter wavelength) as can be seen from Figure 6.

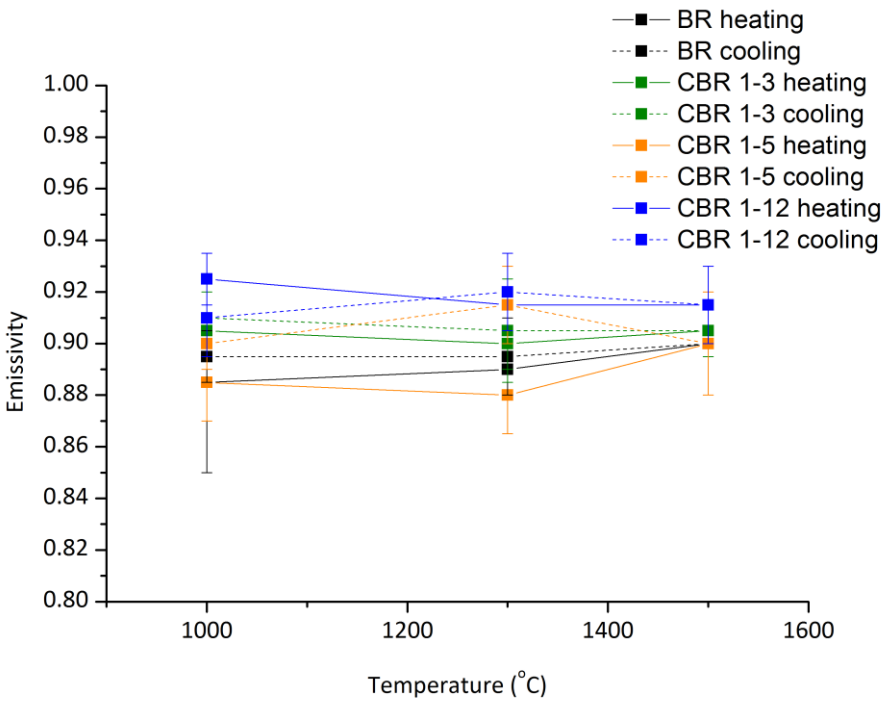


Figure 103. Emissivity of BR (black), CBR 1-3 (green), CBR 1-5 (orange) and CBR1-12 (blue) at 137GHz (radio frequency) at 1000, 1300 and 1500°C on heating (solid line) and cooling (dash line).

#### 5.3.1.2 IREM

The IREM emissivity of all samples over their steady range (9000-12000cm$^{-1}$) is presented in Figure 104. The data shown in Figure 104 are analysed in 5 aspects; 1) comparing emissivity results of each sample at different temperatures, 2) comparing emissivity of BR sample to CBR samples, 3) comparing the CBR with different composition samples among themselves, 4) comparing thin coating (CBR 1-5) to thick coating (TCBR 1-5), and 5) comparing the sintered $CeO_2$ pellet to all samples.

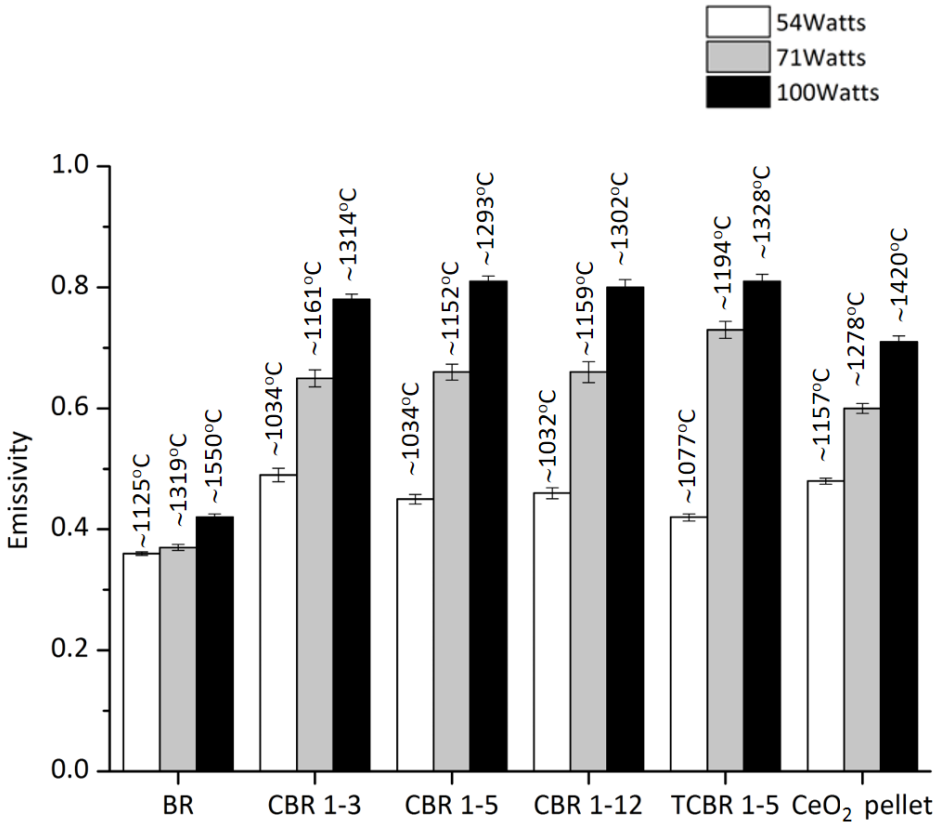


Figure 104. Emissivity of BR, CBR 1-3, CBR 1-5, CBR 1-12, TCBR 1-5 and $CeO_2$ pellet in the steady range (9000-11000$cm^{-1}$) at different temperatures.

Starting with the emissivity of all samples which increases with temperature showing that emissivity in this range is temperature dependent. This increasing trend correlates with the results of Guazzoni [52]. Even though Guazzoni reported emissivity on other rare earth oxides ($Er_2O_3$, $Sm_2O_3$, $Nd_2O_3$ and $Yb_2O_3$) at a higher wavenumber range (at 16,667 $cm^{-1}$), it is not surprising that $CeO_2$ would follow the same trend at a lower wavenumber because the materials are all rare earth oxides with high absorption band.

Second, comparing BR with CBR, CBR emissivity is about twice that of BR leading to the conclusion that the $CeO_2$-$AlH_6O_{12}P_3$ coating can improve the basic refractory (BR) emissivity. The reason for this is likely because the cerium atom, contained in the coating, has a higher atomic number meaning that it has more electrons than magnesium, in the basic refractory, hence, cerium is easily thermally activated and creates electron-hole defects easier than magnesium.

Our experiments have reported emissivity values of a high emissivity coating for kiln applications, ensuring that when these coatings are used, it can be certain that the energy saving

comes from emissivity. This is unlike the work of Hellander [53, 54] who examined high emissivity coatings that can save furnace energy but did not report any emissivity values. Holcombe *et al.* [56] also only mentioned that $CeO_2$ has emissivity of 0.9 at 1000-2000°C but did not report the source of the information or what was their coating emissivity value was.

Third, when the CBR samples with different $CeO_2$-$AlH_6O_{12}P_3$ ratios are compared among themselves, there was no significant difference. This means that the different ratio of $CeO_2$ to $AlH_6O_{12}P_3$ between 1-3 to 1-12 do not affect the emissivity significantly. Although CBR samples did not show a significant difference in emissivity among themselves, it must be kept in mind that they did show a significant difference in rheology as mentioned in section 4.2.2 and cost mentioned in section 4.3.3.

Fourth, increasing coating thickness by comparing emissivity of CBR 1-5 with TCBR 1-5 also did not show a significant difference. This reveals that the thickness of ~120μm is sufficient for the coating to be considered as opaque in the 9000-11000 $cm^{-1}$ wavenumber range. Increasing the thickness might not significantly affect the emissivity, but it might affect corrosion, abrasion and thermal shock resistance. Partial corrosion testing is conducted in chapter 6, abrasion and thermal shock resistance is suggested for future work (Chapter 9).

Fifth, comparing emissivity of $CeO_2$ pellet with the BR and CBR shows that the $CeO_2$ pellet has higher emissivity than BR confirming that the increase for CBR is from the $CeO_2$ contained in the coatings. However, the $CeO_2$ emissivity is slightly lower than CBRs at temperatures above 1000°C, possibly because the $CeO_2$ pellet surface is smoother than coated samples. Rough surface increases heat flux contact point to the surface which increases absorption, reduces reflectivity and therefore, increases emissivity [183]. A schematic of how the heat flux reflects on a smooth and rough surface is presented in Figure 105.

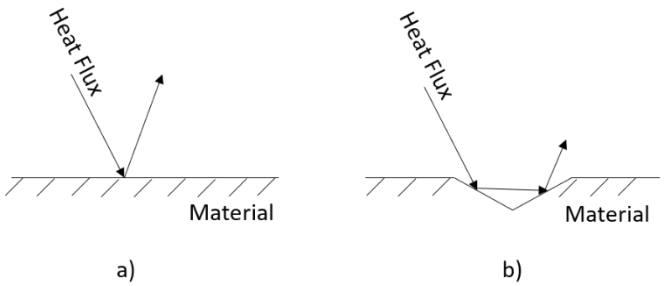


Figure 105. Schematic of heat flux reflection a) on a smooth material surface and b) on a rough material surface (author's figure).

It is interesting to compare our results with the results Huang *et al*. [77] reported for their $CeO_2$ coating (Table 18). Even though the emissivities were all measured at about 1000°C, they are measured over different wavenumber ranges and using different methods. However, the emissivity values are not significantly different. Unfortunately, Huang *et al.* did not measure the coating emissivity at a higher temperature, which may be due to equipment limitations, and therefore results could only be compared at 1000°C.

Table 18. Emissivity comparison among average of CBR 1-3, 1-5 and 1-12, $CeO_2$ pellet and Huang *et al.* [77] coating results.

| | CBR 1-3, 1-5 and 1-12 | $CeO_2$ pellet | Huang *et al.* |
|---|---|---|---|
| Composition | $CeO_2$ + $CePO_4$ + Glass + Pores | $CeO_2$ | $CeO_2$ |
| Appling technique | Air spray | Uni-axial compression | EB-PVD |
| Emissivity | 0.46 ±0.008 | 0.48 ±0.005 | 0.4-0.6 |
| Temperature (°C) | ~1000 | ~1000 | ~1000 |
| Wavenumber ($cm^{-1}$) | 9000-12000 | 9000-12000 | 700-10000 |
| Measuring method | Emissivity Apparatus, Orleans, France | Emissivity Apparatus, Orleans, France | FT-IR |

### 5.3.2 Comparison of the two types of measurements, and two different spectral ranges of uncoated and coated samples

Infrared emissivity measurement method (IREM) differs from the radio emissivity measurement (REM) in the electromagnetic wave range; REM is measured at a fixed radio frequency (135Hz) while the IREM measures in a wavenumber ranging from 700-12000 $cm^{-1}$. Another difference is the heating condition; REM samples are heated in an electric furnace while IREM samples are heated with $CO_2$ laser.

It is clear that the results in the millimetre wave (radio range) and infrared ranges are different (Figure 103 and Figure 104 respectively). Emissivity results in the millimetre range are 0.85-0.95 and independent of temperature and the emissivity of the coated and uncoated are similar (Figure 103). On the other hand, emissivity results in the infrared range indicate it is dependent on temperature and coated samples give higher emissivity than those that are not coated (Figure 104). This is because the millimetre wavelength is significantly further away from the infrared range and cannot be used to represent heat energy even though the experimental set up and sample heating conditions are more representative of the real application situation. It can be noted for the millimetre wave experiment that refractory bricks, with or without coating, generate high millimetre wave emission (>0.85) when heated above 1000°C. For the infrared range experiment, results are more representative of heat emission and give more information on the differences between the coated and uncoated samples at different temperatures.

### 5.3.3 Impact of coating on heat reduction

The ultimate goal of this research is to save energy in cement rotary kilns. Energy saving from using the high emissivity coating can be estimated by using Equation 3. To calculate heat emission in the upper transition zone, the area of a kiln must be established. For the calculation to be able to compare with the coating price, discussed in section 4.3.3, the same kiln size is used (3.5 m inner diameter and 12 m long). The upper transition zone area is calculated by $2\pi rh$, where r is the kiln radius and h is the length of the upper transition zone. Therefore, the area is about 132 $m^2$. Emissivity ($\varepsilon$) value of the basic refractory brick is 0.4 and the coating is 0.8 from the experiments in section 5.2. The Stefan-Boltzmann constant is 5.67 x $10^{-8}$ $W/m^2K^4$. The inside of the upper transition zone of a rotary kiln temperature ($T_w$) is assumed to be 1300°C [181]. Ambient temperature ($T_0$) in this thesis is a calculated temperature in the centre of the refractory brick (at 0.11 metres) and the calculation is explained in the next paragraph.

All the valuables are known, Table 19, except for heat energy (W) and lower temperature ($T_0$). Lower temperature ($T_0$) can be calculated from a conduction equation for cylinder (Equation 4 from section 1.3).

Table 19. Assumption values for conduction heat transfer calculation.

| Calculate energy from emissivity | Values | Unit | Symbol |
|---|---|---|---|
| Temperature inside the kiln | 1573 | K (1300°C) | $T_i$ |
| Refractory brick thickness | 0.22 | m | $x_1$ |
| Kiln shell thickness | 0.03 | m | $x_2$ |
| Refractory brick thermal conductivity | 3.35 | W·(mK)$^{-1}$ | $k_1$ |
| Kiln shell thermal conductivity | 46 | W·(mK)$^{-1}$ | $k_2$ |
| Kiln radius with refractory lining | 1.75 | m | $r_i$ |
| Kiln radius without refractory lining | 1.97 | m | $r_o$ |
| Kiln radius | 2 | m | r |
| Upper transition zone length | 12 | m | L |

Heat passing through the brick at every thickness is assumed equal to heat at the kiln shell surface and since the kiln shell temperature is known to be about 300°C, heat energy can be calculated as shown below.

$$Q_{cond} = \frac{(1573 - 573)}{\frac{0.22}{3.35 \cdot \frac{2\pi(12)(1.97 - 1.75)}{\ln\frac{1.97}{1.75}}} + \frac{0.03}{46 \cdot \frac{2\pi(12)(2 - 1.97)}{\ln\frac{2.00}{1.97}}}}$$

Conduction heat energy ($Q_{cond}$) calculated from the above equation is equal to 2,114,199 W. This heat energy value is then used to calculate the temperature at the centre of the brick (0.11 m thick, $T_o$ ) from the same equation as presented below, which give a result of 790°C ($T_o$ = 790°C). This temperature is used as the temperature inside the brick ($T_o$) in Table 20.

$$2{,}114{,}199 = \frac{(1573 - T_o)}{\frac{0.11}{3.35 \cdot \frac{2\pi(12)(1.86 - 1.75)}{\ln\frac{1.86}{1.75}}}}$$

The calculated energy saving using the assumed values is presented in Table 20. Applying the assumptions and constant values to Equation 3, the energy emitted back into the kiln is calculated to be 14,506,186 W for basic refractory lining (uncoated, $Q_B$) and 29,012,373 W for coated lining ($Q_C$).

Therefore, an additional 14,506,186 W or ~14.5 MW ($Q_C$-$Q_B$) or 109,180,691 MCal/year of energy is saved. The energy in Watts is converted to MCal/year because fuel price is mostly sold and purchased in this unit. The conversion calculations are shown in Table 21. The approximate fuel price is 0.01 USD/MCal [181], therefore, cost saving is calculated to be 1,091,807 USD/year (~851,735 GBP/year). Although this might not appear to be a significant saving for a large industry like the cement industry, it must be kept in mind that this is an example of saving for just 1 rotary kiln of a specific size. If the size of the kiln or temperature is different, the cost-saving would also change.

Table 20. Assumed values for energy saving calculations

| Calculate energy from emissivity | Values | Unit | Symbol |
|---|---|---|---|
| Temperature inside the kiln | 1573 | K (1300°C) | $T_w$ |
| Temperature inside the brick | 1063 | K (790°C) | $T_0$ |
| Kiln diameter | 3.5 | M | 2r |
| Upper transition zone length | 12 | m | L |
| Emitting area | 132 | $m^2$ | A |
| Brick emissivity | 0.4 | | $\varepsilon_B$ |
| Coating emissivity | 0.8 | | $\varepsilon_C$ |
| Stefan-Boltzmann constant | $5.67 \times 10^{-8}$ | $W \cdot m^{-2} K^{-4}$ | σ |

Table 21. Energy saved from coating emissivity, unit conversion calculations.

| Calculate energy saved from emissivity | Values | Unit | Symbol | Equation | Conversion factor |
|---|---|---|---|---|---|
| Energy saved from coating emissivity | 14,506,186 | W | $Q_1$ | $Q_1 = Q_C - Q_B$ | |
| | 3,462,097 | Cal/s | $Q_2$ | $Q_2 = Q_1 / 4.19$ | 1 Cal/s = 4.19 W |
| | 3.46 | MCal/s | $Q_3$ | $Q_3 = Q_2/1{,}000{,}000$ | 1 MCal = $10^6$ cal |
| | 299,125 | MCal/day | $Q_4$ | $Q_4$ = Q3*86,400 | 1 day = 86,400 s |
| | 109,180,691 | MCal/year | $Q_5$ | $Q_5 = Q_4$*365 | 1 year = 365 days |

Comparison of energy saving from high emissivity coating used in this thesis (14.5 MW) with Engine and Ari [9] mentioned in section 2.1.2 (1 MW from waste heat recovery steam heat and 3 MW from secondary kiln shell), shows a significant increase in energy saving. As a result, it is worth pursuing this work further.

This research confirms that applying a high emissivity coating, containing cerium oxide ($CeO_2$), on magnesia (MgO) and magnesia spinel ($MgAl_2O_4$) containing refractory brick, can increase the refractory brick emissivity. We have also removed the uncertainties about whether the returning heat is from reflection or emission and whether the coating has a significantly higher emissivity than the ceramic substrate. However, further investigation on the coating performance in the cement rotary kiln, for example corrosion abrasion and thermal shock resistance, is needed to be able to determine the lifetime of the coating. At the moment it is not possible to say how long the coating can survive in the cement rotary kiln.

This research has measured emissivity at temperatures up to 1500$^{o}$C for both REM and IREM, where previous literature mostly made these measurements at temperatures below 1300$^{o}$C [77, 82]. This is important because in cement rotary kilns, temperature is $\sim$1300$^{o}$C in the upper transition zone and can be as high as 1500$^{o}$C in the burning zone.

# Chapter 6: Results: Corrosion of coating on refractory bricks

The corrosion experiments are described in the following two sections. Section 1 (6.1) describes results from experiments conducted to understand the reactions between alkaline vapour with basic refractory (BR) and coated basic refractory (CBR). Three coated refractory bricks were used which were CBR 1-3, 1-5 and 1-12. Sample preparation was described in Table 6, section 3.2. Section 2 (6.2) gives results from experiments conducted to understand the alkaline penetration and corrosion to the basic refractory and coated basic refractory. The coatings used in this experiment were CS 1-3, 1-5 and 1-12. Sample preparation was also described in Table 6, section 3.2 and 3.4.6.1 Alkaline vapour reaction with basic refractory (BR) and coatings

## 6.1 Alkaline vapour attack

In this part of the study samples (BR, CBR 1-3, 1-5 and 1-12) were used to cover an alumina crucible which contains $K_2CO_3$ (alkali source) and were heat treated at 1300$^{o}$C for 30 min. SEM was used to investigate how the alkaline vapour affects the basic refractory and coatings microstructure.

### 6.1.1 Alkaline vapour attack on BR

SEM of basic refractory (BR) with and without the alkaline vapour test is presented in Figure 106. a)-c) show the BR microstructure without the alkaline vapour test where a) is an overall image of the basic refractory showing that it consists of MgO, $MgAl_2O_4$ and pores, b) is a magnified image of a) in the MgO area, c) is a magnified image of a) in the $MgAl_2O_4$ area. d)-f) show the BR microstructure after the alkaline vapour test. d) is the overall image of the BR showing that it consists of MgO, $MgAl_2O_4$ and pores, e) is a magnified of d) in the MgO area, f) is a magnified of d) in the $MgAl_2O_4$ area. Comparing images, a) and d) reveals that the basic refractories still consist of MgO and $MgAl_2O_4$ spinel but the gaps between grains become wider. Comparing b) with e) and c) with f) reveals that the MgO grains are still intact but $MgAl_2O_4$ spinel grains become more porous (pores area increases from 1170±40 $\mu m^2$ to 3660 ±125 $\mu m^2$).

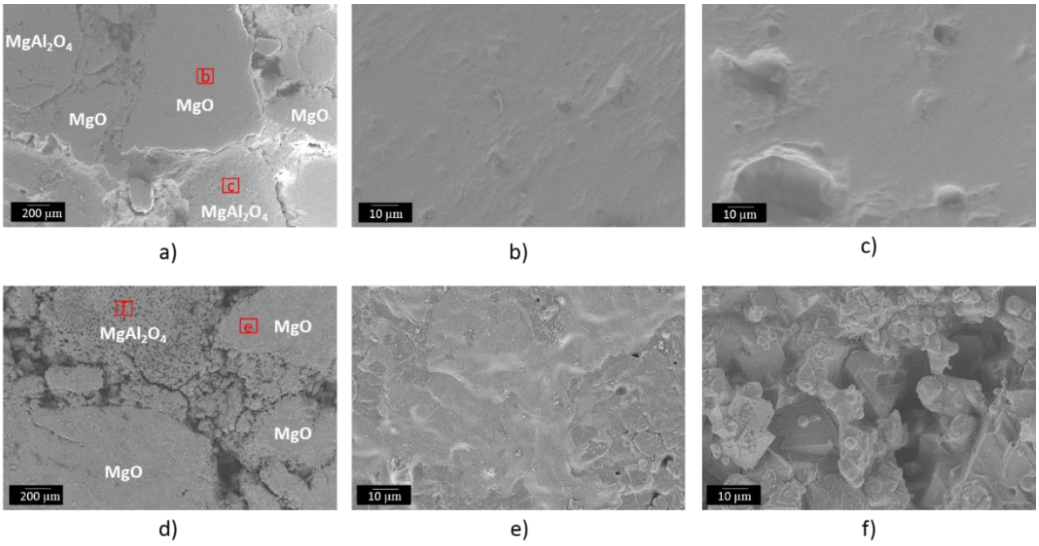


Figure 106. SEM image of top surface of a) basic refractory (BR), b) magnified image of a) in the MgO area (b in the red square), c) magnified image of a) in the $MgAl_2O_4$ area (c in the red square), d) BR after the alkaline vapour test, e) magnified image of d) in the MgO area (e in the red square), f) a magnified image of d) in the $MgAl_2O_4$ area (f in the red square).

### 6.1.2 Alkaline vapour attack on coated basic refractory (CBR).

The alkaline vapour test was conducted on CBR 1-3, 1-5 and 1-12. SEM images of the CBR 1-3, CBR 1-5 and CBR 1-12 with and without the alkaline vapour attack (Figure 107) reveal that the samples without the alkaline vapour test consist of $CeO_2$ (Ce) particles and M-P-O glass (glass). When the samples go through the alkaline vapour test, the samples consist of melt-like structure (MLS), pores and cracks. The reason that MLS and cracks are presented after the alkaline vapour test is that at high temperature the glassy phase in the coating (identified from the TEM mentioned in section 4.2.2.5) melted and $K^+$ from the alkaline vapour interfered in structure generating the MLS which has a high thermal expansion (potassium phosphate glass TEC is 20-24 X $10^{-6}$ $K^{-1}$ at 1300°C). Therefore, on cooling, the MLS also has a high shrinkage (higher than the substrate, TEC is ~13 X $10^{-6}$ at 1300°C $K^{-1}$) creating cracks in the structure. Further reasons for crack formation in the coating are discuss in section 6.3.1. Crack lengths were measured using the ImageJ program (detail). 20 random cracks from each sample were taken for measurements. As a result, the CBR 1-5 gives to the shortest average crack length of 8 ±3 µm. CBR 1-3 and CBR 1-12 gives a similar crack average length of 15±8 and 13±6 µm respectively. However, it is still difficult to determine which coating has the highest or lowest number of cracks. Cracks are not desired for corrosion resistance because they act as channels for alkaline vapour to travel through to the substrate.

CBR 1-12 was selected for further investigation to ensure that the MLS generated from the alkaline vapour reaction with the coating glassy phase is the cause of cracks. The CBR 1-12 top surface was magnified in an area that contained particles, melt-like structure and cracks (Figure 108) for EDX. In Figure 108, 3 areas used for the investigation are presented. The element atomic percentage from EDX of the three selected areas are presented in Table 22. Area 1 contains mostly particles covered with a layer of matrix and shows no cracks. EDX revealed that the particles were $CeO_2$ and there was less than 3 atomic% of alkaline (K) present indicating that there was no significant reaction between the alkaline and the $CeO_2$ particles. As mentioned in section 3.1.2 EDX is limited in that it measures X-rays to a depth of ~5 μm from the surface. The particle selected has a diameter of about 5 μm, therefore the EDX result in this area is believed to be accurate. Area 2 contains melt-like structure and cracks. EDX in this area revealed almost 5 times smaller amount of Ce and almost 4 times higher amount of P compared to area 1, suggesting that $CeO_2$ and $CePO_4$ particles may be present hidden underneath the melt-like structure. K in area 2 is almost 6 times higher than area 1. Area 3 is similar with area 2 in that it mostly consists of melt-like structure and is close to a crack. EDX reveal that there was no Ce found in area 3 indicating that there are no $CeO_2$ or $CePO_4$ particles underneath the melt-like structure to a depth of ~5μm. Comparing the EDX results of the 3 areas, reveals that area 2 and 3, where there is melt-like structure and cracks, contain a ~15 at% K and ~7 at% P. This is significantly higher than area 1 (~3 at% of K and ~2 at% of P). Hence, it can be summarised that alkali and phosphate is the cause of melt-like structure formation and cracks.

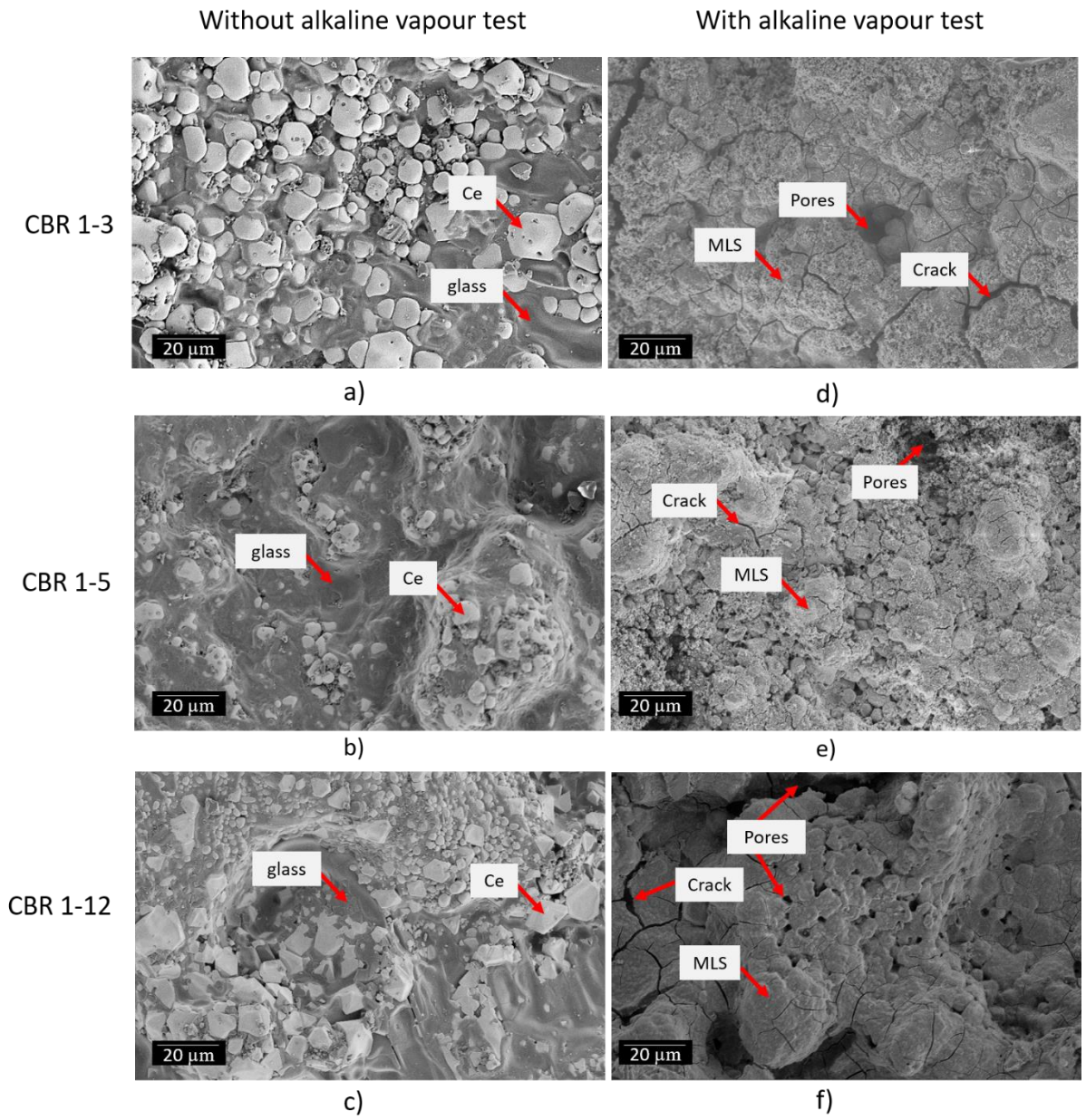


Figure 107. SEM image of top surface of a)-c) are without alkaline vapour test of CBR1-3, CBR 1-5 and CBR 1-12 top surface respectively. d)-f) are with alkaline vapour test of CBR1-3, CBR 1-5 and CBR 1-12 top surface respectively after the alkaline vapour test. Ce is $CeO_2$, glass is Mg-P-O glass (matrix surrounding the $CeO_2$ particles), MLP is melt like structure.

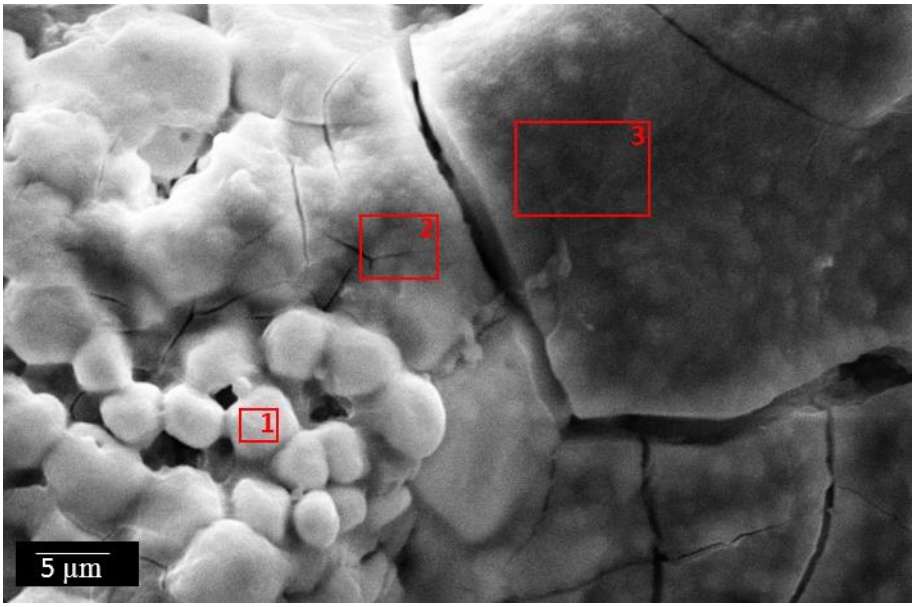


Figure 108. SEM image of top surface of CBR 1-12. Area 1 contains $CeO_2$ particles covered by melt-like phase. Area 2 contains melt-like structure and cracks. Area 3 contains melt-like structure and cracks, but area 3 is closer to a crack than area 2.

Table 22. EDX of area 1-3 from Figure 108 in atomic percent.

| Area No. | Ce (±0.01) | K (±0.02) | P (±0.02) | Al (±0.02) | Mg (±0.02) | O (±0.10) |
|---|---|---|---|---|---|---|
| 1 | 18.79 | 2.62 | 1.80 | 4.15 | - | 72.64 |
| 2 | 3.83 | 14.67 | 6.56 | 8.57 | 2.30 | 64.07 |
| 3 | - | 15.62 | 7.12 | 6.65 | 1.67 | 68.94 |

Cracks present in the coating lead to a question of whether the alkali vapour was able to reach the basic refractory substrate. In other words, although cracks occur in the coating, was the coating able to protect the substrate surface from alkali attack? Cracks may form at temperature or on cooling and if the latter the coating may still have protected the substrate. Further investigation was done by cracking the coating, CBR1-3, off the substrate. SEM was used to observe the top surface of the cracked coating and is shown in Figure 109. EDX mapping (Figure 110) was conducted to observe the elements present and revealed that the substrate in cracked areas was likely $MgAl_2O_4$ spinel because Mg, Al and O element were observed. P was also observed in the substrate area which had diffused from the coating as mentioned in section 4.2.2.4. The coating consists of Ce, P, Al, Mg and O which

correlates with the elements detected earlier (Figure 73 in section 4.2.2.4). K, the focus of this experiment, was detected in both the coating and substrate area indicating that alkali vapour was able to travel through the coating crack channels and reach the substrate.

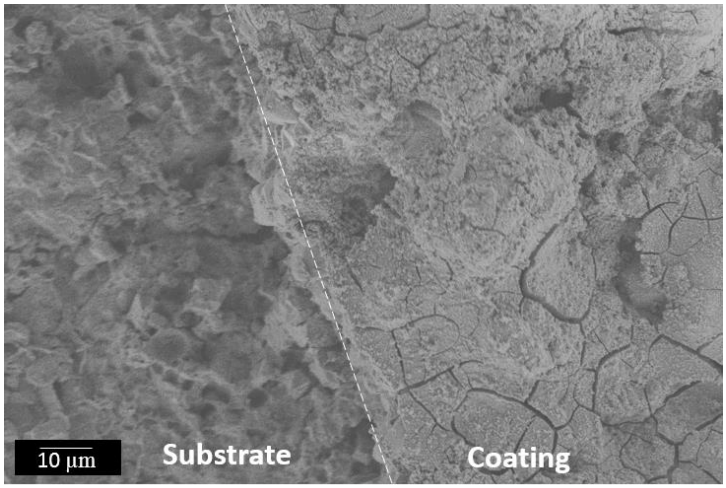


Figure 109. SEM top view image of CBR 1-3 coating on a basic refractory substrate after alkaline vapour test. The image shows a part of the coating and a part of the substrate from which the coating had cracked off.

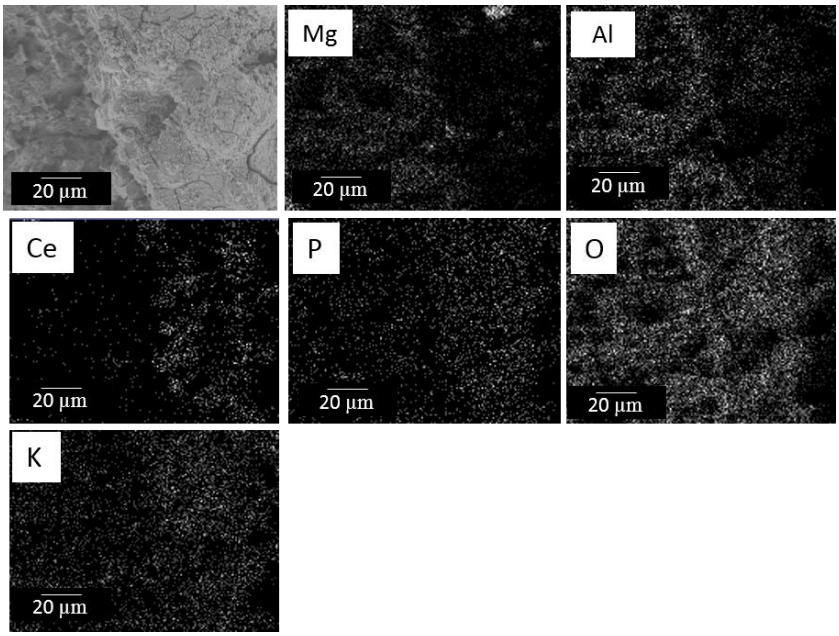


Figure 110. EDX mapping of top view CBR 1-3 coating and basic refractory substrate, from which the coating had cracked off, after alkaline vapour test. EDX shows that the coating contains Ce, P and O and the substrate contains Mg, Al and O. K was found to be in both the coating and the substrate indicating that alkaline was able to penetrate from the coating through to the substrate.

## 6.2 Alkaline corrosion and penetration via cup test

The cup test is a comparison test among samples in sets. Images of one of the samples that was the uncoated cup and the cup that was coated inside with CS 1-3 before and after the corrosion cup test are shown in Figure 111. Not all the samples are present because it is a challenge to gain any scientific data from visual observation. What can be observed is that the coating remained present throughout the test.

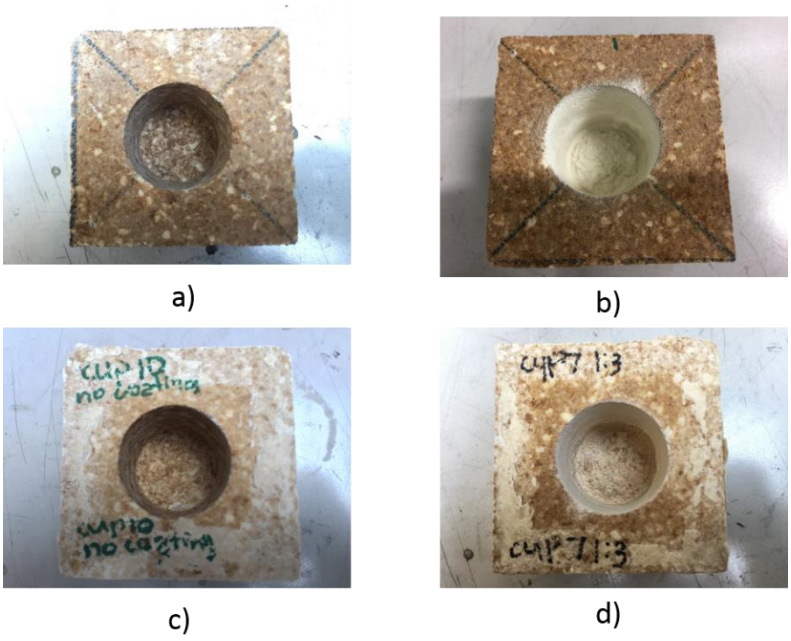


Figure 111. Images of one of the samples before and after the corrosion cup test. a) Uncoated cup, before testing. b) is the CS 1-3 coated cup, top view, before testing. c) Uncoated cup, top view, after testing. d) is the CS 1-3 coated cup, after testing.

Alkaline penetration and corrosion (see section 3.4) on refractory cups and coating via cup tests were analysed by experiments conducted in six steps. First, the inner diameter and the depth of the cup were measured. These values are considered as $d_1$ and $h_1$ in Equation 62. Second, the cup test was conducted as mention in section 3.4. Third, after the test, the inner diameter and the depth of the cup were measured again and are consider as $d_2$ and $h_2$ in Equation 62. Therefore, conducting these three steps, corrosion volume was calculated using Equation 62, and results are presented in Figure 112 (four measurements of the inner-diameter and the depth of the cup were taken for each cup). Fourth, the cups were cut half in a vertical plane. Pictures of the cut cups are presented in Figure 113. Fifth, penetrated stain of a liquid which impregnates porosity was revealed visually, and yellow lines were used to indicate boundaries of the area where alkaline has penetrated in the cups. Yellow

line boundaries were generated using ImageJ program and are also presented in Figure 113. Sixth, average boundaries of penetrated area were determined using blue and red squares as shown in Figure 114. The blue squares represent the edge of the inner cup. The width of the blue squares is $d_3$ and the height is $h_3$ in Equation 63. The red square represents an average area of the alkaline penetrated area where the penetrated area outside the red square is equal to the area where there is no penetrated inside the red square. The width of the red squares is $d_4$ and the height is $h_4$ in Equation 63. Knowing $d_3$, $h_3$, $d_4$ and $h_4$, penetration volume was calculated using Equation 63, and results are presented in Figure 115.

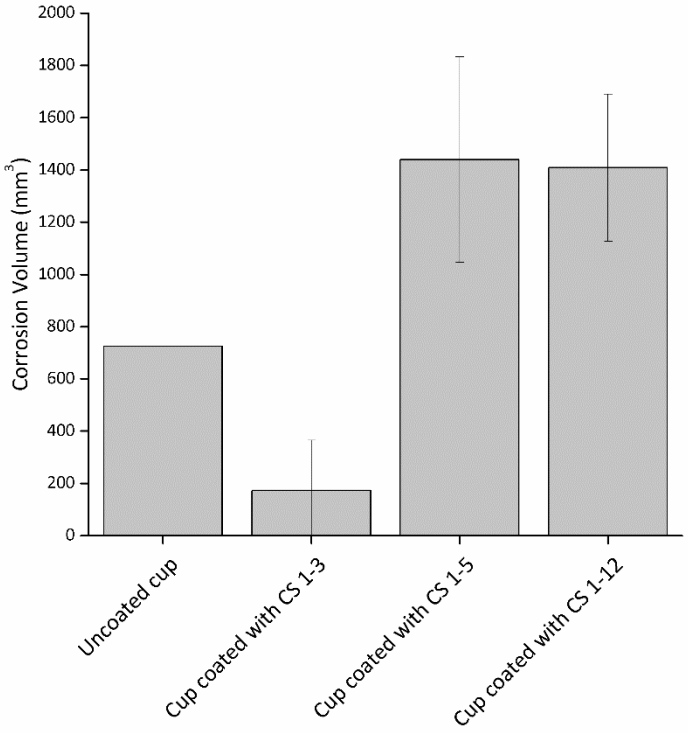


Figure 112. Alkaline corrosion volume of uncoated cups, and cups coated with CS 1-3, 1-5 and 1-12 showing that cup coated with CS 1-3 has the lowest alkaline corrosion volume.

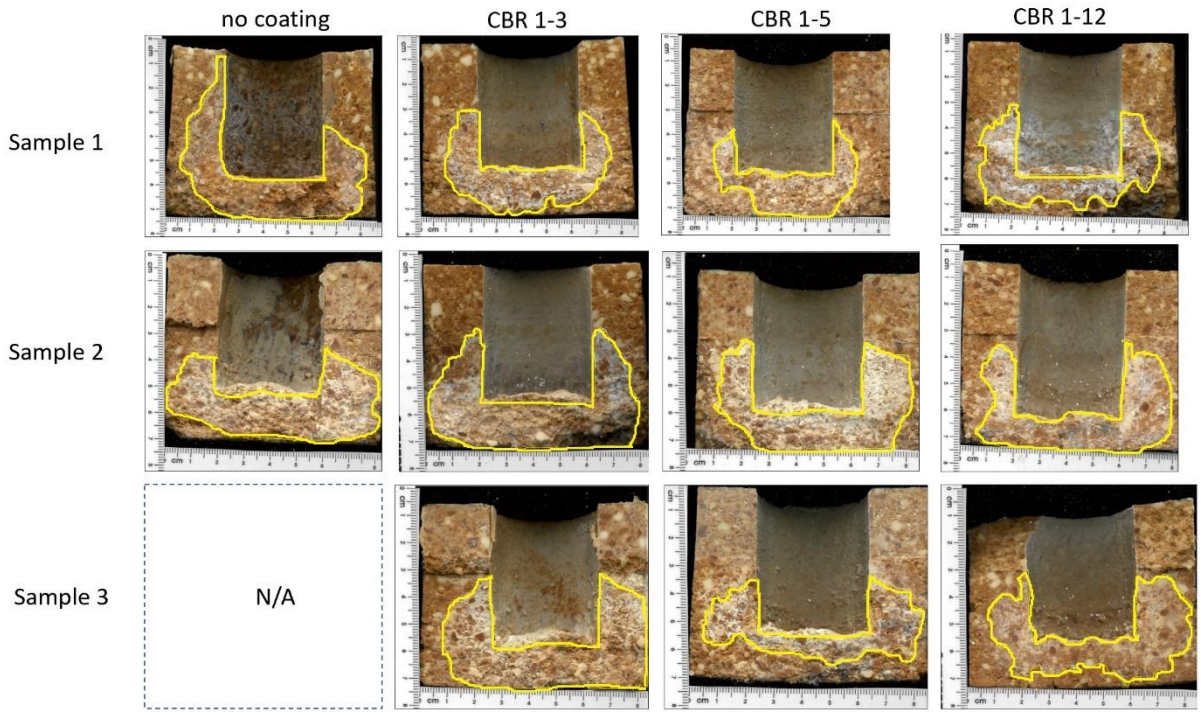


Figure 113. Scanned images of uncoated cups, cups coated with CS 1-3, 1-5 and 1-12. Yellow lines indicate boundaries of the area where alkaline has saturated in the cups.

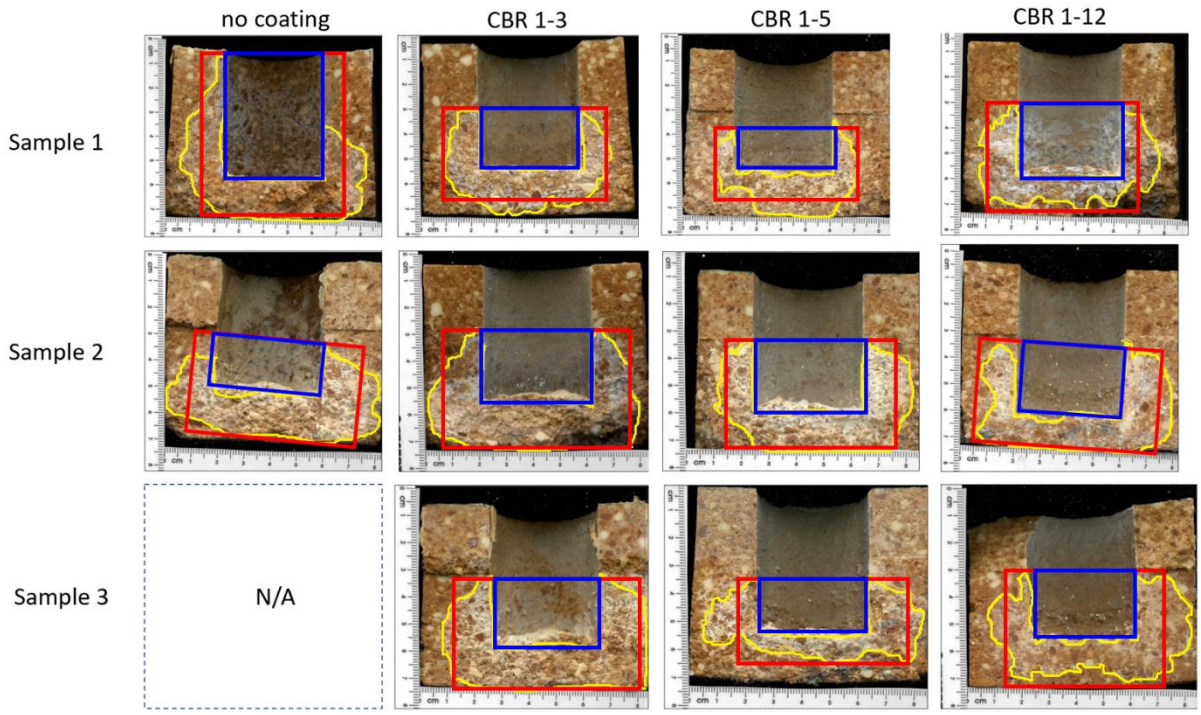


Figure 114. Scanned images of uncoated cup, cup coated with CS 1-3, 1-5 and 1-12. Yellow lines indicate boundaries of the area where alkaline has saturated in the cups. Blue squares represent edge of inner cup and red squares represents an average area of alkaline saturated area.

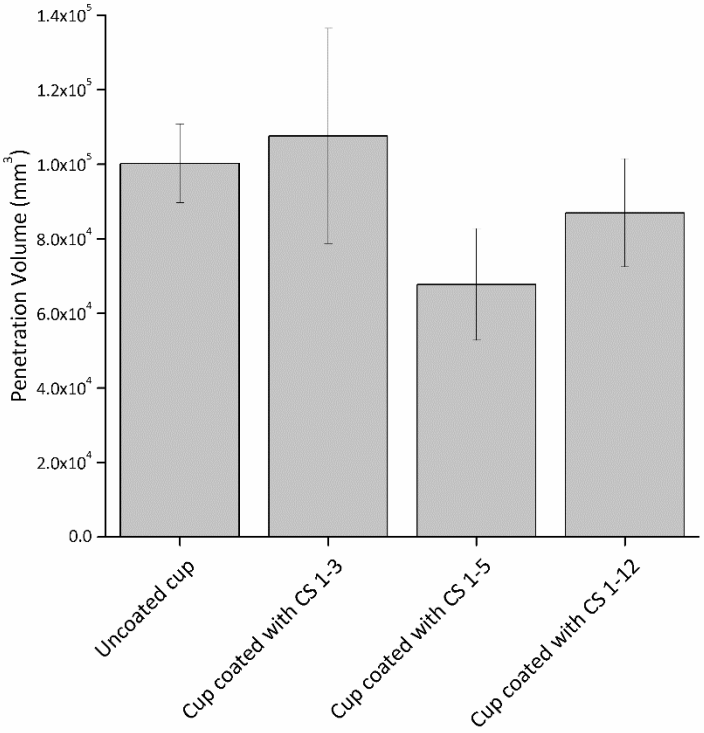


Figure 115. Alkaline penetration volume of uncoated cups, and cups coated with CS 1-3, 1-5 and 1-12 showing that there is no significant difference between each sample.

These results reveal that coated and uncoated cups have a low corrosion volume compared to penetration volume indicate that alkaline is more likely to penetrate through the specimen than to corrode them. It must be kept in mind that the cup test is a static measurement and hence, the corrosion is not as severe as a dynamic measurement. If a dynamic measurement was conducted, the corrosion volume could be higher due to the flow and movement from the corrosive source (alkaline) leading to higher corrosion. Comparing corrosion volume results of all the samples revealed that cups coated with CS 1-3 have the lowest corrosion volume. This is because CS 1-3 contain the highest amount of $CeO_2$, which is an alkaline resistant material, compared with the other coatings (CS 1-5 and CS 1-12) as shown from the XRD results in section 4.2.2.2. As for the penetration results, there was not a significant difference among the cup samples indicating that alkaline penetrates through pores and cracks which are present in all coatings. This means none of the coatings can prevent the alkaline from reaching through to the substrate.

## 6.3 Discussion of Corrosion Test Results

This chapter has measured alkaline corrosion using two different tests: alkaline vapour test and static cup test. This section discusses the findings of each test.

### 6.3.1 Alkaline vapour test - alkaline vapour reaction with BR and coatings

The vapour test revealed an alkaline reaction with the basic refractory and the coatings. $K_2CO_3$ decomposes to $K_2O$ and $CO_2$ at temperature above 1200°C as present in Equation 65. Carbon dioxide ($CO_2$) unlikely to react with either the coating or the refractory brick. On the other hand, $K_2O$ does as revealed by the microstructure changes presented in Figure 106 and Figure 107. Alkaline vapour reacting with the glassy phase in the coatings creating a melt-like structure. The alkaline vapour interferes with the Mg-P-O glass structure by inserting K into the glass structure at high temperature, where the glass phase in the coating melts, breaking the P-O-P bond. A schematic diagram of K interacting with the Mg-P-O glassy phase is presented in Figure 116. This is similar to previous research in which attempts were made to add metal ions into the $P_2O_5$ glass structure to increase the glass durability [187-189]. Potassium ion ($K^+$) has an ionic radius of 290 pm which is much larger than for other ions in the glass ($Mg^{2+}$ 173 pm, $P^{5+}$ 195 pm and $O^{2-}$ 60 pm), therefore, adding potassium ions into a glass structure leading to structure stress. Potassium phosphate glass has a high thermal expansion, therefore, as the coating cools it also has a high shrinkage leading to thermal expansion mismatch as mentioned in section 2.5. Table 23 presents TEC of the substrate and the coating materials which shows that the potassium phosphate's TEC is significantly higher than the other materials leading to a high thermal expansion mismatch. Therefore, increasing melt-like structure effects potential for cracks to form in the coating. Alkaline could also have reacted with $CePO_4$. Even though there is no available phase diagram between $CePO_4$ and $K_2O$, there is a binary phase diagram between $CePO_4$ and $K_3PO_4$ in which $K_3PO_4$ is a product of reaction between $K_2O$ and $P_2O_5$. Although this diagram is not a direct reaction between $CePO_4$ and $K_2O$, it may be useful as a guideline. The binary phase diagram of $CePO_4$ - $K_3PO_4$ (Figure 117) showing a eutectic point at 1380°C. The only interaction between $CePO_4$ and $K_3PO_4$ was $K_3Ce(PO_4)_2$ which melts at 1500°C ±20. Both temperatures; first liquid (1380°C) and product melting point (1500°C ±20) are higher than our testing temperature, therefore, it is possible that $CePO_4$ does not have a significant reaction with alkaline vapour at temperatures ≤ 1300°C.

Equation 65 $K_2CO_3 \leftrightarrow K_2O + CO_2$ at ≥ 1200°C

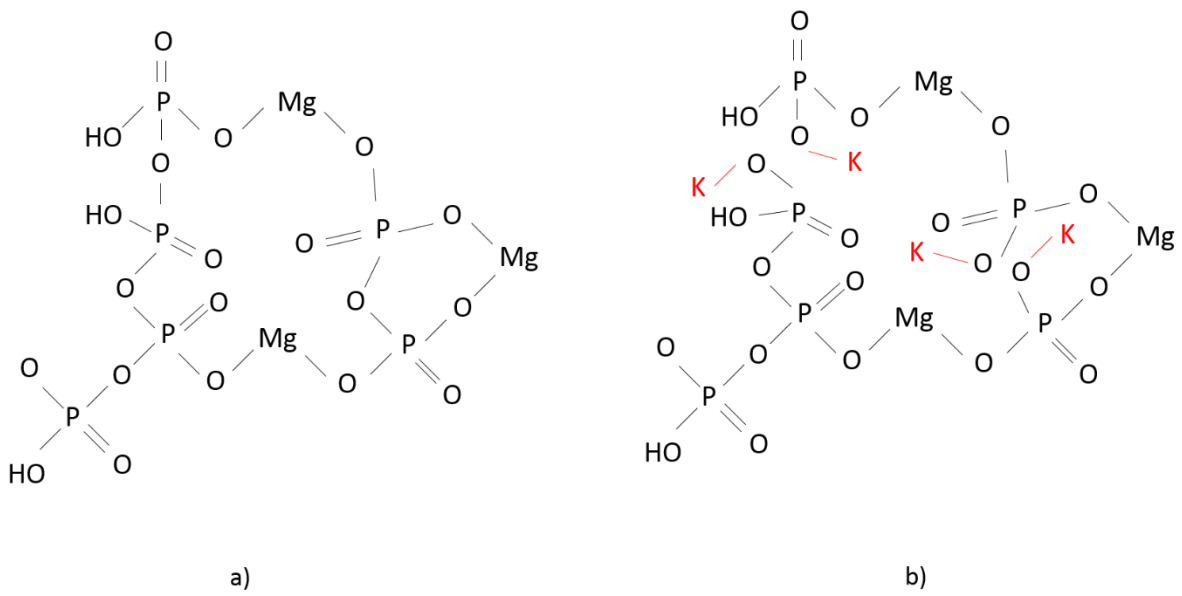


Figure 116. Schematic of phosphate glass structure. a) Mg-P-O glass (coating matrix) b) K replacing itself in the glass by breaking the P-O-P bond causing stress in the structure (author's figure).

Table 23. TEC of cerium oxide [144, 190], cerium phosphate [191], potassium phosphate glass [142, 143] and refractory brick.

| | Materials | TEC ($K^{-1}$) |
|---|---|---|
| Materials in the coating | Cerium dioxide | 12-16 X $10^{-6}$ at 1200°C |
| | Cerium phosphate | 10-13 X $10^{-6}$ at 1300°C |
| | Potassium phosphate glass | 20-24 X $10^{-6}$ at 1050°C |
| Substrate | Refractory brick | ~13 X $10^{-6}$ at 1300°C |

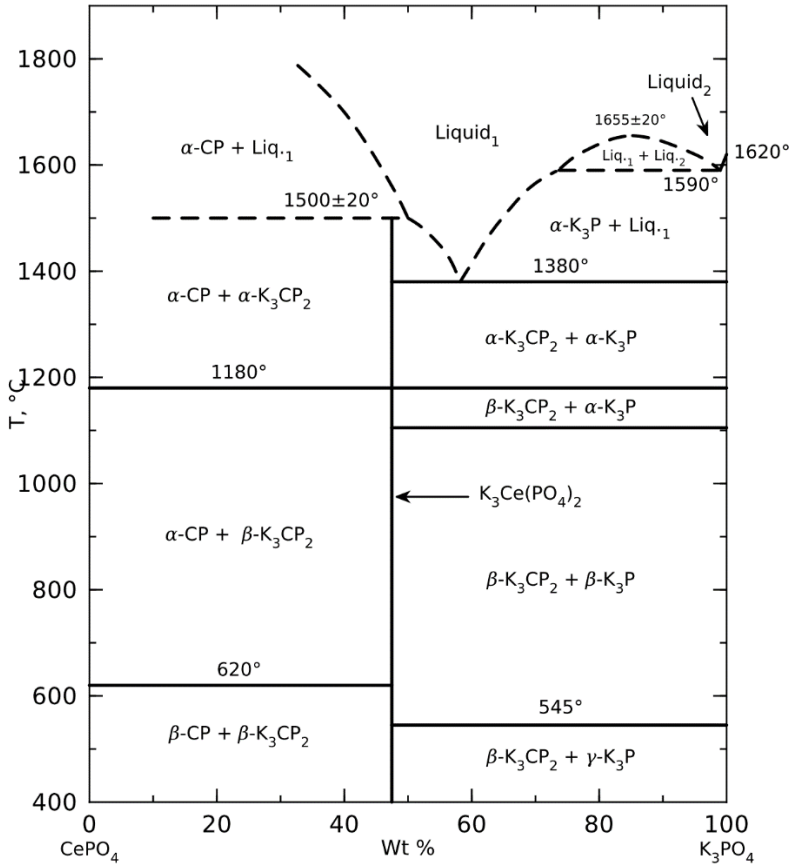


Figure 117. Binary phase diagram of $CePO_4$ - $K_3PO_4$ showing a eutectic point at 1380°C [192, 193].

The alkaline travels through the coating and cracks to the substrate. The alkaline also influences the substrate, especially the $MgAl_2O_4$. $K_2CO_3$ reacts with the $MgAl_2O_4$ spinel at 600-1200°C and forms $KAlO_2$ (Equation 66) . At temperature above 1200°C, $K_2O$ reacts with the refractory material. The reactions between $K_2O$, MgO and $MgAl_2O_4$ are presented in Figure 118 as a red triangle in a ternary phase diagram of $Al_2O_3$-$K_2O$-MgO. It is possible that $K_2O$ reacts with $Al_2O_3$ and forms $KAlO_2$, similar to the reaction that Naeshirozako [122] reported ($Na_2O$ reacts with $Al_2O_3$ and forms $NaAlO_2$, section 2.3). The ternary eutectic (red dot in Figure 118) in the region of interest; $MgAl_2O_4$-$K_2O$-MgO, is among the three phases which are $KAlO_2$, MgO and $MgAl_2O_4$ (~1818°C [194]). Figure 119 presents the possible phases of $Al_2O_3$-$K_2O$-MgO at 1300°C, which is the experimental corrosion temperature examined in this thesis. Product phases occur differently (Liquid + MgO + $KAlO_2$ or $KAlO_2$ + MgO + $MgAl_2O_4$) depending on the quantity of the original substance. Although pure $K_2O$ in the phase diagram is present as a liquid, previous studies report that it also evaporates and generates alkaline vapour [195, 196].

Equation 66 $K_2CO_3 + MgAl_2O_4 \rightarrow 2KAlO_2 + MgO + CO_2$ at $\geq 600$°C

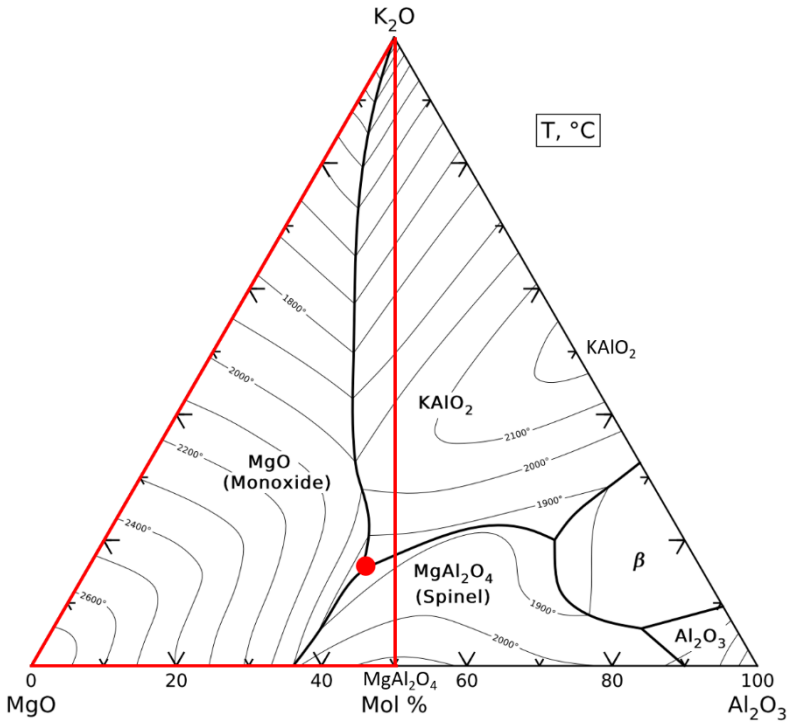


Figure 118. $Al_2O_3$-$K_2O$-MgO ternary phase diagram. The red triangle is the $MgAl_2O_4$-$K_2O$-MgO region and the red dot represents a eutectic point among $MgAl_2O_4$-$KAlO_2$-MgO (modified from [194, 197]).

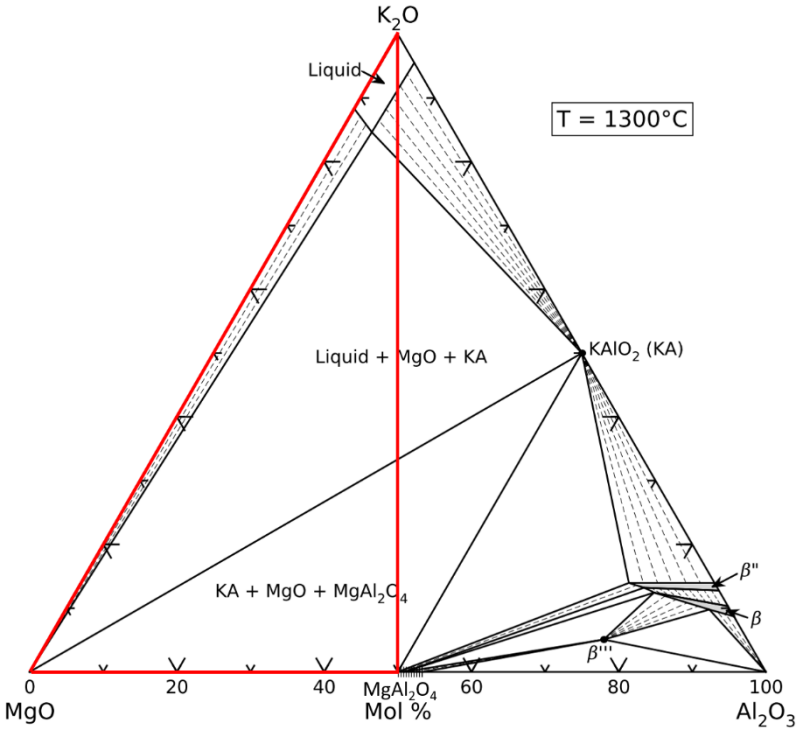


Figure 119. $Al_2O_3$-$K_2O$-MgO ternary phase diagram at 1300°C. The red triangle represents a $MgAl_2O_4$-$K_2O$-MgO ternary phase diagram at 1300°C (modified from [194, 198]).

### 6.3.2 Static cup test - alkaline corrosion and penetration

Static cup test revealed alkaline corrosion (where material loss occurs) and penetration (physical penetration of the alkaline through the sample) on basic refractory and coatings. This part discusses possible reasons for alkaline penetration and corrosion in the cup tests. $K_2CO_3$ melting point is ~895°C (Figure 12a), therefore, during heating from 895°C to 1200°C, the $K_2CO_3$ melts penetrates through the coating pores and cracks, through to the basic refractory cup behind it. Once the $K_2CO_3$ melt reaches the refractory cup, it continues to penetrate through the cup pores leaving an alkaline stain. All coatings contain cracks which is the reason why all samples gave similar alkaline penetration results. Alkaline penetrating into the refractory bricks can lead to brick distortion from volume expansion ($K_2CO_3$ TEC is 43.3 X $10^{-6}$ $K^{-1}$) and density gradient which can leads to spalling as mentioned in section 2.3. As for corrosion, alkaline should not have a significant effect with $CeO_2$ and $CePO_4$ as discussed in section 6.1.2. Alkaline corrosion with the M-P-O glass can be complicated. $K_2CO_3$ reaction with M-P-O glass is discussed in section 6.3.1. As the temperature increases $K_2CO_3$ decomposes to $K_2O$ at about 1200°C. Many reactions can occur depending on the quantity of the initial substance as presented in a partial phase diagram of $K_2O$-MgO-$P_2O_5$, Figure 120. In this research, the reaction between $K_2O$ and M-P-O glass generates melt-like structure which needs further identification (see Chapter 9) because reactions between $K_2O$ and the M-P-O glass could also form a low melting phase such as $KMg(PO_3)_3$ ($B_1$, Figure 120 ), melting point at ~900°C, and this has to be prevented from happening. Alkaline corrosion reactions with the refractory brick should be similar to those discussed in section 6.3.1; at temperature 600-1200°C, $K_2CO_3$ reacts with $MgAl_2O_4$ and form $KAlO_2$ (Equation 66). Above 1200°C, $K_2CO_3$ decomposes to $K_2O$ (Equation 65) which reacts with $Al_2O_3$ in the $MgAl_2O_4$ and also forms $KAlO_2$ (Figure 119).

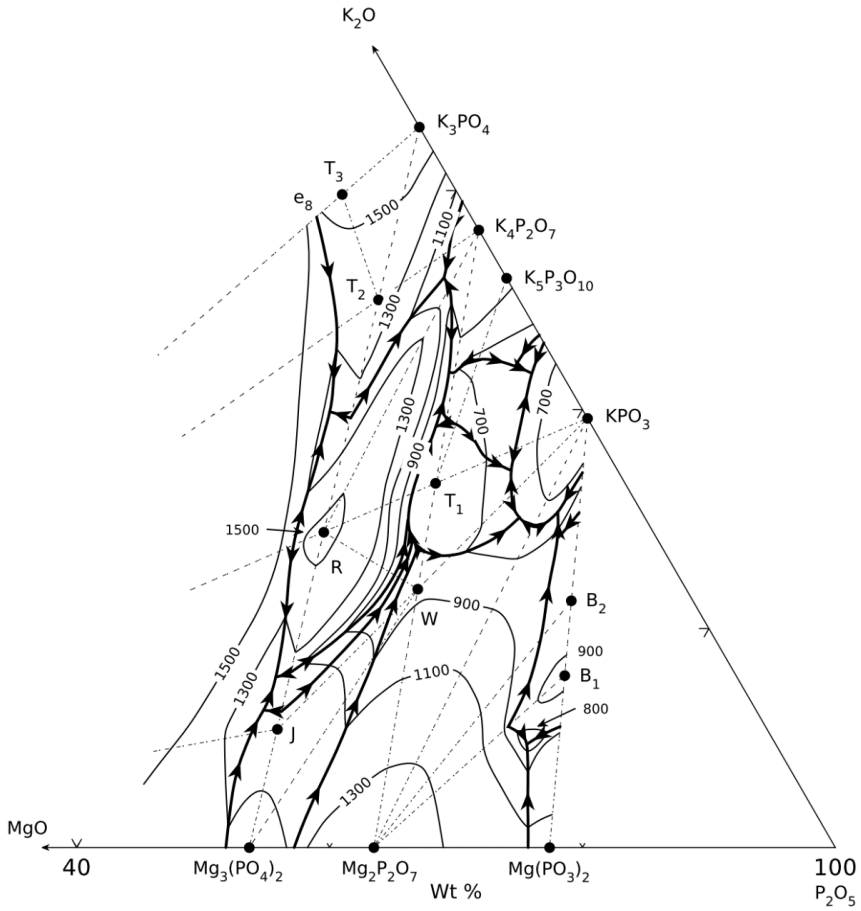


Figure 120. A partial ternary phase diagram of $K_2O$-MgO-$P_2O_5$. R is $KMgPO_4$. J is $KMg(PO_4)_3$. W is $K_4Mg_4P_6O_{12}$. $T_1$ is $K_2MgP_2O_7$. $T_2$ is $K_4Mg(PO_4)_2$. $T_3$ is $K_6MgP_2O_9$. $B_1$ is $KMg(PO_3)_3$. $B_2$ is $K_2Mg(PO_3)_4$ [199].

It is a challenge to rank the cup specimens because none of the cups gave an outstanding result. Although the cup specimens were not able to be ranked, they can be fitted into the four scenarios described at the end of section 3.4;

scenario 1: low alkaline corrosion and low alkaline penetration

scenario 2: low alkaline corrosion and high alkaline penetration

scenario 3: high alkaline corrosion and low alkaline penetration

scenario 4: high alkaline corrosion and high alkaline penetration

The uncoated cup, cups coated with CS 1-5 and 1-12 fall into scenario 4 and cups coated with CS 1-3 fall in scenario 3 (for the reasons mentioned at the end of section 6.2). Therefore, the cup coated with CS 1-3 is the one that gives the best corrosion resistance.

The effect of alkalis on the coating and refractory substrate is summarized in Figure 121. Figure 121a presents the measurement set up at room temperature, the alkaline source ($K_2CO_3$) is on top of the coating which contains $CeO_2$, $CePO_4$ particles, M-P-O glass and pores. The coating is located on the refractory brick substrate which contains MgO, $MgAl_2O_4$ and pores. Figure 121b presents the system being heated at 895-902°C, where $K_2CO_3$ has melted. Several reactions are possible at this temperature.

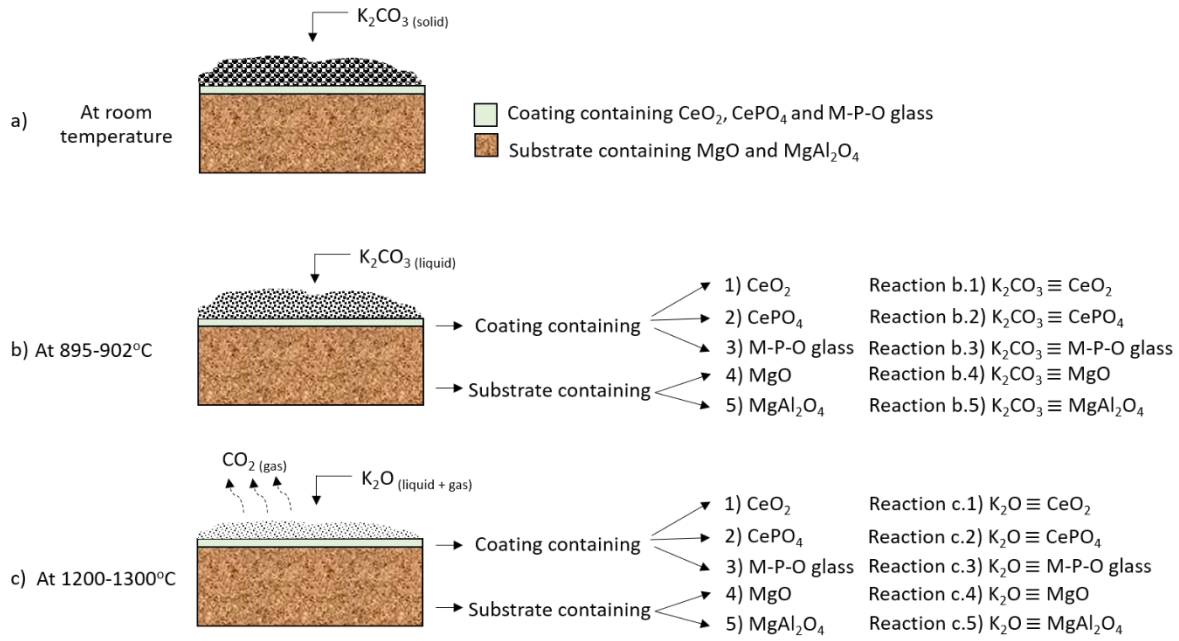


Figure 121. Schematic diagram summarizing alkaline reactions with the coating and refractory substrate at different temperatures; a) at room temperature, b) at 895-902°C and c) at 1200-1300°C.

b.1) There is no significant reaction between $K_2CO_3$ and $CeO_2$ as discussed in section 6.1.2.

b.2) Reaction between $K_2CO_3$ and $CePO_4$ is still unknown and further study is needed (discussed further in chapter 9).

b.3) Reaction between $K_2CO_3$ and the M-P-O glass is still unknown and further study is needed (discussed further in chapter 9).

b.4) Reaction between $K_2CO_3$ and MgO reduces the MgO melting point from ~2850°C to ~895°C as revealed by the phase diagram in Figure 12a.

b.5) Reaction between $K_2CO_3$ and $MgAl_2O_4$ (spinel) generates $KAlO_2$ corroding the spinel and leaving pores in the spinel (Equation 66 section 6.3.1).

As temperature increase to 1200-1300°C (Figure 121c), $K_2CO_3$ decomposes to $K_2O$ and $CO_2$ (Equation 65) and the reactions between $K_2O$ and the coating and refractory substrate are as follows.

c.1) There is no significant reaction between $K_2O$ and $CeO_2$ as discussed in section 6.1.2.

c.2) There is no hard evidence on the reaction between $K_2O$ and $CePO_4$ at 1300°C. However, looking at the reaction between $CePO_4$ and $K_3PO_4$ (Figure 117), $K_3PO_4$ is a product between $K_2O$ and $P_2O_5$. The eutectic point is at 1380°C which is higher than the experiment temperature. The solid-state reactions were mostly structured formation changes. The only reaction occurs when the ratio between $K_3PO_4$ and $CePO_4$ is 53:47, $K_3Ce(PO_4)_2$ is formed and has a melting point of 1500 ±20°C which is higher than the experiment temperature. Although the reactions between $K_3PO_4$-$CePO_4$ and $K_2O$-$CePO_4$ are not the same, they should be indicative and able to predict that $K_2O$-$CePO_4$ reactions may occur at a temperature higher than 1300°C. Therefore, there should not be a significant reaction between $K_2O$ and $CePO_4$ at 1300°C.

c.3) Reactions between $K_2O$ and the M-P-O glass generates MLS. Figure 120 shows that, depending on the original composition, the final product from the reaction can be a high melting phase such as $KMgPO_4$ (R in Figure 120, eutectic point at ~1520°C) or a low melting phase such as $KMg(PO_3)_3$ ($B_1$ in Figure 120, melting point at ~900°C). K can also be inserted into the glass structure generating stress in the glass. Having more glass in the coating also leads to cracks from thermal expansion mismatch from TEC differences.

c.4) and 5) Reaction between $K_2O$, MgO and $MgAl_2O_4$ are as discussed at the end of section 6.3.1. The final composition depends on the original composition. Possible products at 1300°C are Liquid + MgO + $KAlO_2$ or $KAlO_2$ + MgO + $MgAl_2O_4$.

# Chapter 7: General Discussion

## 7.1 Innovation in this study

The data from this research has revealed that using $CeO_2$ with $AlH_6O_{12}P_3$ solution as a starting material for high emissivity coatings leads to four main phases after sintering at 1300°C for 3 h. The phases are unreacted $CeO_2$, $CePO_4$, M-P-O glass and pores. The coatings containing these phases have proven to be easily applicable to a basic refractory brick by gun spray and give emissivities of ~0.8 at 1300°C in the wavenumber range of 9000-12000 $cm^{-1}$. This result has shown potential for use of the coating as a high emissivity coating for energy-saving purposes. This removes the ambiguity on whether $CeO_2$ can provide high emissivity value to a coating when it is applied by a conventional process like a gun spray onto a refractory ceramic. Holcombe Jr *et al.* [56] have claimed to use $CeO_2$ as high emissivity material applied by painting but they did not provide any emissivity measurements. On the other hand, Huang *et al.* [76, 77] have measured $CeO_2$ coatings and have proven that they provide high emissivity, however, Huang's coatings were developed for TBCs application, in which the coatings were applied via APS or EB-PVD techniques onto stainless steel, alloy or Inconel substrates, and the emissivities of the coatings were only measured at a temperature of 1000°C, which is too low for cement-kiln application. Comparison between coatings in the literature and this research is presented in Table 24; this research results have filled in the gaps which are highlighted in grey. Moreover, the research has also contributed additional information on the EBCs application. There has not been much study on emissivity for EBCs application although rare earth oxide use in EBCs application has been studied to improve water vapour resistance [64, 65]. Therefore, our emissivity study, which proves that rare earths can be used as emissive materials for coating applied via slurry gun spray on ceramics, suggest that it should give a similar effect for EBC's applications in which the coating can be applied in a similar manner and on a ceramic substrate.

Table 24. Comparison between conventional coating for furnaces with the thermal barrier coatings (TBCs) and environment barrier coatings (EBCs) technology

| | Application | Applying technique | Substrate | Emissive materials | Emissivity measurement |
|---|---|---|---|---|---|
| Literature | Coating for furnace | Paint, gun spray | Ceramic | Code names, carbon black and rare earth materials | No |
| | TBCs | APS, EB-PVD | Stainless-steel. Alloy and Inconel | Rare earth materials | Yes, up to 1000$^{o}$C |
| | EBCs | APS, EB-PVD, sputtering, slurry deposition | Ceramics, CMCs most likely to be silica base | - | No |
| This research | Coating for cement rotary kiln | Gun spray | Ceramic (basic refractory) | Rare earth ($CeO_2$) | Yes, up to 1500$^{o}$C |

The coatings may have shown an improvement in emissivity; however, they did not show an improvement in alkaline corrosion resistance. Previous studies reported that alkaline corrosion is either from alkaline reacting with the specimen to form a melt formation, change in density and volume, expansion of salt in pores and water condensation inside the refractory [111, 112]. The corrosion results in this experiment are in line with the literature, especially between the alkaline ($K_2CO_3$) and the M-P-O glass in the coating. The reaction has caused a melt-like structure that leads to cracks in the coating. The cracks act as pores and channels for the alkaline to travel through to the substrate. The alkaline and the substrate also react to form melts. A key lesson learned from this thesis that M-P-O glass is an undesirable phase for alkaline corrosion resistance. There have been few previous reports on rare earth alkaline resistance, but this research has provided information that $CeO_2$ shows little to no reaction with the alkaline and is considered a good candidate for alkaline corrosion resistance. $CePO_4$ shows greater potential to react with alkaline than $CeO_2$ but the reaction is more likely to occur at a temperature higher than 1300$^{o}$C and therefore, $CePO_4$ may also be a candidate for alkaline corrosion resistance.

## 7.2 Overall discussion of results.

This research has revealed that the unfired $CeO_2$-$AlH_6O_{12}P_3$ reacts on firing to produce a coating containing $CeO_2$, $CePO_4$ particles, Mg-P-O glass matrix and pores. This section discusses what effect these phases have on emissivity and corrosion.

The presence of $CeO_2$ confers the high emissivity on the coating. This was confirmed by comparing emissivity values of BR, CBR and $CeO_2$ pellet at ~1300°C as discussed in section 5.3.1.2. $CeO_2$ is resistant to alkaline corrosion as revealed by the results presented in section 6.1.2.

The effect of the presence of $CePO_4$ on the coating emissivity is not clear. However, it has the potential for high emissivity because it also contains a cerium cation with high atomic number that can easily be thermal activated. However, further measurements of pure $CePO_4$ are needed to confirm this assumption. If $CePO_4$ is proven to also give high emissivity, this would be the first time such behaviour has been determined in a rare earth phosphate. While they may be positive for emissivity identifying $CePO_4$ effects on alkaline corrosion is a challenge because the particles are small (~2μm, Figure 72c), and are mostly embedded in the glass phase (Figure 108) so it is difficult to distinguish them from the glass. However, the $CePO_4$- $K_3PO_4$ phase diagram indicates that $CePO_4$ is more likely to interact with alkaline at a temperature higher than 1300°C.

The effects of Mg-P-O glassy phase on emissivity need further investigation. However, it does have an effect on alkaline corrosion. Although alkaline corrosion was briefly studied in this thesis, it can be concluded that the coating is not alkaline proof. This is because at high temperature the Mg-P-O glass melts and reacts with potassium vapour creating a melt-like structure in which cracks are generated during cooling. However, the problem is when the coating is being used in the cement rotary kiln, the cement clinker dust can easily abrade the coating off the basic refractory. This means the energy will not be saved, and the cost that was put into the coating would be wasted. In summary, the glassy phase is an unwanted phase in the coating and further investigation is needed to reduce the content of this phase as much as possible.

Pores in the coating structure might give a positive effect on emissivity as they might act as a blackbody as Huang *et al*. [76] have reported. However, further study is needed to confirm this concept because of the differences in this study and Huang *et al.'s*, especially the applying technique in which they used an EB-PVD technique while we used a gun spray technique. To ensure that there is no hidden factor in these differences, the emissivity of a denser coating, prepared in the same fashion as this research, should be used for comparison. On the other hand, the impact of pores on

corrosion resistance depends on their type. Open pores would lower corrosion resistance because they act as channels for alkaline vapour to penetrate through to the substrate. Closed pores have less effect on corrosion resistance. Pores in the coating in this thesis are more likely to be closed pores (Figure 72). It must be noted that while closed pores might not have a major effect on corrosion, they are likely to have a major effect on abrasion resistance. In the rotary kiln, there is harsh cement clinker dust that might scrub the coating off and again energy would not be saved, and the cost put into the coating would be wasted. In another aspect, pores can also beneficially induce low thermal conductivity but it must be kept in mind that the coating is thin and its conductivity is dependent on thickness as present in Equation 1, therefore, it would only save a very small amount of heat.

From the overall discussion of results, we can make the conclusions in Table 25.

Table 25. Impact of each phase in the coating on emissivity and corrosion resistance.

| Phase in the coating | Emissivity | Corrosion resistance |
|---|---|---|
| $CeO_2$ | Good | Good |
| $CePO_4$ | Maybe good but need more study | Maybe good but need more study |
| Mg-P-O glass | Not enough information to conclude | Not good |
| Pores | Maybe good but need more study | Open pores not good<br>Closed pores neutral |

## 7.3 Economic aspects of the coating

Knowing the emissivity values of the basic refractory bricks with and without the high emissivity coatings, made it possible to estimate energy saving and cost saving. Energy saving is 14,506,186 W (109,180,691 MCal/year) and cost saving is 1,091,807 USD/year (~850,000 GBP/year) for cement produced in a 4 m diameter and 12 m in length kiln, for 1 year (as calculated in section 5.3.3). The coating cost of CS 1-3 was estimated to be 30,000 GBP for the materials to coat the same size kiln for 120 µm thickness (as calculated in section 4.3.3). A brief calculation of the breakeven point is approximately 13 days. The coating has proven that it can potentially save energy and cost from its emissive function, but it has not yet been proven about its lifetime. The longer the coating lifetime, the greater the cost saving. However, the environment in the cement kiln is severe, containing

corrosive gas (alkaline gas), abrasion from the cement clinker dust and high fluctuation of temperature (thermal shock). All these factors must be considered to estimate the coating lifetime. If the coating is not well developed it is unlikely to last even 13 days.

# Chapter 8: Conclusions

Energy consumption in the cement industry is massive. Raw materials must be heated to temperatures as high as 1450°C in a rotary kiln. Unfortunately, 40% of the input energy is lost from heat, with 20% of the heat being lost through the rotary kiln shell. This thesis addresses this problem by developing a high emissivity coating that can be applied to the basic refractory bricks, in the upper transition zone, inside the rotary kiln. The function of this high emissivity coating is to absorb the heat and re-emit it back inside the rotary kiln, which will lead to energy savings.

The review of the literature on coatings for energy savings divided the coating use into two main segments: traditional coating and advanced coating (TBC and EBC). Both types have their advantages and disadvantages with regard to this research. The traditional coating uses ceramics as a substrate and a simple application technique (gun spray, paint) which matches the aims of this research; however, the literature on the traditional coating lacks the emissivity measurements and material details, as code names are commonly used in this research area. In contrast, the advanced coating uses Inconel or stainless steel as substrates, and ASP or EB-PVD are used as the coating application technique, which does not match the research aims but this type of coating has been used for emissivity measurements and the material details are presented. Combining the traditional and advanced coating types, this research has conducted emissivity measurements on coatings that contain a highly emissive material from the advanced coating segment, in which the coating is applied via air gun on a ceramic surface (basic refractory brick), from the traditional coating segment.

The research started with mixing $CeO_2$ (emissive material) and $AlH_6O_{12}P_3$ (binder). The materials were mixed with different ratios ($CeO_2$- $AlH_6O_{12}P_3$; 1-3, 1-5 and 1-12 volume ratios) to produce coating slurries that were prepared for analysis by four main methods.

1. The coatings slurries were used as-is for rheology, DSC, and TGA measurements.
2. The coating slurries were calcined at 600°C, 1 h for HT-XRD measurements.
3. The coatings slurries were heat treated at 1300°C, 3 h for XRD, XPS, density measurements.
4. The coating slurries were gun sprayed onto a basic refractory substrate then were sintered at 1300°C, 3 h, SEM, TEM, emissivity and corrosion testing.

The results from the measurements were used to construct the information presented in this thesis and are separated into three main sections: the coating phase evolution and microstructure,

the coating emissivity testing and the coating corrosion testing. The main conclusions from each of these sections are presented below.

- Coatings containing $CeO_2$ and $AlH_6O_{12}P_3$ phase evolution and microstructure were examined. As the temperature was increased, the $CeO_2$ reacted with the $AlH_6O_{12}P_3$ generating $CePO_4$ crystals, Mg-P-O glass and pores. The reactions started with the dehydrogenation of the $AlH_6O_{12}P_3$ at approximately 500°C and $CePO_4$ crystals started to form at about 850°C. Although the amount of the new phases generated was not fully quantified, the amounts were determined to be dependent on the coating composition from the XRD peak intensities. The higher the $CeO_2$: $AlH_6O_{12}P_3$ ratio the higher the $CeO_2$ remaining after the firing reactions and the less $CePO_4$ was generated. The $CeO_2$: $AlH_6O_{12}P_3$ ratio also has an impact on the coating rheology and cost. The higher the ratio, the more viscous the coating is and the more expensive.
- The emissivity of the coatings sprayed on the basic refractory substrate was measured with two different methods: radio emissivity measurement (REM) and infrared emissivity measurement (IREM). The coating emissivity measured by the REM method did not show a significant difference compared with the uncoated sample due to the frequency used in the measurement (radio frequency) being too low. On the other hand, the coated sample measured with the IREM (infrared range) showed a significant improvement of about 100% compared to the uncoated sample due to the presence of $CeO_2$ in the coating has a high thermal activation, which leads to high lattice vibration and polaron absorption. Measuring the emissivity with the IREM also indicated that the emissivity is dependent on temperature, the different ratios between $CeO_2$ and $AlH_6O_{12}P_3$ did not result in any significant effect on the emissivity and the coating thickness of ~120 μm is sufficient for the emissivity to perform well.
- The corrosion tests were conducted using two methods: the alkaline vapour test and the static cup test. The samples used in these experiments included the basic refractory brick and the refractory brick coated with coating slurry containing $CeO_2$ and $AlH_6O_{12}P_3$ in the volume ratios of 1-3, 1-5 and 1-12. The alkaline vapour test results indicated that the alkaline had corroded the $MgAl_2O_4$ spinel present in the basic refractory brick, generating $KAlO_2$ and leaving pores in the grains. As for the alkaline reaction with the coating, the alkaline reacted with the M-P-O glassy phase in the coating, which at high temperatures is melted, generating a melt-like structure. This melt-like structure cracked during the cool down from high thermal expansion and shrinkage. However, it must be kept in mind that, in the real application, the melted glass in the coating will make the coating easily abrade off from the clinker dust. As for the static cup test results, all of the samples, both with and without the coating, gave a similar result regarding the alkaline vapour volume penetration. As for the alkaline

volume corrosion, the coated basic refractory 1-3 (CBR 1-3) demonstrated the lowest corrosion material loss after the static cup test. Although CBR 1-3 might have the best corrosion resistance compared to the other coatings, improvement in its corrosion resistance is still needed, especially regarding solving how to reduce the glassy phase in the coating.

The experiments that were conducted have led us to two main findings

1. Regarding the knowledge contribution to the field, conducting these experiments has decreased the gap between the traditional and advanced coatings. The research has shown that a coating containing emissive material such as $CeO_2$, known from the advanced coating, can also be applied and used on basic refractory brick similar to the traditional method and provide high emissivity results.

2. Regarding the possibility of the coating being used in the cement rotary kiln application, this thesis has proven that the coating developed in this research provides high emissivity in the infrared range and that the coating will only be economical if it lasts in the cement rotary kiln for longer than 13 days (for coating CS 1-3 used in a kiln with a 4 m in diameter and 12 m in length kiln and a coating thickness of 120 μm). This may help the industry save up to 850 thousand GBP if the coating is fully functional in the kiln for a year. However, the coating was not fully tested for alkaline corrosion resistance, and this is not the only limitation that this coating has. The environment inside the cement kiln is not only filled with rich alkaline corrosion products but it is also filled with cement clinker dust, which can easily abrade the coating off and sudden change in temperature (thermal shock). This type of temperature change can cause the coating to crack and peel off the substrate. Therefore, further studies and improvement on these aspects are needed in order to be able to confirm whether the use of this coating is worthwhile as an energy-saving coating in cement rotary kilns.

# Chapter 9: Further Work

This research has worked on understanding the high emissivity coating phase evolution with temperature, emissivity and alkaline corrosion resistance. However, during the experiment, there are weaknesses and factors that were not considered which need further examination. The weaknesses and experiments that need improvement are mentioned below.

- As presented in section 4.2.2.4, the coating microstructure is heterogeneous. A possible way to improve the coating homogeneity is by adding a dispersion agent to avoid $CeO_2$ sedimentation. However, due to the large particle size (~10µm) of the $CeO_2$, as commercially received, and its high density (7.22 g/cm$^3$), the $CeO_2$ powder might need to be subject to further grinding for the dispersion to work effectively. Two things should be borne in mind; 1) grinding dense materials such as $CeO_2$ can be time consuming and expensive, and 2) grain size has an influence on emissivity. Jones *et al.* [183] reported that larger grain size gives higher emissivity [183]. Another way to approach coating homogeneity is to try new binders. As discussed in section 4.3.1 the $AlH_6O_{12}P_3$ binder starts to dehydrogenate at about 500°C generating gases in the coating which later become pores. Therefore, other binders such as colloidal alumina, should be studied and compared with this research.
- For a better understanding of how the $CeO_2/AlH_6O_{12}P_3$ ratio affects the coating composition at high temperature, Rietveld refinement for quantifying phase contents should be done. Knowing the actual fired coating composition can help to calculate the coating density. It can also help to understand the phases that are possible to form when the coating is attacked by alkaline.
- $CePO_4$ has the potential to give high emissivity, however, a study needs to be made to determine its properties. Pure $CePO_4$ should be used for emissivity measurement at different temperatures in the infrared range. $CePO_4$ emissivity in the infrared range has not yet been reported, by conducting the emissivity measurement can contribute new information to the emissive material field.
- As discussed in section 5.3.1.2, surface roughness effects emissivity. Therefore, future studies should take surface roughness into account. Emissivity experiments on samples with different roughness should be conducted to find the optimum surface roughness that functions best in the infrared range at different temperatures.
- This thesis has shown that a coating thickness of 120 µm is sufficient for the coating to be opaque to heat flux. Research should investigate how thin the coating can go down to before it starts to become translucent to heat flux and can still confer high emissivity. The thinner the coating gets, the lower the coating cost will be and is better for thermal shock resistance as mentioned in

section 2.4.3. However, the thinner the coating, also means the more easily the coating can be abraded off by the cement clinker dust. Therefore, the coating thickness must be carefully optimized.

- How alkalis effect the coating and refractory materials needs further investigation. For example, reactions between $K_2CO_3$ with $CePO_4$ and M-P-O glass is still unknown. It must be kept in mind that, although understanding every reaction in the experiment is essential, in the real cement application alkalis are more likely to come in the form of vapour other than $K_2CO_3$ solid or liquid. Therefore, it might not be a priority investigation. Experiments on reactions between $K_2O$ and M-P-O should be studied because they have a complex relationship and if the composition is not right, a low melting phase is formed which will not benefit the application.
- Measuring the coating emissivity after corrosion testing would give useful information. It would help to determine how the new phases, formed from corrosive attack, affect the coating emissivity. If the new phases have no effect on emissivity, then the coating is likely to continue to give energy saving for as long as the coating is attached to the refractory substrate. On the other hand, if the new phases reduce the coating emissivity, the coating is then no longer useful for energy saving.

Problems still needing to be resolved for successful use of high emissivity coatings in a cement rotary kiln include:

- Corrosion

Initial corrosion testing studied in this thesis revealed that the developed coating is not alkaline vapour resistant because of cooling stress, thermal expansion mismatch with the substrate and alkaline reacts with Mg-P-O glass generating stress and cracks. Reducing cracking can be achieved by either control of the reaction between the alkaline and the Mg-P-O glass or studies on other binders that have better corrosion resistance. Another improvement needed is to develop the corrosion test method. Corrosion tests performed in this thesis were alkaline vapour test and static cup test all of which are static tests but well known to be simple and informative. However, for cement rotary kiln application where the kiln rotates, conducting dynamic corrosion tests would provide a better understanding of corrosion [123].

- Adhesion and abrasion

Adhesion and abrasion tests determine how well the coating and the substrate are attached together. There are several methods to measure adhesion (see section 2.4.1). However, there are not yet any standards to measure adhesion at a temperature as high as 1300$^{o}$C. Abrasion tests measure

abrasive between the coating and the substrate. The environment in the cement kiln is harsh and finding suitable testing that represents the real condition is important. Wellmen *et al*. [134] developed an instrument (section 2.4.2) which shows promise due to its adjustable parts. If the sample chamber can be modified to be able to heat to 1300$^{o}$C and the sample holder can be adjusted to approaching 180$^{o}$ (parallel) to the abrasive material and air velocity path, this method would be more representative of the situation in a cement rotary kiln.

- Thermal shock

Cement rotary kiln heating source is a flame burner and there is uncertainty as to the flame direction. The burner flame shape and size are controlled by the kiln operaters. The flame can be adjusted to be long and thin or short and wide depending on the on-site situation they are facing. Therefore, there is a high temperature fluctuation (high thermal shock) in the kiln. To ensure that the coating has the potential to survive in the rotary kiln, thermal shock resistance is one of the most important tests that should be studied.

- Simulation and pilot plant

Once all the coating factors are revealed, simulation is a tool that can help the cement producers to determine whether application of the high emissivity coating will be cost effective. Another way to gain cement producer confidence is by checking the coating performance in a pilot plant. It must be noted that a pilot plant kiln is a smaller kiln than the actual one and the fuel used is liquefied petroleum gas (LPG) and therefore there are less alkaline corrosive gasses in the system.

# References

[1] W. Shen, L. Cao, Q. Li, W. Zhang, G. Wang, C. Li, Quantifying $CO_2$ emissions from China's cement industry, Renewable and Sustainable Energy Reviews 50 (2015) 1004-1012.

[2] A. Hasanbeigi, L. Price, E. Lin, Emerging energy-efficiency and $CO_2$ emission-reduction technologies for cement and concrete production: A technical review, Renewable and Sustainable Energy Reviews 16(8) (2012) 6220-6238.

[3] L. Shen, T. Gao, J. Zhao, L. Wang, L. Wang, L. Liu, F. Chen, J. Xue, Factory-level measurements on $CO_2$ emission factors of cement production in China, Renewable and Sustainable Energy Reviews 34 (2014) 337-349.

[4] A. Atmaca, R. Yumrutaş, Analysis of the parameters affecting energy consumption of a rotary kiln in cement industry, Applied Thermal Engineering 66(1) (2014) 435-444.

[5] N. Madlool, R. Saidur, N. Rahim, M. Kamalisarvestani, An overview of energy savings measures for cement industries, Renewable and Sustainable Energy Reviews 19 (2013) 18-29.

[6] Major countries in worldwide cement production from 2015 to 2019, US Geological Survey, USGS - Mineral Commodity Summaries 2020, 2020, p. 43.

[7] M. Garside, Cement production worldwide from 1995 to 2019, Global Cement Magazine, Pro Global Media, Surrey, UK, 2019, p. 11.

[8] M.F. Modest, Radiative heat transfer, Academic Press, Kidlington, Oxford, UK, 2013.

[9] T. Engin, V. Ari, Energy auditing and recovery for dry type cement rotary kiln systems- a case study, Energy Conversion and Management 46(4) (2005) 551-562.

[10] W.E. Lee, R.E. Moore, Evolution of *in situ* refractories in the 20th century, Journal of the American Ceramic Society 81(6) (1998) 1385-1410.

[11] G.C. Bye, Portland cement: composition, production and properties, Thomas Telford, Heron Quay, London, UK, 1999.

[12] H.F.W. Taylor, Cement Chemistry, Thomas Telford, Heron Quay, London, UK, 1997.

[13] A. Paul, D.D. Jayaseelan, S. Venugopal, E. Zapata-Solvas, J. Binner, B. Vaidhyanathan, A. Heaton, P.M. Brown, W.E. Lee, UHTC composites for hypersonic applications, American Ceramic Society Bulletin 91(1) (2012) 22-28.

[14] J. Binner, M. Porter, B. Baker, J. Zou, V. Venkatachalam, V.R. Diaz, A. D'Angio, P. Ramanujam, T. Zhang, T. Murthy, Selection, processing, properties and applications of ultra-high temperature ceramic matrix composites, UHTCMCs– a review, International Materials Reviews (2019) 1-56.

[15] R. Naslain, Design, preparation and properties of non-oxide CMCs for application in engines and nuclear reactors: an overview, Composites Science and Technology 64(2) (2004) 155-170.

[16] S. Caniglia, G.L. Barna, Handbook of industrial refractories technology: principles, types, properties and applications, William Andrew, Park Ridge, New York, USA, 1992.

[17] ASTM C71-12 Standard Terminology Relating to Refractories, ASTM International, West Conshohocken, PA, USA 2018.

[18] R. Sarkar, Refractory technology: Fundamentals and applications, CRC Press, The National Council of YMCAs of India, 2016.

[19] D.J. Bray, Toxicity of chromium compounds formed in refractories, American Ceramic Society Bulletin 64(7) (1985) 1012-1016.

[20] G. Liu, N. Li, W. Yan, C. Gao, W. Zhou, Y. Li, Composition and microstructure of a periclase–composite spinel brick used in the burning zone of a cement rotary kiln, Ceramics International 40(6) (2014) 8149-8155.

[21] S. Belgacem, H. Galai, H. Tiss, Qualitative and quantitative investigation of post–mortem cement refractory: The case of magnesia–spinel bricks, Ceramics International 42(16) (2016) 19147-19155.

[22] Y. Zhao, G. Cheng, Y. Xiang, F. Long, C. Dong, Thermodynamic study of the corrosion of refractories by sodium carbonate, Materials 11(11) (2018) 2197.

[23] C. Wyatt, Radiometric calibration: theory and methods, Elsevier, Oval Road, London, UK, 2012.

[24] R.W. Serth, Process heat transfer, Academic Press, Cambridge, MA, USA, 2010.

[25] J.H. Lienhard, A heat transfer textbook, Courier Dover Publications, Mineola, NY, USA, 2019.

[26] J.R. Simonson, Engineering heat transfer, Springer, NYC, NY, USA, 1988.

[27] T.S. Kuhn, Black-body theory and the quantum discontinuity, 1894-1912, University of Chicago Press, Chicago, IL, USA, 1987.

[28] J.R. Howell, M.P. Menguc, R. Siegel, Thermal radiation heat transfer, CRC Press, Boca Raton, FL, USA 2015.

[29] L. Tambara Jr, M. Cheriaf, J. Rocha, A. Palomo, A. Fernández-Jiménez, Effect of alkalis content on calcium sulfoaluminate (CSA) cement hydration, Cement and Concrete Research 128 (2020) 105953.

[30] M. Ali, S. Gopal, S. Handoo, Studies on the formation kinetics of calcium sulphoaluminate, Cement and Concrete Research 24(4) (1994) 715-720.

[31] W. Lan, F. Glasser, Hydration of calcium sulphoaluminate cements, Advances in Cement Research 8(31) (1996) 127-134.

[32] F. Bullerjahn, M. Zajac, M.B. Haha, CSA raw mix design: effect on clinker formation and reactivity, Materials and Structures 48(12) (2015) 3895-3911.

[33] L. Li, R. Wang, S. Zhang, Effect of curing temperature and relative humidity on the hydrates and porosity of calcium sulfoaluminate cement, Construction and Building Materials 213 (2019) 627-636.

[34] F. Winnefeld, B. Lothenbach, Hydration of calcium sulfoaluminate cements—experimental findings and thermodynamic modelling, Cement and Concrete Research 40(8) (2010) 1239-1247.

[35] F. Winnefeld, L.H. Martin, C.J. Müller, B. Lothenbach, Using gypsum to control hydration kinetics of CSA cements, Construction and Building Materials 155 (2017) 154-163.

[36] E. Gartner, H. Hirao, A review of alternative approaches to the reduction of $CO_2$ emissions associated with the manufacture of the binder phase in concrete, Cement and Concrete Research 78 (2015) 126-142.

[37] M. Schneider, M. Romer, M. Tschudin, H. Bolio, Sustainable cement production—present and future, Cement and Concrete Research 41(7) (2011) 642-650.

[38] P. Li, X. Gao, K. Wang, V.W. Tam, W. Li, Hydration mechanism and early frost resistance of calcium sulfoaluminate cement concrete, Construction and Building Materials 239 (2020) 117862.

[39] O. Canbek, S.T. Erdoğan, Influence of production parameters on calcium sulfoaluminate cements, Construction and Building Materials 239 (2020) 117866.

[40] Z. Kubba, G.F. Huseien, A.R.M. Sam, K.W. Shah, M.A. Asaad, M. Ismail, M.M. Tahir, J. Mirza, Impact of curing temperatures and alkaline activators on compressive strength and porosity of ternary blended geopolymer mortars, Case Studies in Construction Materials 9 (2018) e00205.

[41] W.K. Part, M. Ramli, C.B. Cheah, An overview on the influence of various factors on the properties of geopolymer concrete derived from industrial by-products, Construction and Building Materials 77 (2015) 370-395.

[42] A.A. Aliabdo, A.E.M.A. Elmoaty, H.A. Salem, Effect of cement addition, solution resting time and curing characteristics on fly ash based geopolymer concrete performance, Construction and Building Materials 123 (2016) 581-593.

[43] M. Schneider, Process technology for efficient and sustainable cement production, Cement and Concrete Research 78 (2015) 14-23.

[44] E. John, T. Matschei, D. Stephan, Nucleation seeding with calcium silicate hydrate–A review, Cement and Concrete Research 113 (2018) 74-85.

[45] U. Dewald, M. Achternbosch, Why more sustainable cements failed so far? Disruptive innovations and their barriers in a basic industry, Environmental Innovation and Societal Transitions 19 (2016) 15-30.

[46] H.-M. Ludwig, W. Zhang, Research review of cement clinker chemistry, Cement and Concrete Research 78 (2015) 24-37.

[47] P. Stemmermann, G. Beuchle, K. Garbev, U.C. Schweike, A new sustainable hydraulic binder based on calcium hydrosilicates, Proceedings of the 13th international congress on the chemistry of cement, Instituto de Ciencias de la Construcción, Madrid, Spain, 2011.

[48] J.R. Parsons, Lightweight refractory aggregate and process for making same, United Stated Patent Office, 3150989, 1964.

[49] F.H. Raymond, H.S.B. Charles, J.S. William, Refractory products and the production thereof, United States Patent Office, 3232772, 1966.

[50] C.L. Macey, R.J. Knauss, Low thermal conductivity magnesite-spinel brick and method, United States Patent, 4833109, 1989.

[51] J.-J.A. Cheng, W.A. Martinez, A.P. Hale, Lightweight tundish refractory composition, United States Patent Office, 3150989, 1991.

[52] G.E. Guazzoni, High-temperature spectral emittance of oxides of erbium, samarium, neodymium and ytterbium, Applied Spectroscopy 26(1) (1972) 60-65.

[53] J. Hellander, How high emissivity ceramic coatings function advantageously in furnace applications, Materials & Equipment/Whitewares: Ceramic Engineering and Science Proceedings (1991) 162-169.

[54] J. Hellander, Use of ceramic coatings to enhance performance of metal furnace components, Materials & Equipment/Whitewares: Ceramic Engineering and Science Proceedings (1991) 152-161.

[55] G. Neuer, Total normal and spectral emittance of refractory materials for high temperature ovens, Thermochimica acta 218 (1993) 211-219.

[56] C.E. Holcombe Jr, L.R. Chapman, High emissivity coating, United States Patents, 5668072, 1997.

[57] X. Li, T. Wang, R.T. Tonti, L. Edwards, Analysis of energy savings by painting a rotary kiln surface, (2007).

[58] R. Brandt, C. Bird, G. Neuer, Emissivity reference paints for high temperature applications, Measurement 41(7) (2008) 731-736.

[59] J. Staggs, H. Phylaktou, The effects of emissivity on the performance of steel in furnace tests, Fire Safety Journal 43(1) (2008) 1-10.

[60] BS 476-20 Fire tests on building materials and structures. , Part 20: method for the determination of fire resistance of elements of construction—general principles, BSI, 1987.

[61] BS 476-21 Fire tests on building materials and structures. , Part 21: Methods for determination of the fire resistance of loadbearing elements of construction., BSI, 1987.

[62] M. Dietrich, V. Verlotski, R. Vassen, D. Stöver, Metal-glass based composites for novel TBC-systems, Materialwissenschaft und Werkstofftechnik: Materials Science and Engineering Technology 32(8) (2001) 669-672.

[63] J. Huang, G. Song, H. Lv, Y. Li, Y. Sun, X. He, S. Zhang, Y. Fu, S. Du, Y. Li, Microstructure and thermal cycling behavior of $CeO_2$ coatings deposited by the electron beam physical vapor technique, Thin Solid Films 544 (2013) 270-275.

[64] N. Al Nasiri, N. Patra, D. Jayaseelan, W.E. Lee, Water vapour corrosion of rare earth monosilicates for environmental barrier coating application, Ceramics International 43(10) (2017) 7393-7400.

[65] E. Dayi, N. Al Nasiri, Diffusion study of rare-earth oxides into silica layer for environmental barrier coating applications, Journal of the European Ceramic Society 39(14) (2019) 4216-4222.

[66] K.N. Lee, D.S. Fox, N.P. Bansal, Rare earth silicate environmental barrier coatings for SiC/SiC composites and Si3N4 ceramics, Journal of the European Ceramic Society 25(10) (2005) 1705-1715.

[67] D. Zhang, Z. Zhao, B. Wang, S. Li, J. Zhang, Investigation of a new type of composite ceramics for thermal barrier coatings, Materials & Design 112 (2016) 27-33.

[68] X. Cao, R. Vassen, D. Stöver, Ceramic materials for thermal barrier coatings, Journal of the European Ceramic Society 24(1) (2004) 1-10.

[69] S. Sodeoka, M. Suzuki, T. Inoue, K. Ueno, S. Oki, Thermal and mechanical properties of plasma sprayed ZrO 2-CeO 2-Y 2 O 3 coatings plasma, Thermal spray: Practical solutions for engineering problems (1996) 295-302.

[70] J. Holmes, B. Pilsner, Cerium oxide stabilized thermal barrier coatings, Thermal Spray: Advances in Coatings Technology (1988) 259-270.

[71] D.L. Chubb, A.T. Pal, M.O. Patton, P.P. Jenkins, Rare earth doped high temperature ceramic selective emitters, Journal of the European Ceramic Society 19(13-14) (1999) 2551-2562.

[72] S. Ding, J. Mao, X. Zeng, X. Cheng, Enhanced infrared emission property of NiCr spinel coating doped with $MnO_2$ and rare-earth oxides, Surface and Coatings Technology 344 (2018) 418-422.

[73] W. Tan, C.A. Petorak, R.W. Trice, Rare-earth modified zirconium diboride high emissivity coatings for hypersonic applications, Journal of the European Ceramic Society 34(1) (2014) 1-11.

[74] W. Tan, M. Adducci, C. Petorak, B. Thompson, A.E. Brenner, R.W. Trice, Effect of rare-earth dopant (Sm) concentration on total hemispherical emissivity and ablation resistance of $ZrB_2$/SiC coatings, Journal of the European Ceramic Society 36(16) (2016) 3833-3841.

[75] F. Liu, X. Cheng, J. Mao, Q. Li, X. Zeng, Effects of rare-earth oxide doping on the thermal radiation performance of $HfO_2$ coating, Ceramics International 45(10) (2019) 13004-13010.

[76] J. Huang, Y. Li, G. Song, X. Zhang, Y. Sun, X. He, S. Du, Highly enhanced infrared spectral emissivity of porous $CeO_2$ coating, Materials Letters 85 (2012) 57-60.

[77] J. Huang, C. Fan, G. Song, Y. Li, X. He, X. Zhang, Y. Sun, S. Du, Y. Zhao, Enhanced infrared emissivity of $CeO_2$ coatings by La doping, Applied Surface Science 280 (2013) 605-609.

[78] E.Y. Sako, H.D. Orsolini, M. Moreira, V.C. Pandolfelli, High Temperature Ceramic Coatings for Energy Saving Applications, Unified International Technical Conference on Refractories (UNITECR) Yokohama, Japan, 2019, pp. 532-535.

[79] D. De Sousa Meneses, P. Melin, L. del Campo, L. Cosson, P. Echegut, Apparatus for measuring the emittance of materials from far infrared to visible wavelengths in extreme conditions of temperature, Infrared Physics & Technology 69 (2015) 96-101.

[80] R. Simmat, C. Dannert, B. Bernard, V. Finke, L. Guaita, Measuring the effect of coatings on the heat transfer through refractory linings in the laboratory, Proceedings 61st International Colloquium on Refractories, Aachen, Germany, 2018, pp. 157-159.

[81] R. Simmat, C. Dannert, S. Otto, V. Finke, A. Mezquis, S. Ferrer, I. Celades, L. Guaita, Effect of a ceramic coating on the heat loss through the refractory walls and on the hot refractory surface stability of a ceramic roller kiln, Unified International Technical Conference on Refractories (UNITECR) Yokohama, Japan, 2019, pp. 528-531.

[82] X. He, Y. Li, L. Wang, Y. Sun, S. Zhang, High emissivity coatings for high temperature application: progress and prospect, Thin Solid Films 517(17) (2009) 5120-5129.

[83] H. McMahon, Thermal radiation from partially transparent reflecting bodies, Journal of the Optical Society of America (JOSA) 40(6) (1950) 376-380.

[84] W. Coblentz, Supplementary Investigations of Infrared Spectra (The Carnegic Institution), Washington, Publication (97) (1908) 16.

[85] R. Gardon, The emissivity of transparent materials, Journal of the American Ceramic Society 39(8) (1956) 278-285.

[86] H.O. McMahon, Thermal radiation characteristics of some glasses, Journal of the American Ceramic Society 34(3) (1951) 91-96.

[87] B. Kellett, Transmission of radiation through glass in tank furnaces–correction, Journal of the Societh Glass Technology 37(178) (1953) 268.

[88] M. Czerny, L. Genzel, Depth to which diffuse radiation penetrates glass, Glastech. Ber. 25(5) (1952) 134-39.

[89] W. Geffcken, Transmission of heat in glass at high temperature I, Glastech. Ber. 25(12) (1952) 392-396.

[90] M. Low, Infra-red emission spectra of minerals, Nature 208(5015) (1965) 1089-1090.

[91] C. Christiansen, T. Stolberg-Rohr, A. Fateev, S. Clausen, High temperature and high pressure gas cell for quantitative spectroscopic measurements, Journal of Quantitative Spectroscopy and Radiative Transfer 169 (2016) 96-103.

[92] S. Clausen, A. Morgenstjerne, O. Rathmann, Measurement of surface temperature and emissivity by a multitemperature method for Fourier-transform infrared spectrometers, Applied optics 35(28) (1996) 5683-5691.

[93] S. Clausen, Spectral emissivity of surface blackbody calibrators, International Journal of Thermophysics 28(6) (2007) 2145-2154.

[94] D. Chase, The sensitivity and limitations of condensed phase infrared emission spectroscopy, Applied Spectroscopy 35(1) (1981) 77-81.

[95] F.J. Deblase, S. Compton, Infrared emission spectroscopy: a theoretical and experimental review, Applied spectroscopy 45(4) (1991) 611-618.

[96] J. Markham, K. Kinsella, R. Carangelo, P. Best, P. Solomon, Bench top fourier transform infrared based instrument for simultaneously measuring surface spectral emittance and temperature, Review of Scientific Instruments 64 (1993) 2515-22.

[97] J.R. Markham, P. Solomon, P. Best, An FT-IR based instrument for measuring spectral emittance of material at high temperature, Review of Scientific Instruments 61(12) (1990) 3700-3708.

[98] J.R. Markham, P.E. Best, P.R. Solomon, Spectroscopic method for measuring surface temperature that is independent of material emissivity, surrounding radiation sources, and instrument calibration, Applied Spectroscopy 48(2) (1994) 265-270.

[99] ASTM C835-06 Standard test method for total hemispherical emittance of surfaces up to 1400°C, West Conshohocken, PA, 2006.

[100] B.P. Keller, S.E. Nelson, K.L. Walton, T.K. Ghosh, R.V. Tompson, S.K. Loyalka, Total hemispherical emissivity of Inconel 718, Nuclear Engineering and Design 287 (2015) 11-18.

[101] A.J. Gordon, K.L. Walton, T.K. Ghosh, S.K. Loyalka, D.S. Viswanath, R.V. Tompson, Hemispherical total emissivity of Hastelloy N with different surface conditions, Journal of Nuclear Materials 426(1-3) (2012) 85-95.

[102] R.K. Maynard, T.K. Ghosh, R.V. Tompson, D.S. Viswanath, S.K. Loyalka, Total hemispherical emissivity of potential structural materials for very high temperature reactor systems: Hastelloy X, Nuclear Technology 172(1) (2010) 88-100.

[103] C.B. Azmeh, K.L. Walton, T.K. Ghosh, S.K. Loyalka, D.S. Viswanath, R.V. Tompson, Total hemispherical emissivity of grade 91 ferritic alloy with various Surface conditions, Nuclear Technology 195(1) (2016) 87-97.

[104] F.N. Al Zubaidi, K.L. Walton, R.V. Tompson, T.K. Ghosh, S.K. Loyalka, The effect of long-term oxidation on the total hemispherical emissivity of type 316L stainless steel, Nuclear Technology 205(6) (2019) 790-800.

[105] B. Rousseau, J. Brun, D.D.S. Meneses, P. Echegut, Temperature measurement: Christiansen wavelength and blackbody reference, International Journal of Thermophysics 26(4) (2005) 1277-1286.

[106] P.P. Woskov, S. Sundaram, Thermal return reflection method for resolving emissivity and temperature in radiometric measurements, Journal of Applied Physics 92(10) (2002) 6302-6310.

[107] J.S. McCloy, J.V. Crum, S. Sundaram, R. Slaugh, P.P. Woskov, High temperature millimeter wave radiometric and interferometric measurements of slag-refractory interaction for application to coal gasifiers, Journal of Infrared, Millimeter, and Terahertz Waves 32(11) (2011) 1337-1349.

[108] J. McCloy, S. Sundaram, J. Matyas, P. Woskov, Simultaneous measurement of temperature and emissivity of lunar regolith simulant using dual-channel millimeter-wave radiometry, Review of Scientific Instruments 82(5) (2011) 054703.

[109] S. Chotchutima, K. Kangvansaichol, S. Tudsri, P. Sripichitt, Effect of spacing on growth, biomass yield and quality of Leucaena (Leucaena leucocephala (Lam.) de Wit.) for renewable energy in Thailand, Journal of Sustainable Bioenergy Systems 3(01) (2013) 48.

[110] N. Li, E. Vainio, L. Hupa, M. Hupa, E. Coda Zabetta, High-temperature corrosion of refractory materials in biomass and waste combustion: method development and tests with alumina refractory exposed to a $K_2CO_3$–KCl mixture, Energy & Fuels 31(9) (2017) 10046-10054.

[111] E. Schlegel, C.G. Aneziris, U. Fischer, Alkali corrosion of refractory installations in cement kilns—comparison of theory, laboratory tests and practice, Proceeding 52th International Colloquium on Refractories, Aachen, Germany, 2009, pp. 23-24.

[112] E. Schlegel, C.G. Aneziris, U. Fischer, Alkali corrosion in cement rotary kilns, International Ceramic Review 58 (2009) 6-8.

[113] T. Honda, H. Kozuka, Y. Tsuchiya, Y. Mizuno, K. Tokunaga, S. Ota, Damages of refractory bricks in cement rotary kiln, Journal of the Ceramic Society of Japan, Supplement Journal of the Ceramic Society of Japan, Supplement 112-1, PacRim5 Special Issue, The Ceramic Society of Japan, 2004, pp. S1272-S1277.

[114] C. Aneziris, U. Fischer, E. Schlegel, Illustration of alkali corrosion mechanisms in high temperature thermal insulation materials, Unified International Technical Conference on Refractories (UNITECR) Dresden, Germany, 2007, pp. 117-120.

[115] Phase equillibria diagrams online database (NIST standard reference database 31), The American Ceramic Society and Natioanl Institute of Standards and Technology, 2020, Figure number 4673, www.nist.gov/srd/nist31.cfm.

[116] Phase equillibria diagrams online database (NIST standard reference database 31), The American Ceramic Society and Natioanl Institute of Standards and Technology, 2020, Figure number 4713, www.nist.gov/srd/nist31.cfm.

[117] G.E. Gonçalves, G.R.C. Pacheco, M.A.d.M. Brito, S.L.C.d. Silva, V.d.F.C. Lins, Influence of magnesia in the infiltration of magnesia-spinel refractory bricks by different clinkers, Rem: Revista Escola de Minas 68(4) (2015) 409-415.

[118] P. Bartha, J. Sodje, Degradation of refractories in rotary cement kilns fired with waste fuels, China's Refractories 5 (2001) 62-71.

[119] J. Poirier, Rigaud, M, Corrosion of refractories: the impacts of corrosion, Medialogik, Karlsruhe, Germany, 2018.

[120] U. Fischer, C. Aneziris, E. Schlegel, Corrosion problems of refractories due to the use of secondary fuels, Refractories Manual (2008) 28-33.

[121] M. Sassi, E. Bilbao, J. Poirier, Alkali and slag resistance of calcium hexa-aluminate raw material, Unified International Technical Conference on Refractories (UNITECR) Yokohama Japan, 2019.

[122] N. Takuya, F. Mikiya, S. Masaru, T. Nobuyuki, Corrosion of polycrystalline wool by alkaline vapor, Unified International Technical Conference on Refractories (UNITECR) Yokohama, Japan, 2019.

[123] W.E. Lee, S. Zhang, Direct and indirect slag corrosion of oxide and oxide-c refractories, VII International Conference on Molten Slags Fluxes and Salts, 2004, pp. 309-319.

[124] W.E. Lee, S. Zhang, Melt corrosion of oxide and oxide–carbon refractories, International materials reviews 44(3) (1999) 77-104.

[125] D.S. Campbell, L. Maissel, R. Glang, Handbook of thin film technology, McGraw-Hill, New York, 1970) Ch 12 (1970) 3.

[126] P. Chalker, S. Bull, D. Rickerby, A review of the methods for the evaluation of coating-substrate adhesion, Materials Science and Engineering: A 140 (1991) 583-592.

[127] S. Chiang, D. Marshall, A. Evans, A simple method for adhesion measurements, Surfaces and Interfaces in Ceramic and Ceramic—Metal Systems, Springer1981, pp. 603-617.

[128] P.C. Jindal, D.T. Quinto, G.J. Wolfe, Adhesion measurements of chemically vapor deposited and physically vapor deposited hard coatings on WC Co substrates, Thin Solid Films 154(1-2) (1987) 361-375.

[129] D.T. Quinto, G.J. Wolfe, P.C. Jindal, High temperature microhardness of hard coatings produced by physical and chemical vapor deposition, Thin solid films 153(1-3) (1987) 19-36.

[130] A. Perry, Scratch adhesion testing: a critique, Surface engineering 2(3) (1986) 183-190.

[131] A. Perry, Adhesion studies of ion-plated TiN on steel, Thin Solid Films 81(4) (1981) 357-366.

[132] ASTM D4060-19Standard test method for abrasion resistance of organic coatings by the taber abraser, West Conshohocken, PA, USA, 2010.

[133] ASTM C704/C704M-15Abrasion resistance of refractory materials at room temperature, West Conshohocken, PA, 2019.

[134] R.G. Wellman, M.J. Deakin, J.R. Nicholls, The effect of TBC morphology and aging on the erosion rate of EB-PVD TBCs, Tribology International 38(9) (2005) 798-804.

[135] M. Shinozaki, T.W. Clyne, A methodology, based on sintering-induced stiffening, for prediction of the spallation lifetime of plasma-sprayed coatings, Acta Materialia 61(2) (2013) 579-588.

[136] C. Ying, L. Bei, D. Shijie, W. Huihu, X. Zhixiong, Thermal shock failure mechanism of nanostructured zirconia coating by atmospheric plasma spraying, Rare Metal Materials and Engineering 46(3) (2017) 601-605.

[137] M. Vippola, J. Keränen, X. Zou, S. Hovmöller, T. Lepistö, T. Mäntylä, Structural characterization of aluminum phosphate binder, Journal of the American Ceramic Society 83(7) (2000) 1834-1836.

[138] D. Chen, L. He, S. Shang, Study on aluminum phosphate binder and related $Al_2O_3$–SiC ceramic coating, Materials Science and Engineering: A 348(1-2) (2003) 29-35.

[139] E. Leivo, M. Vippola, P. Sorsa, P. Vuoristo, T. Mäntylä, Wear and corrosion properties of plasma sprayed $Al_2O_3$ and $Cr_2O_3$ coatings sealed by aluminum phosphates, Journal of Thermal Spray Technology 6(2) (1997) 205-210.

[140] B. Formanek, K. Szymański, B. Szczucka-Lasota, A. Włodarczyk, New generation of protective coatings intended for the power industry, Journal of Materials Processing Technology 164 (2005) 850-855.

[141] V.A. Abyzov, Lightweight refractory concrete based on aluminum-magnesium-phosphate binder, Procedia Engineering 150 (2016) 1440-1445.

[142] R.K. Brow, Nature of alumina in phosphate glass: I, properties of sodium aluminophosphate glass, Journal of the American Ceramic Society 76(4) (1993) 913-918.

[143] T. Minami, J.D. Mackenzie, Thermal expansion and chemical durability of phosphate glasses, Journal of the American Ceramic Society 60(5-6) (1977) 232-235.

[144] H.T. Handal, V. Thangadurai, Evaluation of chemical stability, thermal expansion coefficient, and electrical properties of solid state and wet-chemical synthesized Y and Mn-codoped $CeO_2$ for solid oxide fuel cells, Journal of Power Sources 243 (2013) 458-471.

[145] D.C. Harris, Materials for infrared windows and domes: properties and performance, SPIE Press, Bellingham, WA, USA, 1999.

[146] S. Ebert, R. Mücke, D. Mack, R. Vaßen, D. Stöver, T. Wobst, S. Gebhard, Failure mechanisms of magnesia alumina spinel abradable coatings under thermal cyclic loading, Journal of the European Ceramic Society 33(15-16) (2013) 3335-3343.

[147] V.R. Sastri, J.R. Perumareddi, V.R. Rao, G.V.S. Rayudu, J.C. Bünzli, Modern aspects of rare earths and their complexes, Elsevier, Sara burgerhartstraat, Amsterdam, Netherlands, 2003.

[148] B.D. Cullity, Elements of X-ray Diffraction, Addison-Wesley Publishing, Reading, MA, USA, 1956.

[149] C.R. Brundle, L. Wilson, C.A. Evans, S. Wilson, G. Wilson, Encyclopedia of materials characterization: surfaces, interfaces, thin films, Manning Publishing, Greewich, CT, USA, 1992.

[150] J.I. Goldstein, D.E. Newbury, J.R. Michael, N.W. Ritchie, J.H.J. Scott, D.C. Joy, Scanning electron microscopy and X-ray microanalysis, Springer, Berlin/Heidelberg, Germany, 2017.

[151] J.W. Dodd, K.H. Tonge, B.R. Currell, Thermal methods, John Wiley & Sons, Hoboken, NJ, USA, 1987.

[152] J.B. Nelson, D. Riley, An experimental investigation of extrapolation methods in the derivation of accurate unit-cell dimensions of crystals, Proceedings of the Physical Society 57(3) (1945) 160.

[153] K. Siegbahn, C. Nordling, ESCA, atomic, molecular and solid state structure studied by means of electron spectroscopy, Almqvist and Wiksell, Tryckeri AB, Uppsala, Sweden, 1967.

[154] C.B. Carter, D.B. Williams, Transmission electron microscopy: Diffraction, imaging, and spectrometry, Springer, Picassopl, Basel, Switzerland, 2016.

[155] D.B. Williams, C.B. Carter, Transmission electron microscopy: a textbook for materials science, Springer science and Business media, LLC, NY, USA, 1996.

[156] ASTM C20-00 Standard test methods for apparent porosity, water absorption, apparent specific gravity, and bulk density of burned refractory brick and shapes by boiling water, West Conshohocken, PA, USA, 2015.

[157] W.D. Kingery, Introduction to ceramics, Wiley, Hoboken, NJ, USA, 1976.

[158] A. Ramezani, S. Nemat, S. Emami, Effects of the size of expanded polystyrene as a pore-former on the properties of insulating firebricks, Ceramics International 44(6) (2018) 6641-6644.

[159] M. Sutcu, S. Akkurt, A. Bayram, U. Uluca, Production of anorthite refractory insulating firebrick from mixtures of clay and recycled paper waste with sawdust addition, Ceramics International 38(2) (2012) 1033-1041.

[160] J.P. Bennett, K.S. Kwong, C.A. Powell, R. Krabbe, H. Thomas, Improved refractory materials for slagging gasifiers in IGCC power systems, Albany Research Center (ARC), Albany, OR, 2005.

[161] A. Starzacher, Slagging test using a modified DIN-1069 method and a more widely applicable new spalling test, Radex Rundschau (2) (1970) 140-157.

[162] J.M. Chiou, D.D.L. Chung, Improvement of the temperature resistance of aluminium-matrix composites using an acid phosphate binder, Journal of Materials Science 28(6) (1993) 1447-1470.

[163] A. Durif, Crystal chemistry of condensed phosphates, Springer Science & Business Media, Berlin, Germany, 2013.

[164] R.D. Johnson III, NIST 101. Computational chemistry comparison and benchmark database, Gaithersburg, MD, USA, 1999.

[165] B.N. Taylor, P.J. Mohr, M. Douma, The NIST Reference on constants, units, and uncertainty, available online from: physics. nist. gov/cuu/index, 2007.

[166] E. Bêche, P. Charvin, D. Perarnau, S. Abanades, G. Flamant, Ce 3d XPS investigation of cerium oxides and mixed cerium oxide ($Ce_xTi_yO_z$), Surface and Interface Analysis 40(3-4) (2008) 264-267.

[167] G. Praline, B.E. Koel, R. Hance, H.-I. Lee, J. White, X-ray photoelectron study of the reaction of oxygen with cerium, Journal of Electron Spectroscopy and Related Phenomena 21(1) (1980) 17-30.

[168] E. Paparazzo, G. Ingo, N. Zacchetti, X-ray induced reduction effects at $CeO_2$ surfaces: An x-ray photoelectron spectroscopy study, Journal of Vacuum Science & Technology A: Vacuum, Surfaces, and Films 9(3) (1991) 1416-1420.

[169] M. Romeo, K. Bak, J. El Fallah, F. Le Normand, L. Hilaire, XPS study of the reduction of cerium dioxide, Surface and Interface Analysis 20(6) (1993) 508-512.

[170] B. Glorieux, R. Berjoan, M. Matecki, A. Kammouni, D. Perarnau, XPS analyses of lanthanides phosphates, Applied Surface Science 253(6) (2007) 3349-3359.

[171] R. Maher, G. Kerherve, D. Payne, X. Yue, P. Connor, J. Irvine, L. Cohen, The reduction properties of M–doped (M= Zr, Gd) $CeO_2$/YSZ scaffolds Co–infiltrated with nickel, Energy Technology 6(10) (2018) 2045-2052.

[172] X. Yu, G. Li, XPS study of cerium conversion coating on the anodized 2024 aluminum alloy, Journal of Alloys and Compounds 364(1-2) (2004) 193-198.

[173] Y. Li, L. Chen, L. Hong, K. Ran, Y. Zhan, Q. Chen, Fabrication of porous silicon carbide ceramics at low temperature using aluminum dihydrogen phosphate as binder, Journal of Alloys and Compounds 785 (2019) 838-845.

[174] J. Juthapakdeeprasert, W. Lerdprom, D. De Sousa Meneses, D.D. Jayaseelan, W.E. Lee, $CeO_2$ and $CePO_4$ – containing high emissvity coating for basic refractory bricks, 61th International Colloquium on Refractories, Aachen, Germany, 2018, pp. 153-156.

[175] C.A. Schneider, W.S. Rasband, K.W. Eliceiri, NIH Image to ImageJ: 25 years of image analysis, Nature Methods 9(7) (2012) 671-675.

[176] T. Masui, H. Hirai, N. Imanaka, G. Adachi, Characterization and thermal behavior of amorphous cerium phosphate, Physica Status Solidi (a) 198(2) (2003) 364-368.

[177] B. Bunker, G. Arnold, J.A. Wilder, Phosphate glass dissolution in aqueous solutions, Journal of Non-Crystalline Solids 64(3) (1984) 291-316.

[178] P.F. Weck, P.-A. Juan, R.m. Dingreville, E. Kim, Density functional analysis of fluorite-structured (Ce, Zr) $O_2$/ $CeO_2$ interfaces, The Journal of Physical Chemistry C 121(27) (2017) 14678-14687.

[179] N. Adelstein, B.S. Mun, H.L. Ray, P.N. Ross Jr, J.B. Neaton, L.C. De Jonghe, Structure and electronic properties of cerium orthophosphate: Theory and experiment, Physical Review B 83(20) (2011) 205104.

[180] S. Al-Ani, I. Al-Hassany, Z. Al-Dahan, The optical properties and a.c. conductivity of magnesium phosphate glasses, Journal of Materials Science 30(14) (1995) 3720-3729.

[181] J. Ravindran, S. Krishnan, Studies on thermal analysis of cement rotary kiln based on clinker coating materials on refractories, energy and monetary savings, International Congress on Recent Development in Engineering and Technology (RDET), Kuala Lumpur, Malasia, 2016.

[182] J. Brun, L. Del Campo, D. De Sousa Meneses, P. Echegut, Infrared optical properties of α-alumina with the approach to melting: γ-like tetrahedral structure and small polaron conduction, Journal of Applied Physics 114(22) (2013) 223501.

[183] J. Jones, P. Mason, A. Williams, A compilation of data on the radiant emissivity of some materials at high temperatures, Journal of the Energy Institute 92(3) (2019) 523-534.

[184] J. Devreese, Moles agitat mentem: ontwikkelingen in de fysika van de vaste stof, Technische Hogeschool Eindhoven, Eindhoven, Netherlands, 1979.

[185] N.I. Santha, M.T. Sebastian, P. Mohanan, N.M. Alford, K. Sarma, R.C. Pullar, S. Kamba, A. Pashkin, P. Samukhina, J. Petzelt, Effect of doping on the dielectric properties of cerium oxide in the microwave and far-infrared frequency range, Journal of the American Ceramic Society 87(7) (2004) 1233-1237.

[186] H. Deng, J. Wang, R. Callender, W. Ray, Relationship between bond stretching frequencies and internal bonding for [$^{16}O_4$]-and [$^{18}O_4$] phosphates in aqueous solution, The Journal of Physical Chemistry B 102(18) (1998) 3617-3623.

[187] X. Yu, D.E. Day, G.J. Long, R.K. Brow, Properties and structure of sodium-iron phosphate glasses, Journal of Non-Crystalline Solids 215(1) (1997) 21-31.

[188] A. Marino, S. Arrasmith, L. Gregg, S. Jacobs, G. Chen, Y. Duc, Durable phosphate glasses with lower transition temperatures, Journal of Non-Crystalline Solids 289(1-3) (2001) 37-41.

[189] X. Fang, C.S. Ray, A. Moguš-Milanković, D.E. Day, Iron redox equilibrium, structure and properties of iron phosphate glasses, Journal of Non-Crystalline Solids 283(1-3) (2001) 162-172.

[190] S. Sameshima, M. Kawaminami, Y. Hirata, Thermal expansion of rare-earth-doped ceria ceramics, Journal of the Ceramic Society of Japan 110(1283) (2002) 597-600.

[191] Y. Hikichi, T. Nomura, Y. Tanimura, S. Suzuki, M. Miyamoto, Sintering and properties of monazite-type $CePO_4$, Journal of the American Ceramic Society 73(12) (1990) 3594-3596.

[192] Phase equillibria diagrams online database (NIST standard reference database 31), The American Ceramic Society and Natioanl Institute of Standards and Technology, 2020, Figure number 13494, www.nist.gov/srd/nist31.cfm.

[193] I. Szczygiel, The system $CePO_4$–$K_3PO_4$, Thermochimica Acta 370(1-2) (2001) 125-128.

[194] D.G. Kim, E. Moosavi-Khoonsari, I.-H. Jung, Thermodynamic modeling of the $K_2O$-$Al_2O_3$ and $K_2O$-MgO-$Al_2O_3$ systems with emphasis on β-and β''-aluminas, Journal of the European Ceramic Society 38(9) (2018) 3188-3200.

[195] J. Park, D.H. Kim, S.J. Park, T.G. Lee, M. Im, J.S. Kim, S. Nahm, Effects of $K_2O$ evaporation on the structural properties of $KSbO_3$ compounds, Journal of the American Ceramic Society 99(7) (2016) 2229-2232.

[196] G.H. Zhang, W.W. Zheng, S. Jiao, K.C. Chou, Influences of $Na_2O$ and $K_2O$ additions on electrical conductivity of CaO-$SiO_2$-($Al_2O_3$) melts, ISIJ International 57(12) (2017) 2091-2096.

[197] Phase equillibria diagrams online database (NIST standard reference database 31), The American Ceramic Society and Natioanl Institute of Standards and Technology, 2020, Figure number 16486-A, www.nist.gov/srd/nist31.cfm.

[198] Phase equillibria diagrams online database (NIST standard reference database 31), The American Ceramic Society and Natioanl Institute of Standards and Technology, 2020, Figure number 16486-C, www.nist.gov/srd/nist31.cfm.

[199] Phase equillibria diagrams online database (NIST standard reference database 31), The American Ceramic Society and Natioanl Institute of Standards and Technology, 2020, Figure number 9973-O, www.nist.gov/srd/nist31.cfm.